Selective Hydrogenation of Butadiene over Non-noble Bimetallic Catalysts

Zhao Wang

Université Pierre et Marie Curie

Ecole Doctorale de Physique et Chimie des Matériaux

Laboratoire de Réactivité de Surface

Selective Hydrogenation of Butadiene over Non-noble Bimetallic Catalysts

Par : **Zhao WANG**

Thèse de doctorat de **CHIMIE**

Dirigée par Catherine LOUIS

Présentée et soutenue publiquement le 26 Juin 2017 devant un jury composé de :

Laurent PICCOLO	**Chargé de recherche HDR (IRCELyon)**	**Rapporteur**
Catherine ESPECEL	**Maitre de conférences HDR (IC2MP)**	**Rapporteur**
Petra de JONGH	**Professeur (Utrecht University)**	**Examinatrice**
Antoine HUGON	**Ingénieur (IFPEN)**	**Examinateur**
Isabelle LISIECKI	**Directrice de recherche (UPMC)**	**Examinatrice**
Laurent DELANNOY	**Maitre de conférences (UPMC)**	**Examinateur**
Catherine LOUIS	**Directrice de recherche (UPMC)**	**Directrice de thèse**

"*Good good study, day day up*."

Chinese aphorism

Acknowledgements

This work was carried out at the Laboratoire de Réactivité de Surface (UMR 7197) of Université Pierre et Marie Curie (UPMC). My first thank goes to the **China Scholarship Council (CSC)** for the funding of this PhD research.

I would like to thank Dr. **Claire-Marie Pradier** and Prof. **Hélène Pernot** for offering me access to the laboratory and research facilities. Without their support it would not be possible to perform this research.

I would like to thank my thesis committee: Dr. **Laurent Piccolo**, Dr. **Catherine Especel**, Prof. **Petra de Jongh**, Dr. **Antoine Hugon** and Dr. **Isabelle Lisieki** for their willingness to read and judge this thesis.

I would like to express my gratitude to my two supervisors: Dr. **Catherine Louis**, who provided me the opportunity to join her team as intern, for her patience, for her continuous support, for her guidance that greatly helped me in all the time of research and writing of this thesis; Dr. **Laurent Delannoy**, who introduced me into the field of catalytic selective hydrogenation, for his brilliant propositions when we met scientific problems, for his well organization throughout my PhD study. Thank you to my supervisors for your kind helps and useful advises that make me have a wonderful PhD experience.

I would like to thank **Guillaume Wang**, **Sandra Casale** and **Dalil Brouri** for their contribution to transmission electron microscopy (TEM) characterization, **Christophe Calers** for the XPS analyses, **Jean-Marc Krafft** for the experiments of DRIFTS and Raman, **Juliette Blanchard** for the DRX analyses, **Cyril Thomas** for the characterization by H_2 chemisorption, **Xavier Carrier** for the experiment of Thermogravimetric Analysis (TGA), **Cyril Domingos** for the temperature program reduction (TPR) experiments.

I would like to thank **Sabine Même**. Thank you for frequent visiting my office, for teaching me French. I would like also thank **Annie Mettendorff** for her kind help when I met some problems in the lab and for her encouragement.

I would like express my joyful and happiness for having friends with PhD students and post-doctorates. Staying with you always make me fell recharged and keep pace with my

thesis: **Gode, Jane, Cédric, Tesnim, Camella, Kim, Antoine, Antonio, Xiaojing, Sarah, Longfei, Lu** and **Miao**. I would also like to thank **Tiago, Yuiry, Diaa, Mariame, Olfa, Achraf** for your kindness.

I would like also thank my friends: **Tuo** and **Meilin**, for helping me out of the hardest time living in Paris; **Association de Boursiers CSC en Ile de France (ABCF)**, for offering me a colorful life in France; **Guangfang**, **Long**, **Tian**, **Yi**, **Xinyue** and **Yang,** for your encouragement.

I would like thank my family: my parents, my sisters and brothers, specially, my wife (**Xiaoyue**) and my son (**Jiarui**) for supporting me spiritually throughout writing this thesis and my life in general.

Last but not least, I would like to thank everyone in the **Laboratoire de Réactivité de Surface (UMR 7197)**. It was great sharing laboratory with all of you during the last four years.

Chapter 1: Introduction

Chapter 1: Introduction

1. Background on selective unsaturated hydrocarbons hydrogenation

In our modern life, we are surrounded by different kinds of polymers, such as plastic containers, furniture, shell of most electronic products and synthetic fabric. These organic products are mainly produced through catalytic polymerization reactions using unsaturated hydrocarbons, especially alkenes, as the raw materials. For instance, ethylene is employed to produce polyethylene, which could be the plastic-based materials; propylene is usually used to produce polypropylene-based materials [1]; Moreover, but-1- and -2-enes, isobutenes and isopentene are also very important hydrocarbons raw materials used in various fields of organic industry e.g., 1-butene can be used as a co-monomer for sec-butyl alcohol, maleic anhydride and polybutylene preparation; 2-butene is used as alkylating agent for the production of high octane gasoline, ethyl methyl ketone and maleic anhydride; the isobutenes and isopentene are mainly used in the field of tert-butyl and tert-pentyl synthesis [2]. The requirement of these raw alkenes for industry can be demonstrated by the dynamic growth of their world output. The demand in ethylene, which is the largest basic chemical building blocks, was only 80.5 million tons in 1998, ~175 in 2015 and the output predicted for 2020 is above 200 million tons [3]. Propylene is expanding at a rapid pace, which is 47 million tons in 1998, ~125 in 2015 and the values predicted for 2020 is ~160 million tons [3].

The unsaturated hydrocarbons are synthesized by cracking of petroleum hydrocarbons including heavy liquid fractions i.e., crude oil, [4]. However, the petroleum hydrocarbons are cracked at high temperature, which usually results in the formation of alkynes or dienes as impurities. i.e., 0.5 to 3% of acetylene in ethylene, 2 to 8% of propyne and propadiene in propene [5] and 0.3 to 6.0% of residual butadiene in butenes [6]. These impurities can poison the catalysts used for the alkenes polymerization reactions [7]. For example, during the 2-butenes polymerization, the 2-butyne impurity in the butenes feed reacts with the $Cp^*_2ScCH_3$ [$Cp^*=(\eta^5\text{-}C_5Me_5)$] catalyst and forms $Cp^*_2ScC(CH_3)=C(CH_3)_2$, no more further reaction can be observed on the catalytic surface [8]. The reaction as follows:

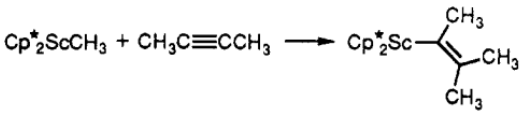

As a result, the contents of alkyne and diene impurities in the feed raw alkenes materials must be controlled and be less than 10, 5, 2 or even 1 ppm, depending on the final polymer products [9-12]. For instance, the polymer-grade ethylene product should not contain more 5 ppm of acetylene [13].

Basically, there are three main paths to remove or transform the alkynes and dienes impurities, (i), remove such impurities by fractional distillation. This method is uneconomic with high energy consumption [14]; (ii), Extract them from alkene stream by solvent extraction [13, 15] or metal-organic frameworks (MOF) adsorption [16] and recover them as a product. However, these two methods are limited considering the safety problems as a high alkyne/dienes partial pressure can be reached in the solvent extraction facility [13] and the low efficiency of the MOF adsorption as the high requirement proposed by industry and environment [16]; (iii), Convert the impurities into useful products by selective catalytic hydrogenation, which is the most widely used method for reducing the concentration of alkynes and dienes impurities. Supported metals catalysts are designed to semi-hydrogenate alkynes and dienes into alkenes, perfectly without any alkanes and oligomers formation, such that there is a net increase in the amount of alkenes (Figure 1-1). As a result, an ideal catalyst for selective hydrogenation should satisfy the low activation barrier for alkynes/dienes conversion (high activity), very limited alkanes formation (no overhydrogenation; high selectivity) and should not favor the formation of oligomers, which are responsible for catalysts deactivation by fouling, through C-C coupling (high stability) [17]. Besides that, considering the industrial requirement for polymer synthesis, the catalysts for selective hydrogenation of alkyne and dienes should also meet a particular set of requirements, such as: low price and easy preparation and regeneration.

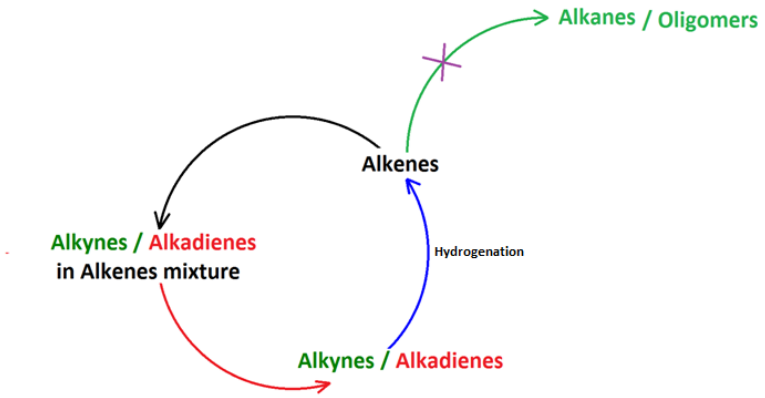

Figure 1-1: a net for increasing alkenes concentration by selective hydrogenation of alkynes impurities

According to the industrial [18-20] and academic [21-26] literature, palladium based catalysts are widely used for industrial selective hydrogenation. However, even though the pure palladium catalysts have high catalytic activity, it has been found that their selectivity to alkenes decreases sharply at high alkyne conversion, e.g., the selectivity to ethylene decreases from ~90 to 10% when acetylene conversion increases from ~80 to 100% for selective acetylene hydrogenation in excess of ethylene on 3wt% Pd/ boehmite catalyst [27] as may be the concentration of alkynes become very low and alkenes start to adsorb and to hydrogenate into alkanes [27-29]. Moreover, the bulk-dissolved hydrogen in the subsurface of palladium is believed to enhance the overhydrogenation of alkynes/dienes to alkanes [21, 24, 30, 31]. Recent studies showed that incorporation of carbon atoms into Pd nanoparticles [32-34] and alloying with a second metal, i.e., Pd-Ag [35-37], Pd-Au [38], Pd-Ni[39], Pd-Cu [40], could highly increase the selectivity to alkenes as it could prevent the diffusion of hydrogen into subsurface and modify the equilibrium of hydrogen between the surface and deeper layer on palladium [30] and hinder the hydride formation [41]. Currently, the palladium based catalysts mostly used in the market are Pd/Al_2O_3 with Pd=0.3 wt% (HDMax PA), Pd-Ag/Al_2O_3 with Pd=0.047 wt% and Ag=0.28 wt% (G58E) and Pd-Ag/Al_2O_3 with Pd=0.018 wt% and Ag=0.08 wt% (G83S) synthesized by Süd-Chemie [9].

As mentioned above a suitable industrial catalyst for selective hydrogenation of unsaturated hydrocarbons impurity does not only require high catalytic performances, but also a low price. As a result, beyond noble metals, several non-noble metal catalysts have also been explored, such as copper, nickel, cobalt and iron [42]. It has been found that supported copper catalysts have relatively high catalytic activity and selectivity to alkenes in alkynes hydrogenation [43]. However, copper catalysts are not stable as oligomerization reaction (green oil formation) occurs on the Cu surface resulting in a rapid deactivation [44, 45]. Only few studies focused on nickel based catalyst [42, 46-48] and almost no work concerned supported iron catalysts for selective hydrogenation in the few recent decades [42], until Studt et al [49] underlined the high potential of the non-noble bimetallic catalysts, such as Ni-Zn alloy for selective acetylene hydrogenation in 2008.

Studt et al [49] proposed that selective hydrogenation reaction of unsaturated hydrocarbons is controlled by desorption barriers as the activation barriers for the reaction was considered to be metal-independent; this has been observed for a number of other hydrogenation reactions by Liu et al [50]. Considering acetylene and ethylene heat of

adsorption as the parameter determining catalytic activity and selectivity to ethylene, Studt et al introduced a scaled relation between the adsorption energies of acetylene and ethylene and the methyl group adsorption energy (ΔE_{CH3}) (Figure 1-2A), based on the fact that the adsorption energy of any hydrocarbon molecule on a metal scales approximately with the adsorption energy of the central C atom, as established using density functional theory calculation (DFT) by Abild-Pedersen et al [51]. Figure 1-2A shows that the higherΔE_{CH3} value gives lower catalytic activity (turnover) and higher catalytic selectivity for acetylene selective hydrogenation as the activation barrier for C_2H_2 is closer to the desorption activation energy of C_2H_2 and the activation barrier for C_2H_4 will be greater than the desorption activation energy of C_2H_4. The authors proposed some interesting non-noble bimetallic catalysts for acetylene selective hydrogenation, underlining the fact that Ni-Zn alloy could have catalytic activity and selectivity similar to palladium-based catalysts. Moreover, these non-noble bimetallic catalysts are very cheap (~10 dollars per kg), which is 100 times lower than that of palladium based catalysts (Figure 1-2B).

To verify their calculation about the non-noble bimetallic catalysts, Studt et al [49] prepared a series of 10 wt% Ni-Zn samples supported on $MgAl_2O_4$ with different Ni/Zn ratios (Ni, $Ni_{0.45}Zn_{0.55}$, $Ni_{0.33}Zn_{0.67}$ and $Ni_{0.25}Zn_{0.75}$) by impregnation method, and compared them with 1 wt% Pd and $Pd_{0.25}Ag_{0.75}$ samples. The catalytic data for selective acetylene hydrogenation showed that with increasing Zn loading, Ni-Zn catalysts show higher selectivity to ethylene even at high acetylene conversion. However, the authors did not present any direct evidence for the supported Ni-Zn alloy formation after thermal treatment and for the catalytic stability of the Ni-Zn/$MgAl_2O_4$ samples, leaving the questions of supported non-noble bimetallic compounds preparation and their catalytic stabilities for the selective hydrogenation reaction unresolved.

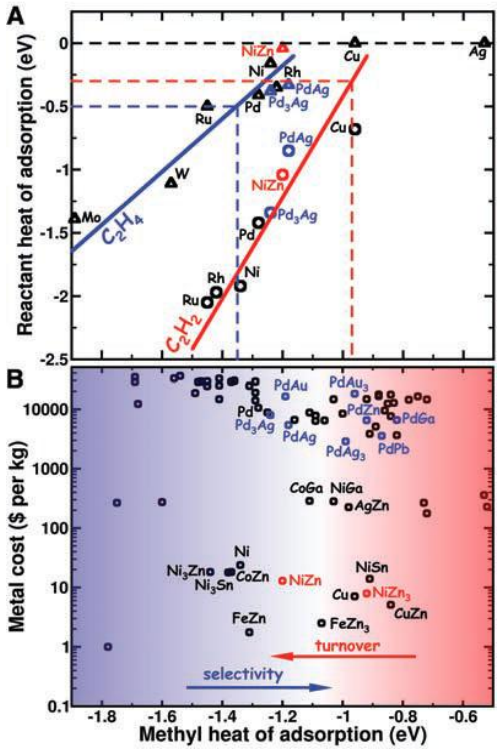

Figure 1-2: (A) Heats of adsorption for acetylene (C_2H_2) and ethylene (C_2H_4) plotted against the heat of adsorption for methyl (CH_3). The solid lines show the predicted acetylene (red line) and ethylene (blue line) adsorption energies from scaling. The dotted lines define the region of interest, where the ethylene binding energy is less than the barrier for further hydrogenation (blue) and where the reactivity of the acetylene hydrogenation step equals 1 s^{-1} per site (red). (B) Price (in 2006) of 70 binary intermetetallic compounds plotted against the calculated methyl binding energies. [49]

In 2014, the questions were partially answered by Spanjers et al [52], who studied the catalytic performances of Ni-Zn alloy using bulk intermetallic Ni-Zn compounds (Ni_4Zn, NiZn and Ni_5Zn_{21} alloy), combined with isotopic labeling in batch reactor ($^{13}C_2H_2$, $^{12}C_2H_4$), in selective acetylene hydrogenation (acetylene: hydrogen: ethylene ratio 1: 10: 20). The authors found that the oligomeric species (e.g., butadiene, propylene, 1-butene, cis-2-butene, isobutylene, and trans-2-butene) are only produced from acetylene ($^{13}C_2H_2$) and not from ethylene ($^{12}C_2H_4$), and zinc inclusion into nickel catalyst could reduce the formation of these oligomeric species. Considering that bulk intermetallic Ni-Zn catalysts have low surface areas (< 1 m^2 g^{-1}) and low catalytic activity (< 2×10^{-8} $mol_{C2H2} \cdot s^{-1} \cdot g_{cat}^{-1}$) [52], the authors also carried out a study on supported Ni/ZnO and Ni/SiO_2 catalysts [53] in 2015 and found that the ZnO supported NiO nanoparticles was directly transformed to α-NiZn at low reduction temperature (<500 ^oC) and β-NiZn alloy was mainly formed when the reduction temperature was higher than 500 ^oC. Moreover, NiZn alloy supported by ZnO catalysts displayed lower selectivity to ethylene than the metallic Ni supported by SiO_2, whatever the reduction

temperatures, which is in contrast to the results from bulk intermetallic Ni-Zn catalysts, which showed that an increasing Zn content leads to an increase of selectivity to ethylene, and also does not agree with the prediction of Studt et al [49]. Thus the authors concluded that the ZnO support has a negative effect on ethylene selectivity. However, neither of their papers reports any information on the catalytic stability of bulk intermetallic Ni-Zn and Ni/ZnO catalysts.

In addition, Liu et al [54] found that unsupported intermetallic Ni_xM_y (M=Ga, Sn) has excellent selectivity to alkenes and good catalytic stability during long term acetylene hydrogenation. Kang M et al [55] also showed that alloying Ni with Cu could increase the selectivity but decrease the catalytic activity of metallic Ni, however, the catalytic stability of Ni-Cu alloy was not mentioned.

Besides Ni-Zn alloy, Studt et al [49] also predicted using DFT calculation that Cu-Zn alloy could have a higher selectivity than metallic Cu in selective acetylene hydrogenation. However, the main problem of metallic Cu as a catalyst for selective hydrogenation reaction is not the selectivity to alkenes but its low stability. Moreover, currently, the modification of the catalytic performance of Cu was mainly studied by alloying with a noble metal as the promoter, such as gold [56], palladium [57-59] and platinum [60], which showed a better catalytic stability than monometallic copper. Regarding copper based non-noble bimetallic catalyst, even though the promotional role of Zn on the activity and selectivity of supported Cu catalysts has been studied in some reactions, e.g., the formation of Cu-Zn active sites for methanol synthesis [61-63], the effect of alloying with Zn on the stability of Cu has not been reported, especially for selective hydrogenation reaction.

Even though iron based catalyst have been used for different applications, such as in Fischer-Tropsch synthesis [64], carbon nanotubes synthesis [65], hydrogenation of ketones [66] and even in some biomedical applications [67-69], only little attention has been paid in the field of selective hydrogenation of polyunsaturated hydrocarbons. Unsupported monodispersed iron nanoparticles (~2 nm) were found to be active in the hydrogenation of various alkenes and alkynes under mild conditions [70, 71]. Recently, the catalytic performance of the bulk intermetallic $Al_{13}Fe_4$ compound has been compared with a commercial 5 wt% Pd/Al_2O_3 catalyst and an industrial benchmark catalyst for selective acetylene hydrogenation (C_2H_2 : H_2 : C_2H_4 ratio 1 : 10 : 100) by Armbruster et al [72] (Figure. 1-3). Unsupported $Al_{13}Fe_4$ showed high catalytic stability (red dotted line in Figure 1-3) with only 6% lower selectivity (red full line in Figure 1-3) to ethylene than the industrial

benchmark catalyst (blue dotted and full lines in Figure 1-3). Note that the industrial benchmark catalyst has been highly optimized for selective hydrogenation of ethylene reaction, whereas the $Al_{13}Fe_4$ could still be optimized.

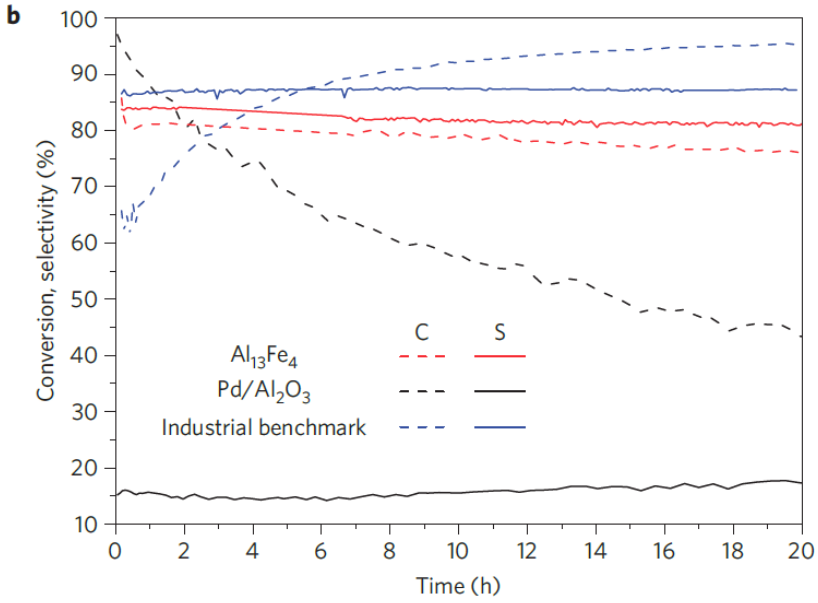

Figure 1-3: Conversion (C, dotted line) and selectivity (S, full line) to ethylene of unsupported $Al_{13}Fe_4$, 5wt% Pd/Al_2O_3 and an industrial benchmark catalyst in the semi-hydrogenation of acetylene over 20 h time on stream (reaction condition: 0.5% C_2H_2, 5% H_2, 50%C_2H_4 in He, 30 ml min^{-1} total flow, 200 ^oC) [72]

$Al_{13}Fe_4$ also showed high activity in butadiene partial hydrogenation with high selectivity to butenes at room temperature [73]. Those studies revealed that iron based non-noble bimetallic catalysts could be a low-cost alternative for palladium in heterogeneous hydrogenation. Thus, it might be very interesting to explore the used of Fe-Zn alloy, which has been already mentioned by Studt et al [49] (Figure 1-2B), as a promising catalyst for selective alkynes hydrogenation.

2. The goal of my thesis

As it has been mentioned above, supported Cu-Zn, Ni-Zn and Fe-Zn catalysts have the potential to replace commercial palladium-based catalysts in the area of unsaturated hydrocarbon selective hydrogenation, and the small number of work related to these kinds of catalysts leaves a large space for the further exploration on their utilizations. Thus, this thesis mainly focuses on the preparation and characterization of supported non-noble mono/bi-metallic catalysts, including Cu-Zn, Ni-Zn and Fe-Zn, and their catalytic properties for the

selective hydrogenation of polyunsaturated hydrocarbons in the presence of excess of alkenes to mimic a catalytic operation of purification of an alkene cut. The goals of this thesis are:

- Catalyst preparation: Firstly, considering that the main method for sample preparations in this thesis is deposition-precipitation with urea (introduced in chapter 2), which is a method based on the gradual increase of the pH of the preparation solution during urea decomposition at 80 ^{o}C in order to favor metal complex deposition on the support surface, the deposition – precipitation behavior of the non-noble metal ions on support will be studied during the pH increasing.

- Catalyst characterization: The conditions for Cu-Zn, Ni-Zn and Fe-Zn alloy formation are explored. To verify the formation of bimetallic compounds in the bimetallic catalysts, X-Ray Diffraction (XRD) is applied to determine the metallic phases existing in the sample after thermal treatment. Moreover, scanning transmission electron microscopy (STEM) allows not only studying the particle size and dispersion of the particles on the support surface by high annular dark-field mode (HAADF), but also analyzing the composition of the nanoparticles on the TiO_2 surface by energy dispersive X-ray spectrometry (EDS).

- Catalytic performances: Lastly, after *in situ* activation at a given temperature, the catalytic properties of the mono and bimetallic catalyst will be studied and compared in the selective hydrogenation of 1,3-butadiene in the presence of an excess of propene (introduced in Chapter2). Meanwhile, the effect of alloying of copper, nickel and iron with zinc on the catalytic activity, selectivity and stability will be studied.

3. Selective hydrogenation of 1,3-butadiene

In this part, the molecular structure of 1,3-butadiene is analyzed by valence-bond theory [74] and molecular orbital theory [75]. After that, different routes of hydrogen addition reactions in 1,3-butadiene molecule are described, including: 1,2-addition, 1,4-addition and 2,3-addition reactions. At last, the expected selective hydrogenation of 1,3-butadiene in excess of propene route is introduced for this study.

3.1 The structure of 1,3-butadiene

There are two different structures in 1,3-butadiene molecule: trans-1,3-butadiene (Figure 4A) and cis-1,3- butadiene (Figure 4B). In both 1,3-butadiene molecules, the bond lengths of C-H and C-C are 0.108 and 0.148 nm, which are shorter than the typical bond lengths (0.109 and 0.154), respectively, and the C=C bond length, 0.137nm, is longer than the typical C=C bond length (0.134nm). The C-C=C angle is 122.4^{o} and the C=C-H angle is 119.8^{o}. Considering the fact that all the C and H atoms of butadiene are in the same plane and the bond between C2 and C3 (Figure 1-4) cannot rotate freely, according to the valence orbital theory, it can be concluded that there is a super π bond, which is formed by the orbital overlapping of 2p-2p in carbon atoms, connecting all the four C atoms in butadiene molecule, as represented in Figure 4A-2 for trans-1,3-butadiene and Figure 4B-2 for cis-1,3-butadiene, respectively.

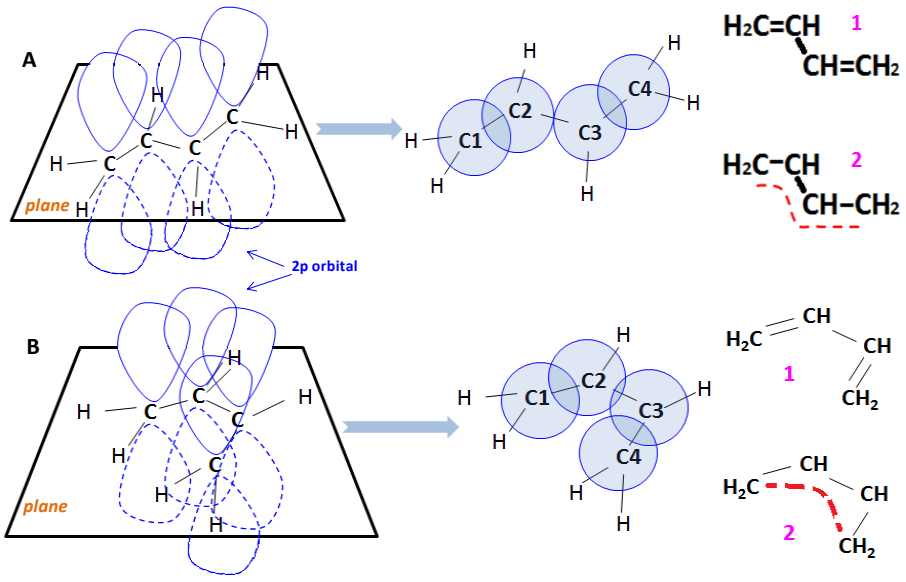

Figure 1-4: Conformation of Molecular: A, Trans-1,3-butadiene; B, Cis-1,3-butadiene

When the molecular orbital theory, the molecular orbital of 1,3-Butadiene can be described as in the following graph (Figure 1-5). Four 2p_z atomic orbitals in the four carbon atoms resulted into four molecular orbitals (π1, π2, π*1, π*2). The energy sequence is π1 < π2 < isolated p orbital < π*1 < π*2.

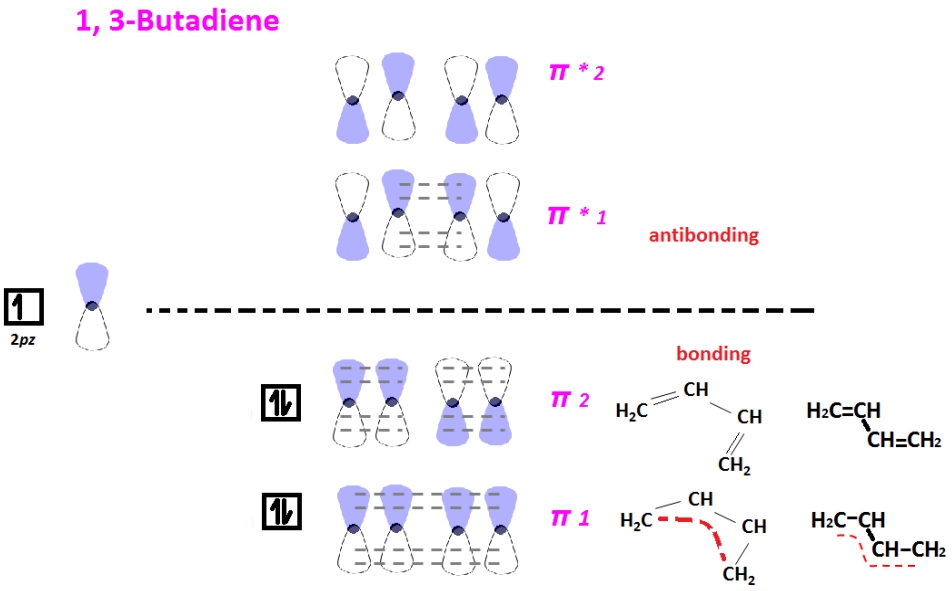

Figure 1-5: molecular orbital of 1,3-Butadiene

3.2 Hydrogenation of 1,3-butadiene

Since there is a super π bond in 1,3-butadiene molecular, normally, there are three possible routes for the hydrogen addition in butadiene (Figure 1-6): 1,2-addition, 1,4-addition and 2,3-addition. 1,2-addition means that two hydrogen atoms are added onto the C1 and C2 atom resulting in 1-butene formation. For 1, 4-addition, two hydrogen atoms are added onto the C1 and C4 atom with 2-butenes (cis-2-butene and/or trans-2-butene) formation. With hydrogenation going on, these three unsaturated butenes can transform to butane. Whereas for 2,3-addition, the butadiene will be fully hydrogenated to butane as the formation of the intermediate product ($*CH_2CH_2CH_2CH_2*$) is unstable and can reacts with other two H atoms quickly. Note that a transformation between trans-2-butene and cis-2-butene can happen through isomerization reaction, which has been verified by Gómez et al [76] through DFT calculation using Pd/Ni (111) bimetallic as the model.

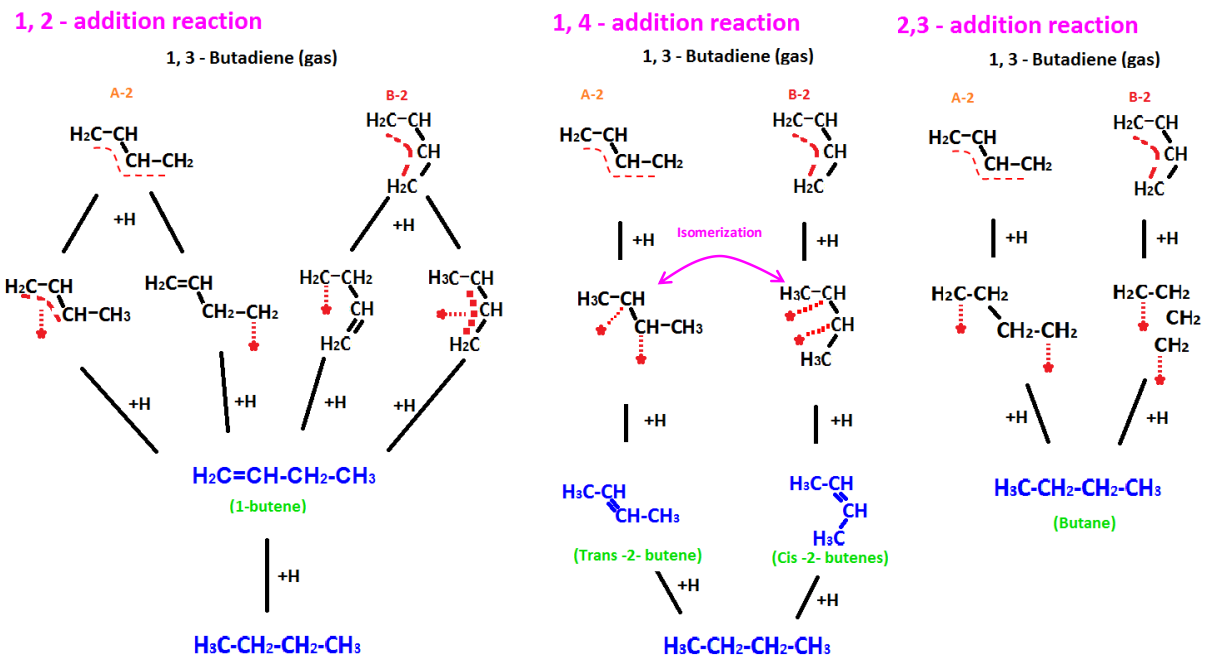

Figure 1-6 three different hydrogen addition reactions on butadiene molecular: 1,2-addition, 1,4- addition and 2,3-addition

As it was described in the first part of this Chapter, 1,3-butadiene is considered as an impurity in butenes stream produced from oil cracking, with concentration 0.3 to 6% [6], and the purpose of using catalytic selective hydrogenation of 1,3-butadiene is to form butenes, and to avoid butane formation, thus 1,2-addition and 1,4-addition reactions are expected on the surface of the catalyst without any further hydrogenation reactions.

In this study, in order to simulate the process required for the purification of industrial alkenes streams to prevent further poisoning of the polymerization catalysts used for polyalkene production, a gas phase 1,3-butadiene in an excess of propene (0.3% butadiene, 30% propene and 20% hydrogen) is used for the investigation of catalytic performance. Here, propene is selected as the main alkene instead of butenes for the ease of detection by gas chromatography of the alkane (butane) arising from the reaction of hydrogenation of 1, 3-butadiene from the alkane (propane) arising from the hydrogenation of alkene (propene) in excess. As a result, during hydrogenation of the gas mixture, 1,3- butadiene is expected to be semi-hydrogenated to butenes (1-butene, trans-2-butene or cis-2-butene) with no further butane formation and no propane formation arising from propene hydrogenation (Figure 1-7).

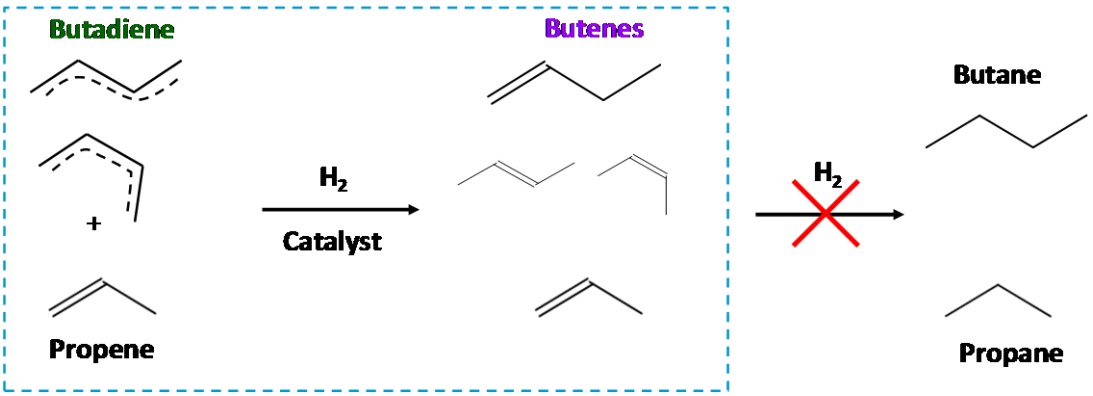

Figure 1-7, selective hydrogenation in the gas mixture during catalytic reaction

4. Review of the research experience on noble bimetallic catalysts for selective hydrogenation in the Laboratoire de Réactivité de Surface (LRS)

Since supported gold nanoparticles have been discovered to be highly catalytic active in CO oxidation at room temperature in the late eighties [77, 78], the Laboratoire de Réactivité de Surface carried out various studies focusing on the preparation of supported gold based catalysts [79-81] i.e., deposition-precipitation (DP), ion adsorption (IA), impregnation in excess of solution (IE), and on applications of these catalysts, such as for catalytic oxidation reactions [82-85] and hydrogenation reactions [80, 86, 87]. In the selective hydrogenation of 1,3-butadiene in excess of propene reaction, it was found that mono metallic gold catalysts are highly selective to alkenes, but with a low activity [56, 80]. In addition, different kinds of gold-based bimetallic catalysts were also explored in the recent years, such as supported Au-Pd bimetallic catalysts with high Au/Pd atomic ratios that were found to be more active than monometallic gold for butadiene selective hydrogenation and more selective to butenes than palladium catalysts [88, 89]. Supported Au-Cu [56] and Au-Zn [90] bimetallic catalysts were also studied for the same reaction.

5. Review of few non-noble metal catalyst preparations and characterizations work in the Laboratoire de Réactivité de Surface (LRS)

In the past the Laboratoire de Réactivité de Surface also studied the preparation and characterization of supported non-noble metal catalysts, i.e., Ni/SiO_2, Cu/SiO_2, Zn/SiO_2 and Cu/ZnO.

In the 90th, the preparation of Ni/SiO_2 catalysts was studied. They were prepared by different methods, e.g., incipient wetness impregnation (IWI) [91, 92] and deposition-precipitation with urea (DPu) [93-96], and the mechanism of deposition-precipitation of Ni (II) phase on silica and the formation of nickel phyllosilicate (1:1) was deeply explored at the molecular level [97].

The preparation of supported Cu catalysts was also explored. The influence of the experimental conditions (i.e., sample preparation method, and thermal treatment) on the size of the Cu particles supported on SiO_2 was explored [98], and revealed that the drying step has a drastic influence on the size of the metal particles after calcination and reduction for the sample prepared by impregnation and the presence of chemical bonds between Cu^{2+} and the SiO_2 for the sample prepared by cationic exchange. Later, the interaction between Cu complexes and SiO_2 support was studied by EXAF spectroscopy [99] using Cu/SiO_2 sample prepared by cationic exchange, it has been found that the interaction between Cu complexes and SiO_2 surface is probably simple electrostatic adsorption when the sample is wet, and that grafting occurs during the sample drying step. Moreover, as for Cu/SiO_2 prepared by cationic exchange, a kind of copper phyllosicate was also formed in the as-prepared Cu/SiO_2 samples [98, 100].

In 2003, supported Zn samples prepared by incipient wetness impregnation have been studied. The evolution of zinc species on silica surface during sample drying and calcinations was studied by Chouillet et al [101]. They showed that the zinc silicate ($Zn_4Si_2O_7(OH)_2 \cdot H_2O$, called hemimorphite) was the main phase and the ZnO formation strongly depends on the drying temperature after impregnation.

Based on the works performed on supported mono-metallic samples mentioned above, bimetallic Cu-Zn $/SiO_2$ catalysts was prepared by Catillon-Mucherie et al [102] using co-impregnation in 2007. However, instead of Cu-Zn alloy formation, Cu^0 and Zn^{II} species with good dispersion were observed in the $Cu\text{-}Zn/SiO_2$ sample after calcination at 450 ^oC and reduction at 350 ^oC. Then the catalytic behavior of the $Cu^0\text{-}Zn^{II}/SiO_2$ samples was studied in selective hydrogenation of crotonaldehyde in collaboration with R. Touroude in Strasbourg [103]. The results showed that $Cu^0\text{-}Zn^{II}/SiO_2$ has 10~20% higher selectivity to crotyl alcohol than Cu/SiO_2 sample. Cu_3Zn alloy formation was found by XRD in mono Cu/ZnO after thermal treatment under H_2 in 2012 by Derrouiche et al [104]. The authors observed that metallic Cu was formed after sample reduction at 280 ^oC. However, zinc atom migrates into

the Cu crystal gradually with increasing reduction temperature and Cu_3Zn alloy was formed after reduction at 350 °C for 2 h (Figure 1-8).

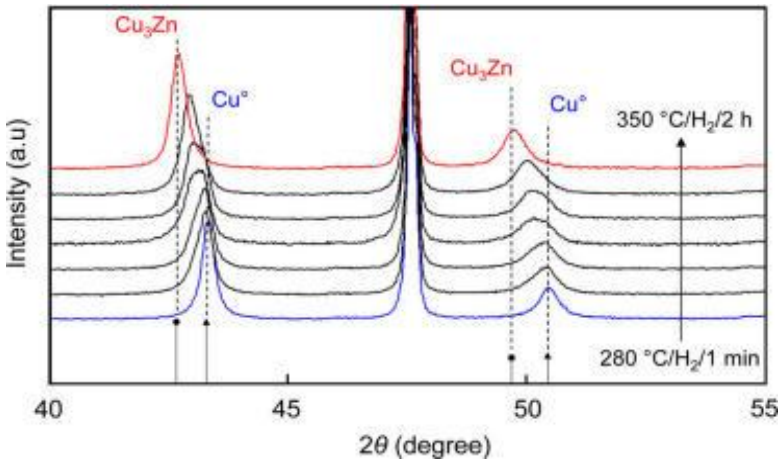

Figure 1-8: XRD patterns (in the range 2θ=40-55°) of sample 10 wt% Cu/ZnO sample calcined at 400°C followed by H_2 reduction at different temperatures and for different times: 1 min at (a) 280°C, (b) 330°C, (c) 340°C, and (d) 350°C, and T_R=350°C for (e)5 min, (f) 30 min, and (g) 2 h.▲ and ●: the most intense peaks from the JCPDS files of Cu^0(#04-0836) and Cu_3Zn (#65-6567), respectively [104].

These previous works focusing on supported non-noble metal catalyst preparation and characterization in the LRS provides a suitable platform for the study of non noble bimetallic catalysts study. Moreover, the discovery of Cu-Zn alloy formation in the mono Cu/ZnO sample after calcination and reduction [104] makes the studies of supported non-noble bimetallic catalyst preparation, characterization and catalytic properties particularly promising.

6. The outline of this Thesis

This thesis mainly focuses on the preparation, characterization and evaluation of the catalytic properties of supported non-noble bimetallic catalysts. The supported non-noble bimetallic Cu-Zn, Ni-Zn and Fe-Zn are selected and studied. In this thesis, Chapter 2 mainly introduces the methods for samples preparation and characterization. The preparation of monometallic catalysts (i.e., Cu, Zn, Ni) for selective hydrogenation of butadiene is described in Chapter 3. After that, one can find the studies of bimetallic Cu-Zn, Ni-Zn and Fe-Zn for selective hydrogenation of butadiene in Chapter 4, 5 and 6. At the end of this thesis, a conclusion is made in Chapter 7.

7. Reference

1. N.N. Lebedev, *Chemistry and technology of basic organic and petrochemical synthesis*. Vol. 1. 1984: Imported Pubn.
2. P.W.N.M.v.L.J.A.M. R.A. van Santen and B.A. Averill, Editors. *Chapter 2 Catalytic processes in industry*, in *Studies in Surface Science and Catalysis*, 1999, Elsevier. p. 29-80.
3. M. Eramo, *Global Ethylene Market Outlook: Low Cost Feedstocks Fuel The Next Wave Of Investments In North America and China.*
4. C. Marcilly, Oil & gas science and technology, 56 (2001) 499.
5. M.L. Derrien, *Chapter 18 Selective Hydrogenation Applied to the Refining of Petrochemical Raw Materials Produced by Steam Cracking*, in *Studies in Surface Science and Catalysis*, L. Cerveny, Editor 1986, Elsevier. p. 613-666.
6. F.H. Puls and K.D. Ruhnke, *Butene-1 containing feed purification process (CS-165)*, 1981, Google Patents.
7. M.D. Argyle; C.H. Bartholomew, Catalysts 5(2015) 145.
8. B.J. Burger; M.E. Thompson; W.D. Cotter; J.E. Bercaw, Journal of the American Chemical Society, 112 (1990) 1566.
9. S.A. Nikolaev; I.N. Krotova, Petroleum Chemistry, 53 (2013) 394.
10. N.S. Schbib; M.A. Garcia; C.E. Gigola; A.F. Errazu, Industrial & Engineering Chemistry Research, 35 (1996) 1496.
11. B.M. Collins, *Selective hydrogenation of highly unsaturated hydrocarbons in the presence of less unsaturated hydrocarbons*, 1978, Google Patents.
12. E.L. Mohundro, *Overview on C2 and C3 selective hydrogenation in ethylene plants*. in *American Institute of Chemical Engineers 15th Ethylene Producers Conference, New Orleans*. 2003.
13. S.H. Lee, Chelical & Biomolecular Engineering, 2004,
14. C.N. Thanh; B.Didillon; P. Sarrazin; C. Cameron, *Selective hydrogenation catalyst and a process using that catalyst*, 2000, Google Patents.
15. L. Kniel, O. Winter, K. Stork, *Ethylene, keystone to the petrochemical industry*1980, New York: Marcel Dekker, Inc.
16. J.-R Li, R.J. Kuppler, H.-C. Zhou, Chemical Society Reviews, 38 (2009) 1477.

17. M. García-Mota, J. Gomez-Diaz, G. Novell-Leruth, C. Vargas-Fuentes, L. Bellarosa, B. Bridier, J. Perez-Ramirez, N. Lopez, Theoretical Chemistry Accounts, 128 (2011) 663-673.
18. M.M. Johnson, D.W. Walker, G.P. Nowack, *Selective hydrogenation catalyst*, 1983, Google Patents.
19. G.L. Debras, *Process for the selective hydrogenation of alkynes*, 1989, Google Patents.
20. G.R. Gildert, H.M. Putman, D. Hearn, *Process for concurrent selective hydrogenation of acetylenes and 1, 2 butadine in hydrocarbon streams*, 1999, Google Patents.
21. M. García-Mota, B. Bridier, J. Perez-Ramirez, N. Lopez, Journal of Catalysis, 273 (2010. **273)** 92.
22. M.W. van Laren, C.J. Elsevier, Angewandte Chemie International Edition, 38 (1999) 3715.
23. T. Nijhuis, G. Van Koten, J. Moulijn, Applied Catalysis A: General, 238(2003) 259.
24. D.Teschner, E.Vass, M.Havecker, S.Zafeiratos, P. Schnorch, H.Sauer, A. Knop-Gericke, R. Schlogl, M. Chamam, A.Wootsch, Journal of Catalysis, 242 (2006) 26.
25. J. Boitiaux, J. Cosyns, S. Vasudevan, Applied catalysis,15 (1985) 317.
26. J.Luo, R.Theron, J.S.Laura, N.H.Thomas, S.W.Weller, G.O.Allen, J.S.Mclndoe Organometallics, 34(2015) 3021.
27. Q. Zhang, J. Li, X. Liu, Q. zhu, Applied Catalysis A: General, 197 (2000) 221.
28. A.Borodziński, G.C. Bond, Catalysis Reviews, 48 (2006) 91.
29. A.Borodziński, G.C. Bond, Catalysis Reviews, 50 (2008) 379.
30. D.Teschner, J.Borsodi, A. Wootsch, Z.Revay, M.Havecker, A.Knop-Gericke, S.D. Jackson, R.Schlogl, Science, 320 (2008) 86.
31. D.Teschner, Z.Revay, J.Bborsodi, M.Havecher, A. Knop-Gericke, R. Schlogl, D. Milroy, D. Jackson, D.Torres, P.Sautet, Angewandte Chemie International Edition, 47 (2008) 9274.
32. W.Ludwig, A.Savara, R.J.Madix, S.Schauermann, H.J.Freund, The Journal of Physical Chemistry C, 116 (2012) 3539.
33. W.Ludwig, A.Savara, J.M. Jobert, S.Schauermann, H-J.Freund, Journal of Catalysis, 284 (2011) 148.
34. M. Wilde, K. Fukutani, W. Ludwig, B. Brandt, J.H. Fischer, Schauermann, H-J.Freund Angewandte Chemie International Edition, 47 (2008) 9289.

35. B. Ngamsom, N. Bogdanchikova, M.A.Borja, P.Praserthdam, Catalysis Communications, 5 (2004) 243.
36. A. Pachulski, R. Schödel, P. Claus, Applied Catalysis A: General, 400 (2011) 14.
37. Y.Jin, A.K.Datye, E.Rightor, R.Gulotty, W. Waterman, M.Smith, M. Holbrook, J. Maj, J.Blackson, Journal of catalysis, 197 (2000) 221.
38. A.Sarkany, A. Horvath, A. Beck, Applied Catalysis A: General, 229 (2002) 117.
39. R. Hou,. Journal of Catalysis, 316 (2014) 1.
40. S. Leviness, V.Nair, A.H Weiss, Journal of Molecular Catalysis, 25 (1984) 131.
41. N.A.Khan, S. Shaikhutdinov, H.-J. Freund, Catalysis Letters, 108 (2006) 159.
42. J. Phillipson, P. Wells, G. Wilson, Journal of the Chemical Society A: Inorganic, Physical, Theoretical, 1969, 1351.
43. R.A. Koeppel, J.T.Wehril, M.S.Wainwrigh, D.L.Trimma, N.W.Cant, Applied Catalysis A: General, 120 (1994) 163.
44. M.R.,Stammbach,D.J. Thomas, D.L.Trimm, M.S.Wainwright, Applied catalysis, 58 (1990) 209.
45. N.J.Ossipoff, N. Cant, Journal of Catalysis, 148 (1994) 125.
46. J. Grant,R.B.Moyes, R.G.Oliver, P.B.Wells, Journal of Catalysis, 42 (1976) 213.
47. P.Wells, G. Wilson, Journal of the Chemical Society A: Inorganic, Physical, Theoretical, 1970, 2442.
48. C.Park, R.T.K. Baker, The Journal of Physical Chemistry B, 102 (1998) 5168.
49. F.Studt,F. Abild-Pedersen, T. Bligaard, R.Z. Sorensen, C.H.Christensen, J.K.Norskov, Science, 320 (2008) 1320.
50. Z.-P. Liu, P. Hu, Journal of the American Chemical Society, 125 (2003) 1958.
51. F.Abild-Pedersen, J.Greeley, F.Studt, J.Rossmeisl, T.R.Munter,P.G.Moses, E.Skulason, T.Bligaard, J.K.Norskov, Physical review letters, 99(2007) 016105.
52. C.S.Spanjers,J.T.Held, M.J.Jones, D.D.Stanley, R.S.Sim, M.J.Janik, R.M.Rioux, Journal of Catalysis, 316 (2014) 164.
53. C.S.Spanjers, R.S.Sim, N.P.Sturgis, B.Kabius, R.M.Rioux, ACS Catalysis, 5 (2015) 3304.
54. Y.Liu, X. Liu, Q.Feng, D.He, L.Zhang, L.Chao, R.Shen, Y.Ji, D.Wang, G.Zhou,Y.Li, Advanced Materials, 28 (2016) 4747.
55. M.Kang, M.W.Song, T.W.Kim, K.L.Kim, The Canadian Journal of Chemical Engineering, 80 (2002) 63.

56. L.Delannoy, G.Thrimurthulu, P.S.Reddy, C.Methivier, J.Nelayah, B.m.Reddy, C.Ricolleau, C.Louis, Physical Chemistry Chemical Physics, 16 (2014) 26514.
57. A.J.McCue,C.J.McRitchie, A.M.Shepherd, J.A.Anderson, Journal of Catalysis, 319 (2014) 127.
58. M.B.Boucher, B.Zugic, G.Cladras, J.Kammert, M.D.Marcinknowsk, T.J.Lawton, E.C.H.Sykes, M. Flytzani-Stephanopoulos, Physical Chemistry Chemical Physics, 15 (2013) 12187.
59. A.J.McCue, A.M. Shepherd, J.A. Anderson, Catalysis Science & Technology, 5 (2015) 2880.
60. F.R. Lucci, J. Liu, M.D. Marcinkowski, M. Yang, L.F. Allard, M. Flytzani-Stephanopoulos, E. C. H. Sykes, Nature communications, 6(2015) 8550.
61. M.Behrens, F.Studt, I.Kasatkin, S.Kühl, M. Hävecker, F.Abild-Pedersen, S. Zander, F.Girgsdies, P.Kurr, B.L.Kniep, M.Tovar, R.W. Fischer, J.K.Nørskov, R.Schlögl, Science, 336 (2012) 893.
62. Y.Choia, K.Futagamia, T.Fujitanib, J. Nakamuraa, Applied Catalysis A: General, 208 (2001) 163.
63. J. Nakamura, T.Uchijima, Y.Kanai, T.Fujitani, Catalysis Today, 28 (1996) 223.
64. H.M.Torres Galvis, J.H.Bitter, C.B. Khare, M.Ruitenbeek, A. Iulian Dugulan, K.P. de Jong, Science, 335 (2012) 835.
65. Y.Li , W. Kim, Y.Zhang, M.Rolandi, D.Wang, H.Dai, The Journal of Physical Chemistry B, 105 (2001) 11424.
66. C.P.Casey, H.Guan, Journal of the American Chemical Society, 129 (2007) 5816.
67. A.Meffre, B.Mehdaoui, V.Kelsen, P.F.Fazzini, J.Carrey, S.Lachaize, M.Respaud, B.Chaudret, Nano Letters, 12 (2012) 4722.
68. B.Mehdaoui, A.Meffre, J.Carrey, S.Lachaize, L.M.Lacroix, M.Gougeon, B.Chaudret, M.Respaud, Advanced Functional Materials, 21 (2011) 4573.
69. C.G.Hadjipanayis, M.J. Bonder, S.Balakrishnan, XWang, H.Mao, G.C.Hadjipanayis, Small, 4 (2008) 1925.
70. V.Kelsena, B.Wendtb, S.Werkmeisterb, K.Jungeb, M.Bellerb, B.Chaudret, Chemical Communications, 49 (2013) 3416.
71. P.H.Phua, L.Lefort, J.A.F.Boogers, M.Tristany, J.G.de Vries, Chemical Communications, 25 (2009) 3747.

72. M. Armbrüster, K. Kovnir, M. Friedrich, D. Teschner, G. Wowsnick, M. Hahne, P. Gille, L.Szentmiklósi, M.Feuerbacher, M.Heggen, F.Girgsdies,D.Rosenthal,R.Schlögl, Y. Grin, Nature Materials, 11 (2012) 690.
73. L.Piccolo, Chemical Communications,49 (2013) 9149.
74. D. Cooper, *Valence bond theory*. Vol. 10. 2002: Elsevier.
75. F.E. Harris, *Molecular orbital theory.* Advances in quantum chemistry, 3 (1967) 61.
76. G.Gómez, P.G. Belelli, G.F. Cabeza, N.J. Castellani, Applied surface science, 353 (2015) 820.
77. M.Haruta, T.Kobayashi, H.Sano, N.Yamada, Chemistry Letters, 16 (1987) 405.
78. M.Haruta, N.Yamada, T.Kobayashi, S.Iijima, Journal of Catalysis, 115 (1989) 301.
79. R.Zanella, S.Giorgio, C.R. Henry, C.Louis, The Journal of Physical Chemistry B, 106 (2002) 7634.
80. A.Hugon, L. Delannoy, C. Louis, Gold Bulletin, 41 (2008) 127.
81. L.Delannoy, N.E.Hassan, A.Musi, N.N.L.To, J.M.Krafft, C.Louis, The Journal of Physical Chemistry B, 110 (2006) 22471.
82. M.Bessona, A.Kallela, P.Gallezota, R.Zanellab, C.Louis, Catalysis Communications, 4 (2003) 471.
83. R.Zanellaa, S.Giorgiob, C.H.Shinc, C.R.Henryb, C.Louis, Journal of Catalysis, 222 (2004) 357.
84. P. Lakshmanan, L. Delannoy, V. Richard, C. Méthivier, C. Potvin, C. Louis, Applied Catalysis B: Environmental, 96 (2010) 117.
85. L.Delannoy, K.Fajerwerg, P.Lakshmanan, C.Potvin, C.Méthivier, C.Louis, Applied Catalysis B: Environmental, 94 (2010) 117.
86. R.Zanella, C.Louis, S.Giorgio, R. Touroude, Journal of Catalysis, 223 (2004) 328.
87. T.Chaieb, L.Delannoy, S.Casale, C.Louis, C.Thomas, Chemical Communications, 51 (2015) 796.
88. A.Hugon, L.Delannoy, J.M. Krafft, C.Louis, The Journal of Physical Chemistry C, 114 (2010) 10823.
89. N.E.Kolli, L.Delannoy, C.Louis, Journal of Catalysis, 297 (2013) 79.
90. S.Derrouiche, C.L.Fontaine, G.Thrimurtulu, S.Casale, L.Delannoy, H.Lauron-Pernot, C.Louis, Catalysis Science & Technology, 6 (2016) 6794.
91. C.Louis, Z.X. Cheng, M. Che, The Journal of Physical Chemistry, 97 (1993) 5703.
92. M.Che, Z.X. Cheng, C. Louis, Journal of the American Chemical Society, 117 (1995) 2008.

93. P.Burattin, M. Che, C.Louis, The Journal of Physical Chemistry B, 101 (1997) 7060.
94. P.Burattin, M.Che, C.Louis, The Journal of Physical Chemistry B, 103 (1999) 6171.
95. P.Burattin, M.Che, C.Louis, The Journal of Physical Chemistry B, 104 (2000) 10482.
96. R.Nares, J.Ramírez, A.Gutiérrez-Alejandre, C.Louis, T.Klimovan, The Journal of Physical Chemistry B, 106 (2002) 13287.
97. P.Burattin, M.Che, C.Louis, The Journal of Physical Chemistry B, 102 (1998) 2722.
98. T.Toupance, M. Kermarec, C.Louis, The Journal of Physical Chemistry B, 104 (2000) 965.
99. L.Trouillet, T.Toupance, F.Villain, C.Louis, Physical Chemistry Chemical Physics, 2 (2000) 2005.
100. T.Toupance, M.Kermarec, J.F.Lambert, C.Louis, The Journal of Physical Chemistry B, 106 (2002) 2277.
101. C.Chouillet, F.Villain, M.Kermarec, H.Lauron-Pernot, C.Louis,The Journal of Physical Chemistry B, 107 (2003).
102. S.Catillon-Mucherie, F.Ammari, J.M.Krafft, H.Lauron-Pernot, R.Touroude, C.Louis, The Journal of Physical Chemistry C, 111 (2007) 11619.
103. S.Catillon-Mucherie, H. Lauron-Pernot, C. Louis, Journal of Physical Chemistry C, 114 (2010) 11140.
104. S.Derrouiche, H. Lauron-Pernot, C. Louis, Chemistry of Materials, 24 (2012) 2282.

Chapter 2: Techniques for catalysts preparation and characterization

Chapter 2: Techniques for catalysts preparation and characterization

The methods for catalysts preparation and the characterization techniques used during the thesis are summarized in this chapter, which is divided into four parts: the raw chemical materials used are first presented, followed by the methods selected for samples preparation, i.e., deposition-precipitation with urea (at increasing pH) and deposition-precipitation at fixed pH, then the techniques chosen for samples characterization, and finally the equipment and procedures used for the reaction of selective hydrogenation of butadiene. The mechanism and principle of the preparation methods are also introduced and discussed in the "methods for samples preparation" part. In this part, some calculations have also been done on the evolution of the solubility of metal hydroxide with pH in the deposition-precipitation with urea, and on the critical metal precursor concentration that guarantees that there will be no precipitation in solution during the deposition-precipitation at fixed pH.

1. Raw chemical materials for the study

To study the morphology, structure and catalytic property of the bimetallic nanoparticles, the support must be carefully selected. The requirements for the support are: 1, the support must be stable during the sample preparation and the following thermal treatments; 2, it must have no catalytic activity for selective hydrogenation of unsaturated hydrocarbon. Compared with SiO_2 and Al_2O_3 supports, which easily form silicates species (e.g., nickel phyllosilicate in Ni/SiO_2 samples [1]) or aluminates (e.g., copper aluminates in Cu/Al_2O_3 samples [2]) during sample preparation, TiO_2 support is stable in solution, and there are no reports about titanates formation during sample preparation at low temperature [3]. Herein, TiO_2 (50 m^2 g^{-1}, P25 from Evonik) was selected as support, it is known to contain anatase and rutile phases in a ratio of about 3:1 (see Figure 2-1). ZnO (8 m^2 g^{-1}, KADOX 911) was also used to explore the formation bimetallic alloy in the study of Ni-Zn and Fe-Zn samples.

Solid $CO(NH_2)_2$ (Sigma-Aldrich, purity: >98%) and aqueous 0.5 M NaOH solution were used as the precipitation agent for sample preparation.

$Cu(NO_3)_2 \cdot 3H_2O$ (Sigma-Aldrich, purity: >99%), $Zn(NO_3)_2 \cdot 6H_2O$ (Sigma-Aldrich, purity: >99%), $Ni(NO_3)_2 \cdot 6H_2O$ (Sigma-Aldrich, purity: >98.5%) were used as precursors for copper, zinc and nickel containing samples. $Fe(NO_3)_3 \cdot 9H_2O$ (Sigma-Aldrich, purity: >99%) and $FeCl_2 \cdot 4H_2O$ (Sigma-Aldrich, purity: >99%) were used for the iron-zinc study.

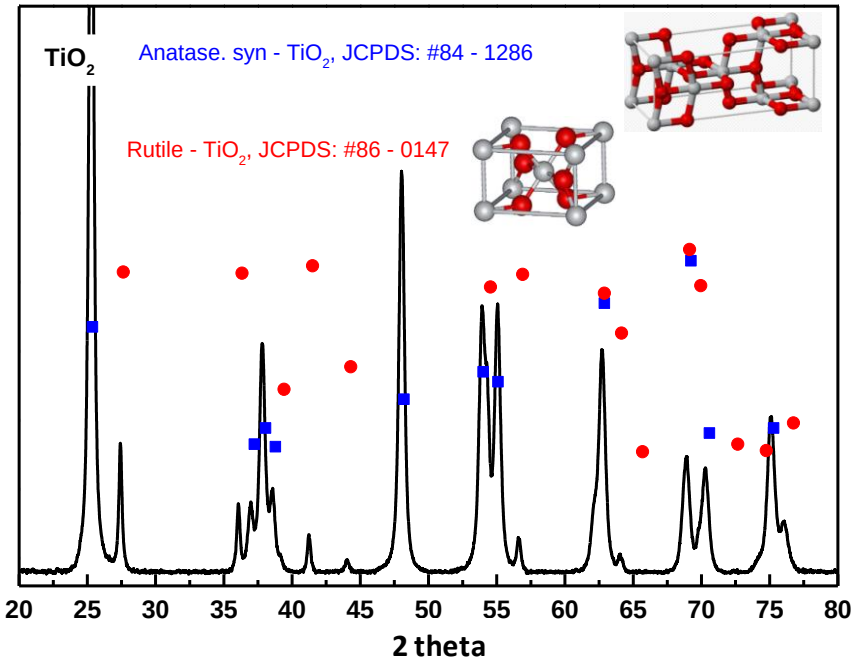

Figure 2-1: XRD of TiO_2 P25 support

2. Methods of sample preparation

In this study, two methods were selected for sample preparation: deposition-precipitation with urea (DPu) and deposition-precipitation at fixed pH. Note that these two methods were performed in isothermal condition, i.e., at 80 ^oC for DPu and room temperature for DP at fixed pH, and were based on the gradual change of reactants concentration, i.e., OH^- concentration for DPu, while metal ions concentration for DP at fixed pH.

Deposition-precipitation by a gradual and continuous increase of the pH of the suspension as a method for supported metal catalysts preparation was first proposed by Geus et al [4-6] in 1977 for the preparation of Ni/SiO_2 catalyst and consisted in the precipitation of nickel onto the silica surface (and not in solution) by basification of a nickel salt solution. In

this method, the basification of the preparation solution is achieved thanks to the controlled addition of a base (e.g., sodium hydroxide, ammonia and urea). According to Geus et al [4-6], one must consider the phase diagram of the precipitated solid in equilibrium with a solution containing its metal precursors as a function of temperature and concentration of a reactant (Figure 2-2). The solubility curve (S) corresponds to the equilibrium curve separating the monophasic domain (the solution containing the metal precursor) from the biphasic one (the precipitating solid and the solution), which is in fact reached when above the supersolubility (SS) curves. The intermediate domain between the S and SS curves corresponds to the nucleation. When in addition, the solution contains a finely dispersed support in suspension (usually an oxide one), both the solubility ($S_{support}$) and supersolubility curves ($SS_{support}$) are shifted to lower concentrations provided that interaction between ionic metal species and the surface of the support can occur, and favors nucleation at the surface of the support, and therefore decreases the nucleation barrier. Thus, to favor the metal precipitation on the support and avoid the precipitation of the metal in solution, the concentration of the metal complexes or the pH must be controlled between the concentration of the two supersolubility curves ($SS_{support}$ and SS). Note that, according to Geus et al [7], the gap in the concentration between the two supersolubility curves, SS and $SS_{support}$, is related to the bond strength between the ion species and the support surface.

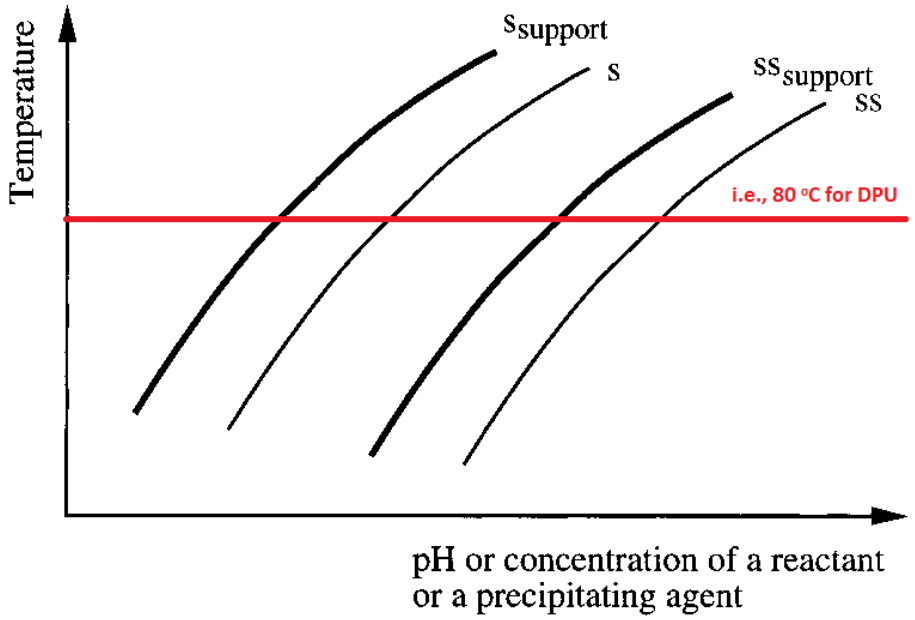

Figure 2-2: Phase diagram of precipitation and dissolution equilibrium of metal species in solution as a function of temperature and concentration of a reactant: in a pure solution (solid lines) and in the presence of a support in solution (bold lines) [7]

2.1 Deposition-precipitation with urea (DPu)

Deposition-precipitation with urea (DPu) is a deposition-precipitation method using urea as the precipitating agent. Compared to NaOH and ammonia, which can locally strongly increase the pH in the solution from their rapid hydrolysis and induce uncontrolled metal precipitation in the solution, the advantage of using urea is that it is a delay-base, i.e., its dissolution and decomposition to basify the solution can occur into two separated steps, which are controlled by the solution temperature. In other words, urea can dissolve into solution at room temperature and then decompose to CO_2, NH_4^+ and OH^- (eq.1) when the temperature of the suspension is raised above 60 ^oC [8].

$$CO(NH_2)_2 + 3H_2O \xrightarrow{>60\ ^oC} CO_2 + 2NH_4^+ + 2OH^- \qquad \text{eq. 1}$$

It allows homogeneous basification all over the solution, and favors the precipitation onto the support. It is possible to obtain high metal loadings (i.e., >20 wt% for Ni/SiO_2 [1]) depending on the precursor concentration and the time of deposition-precipitation. Moreover, after catalyst reduction, small metal particles can be obtained with rather narrow particle size distribution [9, 10].

Normally, the method of deposition-precipitation consists of 1, the transformation of a highly soluble metal precursor into another compound of lower solubility; 2, the deposition-precipitation of the lowly soluble compound onto a support after creation of an interaction between them by adjusting the initial pH. These two steps are usually achieved by raising the pH of the preparation solution.

2.1.1 Low solubility metal precursor conversion

Considering the fact that deposition-precipitation is an isothermal preparation method (i.e., 80 ^oC for DPu; red line in Figure 2-2), the concentration of soluble ions in the preparation solution gradually decreases as a result of deposition-precipitation onto the support surface during the pH increasing process of DPu. Moreover, since the relationship between the soluble ions concentration and the pH of the preparation solution is not reflected from Figure 2-2, a phase diagram showing the evolution of a solubility curve of a metal ion as a function of pH was introduced as follows and shown in Figure 2-3.

Before introducing the whole system, the definition of ionic product (J) should be first introduced. Based on the "Solubility Product Rule" [11], the precipitation and dissolution equilibrium of A_nB_m compound could be written as:

$$A_nB_m(s) \Leftrightarrow nA^{m+}(aq) + mB^{n-}(aq) \qquad \text{eq. 2}$$

The ionic product (J) is:

$$J = \left\{c(A^{m+})\right\}^n \bullet \left\{c(B^{n-})\right\}^m$$

Note that when the solution is saturated and solid formation (precipitation) occurs, the ionic product (J) is equal to the solubility products, K_{sp}^{Θ}.

In the case of supported metal catalyst preparation, the precipitation and dissolution equilibrium of the metal species can be written as follows:

$$M(OH)_{n(s)} \Leftrightarrow M^{n+}{}_{(aq)} + nOH^{-}{}_{(aq)} \qquad \text{eq. 3}$$

Once the equilibrium between dissolution and precipitation shows up during pH increasing, the concentrations of each part have a correlation like:

$$K_{sp}^{\Theta}M(OH)_n = C_{M^{n+}} \bullet \left(C_{OH-}\right)^n$$

Here, $K_{sp}^{\Theta}M(OH)_n$ is the solubility product constant of $M(OH)_n$. The solubility of $M(OH)_n$ (S_M) can be calculated as follows:

$$S_M = C_{M^{n+}} = \frac{K_{sp}^{\Theta}M(OH)_n}{\left(C_{OH-}\right)^n} \text{ mol/ L} \qquad \text{Formula 2-1}$$

Moreover,

$$K_W^{\Theta}H_2O = C_{H+} \bullet C_{OH-}$$

$$C_{H+} = 10^{-pH}$$

Thus Formula 2-1 can be written as:

$$S_M = C_{M^{n+}} = \frac{K_{sp}^{\Theta} M(OH)_n}{\left(K_W^{\Theta} H_2O\right)^n} (10^{-npH}) \text{ mol/ L} \qquad \text{Formula 2-2}$$

Considering that $K_{sp}^{\Theta} M(OH)_n$ and $K_W^{\Theta} H_2O$ are constant at a given temperature and for a given metal compound, the relationship between solubility of $M(OH)_n$ and pH was deduced from Formula 2-2 and shaped in Figure 2-3 (black solid line). Similarly to Figure 2-2, the supersolubility curve of $M(OH)_n$ species is also represented in Figure 2-3, at higher pH than that of solubility curve with the assumption that it has the same shape as that of solubility. Finally, the effect of the presence of a support in solution on the precipitation and dissolution equilibrium of metal compounds is also represented in Figure 2-3, shifted to lower pH as discussed for Figure 2-1.

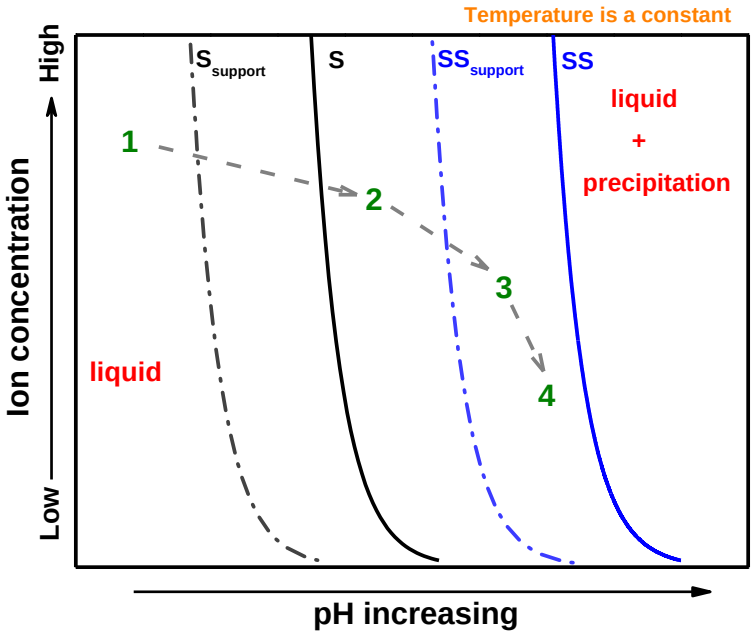

Figure 2-3: Phase diagram of the precipitation and dissolution equilibrium of metal species in solution as a function of pH and ion concentration: a pure solution (solid lines) and in the presence of a support (dotted lines)

From Figure 2-3, it can be seen that the initial concentration of soluble ions set to prepare a catalyst with a given metal loading decreases as the pH of solution increases (black solid line). The gradual increase in the concentration of precipitating agent (OH^-) promotes the deposition-precipitation procedure by hydrolysis of the metal complexes on the surface of the support, which brings a fluctuation in OH^- concentrations. In other words, the deposition

behavior of metal complexes can be roughly reflected by the pH evolution during DPu preparation, e.g., the pH of the preparation solution increases fast when it is lower than the solubility line (1→2 in Figure 2-3), then the rate of pH increasing gradually decreases when it reaches the nucleation-precipitation area (2→3→4 in Figure 2-3). Detailed information about pH evolution during sample preparation will be reported in the part devoted to the preparation of monometallic Cu/TiO_2 catalysts in Chapter 3. Besides that, a high pH has to be achieved for the deposition process when the concentration of an ion becomes very low.

Apart from the DPu preparation of mono-metallic catalyst system that was discussed above, the deposition-precipitation of two metal ions on a single oxide support must be also discussed as it is one of the purposes of this thesis. According to Figure 2-2, if one wants that the two different metal ions are co-deposited on the support surface in a single step, the solubility products of the two metal compounds must be closed to each other. The solubility products of Cu(II), Zn(II), Ni(II), Fe(II) and Fe(III) hydroxide compounds at room temperature are summarized in Table 2-1. Moreover, the precipitation and dissolution equilibrium of these metal compounds were calculated from Formula 2-2 and shown in Figure 2-4. The presence of the oxide support is not taken into consideration.

Table 2-1: the solubility products of non-noble metal hydroxide under 298 K [12]

M(OH)n	$K_{sp}^{\Theta} M(OH)_n$
$Zn(OH)_2$	**4.1×10^{-17}**
$Cu(OH)_2$	**2.0×10^{-19}**
$Ni(OH)_2$	**5.5×10^{-16}**
$Fe(OH)_2$	**4.9×10^{-17}**
$Fe(OH)_3$	**6.0×10^{-38}**

Although Figure 2-4 only considers the precipitation and dissolution equilibrium behavior of metal ions as a function of pH in water (i.e., in the absence of oxide support) at room temperature, the large differences in solubilities between Cu^{2+} and Zn^{2+} or between Ni^{2+} and Zn^{2+} ions certainly also indicate that the two cations cannot be simultaneously deposited onto a support during increasing pH. This may be different for Fe^{2+} and Zn^{2+} since they have similar solubility.

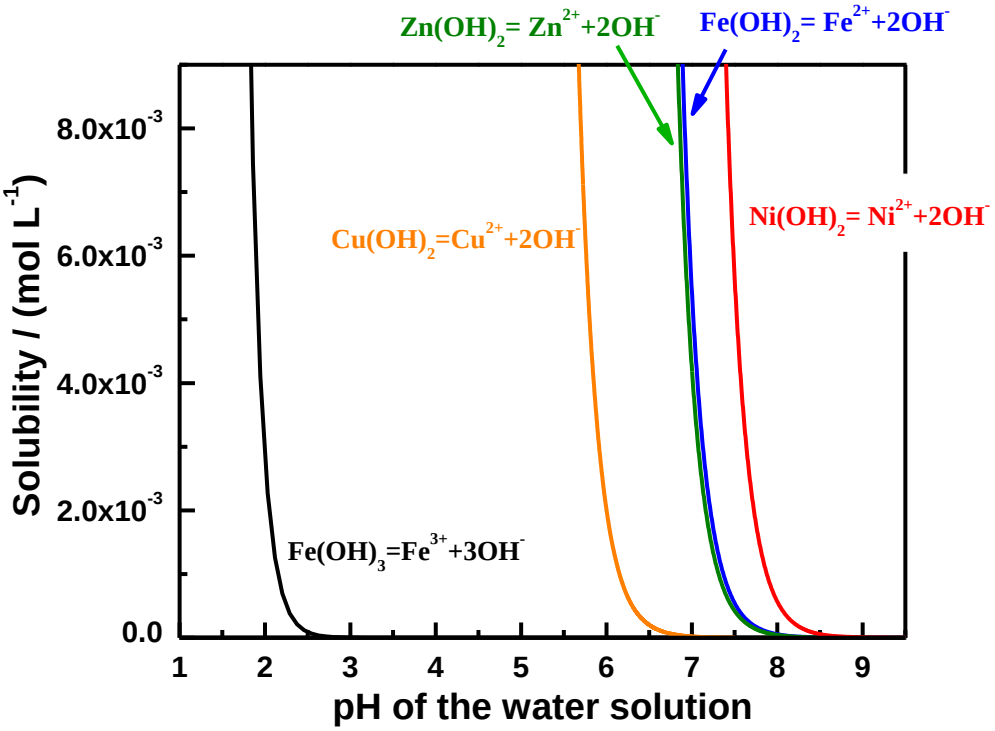

Figure 2-4: Solubility of metal hydroxides in pure water solution at T=298 K

2.1.2 Surface charge of the support

Although the transformation of highly soluble metal precursor into another compound with low solubility, e.g., a hydroxide, is a necessary step for DPu process, the interaction between metal complexes and support surface is considered as the initial step for the deposition-precipitation preparation. Currently, this kind of interaction can be generated through electrostatic interaction, resulting from opposite surface charges between the metal complexes and the support, which has been testified by some quartz crystal microbalance (QCM) experiments [13, 14]. The surface charge of an oxide can be defined by its point of zero charge (PZC) [15, 16]. When the pH of the preparation solution is lower than the PZC of support, the support surface is positively charged and suitable for anion adsorption; when the pH of the solution is higher than the PZC of support, it is negatively charged and suitable for cation adsorption, and a neutral surface can be found on oxide surface at the pH equal to the PZC of support. (Figure 2-5). Practically, the adsorption of $[Pt(NH_3)_4]^{2+}$ on silica occurred at high pH when silica surface is negatively charged while the adsorption of $[PtCl_6]^{2-}$ appeared on alumina at low pH, which generates a positively charged alumina surface [13].

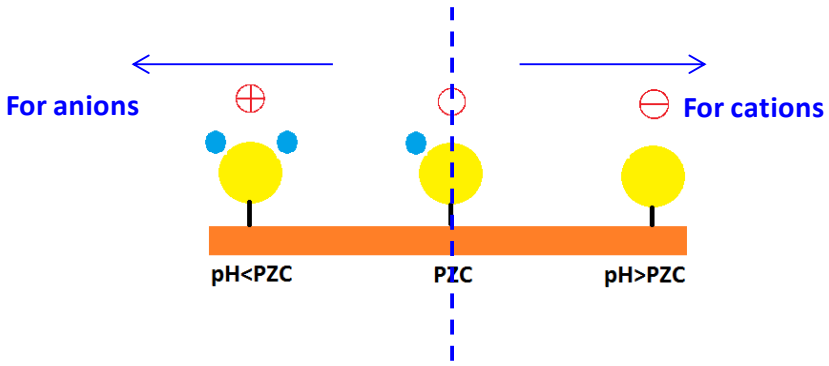

Figure 2-5: Surface charge at pH above, below the PZC of oxide

The PZC of some oxides, measured by potentiometric titration [17-20] and/or mass titration [21-23], are summarized in Table 2-2.

Table 2-2: the point of zero charge of common oxides

Oxide	PZC
SiO_2	~2
CeO_2	~7.5
ZnO	8.7-10.3
NiO	10-11
Al_2O_3	~8
TiO_2	~6

However, a specific adsorption behavior has been found for TiO_2, it is able to adsorb cations even at pH lower than its PZC, and detailed information about the reason for such an adsorption behavior will be discussed in the "mono metallic Cu/TiO_2 preparation" part in chapter 3.

In summary, in the process of deposition-precipitation with urea (DPu), the interaction between the metal precursor and the surface of the support generates nuclei that allow specific precipitation of the hydroxide onto the support surface, and promotes the formation of highly dispersed particles after thermal treatment.

2.1.3 The steps of deposition-precipitation with urea

In practice, 3 g of support is weighted and dispersed into an 300 mL aqueous solution ($m_{support(g)}$: $V_{water(ml)}$ = 1:100) containing a given amount of dissolved metal precursor(s). Initially, the pH of the precursor solution needs to be set at a value below the solubility curve of metal compounds and below the PZC of the support to favor first electrostatic interaction

between the metal ion complex and the support surface. Then the precipitating agent (urea) is added into the mixture, with a concentration ratio [urea]/ [metal] ≥ 100 at room temperature. The mixture is heated at 80 °C and stirred for 20 h. After that, the solid is separated from the liquid phase by centrifugation and subsequently repeatedly washed with distilled water and centrifuged (three times). Then, the sample is dried under vacuum at room temperature for 24 h then activated through thermal treatment (Figure 2-6).

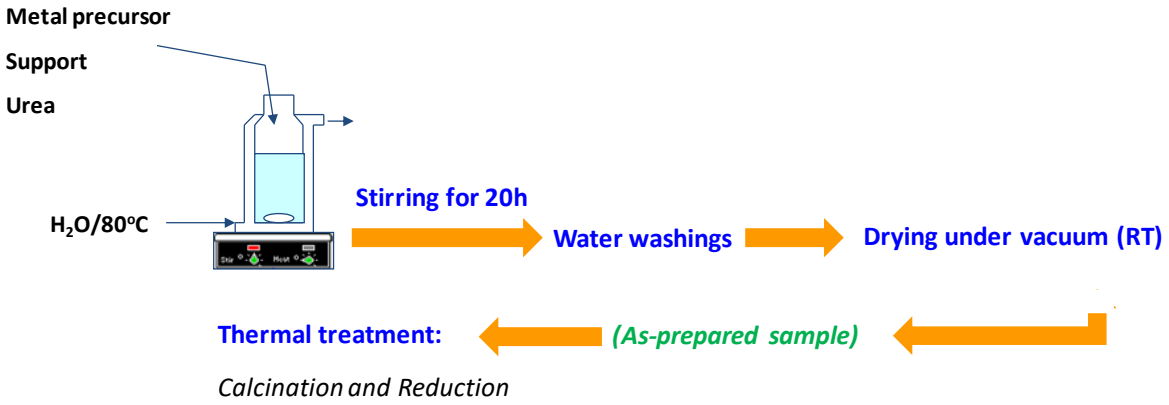

Figure 2-6: Steps of preparation of supported metal catalyst by DPu

2.2 Deposition-precipitation at fixed pH

As presented above, when there is a gap between the two solubility curves (Figure 2-4), the two metal compounds cannot be simultaneously deposited on the surface of the support during a preparation performed by gradual increase of pH (i.e., DPu). In order to achieve a co-deposition of two metal compounds on the support, another method, called deposition-precipitation at fixed pH, is proposed here.

In this method, the pH, and thus the concentration of the precipitating agent, of the preparation solution is kept constant by gradual addition of precipitating agent during the whole deposition-precipitation process, while, the metal precursors are also slowly injected into the solution. Note that the precipitating agent and the metal precursor solution are directly injected inside the solution (enlarged graph in Figure 2-7). Electrostatic interaction between the metal complex and the surface of the support can be controlled by selecting the pH. In addition, a suitable flow rate for aqueous metal precursor injection must be chosen to keep the concentration of dissolved metal ion slightly lower than that of the supersolubility curves (SS), to avoid the precipitation in solution, as it was shown in Figures 2-2 and 2-3. The preparation process can be carried out at RT.

2.2.1 The steps of deposition-precipitation at fixed pH

The general procedure of sample preparation by deposition-precipitation at fixed pH is summarized in Figure 2-7. In practice, 3 g of support is dispersed into 250 mL water in a beaker at room temperature and the metal precursors are dissolved into 50 mL water, here, $m_{support(g)}$: $V_{water(mL)}$ =1:100. Then, the pH of the support suspension is adjusted to a chosen pH by addition of an aqueous NaOH solution (0.5 M). After stirring for 30 min, the aqueous solution of the metal precursor is injected into the support suspension with a controlled rate that will be discussed below, and vigorous stirring. After that, the mixture is stirred for 1 h. The pH of the support suspension is kept constant by regular addition of NaOH solution during the whole preparation procedure. The solid sample is collected by centrifugation and subsequently washed with distilled water and centrifuged again (three times) in the same way as for the DPu samples.

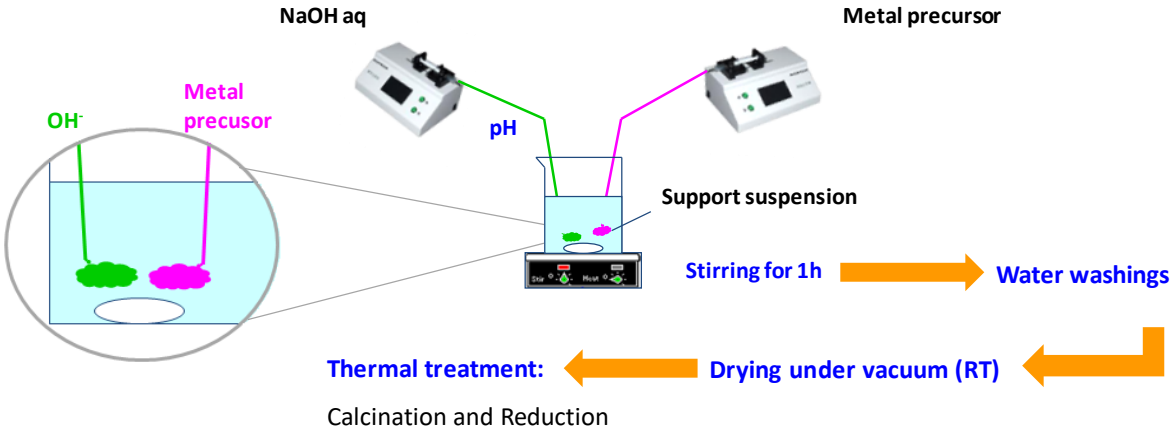

Figure 2-7: Steps of preparation of supported catalyst by deposition-precipitation at fixed pH

2.2.2 Theoretical calculation for the selection of preparation condition

To clearly present this method, one example is given to explain how to select the rate for injecting metal precursors in the support suspension at a constant pH. The example is based on the preparation of 3 g of a CuZn 1:1/TiO_2 sample with 2.5 wt% Cu and 2.5 wt% Zn performed at RT and pH~8 (i.e., at a pH where the TiO_2 surface is negatively charged, and the metal complexes are positively charged). 3 g of TiO_2 are dispersed in 250 mL of water, and the pH is adjusted to 8 by injecting a solution NaOH (0.5 M). The metal precursors ($Cu(NO_3)_2$•$3H_2O$ and $Zn(NO_3)_2$•$6H_2O$) are dissolved in 50 mL of water. The concentration of Cu^{2+} and Zn^{2+} ions are 2.46×10^{-2} mol L^{-1} and 2.4×10^{-2} mol L^{-1}, respectively. Considering the

fact that the catalyst preparation is performed under air at room temperature in a basic solution, the metal complexes that might form during metal hydrolysis are metal hydroxides or metal carbonates, thus the solubility at room temperature of all these metal compounds are summarized in Table 2-3.

Table 2-3: the solubility product of the metal compounds at room temperature [12]

Metal species	**$Zn(OH)_2$**	**$ZnCO_3$**	**$Cu(OH)_2$**	**$CuCO_3$**
K_{sp}	**4.1×10^{-17}**	**1.2×10^{-10}**	**2×10^{-19}**	**1.3×10^{-10}**

It can be seen that $Zn(OH)_2$ and $Cu(OH)_2$ have a much lower solubility than their carbonate compounds, thus these two compounds will be precipitated first during the gradual increase of Cu^{2+} and Zn^{2+} concentrations in the solution. Besides that, since $Zn(OH)_2$ has a higher solubility than $Cu(OH)_2$, the rate of injection must be controlled in such a way that the concentration of soluble Zn^{2+} ion in the preparation solution remains slightly below or at the solubility value of $Zn(OH)_2$ if one wants to co-deposit(precipitate) Cu^{2+} and Zn^{2+} through one single injection of aqueous Cu^{2+}/Zn^{2+} mixtures containing similar ion concentration. As a result, based on the solubility of $Zn(OH)_2$, the limitation of the concentration of Zn^{2+} in the solution that could both avoid the precipitation of $Zn(OH)_2$ in solution and achieve the goal of co-deposition-precipitation of Cu and Zn could be calculated as follows:

The hydrolysis of Zn^{2+} is:

$$Zn(OH)_2 \leftrightarrow Zn^{2+} + 2OH^-$$

The solubility parameter of $Zn(OH)_2$ is:

$$K_{sp}^{\Theta} Zn(OH)_2 = C_{Zn^{2+}} \times (C_{OH-})^2 \qquad \text{Formula 2-3}$$

When the pH of the suspension is 8 at RT, the C_{OH-} can be calculated as follows:

$$C_{OH^-} = \frac{K_W^{\Theta} H_2O}{C_{H+}} = \frac{1\times10^{-14}}{1\times10^{-8}} = 1\times10^{-6} \text{ mol } L^{-1}$$

As a result, the limitation of the concentration of Zn^{2+} in the support suspension can be calculated by Formula 2-3:

$$C_{Zn^{2+}} = \frac{K_{sp}^{\Theta} Zn(OH)_2}{(C_{OH-})^2} = \frac{4.1*10^{-17}}{(1*10^{-6})^2} = 4.1\times10^{-5} \text{ mol } L^{-1}$$

Since the total volume of the suspension is 250 mL, the limitation of the molar amount of Zn^{2+} that can avoid $Zn(OH)_2$ precipitation appears in solution is

$$n_{Zn^{2+}} = C_{Zn^{2+}} \bullet V_{total} = 4.1\times10^{-5} \times 0.25 = 1.025\times10^{-5} \text{ mol}$$

The average concentration of Zn precursor in the 50 ml Cu^{2+} and Zn^{2+} aqueous solution is 2.4×10^{-2} mol L^{-1}, thus the volume of the Cu^{2+} and Zn^{2+} aqueous solution injected into the support suspension should be below the V_{mix}:

$$V_{mix} = \frac{n_{Zn^{2+}}}{C_{average}} = \frac{1.025*10^{-5} mol}{2.4*10^{-2} mol/L} = 0.42 mL$$

Previous Quartz Crystal Microbalance (QCM) study [13] about the transition metal complex adsorption on oxide surface, such as $[Pt(NH_3)_4]^{2+}$ adsorption on SiO_2 at pH=10 showed that electrostatic adsorption occurs very fast. Based on these results, one can assume that 5 s is needed for the interaction between the metal ions (2.42×10^{-2} mol L^{-1}) in the added 0.42 mL solution and TiO_2 surface, thus the injection rate of the aqueous metal solution must be slower than 0.084 mL s^{-1}. The gradual addition of the metal precursors at the injection rate that has been calculated and the interaction between the metal complexes and the support surface would allow the nucleation of metal hydroxides to mainly happen on the surface of the support.

3. Techniques for samples characterization

The pH evolution of the mixture suspension was recorded using a pH probe (PHM201 Portable pH Meter). In the DPu preparation procedure, both the decomposition of urea and the consumption of the OH^- ions by the formation and deposition of the metal hydroxide induce pH evolution. As a result, it was interesting to monitor the pH evolution during DPu preparation. The pH of the suspension during deposition-precipitation at fixed pH also requires to be controlled. Before the pH probe was applied to any measurement, it has to be

calibrated by the pH=4 and pH=7 buffer solutions and the electrode sensitivity of the pH probe needed to be in the range 97-100%.

The metal loadings were measured by X-ray fluorescence (XRF) with a spectrometer XEPOS HE (AMETEK). XRF is based on the emission of the characteristic fluorescence X-ray from a material that has been excited by bombarding with high-energy X-rays or gamma rays, the application of which was first proposed by Glocker and Schreiber et al [24]. The method used for the XRF analyses was based on calibration curves obtained from standard samples for each element.

X-ray Diffraction (XRD) was performed on a diffractometer (D8 Bruker Company) operating with Cu Kα radiation (1.5418 Å; 40 kV and 30 mA) with a Ni filter. It is an analytical technique primarily used for crystal structure identification of crystalline materials, and also can provide an average bulk composition of the crystalline material through matching the XRD peaks detected with the JCPDS cards. The X-rays generated by a cathodic tube, interact with the sample to produce constructive interferences when conditions satisfy the Bragg's Law ($n\lambda = 2d\sin\theta$, in which d is the d-spacing in crystal lattice). The crystallite size of the mineral can be calculated by Scherrer's equation [25] as follows:

$$\bar{d} = \frac{k\lambda}{\beta\cos\theta}$$

In which $\bar{d}$ is the average particle size; k is a dimensionless shape factor with a value close to 0.89; λ is the X-ray wavelength (0.15406 nm); θ is the Bragg angle (unit: °); specifically, β is the full width at half maximum (FWHM) with a unit rad (1° = π/180 rad), and it can be calculated by using the Gaussian formula to "nonlinear fitting" the XRD curve in the "Origin" software. The Gaussian formula is

$$y = y_0 + \frac{Ae^{\frac{-4\ln(2)(x-x_c)^2}{w^2}}}{w\sqrt{\frac{\pi}{4\ln(2)}}}$$

In which, w = FWHM (Figure 2-8).

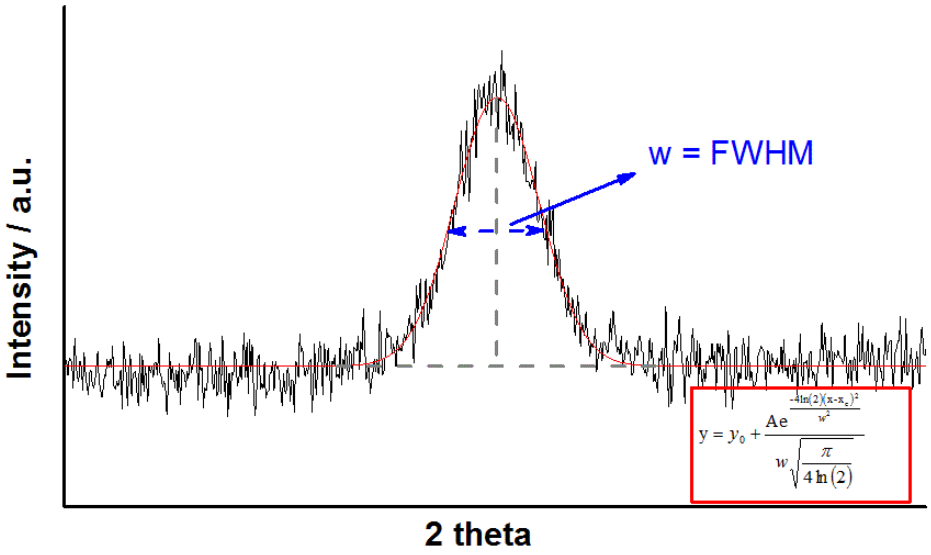

Figure 2-8: FWHM simulation from nonlinear fitting XRD peak by the Gaussian formula

Ultraviolet–visible spectroscopy (UV-Vis) in liquid (transmission mode) and solid phase (diffuse reflectance mode) are recorded on a Cary 5000 spectrometer in the range 1200–350 nm at room temperature. Prior to measurement in solid phase, all the dried powders are finely crushed and lightly pressed into the sample holder of the diffuse reflectance cell. In this study, titanium oxide and pure water are used as references for the analysis of solid and liquid phases, respectively.

The reduction behavior of the supported metal compound was studied by temperature programmed reduction (TPR) in a Micromeritics Autochem Π. In this measurement, a purge under Ar (25 mL min^{-1}) was performed for 30 min to remove the air contained in the reactor at room temperature (RT) before increasing temperature at a linear rate of 7.5 ^{o}C min^{-1} in a 5% H_2/Ar gas mixture flow (25 mL min^{-1}). The reduction behavior of metal compounds can be determined according to the temperature at which the H_2 consumption peaks appear.

The acidic property of the support surface was measured by ammonia temperature program desorption (NH_3-TPD), which was performed in a Micromeritics Autochem II Automated Catalyst Characterization System. After thermal treatment, ammonia was adsorbed on the surface of the support by inletting 5 %NH_3/Ar for few hours, and then the cell was flushed with Ar gas to remove the physically adsorbed ammonia for 30 min. After that, the temperature of the sample was increased and the amount of ammonia desorption was recorded. The strength of acidic sites is related to the temperature at which ammonia desorption occurs, ammonia desorbing from the stronger acidic sites at a higher temperature.

Moreover, the number of acidic sites on the support surface can be determined by the amount of ammonia desorption.

To quantify the amount of NH_3 desorption, Mass Spectrometry (MS) was applied to measure the intensity of the NH fragment (m/z= 15) during the whole TPD test. The mass spectrometry was calibrated by injecting 0.51 mL of pure ammonia (i.e., 1.13829×10^{-6} mol) in the mass spectromer at 273 K for 5 times to get an average value (Figure 2-9).

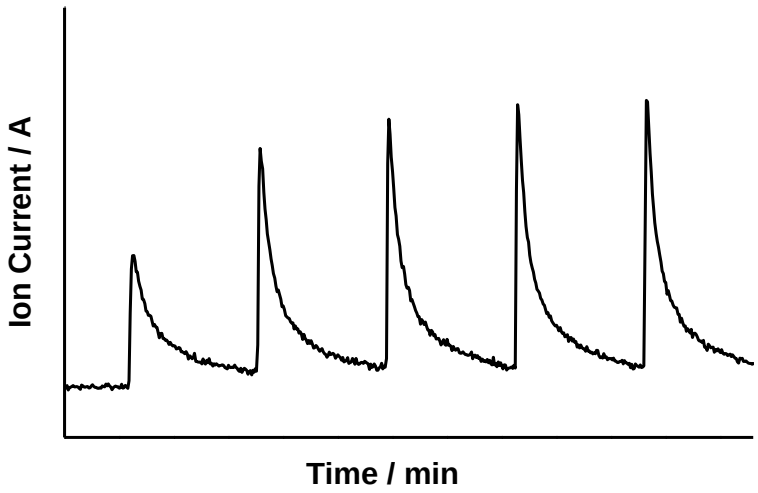

Figure 2-9: calibration of mass spectrometry for NH_3 desorption

Two Transmission Electron Microscopy (TEM) techniques are employed in this thesis. The first one is JEOL JEM-100CX II microscope operating at 100 kV. Specially, for the study of monometallic Cu/TiO_2 catalysts, the Cu/TiO_2 samples were reduced on Mo-grid at 350 ^oC and transferred into TEM machine without contacting with air. The reduction in the cell was performed under hydrogen (100 mL min^{-1}), and temperature program was as follows: the temperature was heated from RT to 350 ^oC in 30 min, maintained at 350 ^oC for 15 min, then cooled down to RT. Besides that, the morphology of the metallic nanoparticles is also observed by Transmission Electron Microscopy (TEM) on a JEOL 2010 microscope. The resolution of this TEM equipment is 0.3 nm at 200 kV. To better distinguish metal particles from the support, scanning transmission electron microscopy in high-angle annular dark-field mode (STEM-HAADF) are also performed to study small mono and bimetallic particles. This was done on a JEOL ARM 200F microscope, equipped with a cold field emission gun and a CEOS aberration corrector of the objective lens, operated at 200kV. The resolution of this

STEM machine is 0.046 nm at 200 kV. Energy-dispersive X-ray spectroscopy (EDS) characterization with different modes (i.e., point, linear and area testing mode) was performed to evaluate the composition of metal particles in bimetallic samples. The powder sample was directly deposited onto the grid without the use of a solvent. Note that Mo-grid was used for Cu-Zn/TiO_2 sample and Cu-grid was used for the other samples observation. Statistical analysis of the metal particle size distributions (PSD) in reduced samples is obtained by counting more than 200 particles, using the free software Image J. The average particle diameter was deduced from the equation $d_m = \sum n_i d_i / \sum n_i$ or $d_m = \sum n_i d_i^3 / \sum n_i d_i^2$ where n_i is the number of the particles of diameter d_i.

Thermogravimetric analysis (TG) was performed on the samples (15 mg) after reaction using a Seiko 320 thermobalance, under air with a total flow rate of 100 ml min^{-1}, from room temperature to 900 ^oC with a heating rate of 7.5 ^oC min^{-1}. The composition of outlet gas was analyzed by Mass Spectrometry (MS) during the temperature ramp for some catalysts, such as bimetallic Ni-Zn/TiO_2. The temperature of the TG/MS interface was held at 160 °C, and the mass spectra were obtained from m/z 10 to 120 with the scan rate of 40 amu/s.

XPS spectra were collected on a SPECS (Pholibos 100-5MCD) X-ray photoelectron spectrometer, using a monochromated Al Kα (*hv* = 1486.6 eV) X-ray source. The samples were *ex situ* calcined then reduced at specific temperature and transferred in air to the XPS chamber. After collection, the binding energies were calibrated with respect to the C-C/C-H components of the C 1s peak (binding energy = 284.6 eV). All spectra processing was carried out using the Casa XPS software package.

4. The selective butadiene hydrogenation in the excess of propene

4.1 The catalytic test system and condition for the experiment

The catalytic equipment is presented in Figure 2-10. In this system, calcination, reduction and catalytic reaction can be performed. As a result, catalytic performance was measured after *in-situ* thermal treatment. For the catalytic test, 100 mg of powder, with particle size between 125 and 200 μm, is filled into a U shape tube reactor (4 mm of internal diameter). Note that the weight of active compounds (i.e., Cu, Ni and Fe) was kept constant for the catalytic tests (e.g., 2.5 mg Cu for bimetallic Cu-Zn/TiO_2 study and 0.05 mg Ni for

bimetallic Ni-Zn/TiO_2 study, 2.5 mg Fe for bimetallic Fe-Zn/TiO_2 study) and pure support was added to reach 100 mg of catalytic bed.

In the procedure of sample pretreatment, air (for sample calcination) then H_2 (for sample reduction) was introduced into the reactor, with a flow rate of 100 mL min^{-1}. The increase in temperature of the reactor in an oven was controlled via a temperature program.

When activation was finished, the sample was cooled down to room temperature in H_2 atmosphere with a flow rate of 100 mL min^{-1}, and the gas mixture containing 0.3% Butadiene/ 20% H_2/ 30% Propene (Table 2-4) was first analyzed by gas chromatograph (GC) before introduction in the reactor, as a reference. After that, the reaction gas mixture was allowed to flow through the reactor, and the outlet gas (reactants and products) was analyzed by a gas chromatograph (Perichrom PR 2100, FID detector) with a 7.5 m column (1/8 inch) filled with sebaconitrile 25% Chromosorb PAW (80/100 Mesh). The data were collected as a function of time/temperature for a temperature programmed catalytic test and as a function of time for an isothermal catalytic test. Software Winilab 4.0 was used for data acquisition and extraction of the concentration of each gas composition. As mentioned in [26], preliminary tests were made to attest that, under the reaction conditions, internal and external diffusion limitations could be neglected. The flow rate of the reaction gas mixture is 50 mL min^{-1}, which corresponded to a space velocity of 30 L g^{-1} h^{-1} (GHSV=20000 h^{-1}).

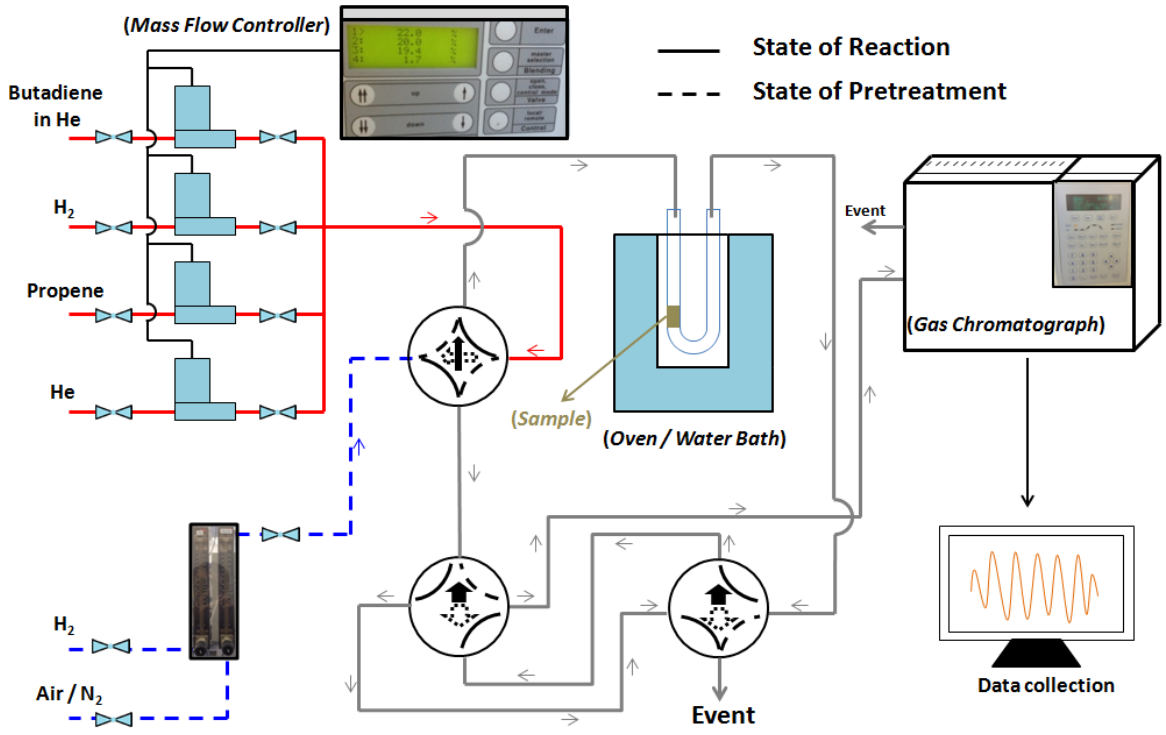

Figure 2-10: schematic diagram of catalytic test system

In this study, the composition of the gas mixture was controlled by mass flow controllers with a concentration ratio between butadiene and propene of 1:100, Table 2-4.

Table 2-4: the composition of the original gas mixture

Composition	Concentration
Butadiene	**0.3% (3000 ppm)**
Propene	**30%**
H2	**20%**
He	**Balance**

In the study of monometallic Cu and Cu-Zn/TiO_2 bimetallic catalysts, activation of the *ex situ* calcined samples was performed in H_2 from RT to 350 ^oC at a heating rate of 2 $^oC\ min^{-1}$, and then for 2 h at 350 ^oC. After catalyst activation, the catalyst was cooled down to RT under H_2 with a flow rate of 100 mL min^{-1}. the activity was measured every 15 min with a temperature increasing from 30 to 300 ^oC at 1 $^oC\ min^{-1}$, and the stability test was carried out at the temperature of 100% butadiene conversion and/or at 105 ^oC for 20 h under the reaction gas mixture with flow rate of 50 mL min^{-1}

In the study of monometallic Ni and Ni-Zn/TiO_2 bimetallic catalysts, the temperature program for the *ex situ* calcined samples activation was reduction in H_2 from RT to 450 ^oC, 3 $^oC\ min^{-1}$, and then staying at 450 ^oC for 2 h with a flow rate of 100 mL min^{-1}. After catalytic activation, the activity measurement was performed every 5 ^oC from 10 ^oC to 80 °C under the reaction gas mixture with flow rate of 50 mL min^{-1}, with stabilizing at each testing temperature for 15 min in water bath. Similar initial butadiene conversion (~85%) was selected for the comparison of catalytic stability of bimetallic Ni-Zn samples with testing time as long as 60 h.

In the study of monometallic Fe and Fe-Zn bimetallic catalyst, the calcined catalyst was activated in H_2 at plateau of 500 ^oC for 2 h, with a heating rate 3 $^oC\ min^{-1}$. After that, the butadiene conversion mensurement was performed every 5 ^oC with an initial temperature at 10 ^oC under the reaction gas mixture with flow rate of 50 mL min^{-1}, with stabilizing at each testing temperature for 15 min in water bath. Once the butadiene conversion reached 100%, the temperature was kept as a constant for other 20 h of isothermal reaction.

4.2 The evaluation of the catalytic performance

Once the data of catalytic reaction were collected by the Winilab software, the catalytic properties were analyzed as follows:

1. The butadiene and propene conversion are expressed as:

$$Conversion_{butadiene}\ (\%) = 100 \times \left(1 - \frac{Butadiene_{outlet}}{Butadiene_{inlet}}\right)$$

$$Conversion_{propene}\ (\%) = 100 \times \frac{propane_{outlet}}{propene_{inlet}}$$

2. The activity and turn over frequency (TOF) are expressed as:

$$Activity\ (mol \cdot s^{-1} \cdot g_{metal}^{-1}) = \frac{(Butadiene_{consumed}\ )_{ppm} \cdot Q}{m_{catal} \times wt\%_{metal}} \cdot \frac{P}{R \cdot T}$$

$(Butadiene_{consumed}\ )_{ppm}$ is the concentration of the butadiene that is converted to alkenes and alkane; Q is the flow rate of the gas mixture; P/RT = 1/V (24 L mol^{-1});

$$TOF(s^{-1}) = \frac{Activity \cdot M_{metal}}{D}$$

$$D(\%) = 10^{21} \times \frac{6 \times M \times \rho_{site}}{d_{metal} \times \rho_{metal} \times N}$$

in which D(%) is the metal dispersion, using the formula described by Scholten et al [27], which assumes the metal nanoparticles are spherical shape, thus the number 6 in the D(%) formula is received from the volume (V) – surface area relationship (S): $S = 6 \times \frac{V}{d_{metal}}$ (detailed information can be found in Scholten et al); M is the metal molar mass (g mol^{-1}); ρ_{site}

is the metal surface site density (e.g., 14.7, 15.4, 16.3 atom nm^{-2} for copper, nickel and iron, respectively [27]); d is average particle; ρ_{metal} is the metal density (8.96, 8.908 and 7.874 g cm^{-3} for copper, nickel and iron, respectively); N is the Avogadro constant (6.02×10^{23} mol^{-1}). For the bimetallic catalysts, the copper and nickel surface site densities were estimated using the average Cu/Zn and Ni/Zn atomic ratios that were determined from EDS analyses.

3. The catalytic selectivity to butenes and to butane was evaluated as follows:

$$Selectivity\ to\ butenes(\%) = \frac{Butenes_{outlet}}{Butenes_{outlet} + Butane_{outlet}} \times 100$$

$$Selectivity\ to\ butane\ (\%) = \frac{Butane_{outlet}}{Butenes_{outlet} + Butane_{outlet}} \times 100$$

5. Reference

1. P.Burattin, M.Che, C. Louis, The Journal of Physical Chemistry B, 101 (1997) 7060.
2. V.Kaushik, C. Sivaraj, P.K. Rao, Applied surface science, 51 (1991) 27.
3. K.Bourikas, C. Kordulis, A. Lycourghiotis, Chemical reviews, 114 (2014) 9754.
4. J.A. van Dillen, J.W.G., L.A Hermans, J. van der Meijden, In "Proceedings of the 6th International Congress on Catalysis" London, 1976.
5. G. C. Bond, P.B.W., F.C. Tompkins, Ed., The Chemical Society: London, 1977, P 677.
6. J.W.E.Coenen, *Reduction of Silica Supported Nickel Catalysts*, in *Studies in Surface Science and Catalysis*, P.G.P.J. B. Delmon and G. Poncelet, Editors. 1979, Elsevier. p. 89-111.
7. J.W.Geus, A.J. Dillen, *Preparation of supported catalysts by deposition–precipitation.* Handbook of heterogeneous catalysis, 1997.
8. W.H.R.Shaw, J.J. Bordeaux, Journal of the American Chemical Society, 77 (1955) 4729.
9. J.T.Richardson, R.J. Dubus, Journal of Catalysis, 54 (1978) 207.
10. M.A.Keane, Canadian Journal of Chemistry, 72 (1994) 372.
11. J.Kragten, , *Atlas of metal—ligand equilibria in aqueous solution*, 1979, Pergamon.
12. J.Bjerrum, , *Stability constants of metal-ion complexes*. 1964: The Chemical Society.
13. J.Blancharda, A.Hervier, G.Costentin, J.Regalbuto, C.Louis, S.Boujday, Catalysis Today, 235 (2014).
14. A.L. J. Olsson, I.R. Quevedo, D.He, M.Basnet, N.Tufenkji, ACS nano, 7 (2013) 7833.
15. G.A.Parks, Chemical Reviews, 65 (1965) 177.
16. R.M.Cornell, A.M.Posner, J.P. Quirk, Journal of Colloid and Interface Science, 53 (1975) 6.
17. S.Mustafa, B.Dilara, Z.Neelofer, A.Naeem, S.Tasleem, Journal of Colloid and Interface Science, 204 (1998) 284.
18. A.L.Valdivieso, J.L.Reyes Bahena, S.Song, R.Herrer Urbina, *interface.* Journal of Colloid and Interface Science, 298 (2006) 1.
19. K.C.Akratopulu, L. Vordonis, A. Lycourghiotis, Journal of the Chemical Society, Faraday Transactions 1: Physical Chemistry in Condensed Phases, 82 (1986) 3697.
20. K.C.Akratopulu, C. Kordulis, A. Lycourghiotis, Journal of the Chemical Society, Faraday Transactions, 86 (1990) 3437.

21. S.Subramanian, J.S.Noh, J.A. Schwarz, Journal of Catalysis,114 (1988) 433.
22. S.Ẑalac, N.Kallay, Journal of Colloid and Interface Science, 149 (1992) 233.
23. K.Bourikas, J.Vakros, C.Kordulis, A.Lycourghiotis, The Journal of Physical Chemistry B, 107 (2003) 9441.
24. R.Glocker, H.Schreiber, Annalen der Physik, 390 (1928) 1089.
25. D.M. Fernandes, R.Silva, A.A.Winkler Hechenleitner, E. Radovanovic, M.A. Custódio Melo, E.A. Gómez Pined, Materials Chemistry and Physics, 115 (2009) 110.
26. A.Hugon, L.Delannoy, J.M.Krafft, C.Louis, The Journal of Physical Chemistry C, 114 (2010) 10823.
27. J.Scholten, A.Pijpers, A. Hustings, Catalysis Reviews, 27 (1985) 151.

Chapter 3: Preparation and Characterization of Monometallic Catalyst (Cu,Zn, Ni)

Chapter 3: Preparation and Characterization of Monometallic Catalyst (Cu, Zn, Ni)

1. Introduction

As mentioned in Chapter 2, Deposition-Precipitation with urea (DPu), which is based on gradual pH increasing of the solution containing the metal precursor, due to urea decomposition at 80 ^{o}C, is the main method used for catalyst preparation in this thesis. The theoretical calculations reported in Figure 2-3 in Chapter 2 indicate that copper, zinc and nickel ions have different "deposition behaviors". As a consequence, the deposition-precipitation of these different transition metals ions onto TiO_2 support surface was experimentally studied, separately, and presented in this chapter. Monometallic Cu/TiO_2 was selected as an example to deeply explore the deposition-precipitation behavior of transition metals ions in the presence of TiO_2 support during the DPu preparation.

Besides the study of deposition-precipitation of transition metals ions, the crystallite structure and the catalytic performances of TiO_2-supported monometallic samples are also explored in this chapter. This will help us to better distinguish the function of each metal in the bimetallic Cu-Zn/TiO_2 and Ni-Zn/TiO_2 catalysts for selective hydrogenation reaction, i.e. which one could be the main active metal and which one would be the promoter or the modifier. The catalytic results over the monometallic Cu/TiO_2 and Ni/TiO_2 and Zn/TiO_2 catalysts will also help at selecting the appropriate catalytic conditions (e.g., metal loading) for the further study of the TiO_2-supported bimetallic catalysts. Besides that, in a previous study, Derrouiche et al [1] of Cu/ZnO catalysts showed that metallic Cu particles were formed after sample reduction at 280 ^{o}C, and that they transformed to intermetallic Cu-Zn particles at higher reduction temperature to form Cu_3Zn_1 alloy at 350 ^{o}C. Thus in this chapter, we also study the Ni/ZnO system to determine whether Ni-Zn alloy can be also evidenced.

In this chapter, the DPu preparation of monometallic catalysts i.e., Cu, Zn and Ni supported on TiO_2 or ZnO, and their catalytic performances for selective hydrogenation of butadiene are studied.

2. Preparation of monometallic catalysts

A series of supported Cu, Zn and Ni catalysts were prepared by deposition-precipitation with urea using the same duration of 20 h (see Section 2 in Chapter 2, Experiment I) according to the following procedure: 300 mL of distilled water and 3 g of support TiO_2 P25 Evonik (80% anatase and 20% rutile, 50 $m^2\ g^{-1}$) or ZnO (Kadox, 8 $m^2\ g^{-1}$) were introduced into a double-wall reactor. The mixture was heated at 80 ^oC. Given amounts of metal precursors (i.e., $Cu(NO_3)_2{\cdot}3H_2O$, $Zn(NO_3)_2{\cdot}6H_2O$ and $Ni(NO_3)_2{\cdot}6H_2O$) were dissolved into the aqueous suspension in order to achieve the desired nominal metal loadings. The initial pH of the preparation solution was 3~4, depending on the acid-base properties of the metal precursor. After addition of a large excess of urea $CO(NH_2)_2$ (Sigma-Aldrich) (i.e. [urea]/[metal] ≥100), the mixture was stirred at 80 ^oC in the closed reactor for 20 h. The solid was separated from the liquid phase by centrifugation and subsequently repeatedly washed with distilled water and centrifuged (three times). Then the samples were dried under vacuum at room temperature for 24 h (so-called as-prepared sample). Cu/TiO_2 with different Cu loading (i.e., 1, 2, 2.5, 3 and 5 wt%), Zn/TiO_2 with 2.5 wt% Zn loading, Ni/TiO_2 with 2.5 and 0.5 wt% Ni loading, Ni/ZnO with 5 wt% and 0.5 wt% Ni loading were prepared.

The pH evolution during the preparation of 2.5 wt% Cu, Zn, Ni/TiO_2 were recorded every 5 min during the first 5 h of DPu from an initial pH of the preparation solution adjusted to ~2 by adding 0.5 M HNO_3 (Experiment II). In addition, the evolution of the metal loading on TiO_2 as a function of time and pH was studied during the sample preparation (using 3 g of TiO_2 in 300 mL). Aliquots of 40 to 50 mL of suspension were withdrawn at different pHs, and treated as above, i.e., centrifuged, washed and dried before chemical analysis.

Specially, in the Cu/TiO_2 study, the pH evolution of the aqueous solutions (100 mL) containing only urea (8.2×10^{-1} mol L^{-1}) or urea and copper (8.2×10^{-3} $mol_{Cu}\ L^{-1}$, i.e., equivalent to 5 wt% Cu on TiO_2) or urea and TiO_2 (1 g) was recorded during heating at 80 °C, as references. Besides that, to study the nature of the Cu precipitate formed in solution during DPu, aliquots of solution containing the precipitate arising from the solution of urea and Cu heated at 80 °C, were withdrawn after 50 and 200 min of heating (Experiment III). After centrifugation, the precipitate was dried under vacuum but without washing because of the too small amount gathered.

To complement Experiment II on Cu loading evolution as a function of pH, a second series of Cu/TiO_2 samples was prepared with the same nominal Cu loading (2.5 wt%) but with different DPu durations, 3, 5, 6, 7 and 20 h (Experiment IV). The procedure of sample preparation was the same as above, except the DPu time. Here, aliquots of 40 to 50 mL of suspension were withdrawn after the different DPu durations, followed by centrifugation, washing and drying under vacuum at room temperature.

3. Monometallic Cu/TiO_2 Catalysts

Studies on the deposition of Cu(II) on titanium oxide are not abundant in the literature [2-13]. The deposition of Cu(II) on titanium oxide has been studied by Bleam and McBride [2] using electron spin resonance (ESR) spectroscopy. They found that adsorption of Cu (II) on the surface of titanium dioxide begins at pH ~2, the surface coverage of Cu(II) starts to increase sharply in the pH range of 4.4~4.6, and the Cu(II) adsorption is complete at pH~6.1 with a low Cu concentration, e.g., 9.04×10^{-5} M, whereas precipitation occurs at pH~6.2 when the initial Cu concentration is high, e.g., 3.61×10^{-4} M. Meanwhile, Ottaviani et al [3] also showed that Cu(II) is specifically adsorbed, with one or two of its water ligands substituted by the surface hydroxyls of TiO_2, by using ESR spectroscopy to study the adsorption of Cu(II) on titanium oxide at low pH. The adsorption of Cu(II) onto TiO_2 was explored by Poznyak et al [8] using electrochemical methods, ESR, XPS and electroreflection spectroscopy, and they found that there are at least four types of copper species formed on TiO_2 surface after adsorption of aqueous Cu^{2+} ions, i.e., (i) individual Cu^{2+} ions coupled to the surface Ti(IV) ions via oxygen; (ii) isolated monovalent copper ions; (iii) cluster of Cu^{2+} ions; (iv) copper hydroxide particles. It also has been found by Kim et al [9], who focused on the removal of Cu(II) from aqueous solution, that the amount of Cu adsorbed on the TiO_2 surface increases with increasing temperature from 15 to 40 ^{o}C. Moreover, the behavior of adsorption of Cu(II) on TiO_2 surface has also be explained by different models i.e., bidentate innersphere [4, 11] (Eq. 3-1) and monodentate inner-sphere [5-7] (Eq. 3-2).

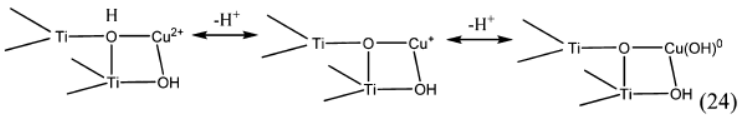

(24) ……. Eq. 3-1

$$TiOH(OH_2) + Cu^{2+} \leftrightarrow Ti(OH_2)O - Cu^{+} + H^{+} \quad (25)$$ ……. Eq. 3-2

Besides that, DPu of Cu has also been recently performed on titania in association with gold to prepare bimetallic Au-Cu particles [14, 15]. It was found that Cu (around 1 wt %) could be easily and quantitatively deposited on titania. However, no detailed study was performed to investigate the mechanism of DPu of copper on TiO_2.

From a catalytic point of view, copper is an interesting metal for various types of reactions such as water-gas-shift reaction [16, 17], methanol synthesis [18-20], propene epoxidation [21-23], alcohol oxidation [24, 25] and selective hydrogenation of CO_2 [26] and of furfural [27]. Only few explorations have been performed on the catalytic property of supported Cu-based catalysts for selective hydrogenation of unsaturated hydrocarbons [28-31].

Thus, the genesis of Cu/TiO_2 samples with different Cu loadings prepared by deposition-precipitation with urea, i.e., the evolution of both the pH, the Cu loading and the nature of supported species was investigated, then the consequence on the metal particle size after reduction and on the catalytic properties in selective hydrogenation of butadiene performed in excess of propene. This reaction can be considered as a model reaction that mimics the challenging industrial process of catalytic purification of alkene cuts from diene impurities, a reaction already studied in our laboratory over other catalytic systems.

3.1 Cu deposition-precipitation process

The XRF analyses of the as-prepared Cu/TiO_2 samples after 20 h DPu with different Cu loadings show that around 80% of Cu was deposited on the TiO_2 support during the DPu process (Table 3-1). The Cu^{2+} ions left in the very light blue supernatants of the 2.5 and 5 wt% Cu/TiO_2 preparation were characterized by UV-Visible (Figure 3-1). The spectra show a Cu^{2+} d-d band around 650 nm (Figure 3-1a, b), strongly shifted with respect to the one of the $Cu(H_2O)_6^{2+}$ complex of a $Cu(NO_3)_2$ solution around 800 nm (Figure 3-1c). The band can be attributed to the d-d transition of a $[Cu(NH_3)_4]^{2+}$ species according to [32]. The formation of this complex results from the decomposition of urea into ammonia (Eq. 3-3) and from the fact that NH_3 is a stronger ligand than H_2O. Figure 3-2 shows that the as-prepared samples exhibit different colorations depending on the Cu loadings: the solid samples with Cu loading lower than 1.6 wt% are green whereas those containing more Cu are gray.

$$CO(NH_2)_2 + 3H_2O \xrightarrow{>60\ ^\circ C} CO_2 + 2NH_4^+ + 2OH^- \qquad \text{Eq. 3-3}$$

Table 3-1: Final Cu loadings in the Cu/TiO_2 samples after 20 h DPu and pH at which the color of the suspension changed with in the first 5 h of DPu

Nominal Cu loading (wt %)	Concentration of Cu^{2+} 10^{-3} mol L^{-1}	Actual Cu Loading after DPu 20 h (wt %)	pH at which the color change	
			white to green	green to gray
2	3.2	~1.6	4.1	-
2.5	4.0	2.1	3.9	-
3	4.9	2.5	3.8	-
5	8.2	4.2	3.7	5.5
5 (B2)	8.2	-	5.2 (green-dirty)	7.2 (green black)

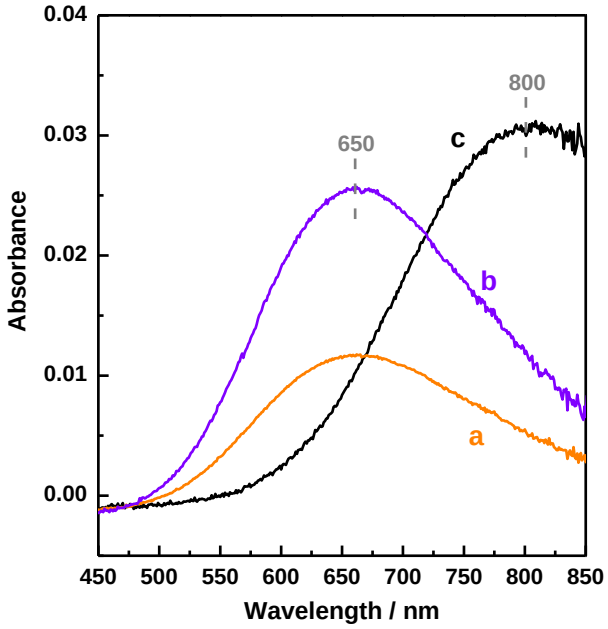

Figure 3-1: UV-visible spectra of the supernatant collected after the DPu preparation for 20 h of 2.5 wt% Cu/TiO_2 (a), 5 wt% Cu/TiO_2 (b), of a $Cu(NO_3)_2$ aqueous solution (c).

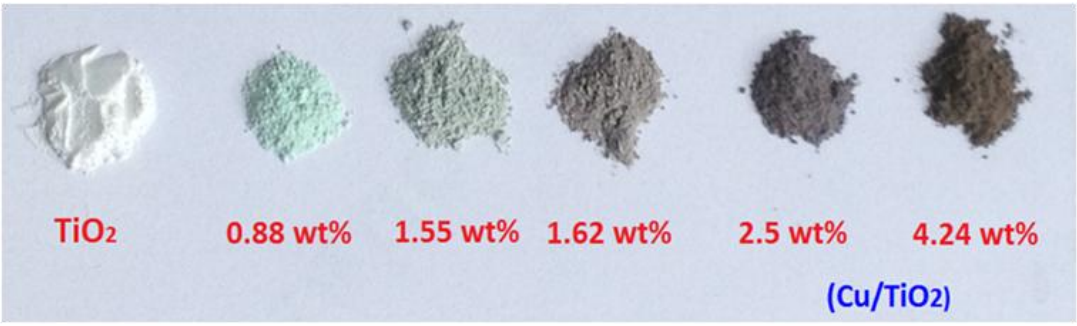

Figure 3-2: Color of as-prepared Cu/TiO_2 with different Cu loadings after 20 h of DPu.

3.1.1. Cu loading at different final pHs

To determine the evolution of the Cu loading during the DPu preparation of the 2.5 wt% Cu/TiO_2 sample, aliquots of the suspension were withdrawn at different pHs and times (see Experimental Section), and the Cu loadings on TiO_2 surface were measured by XRF after sample washing and drying (Figure 3-3). From Figure 3-3, it appears that most of the Cu is deposited on TiO_2 below pH 6, which is the PZC of TiO_2, i.e., before 2.2 h of DPu. This was a surprising result since at pH below the PZC, both the Cu complexes and the titania surface are supposed to be positively charged and not supposed to interact, and it is known at least for the Ni/SiO_2 system also prepared by DPu [33, 34] that cationic Ni complex deposition starts at pH above the PZC of silica when silica surface is negatively charged. It may be also noted that the color of the suspension changed during DPu; it was initially bluish at pH=3.0, green from pH~4.0 to 6, i.e., between 1 and 2.2 h of DPu and finally gray-green at pH ~7 after 7 h of DPu (Table 3-2). Figure 3-3 and Table 3-2 also show that all the copper is already deposited within 3 h since the loading does not vary any more for longer time, but that the sample color change from green to gray after 7 h of DPu occurs while the Cu loading had already reached a maximum.

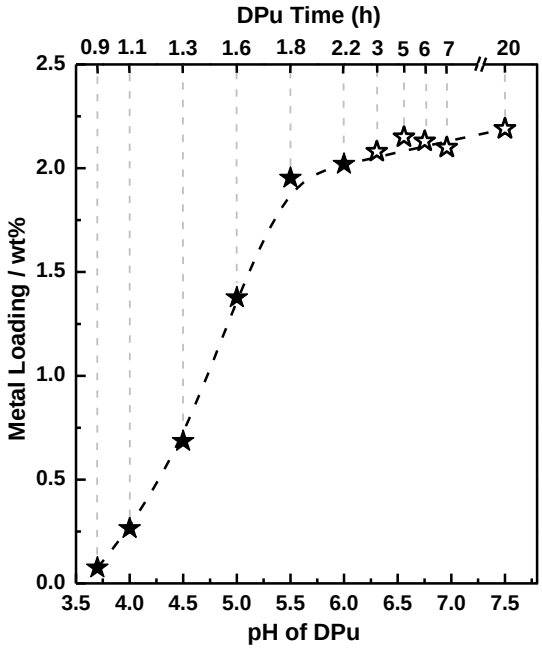

Figure 3-3: Evolution of the Cu loadings in the 2.5 wt % Cu/TiO_2 sample as a function of pH and DPu time. Full stars: experiment I, empty stars: experiment II.

Table 3-2: Evolution of the Cu loading and sample color as a function of the duration of DPu preparation of a Cu/TiO_2 sample with a nominal Cu content of 2.5 wt%. This table gathers two sets of experiments (Experiments I and II; see experimental)

DPu time / h	Cu loading (wt%)	Sample color	Experiment
0.9	0.1	bluish	Experiment I: color changes from bluish to green Cu Loading versus time / pH
1.6	1.4	green	
2.2	2.0	green	
3	2.1	green	Experiment II: no Cu loading change Sample color versus time
5	2.2	green	
6	2.1	green	
7	2.1	gray	
20	2.1	gray	

3.1.2 pH evolution of the mixture solution during deposition-precipitation process

Since the key point in the DPu process is to gradually increase the concentration of precipitating agent in the solution [35], the pH evolution of the suspension was monitored as a function of DPu time. Figure 3-4 displays the pH evolution at 80 ^{o}C during the first 5 h of DPu for four different Cu concentrations corresponding to final samples containing 2, 2.5, 3 and 5 wt% Cu.

Before analyzing the pH evolution during DPu, three blank experiments also reported in Figure 3-4 must be commented: the pH evolution of a solution of urea/ water (gray line, named B1), of a solution of Cu^{2+}/ urea/ water (violet line, named B2) and of a suspension of urea/ TiO_2/ water (black line, named B3). The concentrations of Cu^{2+} and TiO_2 are the same as those used for the preparation of 5 wt% Cu/TiO_2. Urea decomposition at 80 ^{o}C (eq. 1) is attested by the increase of pH of the solution of urea in water (curve B1) up to a final value close to 7.2. The delay in the increase of pH between curves B3 and B1 results from the buffering effect due to the presence of TiO_2 [36]. The delay in the increase of pH between curves B2 and B1 in the 4.5-6.0 pH range attests that OH^- ions resulting from urea decomposition are consumed and involved in a change of copper speciation. This is also attested by the fact that in experiment B2, the solution initially clear blue turned opaque muddy green above pH=5.2 (at the inflexion point around 50 min), indicating copper precipitation, then black-green at pH=7.2, indicating a change in the composition of the precipitate. The UV-Visible spectrum of the supernatant gathered after precipitate

centrifugation is completely flat (not shown), which indicates that all the Cu ions initially present in the solution have precipitated.

If one examines the pH evolution during DPu of the four different Cu/ urea/ TiO_2/ water mixtures (i.e., 2, 2.5, 3 and 5 wt% Cu), one can see in Figure 3-4 that the pH curves initially behave the same way as curve B3 (urea/ TiO_2/ water), then exhibit differences in the pH range 3.5-6. The differences of shape and time shift of the pH curves increase as the copper concentration increases. During these experiments, a change in the color of the suspension from whitish to green was observed at pH close to 4 as reported in Table 3-1. These pHs slightly vary with the Cu concentration, and coincide with the pH values of the inflexion points of the pH curves. For the suspension corresponding to 5 wt% Cu DPu (8.2×10^{-3} mol L^{-1}) (pink curve), the inflexion point is much more visible, and induces a marked delay in the further increase of pH. To some extent, it compares with the shape of curve B2 (5 wt% Cu^{2+}/ urea), but the presence of TiO_2 induces a time delay before pH starts increasing, and lowers the pH of the inflexion point from ~5.2 to ~4.5; this will be discussed in the part 3.4. In addition, the color of the 5 wt% Cu DPu suspension which was deep green from pH 3.7, turned gray when pH reached 5.5; this later color change was not observed with the other three samples, as they remained green in the first 5 h of the DPu process. Note however that for longer DP time (20 h), they also tend to turn grayish except for the lower Cu loadings (Figure 3-2).

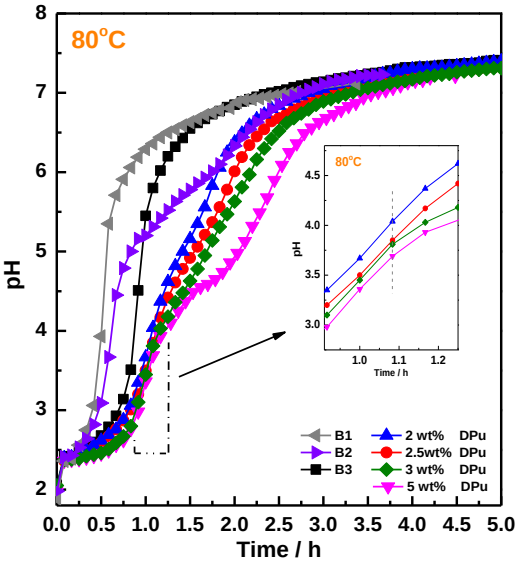

Figure 3-4: Evolution of the pH as a function of time of the suspension during DPu (at 80 °C) (Cu/ urea/ TiO_2 mixture) for different nominal Cu loadings: 2, 2.5, 3 and 5 wt% Cu and of three aqueous solutions or suspension containing, 5 g urea (B1); 5 wt% Cu and 5 g urea (B2) and 1 g TiO_2 and 5 g urea (B3).

3.2 Characterization of the Cu/TiO_2 samples prepared by DPu

As mentioned above, the color of the as-prepared samples changes from green to gray depending on the Cu loadings (Figure 3-2); this indicates the presence of at least two different Cu species on the TiO_2 surface. Attempts to identify the nature of the Cu species on TiO_2 were performed through their characterization by different techniques.

3.2.1 XRD

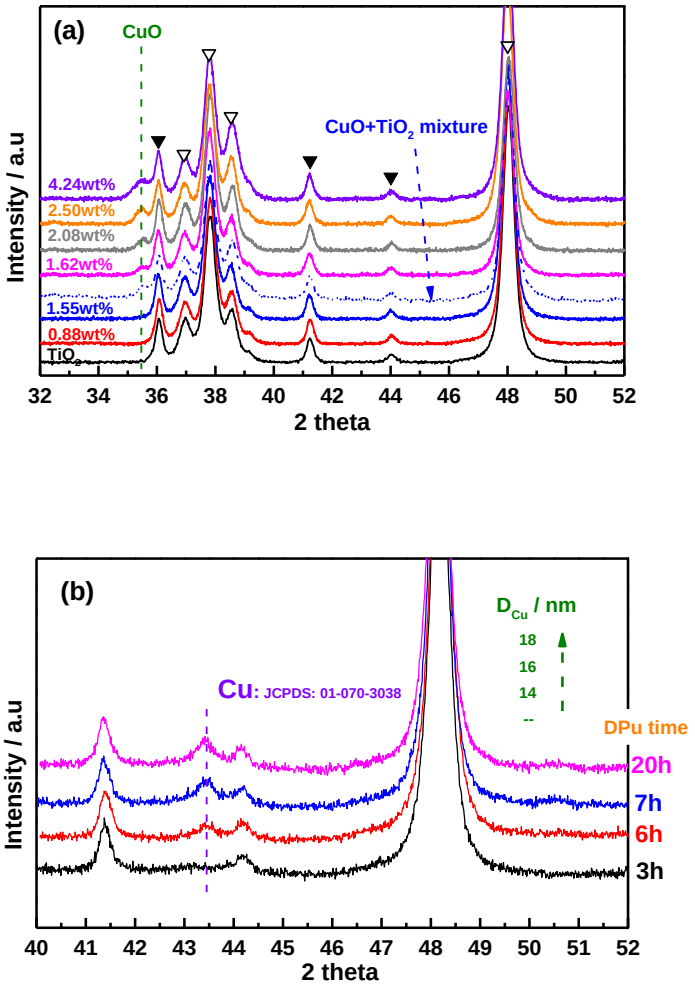

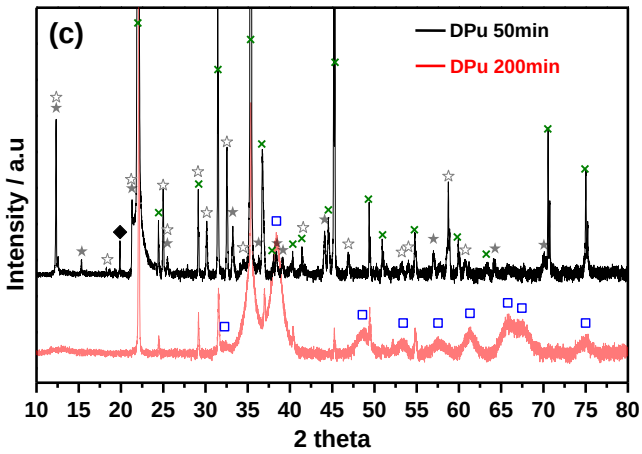

Figure 3-5: XRD patterns of (a) as-prepared Cu/TiO_2 with different Cu loadings after 20 h of DPu. The blue dot line corresponds to the XRD pattern of a physical mixture of CuO and TiO_2 with ~1.5 wt% Cu; ▼stands for rutile TiO_2 (JCPDS: 01-084-1286); ▽ stands for anatase TiO_2 (JCPDS: 01-086-0147); CuO peak position from JCPDS: 03-065-2309; (b) XRD of the reduced samples with the same Cu loading (2.1wt%) but different DPu preparation times; (c) unwashed precipitate collected from a solution containing urea and 5 wt% Cu after 50 min and 200 min at 80 °C; ×: urea (JCPDS# 01-089-2835); ★: $Cu_2(OH)_3NO_3$ (JCPDS# 01-075-0127); ☆: $Cu_2(OH)_3NO_3$ (JCPDS# 00-014-0687); ◆: $Cu_2(CO_3)(OH)_3$ (JCPDS# 00-004-0309); □: CuO (JCPDS# 00-048-1545).

XRD was performed first on the as-prepared samples (Figure 3-5a) prepared for 20 h and containing different Cu loadings. In addition to the peaks of anatase-TiO_2 (JCPDS #: 01-084-1286) and rutile-TiO_2 (JCPDS #: 01-086-0147), a weak peak at 2θ= 35.6° is visible for the Cu loadings higher than 1.62 wt%, i.e., for the gray samples, and its intensity increases with the Cu loading. This XRD peak was also observed at the same angle (35.6°) with the mechanical mixture of CuO in TiO_2 (1.5 wt% Cu, gray color) (Figure 3-5a). This indicates that the gray color of the Cu/TiO_2 samples containing more than 1.6 wt% Cu results from the presence of CuO (confirmed by comparison with the JCPDS file of CuO, 03-065-2309), which is known to be black. These results also indicate that the Cu species responsible for the green color of the sample in the low loaded samples is not detected by XRD because it is either present in too low amount or is amorphous. The average CuO particle sizes deduced from the Scherrer equation in the samples containing 1.6, 2.1, 2.4 and 4.2 wt% Cu are 10, 12, 13 and 15 nm, respectively.

The series of Cu/TiO_2 samples prepared with a Cu loading of 2.1 wt% also showed color changes as a function of the DPu duration (Table 3-2). After sample reduction at 350 °C, the particle size of metallic Cu in these samples was determined by XRD (Figure 3-5b). They

show that the Cu° particle size increases with the DPu time, no matter the sample color. This means that the size of the particles of the Cu compound before reduction also evolves and increases with DPu time although the Cu loading has reached its maximum (~2.1 wt % Cu) in these samples.

In order to identify the green Cu species, two precipitates were collected from the B2 solution (Cu^{2+}/ urea) after precipitation for 50 min (green color) and after aging up to 200 min (black-green color). They were analyzed by XRD after drying but without washing because of the too small amount (see Experimental part). Apart the peaks of residual urea (noted ×), all the peaks visible in the diffraction pattern of the precipitate prepared for 200 min (Figure 3-5c, bottom) can be attributed to CuO. The diffractogram of the precipitate prepared for 50 min is more complex (Figure 3-5c top). Most of the peaks other than those of urea can be attributed to $Cu_2(OH)_3(NO_3)$ with a monoclinic structure and with an orthorombic structure. One single peak at 2 theta ~20 ° remains unassigned (noted ◆ in Figure 3-5c top), and could correspond to the most intense peak of malachite-type hydroxycarbonate, $Cu_2(CO_3)(OH)_2$. As a complement of characterization of the green copper compound, the DRIFT spectra of DPU Cu/TiO_2 (50 min, ~0.3 wt% Cu) and the green precipitate (50 min) were recorded. The two spectra (Figure 3-6) show the same bands at 1430 and 1340 cm^{-1} that can be attributed to the ν4 and ν2 ONO_2^- stretching vibrations of copper hydroxynitrate according to Pereira et al [37]. These bands cannot arise from malachite-type hydroxycarbonate, $Cu_2(CO_3)(OH)_2$ since CO_3^- stretching vibrations must appear at 1506 and 1388 cm^{-1} according to Kondrat et al [38]. The green precipitate was analyzed by TEM and shows large particles between 0.5 and 1 μm (Figure 3-7). Our conclusion is that the green Cu compound in the precipitate is copper hydroxynitrate, and it is unstable, and decomposes into CuO when pH increases at 80 °C; the low stability of copper hydroxynitrate was also mentioned by Pereira et al [37].

Hence, it can be proposed that the green color of the Cu/TiO_2 samples prepared by DPu for 20 h with Cu loadings lower than 1.6 wt% Cu (Figure 3-2) or prepared for 3 to 6 h for Cu/TiO_2 (2.1 wt% Cu) (Table 3-2) originates from the formation of $Cu_2(OH)_3NO_3$ species on TiO_2. The interaction with the titania support is attested by the fact that the Cu particles on titania whether they are either $Cu_2(OH)_3NO_3$ or CuO (≤20 nm) are much smaller than those of the green precipitate (0.5 to 1 μm, Figure 3-7). It is also interesting to note that the interaction with titania stabilizes $Cu_2(OH)_3NO_3$ and prevents its decomposition into CuO after 20 h of DPu at 80 °C, i.e. at pH around 7, since the samples with Cu loadings lower than 1.6 wt%

remain green. In contrast, the gray color of the samples with Cu loadings higher than 1.6 wt% results from the presence of CuO arising from the partial or total decomposition of supported $Cu_2(OH)_3NO_3$.

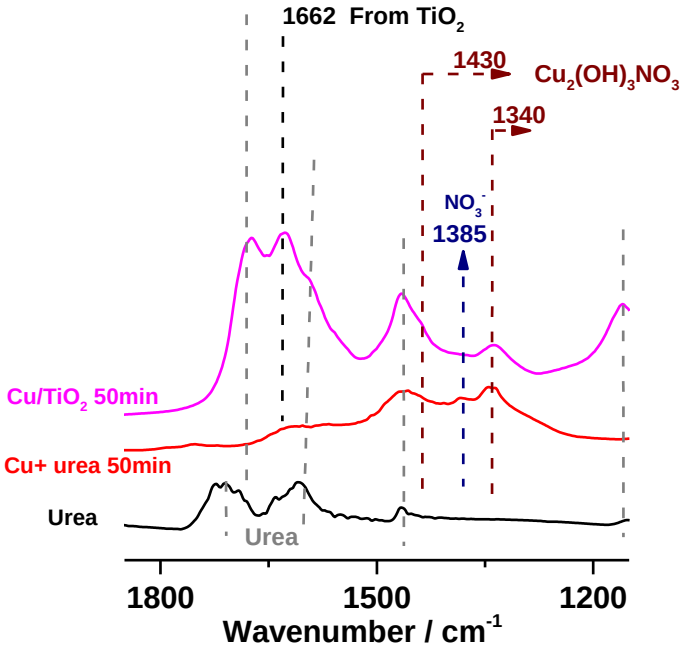

Figure 3-6: DRIFT spectra of DPU Cu/TiO_2 (DPu 50 min, ~0.3 wt% Cu) and the green Cu/urea precipitate (DPu 50 min).

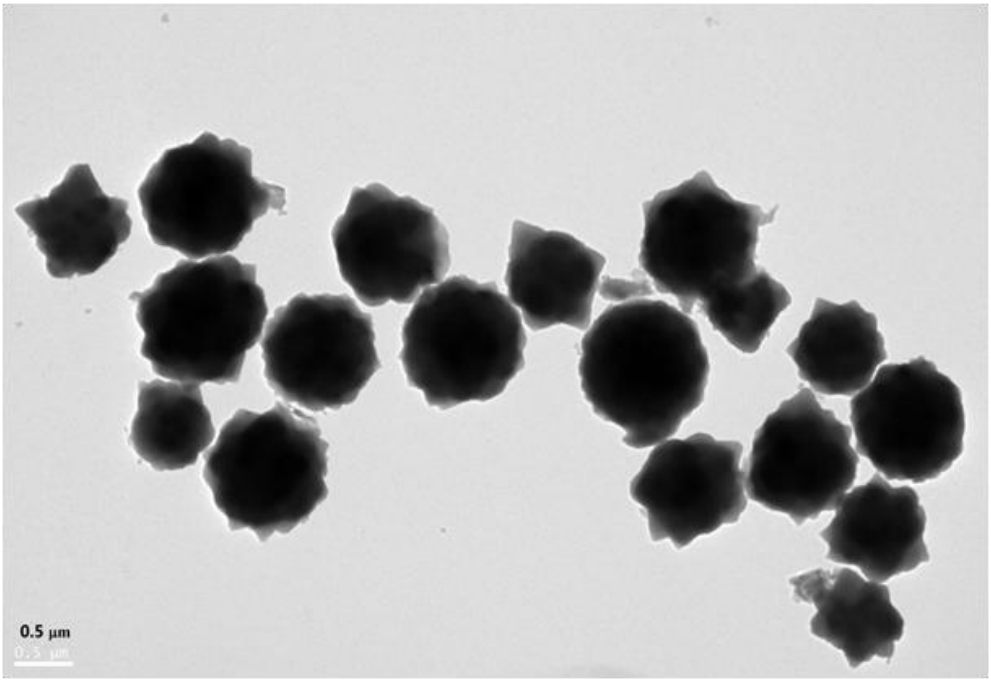

Figure 3-7: TEM of the green precipitate prepared by precipitation Cu^{2+} with urea in the absence of TiO_2 support at 80 °C for 50 min.

3.2.2 UV-Visible

Figure 3-8a displays the UV-visible spectra of the as-prepared Cu/TiO_2 samples with different Cu loadings after 20 h of DPu. The contribution of TiO_2 was removed from the spectra using TiO_2 as a reference for the baseline. One can distinguish two types of spectra, those corresponding to low Cu loadings (<1.6 wt%) and those corresponding to high Cu loadings (>1.6 wt%).

The spectra of the low loaded samples are composed of an absorption band around 420 nm, and a broad one in the 600-1200 nm region that can be assigned to Cu(II) d-d transition [39, 40]. A band around 400 nm has been observed in numerous systems consisting of transition metal ions doping titania or at the surface of titania, and attributed to a band of interfacial charge transfer (IFCT) from the O_{2p} valence band of TiO_2 to M^{x+} ions [41-46]. This band assignment has been very recently confirmed by Platanitis et al [47] in a study on Mo/TiO_2 catalysts combining experimental and theoretical study at the molecular level. This study convincingly rationalizes the relationship between the presence of the band of charge transfer from titania surface oxygen to metal (Mo) in UV-visible spectra and the establishment of a Ti-O-Mo bridge, i.e., the formation of an inner sphere complex between the Cu^{2+} complexes and the surface oxygen of titania. One may wonder whether this Ti-O-Cu bonding occurs in solution during DPu preparation or during the drying step. To attempt to answer this question, the UV-visible spectra of a series of wet DPu Cu/TiO_2 samples (those prepared for different durations, Table 3-2) were recorded. The spectra displayed in Figure 3-8b show that the band at 420 nm is already present in the wet samples, and seem to increase in intensity with the DPu duration, and to be stronger after drying at RT (Figure 3-8c). In addition, Figure 3-8a shows that the spectra of the low loaded samples are similar to the spectrum of the mechanical mixture of $Cu_2(OH)_3NO_3$ and TiO_2 corresponding to 1.5 wt% Cu. This observation is again a good indication of the presence of $Cu_2(OH)_3NO_3$ in the low loaded green samples.

For the highly loaded samples (>1.6 wt% Cu), an additional broad band in the range 450-800 nm in the spectra appears and grows up with the Cu loading, with roughly the same shape and position as the one of the $CuO-TiO_2$ mechanical mixture (1.5 wt% Cu) in Figure 3-8a. The threshold around 850-900 nm corresponds to the energy of the band gap of copper oxide (Eg ~1.4 eV). The bands of $Cu_2(OH)_3NO_3$ seem to be still present in the spectra of the highly loaded Cu/TiO_2, and suggest that these samples contain both copper oxide and copper hydroxynitrate.

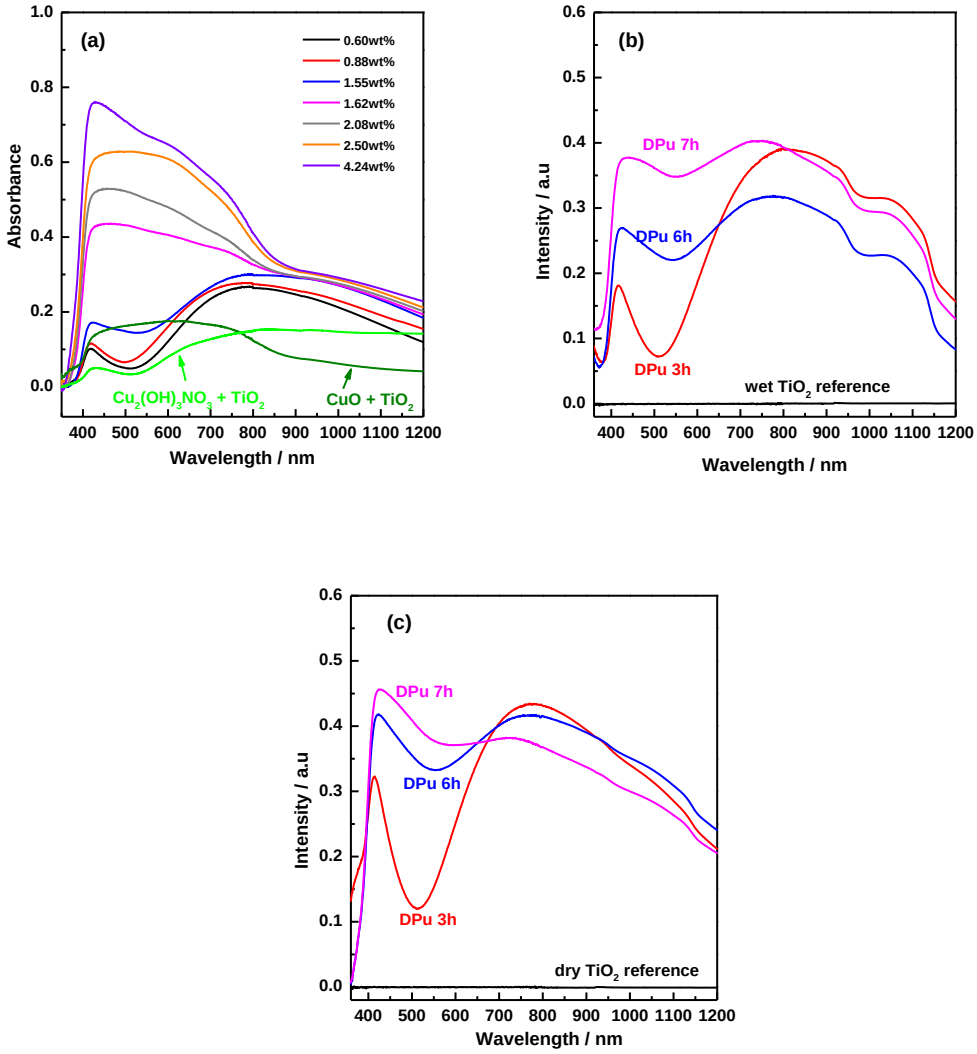

Figure 3-8: UV-visible spectra of (a) the as-prepared Cu/TiO_2 samples with different Cu loadings after 20 h of DPu and physical mixtures of CuO and TiO_2 and of $Cu_2(OH)_3NO_3$ and TiO_2, both containing ~1.5 wt% Cu; (b) the wet Cu/TiO_2 samples containing (2.1 wt% Cu) but prepared during different durations; (c) the same samples after drying at RT.

3.2.3 TPR

The reduction behavior of the as-prepared Cu/TiO_2 samples (20 h of DPu) was studied by TPR (Figure 3-9). TiO_2 does not show any reduction peaks in the temperature range from room temperature to 550 ^oC, thus the two reduction peaks at ~150 and ~175 ^oC correspond to the reduction of Cu species on TiO_2. The intensity of the first reduction peak (~150 ^oC) seems to be independent on the Cu loading whereas the second one, initially around 175 ^oC, shifts to higher temperature and increases in intensity with the Cu loading. It becomes higher than the first peak when the Cu loading exceeds 1.6 wt%. Bulk CuO is known to reduce directly from

Cu^{2+} to Cu^0 because of the lower energy requirement for metallic Cu formation from Cu^{2+} than from Cu^+ [48] (equations 3-4 and 3-5):

$$CuO(S) + H_2 \rightarrow Cu^0(S) + H_2O \qquad \Delta H=14.5kcal/mol \qquad \text{Eq. 3-4}$$

$$Cu_2O(S) + H_2 \rightarrow 2Cu^0(S) + H_2O \qquad \Delta H=27.4kcal/mol \qquad \text{Eq. 3-5}$$

The two TPR peaks should thus correspond to the reduction of two different Cu^{II} species. Several groups [49-52] also found more than one reduction peak in the TPR profile of oxide-supported Cu samples. There is a general agreement to propose that large and crystallized CuO particles reduces at higher temperature than smaller CuO particles or dispersed Cu^{II} species in strong interaction with the oxide support. Their reduction temperature, ~175 ^oC (Figure 3-9), which is far lower than the one of bulk CuO (280 ^oC) [48], could be interpreted as an effect of interaction between CuO and TiO_2 surface [51, 53] and/or smaller CuO particle size [54]. Accordingly, the two reduction peaks in Figure 3-9 can be attributed to Cu^{II} ions that are interacting with TiO_2 and to CuO. The second reduction peak at ~175 ^oC can be easily attributed to CuO as its intensity increases as the Cu loading increases (Figure 3-9), moreover, it slightly shifts to higher temperature in agreement with the fact the CuO particle size increases from 10 nm in 1.62 wt% Cu/TiO_2 to 15 nm in 4.24 wt% Cu/TiO_2 according to XRD. The reason for which CuO was evidenced by TPR but not by XRD in the sample with Cu loading lower than 1.55 wt%, may be the too low CuO content and/or too small particle size. According to the literature, the first reduction peak might belong to amorphous Cu species or to highly dispersed Cu^{II} species in strong interaction with TiO_2 surface [53].

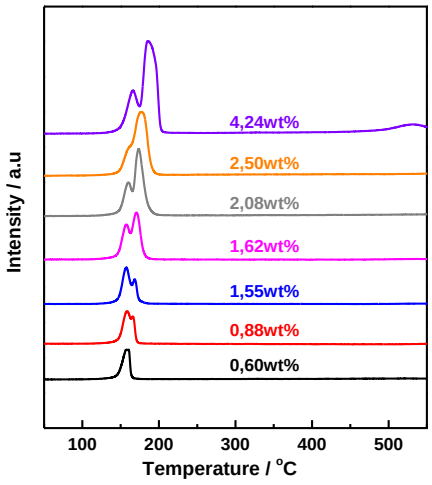

Figure 3-9: TPR of as-prepared Cu/TiO_2 prepared with different Cu loadings after 20 h of DPu.

3.2.4 TEM study of the metal particle size in Cu/TiO_2 samples

The sizes of metallic Cu particles in the Cu/TiO_2 samples prepared for 20 h were estimated by TEM (Figure 3-10) after reduction under H_2 at 350 ^oC, and transfer into the microscope without air contact (See Experimental). It must be mentioned that TiO_2 support has wide particle size distribution with largest size around 50 nm and smallest ones around 10 nm (not shown). The average particle size was deduced from the particle size distributions, also shown in Figure 10. In the 0.88 wt% Cu/TiO_2 sample, only very small metallic Cu particles (< 1 nm) are present (Figure 3-10a); they are visible on the edges of the TiO_2 particles in the TEM images. In the 1.55 wt% Cu/TiO_2 sample, in addition to small particles, particles with larger size (around 3 nm) are also observed on the TEM images (Figure 3-10b). For the 4.24 wt% Cu/TiO_2 sample (Figure 3-10c), the Cu particle size distribution is more complex. Firstly, only few particles with size ~6 nm can be found, which is surprising for a sample with such high Cu loading (~4.24 wt%). To deepen the analysis, dark field imaging (HAADF) was performed to observe more easily the metallic Cu particles (white dots) in the images (Figure 3-10d). Few large (~15 nm) and very small particles (<1 nm) were observed in the sample. Moreover, EDS carried out on these two types of particles confirmed that the large (Figure 3-10e) and the small particles (Figure 3-10f) are metallic Cu. The HAADF results are therefore consistent with the XRD results obtained with the as-prepared samples (Figure 3-5a) since both show that the 4.24wt% Cu/TiO_2 sample contain large particles, Cu^o and CuO, respectively. To summarize, the sample with high Cu loading contains particles smaller than 1 nm, particles around 4 nm and large particles around 15 nm, resulting in a wide particle size distribution.

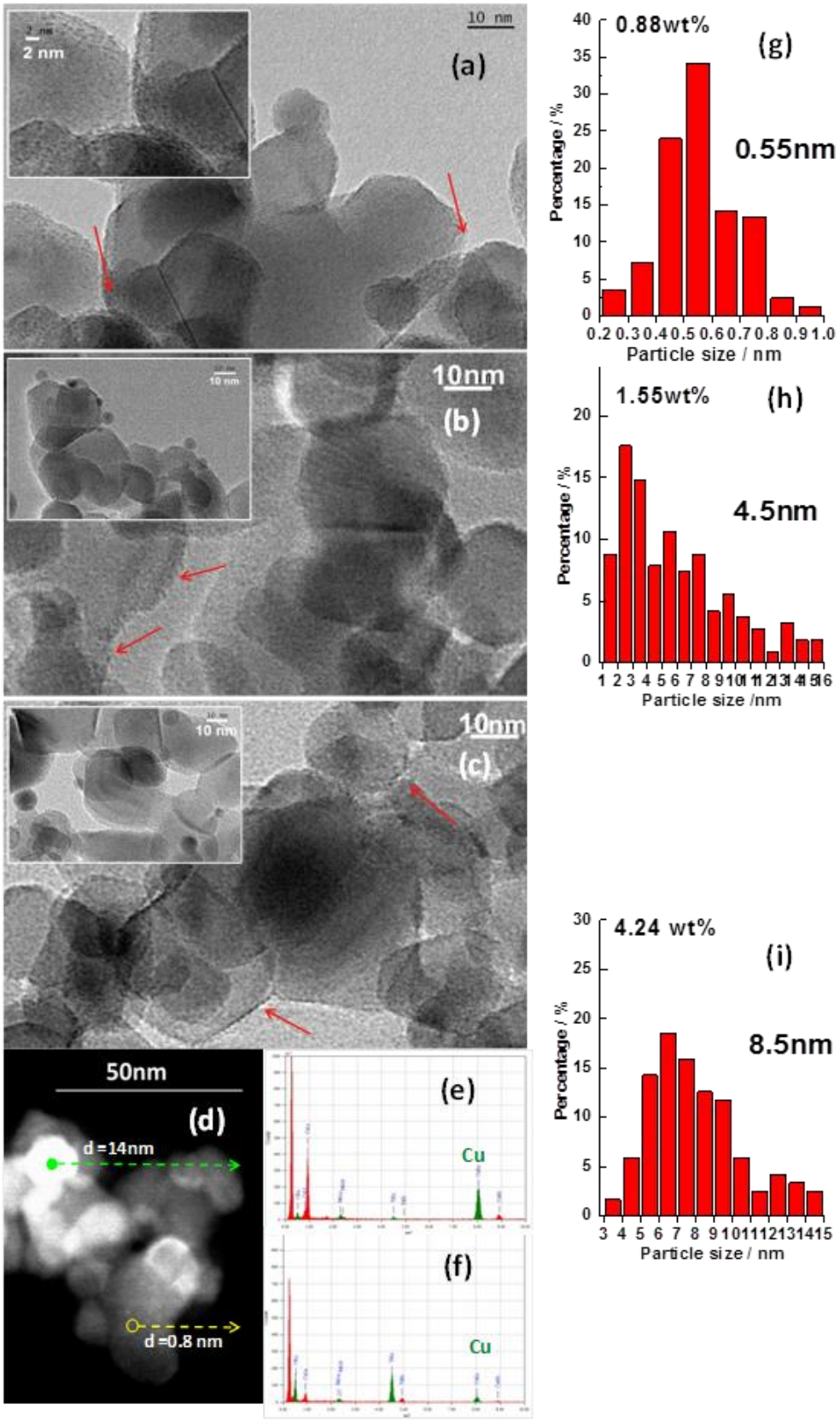

Figure 3-10: TEM bright field micrographs of Cu/TiO_2 (20 h of DPu) after reduction at 350 °C with (a) 0.88; (b) 1.55; (c) 4.24 wt% Cu; (d), STEM-HAADF micrographs of 4.24 wt% Cu/TiO_2; (e) and (f), EDS analysis of two different zones of image (d), and the corresponding particle size distributions: (g), (h), (i).

3.3 Selective hydrogenation of 1,3-butadiene

The evolution of the 1,3-butadiene conversion with temperature over the series of Cu/TiO_2 samples prepared for 20 h is presented in Figure 3-11a. One can see in Figure 3-11b that butadiene is transformed only into butenes up to $T_{100\%}$ (minimum temperature corresponding to 100% butadiene conversion; note that this is an approximate temperature, and that it is possible that the real one is at a temperature between it and the one of the former measurement). A low amount of butane starts to be formed above these temperatures while propene also starts hydrogenating with a very low conversion (<2%, Figure 3-11c). Intuitively, one could have expected that the conversion curve and $T_{100\%}$ will gradually shift to lower temperature as the Cu loading increases (Figure 3-11a). Although the sample containing the lowest Cu loading (0.88 wt%) is the least active and the one containing the highest loading (4.24 wt%) is the most active, the evolution of $T_{100\%}$ of the samples with intermediate Cu loadings seems erratic. However, the calculation of the activity of the catalysts at 60 °C expressed per mass unit of copper shows a decrease as the Cu loading increases (Figure 3-12). This is consistent with the fact that the Cu particle size also increases when the Cu loading increases.

Finally, an experiment was performed in isotherm at 105 °C to test the stability of three Cu/TiO_2 catalysts (0.88, 1.55 and 2.5 wt%), using the same mass of Cu (13.9 ±1 µmol) in 100 mg of catalytic bed thanks to physical mixing of Cu/TiO_2 and TiO_2, to operate with the same contact time. Figure 3-13 shows that the butadiene conversion of the 0.88 wt% Cu/TiO_2 catalyst was 100% during the first 1 h of reaction, then decreased to around 10% in the following 3 h with a rate of 19 ppm min^{-1}. For the 1.55 wt% Cu/TiO_2 sample, butadiene conversion was also 100% at the beginning of the reaction, but it quickly decreased to around 5% after 2.5 h with a rate of 28 ppm min^{-1}. Initial butadiene conversion of the 2.5 wt% Cu/TiO_2 sample was slightly lower than 100% and declined still more sharply to around 2% during the first 1.5 h with a rate of 44 ppm min^{-1}.

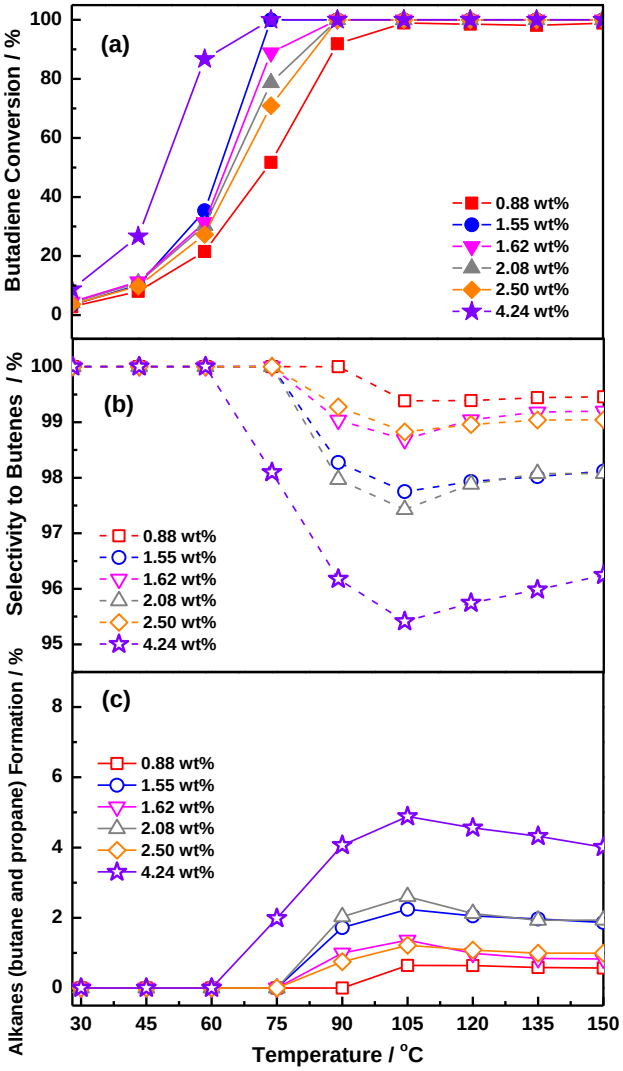

Figure 3-11: Evolution of the butadiene conversion (a), the selectivity to butenes (1-butene + cis-2-butene + trans-2-butene) (b) and the conversion to alkanes (butane and propane) (c) as a function of the reaction temperature for reduced Cu/TiO_2 with different Cu loadings (100 mg of catalyst).

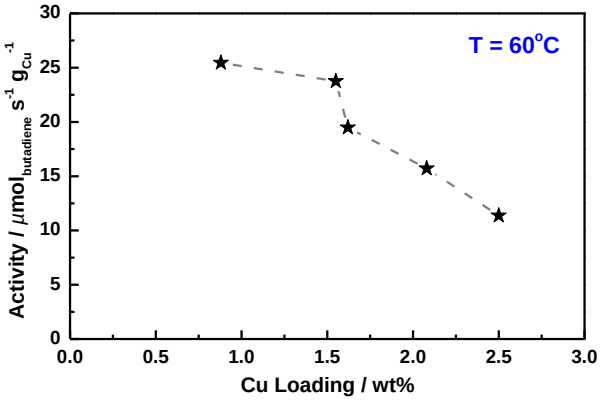

Figure 3-12: Evolution of the catalytic activities at 60 °C of reduced Cu/TiO_2 samples as a function of the Cu loading at butadiene conversion around 20-30%.

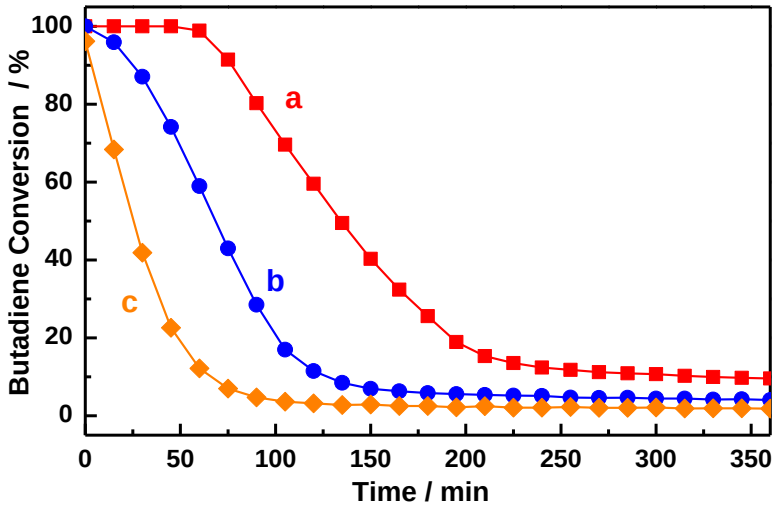

Figure 3-13: Catalytic stability under reaction at 105 °C of reduced Cu/TiO_2 samples with different Cu loadings performed with 100 mg of catalytic bed and the same amount of Cu (13.9±1 µmol): (a) 100 mg of 0.88 wt% Cu/TiO_2; (b) 56.8 mg of 1.55 wt% Cu/TiO_2 + 43.2 mg TiO_2; (c) 35.2 mg 2.5 wt% Cu/TiO_2 + 64.8 mg TiO_2.

3.4 Discussion

The evolution of the Cu loading on titania as a function of pH and of the deposition time reported in Figure 3-3 show that the process of Cu deposition on the TiO_2 surface mainly occurs at pH lower than the PZC of TiO_2 (~6). It starts at the very beginning of the DPu, since a small amount of copper is already deposited on TiO_2 at pH< 3.8 (Figure 3-3), i.e., at a pH at which the TiO_2 surface is not supposed to interact with cationic complexes like $Cu(H_2O)_6^{2+}$ or $Cu(NH_3)_6^{2+}$ (Figure 3-1). Cationic Cu^{II} complexes interaction with titania at low pH has been already reported by Bourikas et al. in a recent review on titania [55]. They mentioned that although literature related to the studies of the deposition of Cu^{II} complexes on TiO_2 is not very abundant and not recent, there are several papers reporting the adsorption of Cu^{II} aqua complexes on TiO_2 surface at pH of 2 or 4, i.e. below the PZC of titania (~6) [2, 3].

The titania P25 used in this study contains two phases, anatase, the main one, and rutile. In these two different crystal structures, each Ti^{4+} ion is surrounded by six oxygen forming octahedral entities (TiO_6), and each oxygen is bonded to three Ti^{4+} ions (Ti_3-O) by two short Ti-O bonds (1.946 Å in rutile, and 1.937 Å in anatase) and one longer (1.984 Å in rutile and 1.964 Å in anatase) [56]. Surface Ti^{4+} ions have lower coordination than in the bulk,

and the surface of TiO_2 possesses in principle three types of surface oxygens, namely singly coordinated surface oxygen (TiO), doubly coordinated one (Ti_2O) and triply coordinated one (Ti_3O). On the basis of different surface ionization models for these surface sites, Bourikas et al [57] proposed a derived model of protonation reactions for TiO and Ti_2O that they consider more realistic than those in the former models:

$$TiO^{-0.35} + H^+ \overset{K_1}{\leftrightarrow} TiOH^{+0.65} \qquad \log K_1 = 7.8 \qquad \text{Eq. 3-6}$$

$$Ti_2O^{-0.57} + H^+ \overset{K_2}{\leftrightarrow} Ti_2OH^{+0.43} \qquad \log K_2 = 4.6 \qquad \text{Eq. 3-7}$$

Note that the oxygen of Ti_3O is not protonated ($\log K_3 = -3.96$) [58] and that the TiO sites are negatively charged ($TiO^{-0.35}$, Eq.3-6) even at pH lower than 3, based on experimental results of Bourikas et al [57].

We can therefore propose that at the very beginning of the DPu preparation, i.e. at pH<4 before precipitation starts (Figure 3-3), part of the Cu^{2+} complexes in solution can interact electrostatically with the $TiO^{-0.35}$ sites of TiO_2 surface and then could form Ti-O-Cu species according to [3]. The formation of inner sphere complexes is attested by the presence of the band at 420 nm in the UV-visible spectra of the wet Cu/TiO_2 samples (Figure 3-8b). At the stage of the present study, it is not possible to discard another hypothesis as the one proposed by Petala et al [46], which is a direct surface reaction between Cu^{2+} complexes and surface OHs of titania that would also lead to the formation of inner sphere complexes. It is interesting to mention that titania behaves differently from silica support. In a former study of one of us [32], dealing with adsorption of $[Cu(NH_3)_4(H_2O)_2]^{2+}$ complexes on silica, the formation of Si-O-Cu bonding was observed only after the sample has been dried at RT and not when it was still wet. In any case, one can propose that once Cu^{II} complexes have interacted with the negatively charged sites of TiO_2 or some surface OHs or when pH has reached 4, the remaining of the Cu complexes in solution start precipitating on titania. The nature of the Cu precipitate is probably the same as the one obtained in the absence of support (Experiment B2 in Section 3.1.2), i.e. copper hydroxynitrate ($Cu_2(OH)_3NO_3$) and not copper hydroxide. In spite of the fact that the diffractogram of as-prepared Cu/TiO_2 (Figure 3-5a) does not show the corresponding diffraction peaks, this hypothesis is consistent with the fact that the samples have the same green color in the presence or in the absence of TiO_2, that their UV-visible and IR spectra are similar (Figures 3-8 and 3-6) and that $Cu_2(OH)_3NO_3$ has been identified previously in Cu/SiO_2 samples prepared by DPu [59]. Moreover, the pH ~4 of Cu

precipitation in the presence of TiO_2, associated to the color change of the suspension is lower than the pH of precipitation in solution (pH 5.2 in the absence of TiO_2), and it corresponds to the inflection point of the pH curves in Figure 3-4. This result is consistent with the principle of the method of deposition-precipitation [33, 60-63], in particular, the precipitation of $Cu_2(OH)_3NO_3$ onto the titania support, also attested by the fact that the particles of the copper hydroxynitrate precipitate are much larger than those formed in the presence of titania. One can therefore propose that the Cu^{2+} species already adsorbed on TiO_2 at low pH act as nucleation sites for the growth of the precipitate onto the support rather than into solution, lowering the pH of precipitation, i.e., lowering the pH of the supersolubility of $[Cu_2(OH)_3NO_3]_{aq}$, and preventing its precipitation into solution.

As the pH of the solution increases during DPu at 80 ^oC, instead of reacting with the dissolved support as for silica and forming copper silicate [59] since TiO_2 is not known to dissolve in the 3-8 pH range, $Cu_2(OH)_3NO_3$ gradually transforms into CuO; this is accompanied by a change of the suspension color from green to gray. The evolution of the nature of the Cu compound on TiO_2 is also attested by the different colors taken by the as-prepared samples as a function of the Cu loading (Figure 3-2) and the DPu duration (Table 3-2). The green color of the samples with less than 1.6 wt% Cu is due to the presence of stable $Cu_2(OH)_3NO_3$ and the more grayish color observed for the higher Cu loadings is related to the additional presence of CuO. The formation of CuO is attested by XRD (Figure 3-5) and by the presence of the broad band at 450-800 nm in the UV-Visible spectra (Figure 3-8a). However, $Cu_2(OH)_3NO_3$ is more stable on titania than in the absence of support since the Cu/TiO_2 suspension (<3 wt% Cu) remains green after 5 h of DPu whereas it turns blackish without support (Table 3-1). The grayish color taken by the sample during DPu when more Cu is deposited (4.24 wt% Cu) (Table 3-1) or when DPu duration increases (Figure 3-2 and Table 3-2), which is due to the presence of large particles of CuO can be explained as follows. It probably initially results from a phenomenon of Ostwald ripening of the $Cu_2(OH)_3NO_3$ particles during DPu as the particle size of metallic Cu increase with DPu time (Figure 3-5b). In addition, very small Cu° particles were also observed by TEM (Figure 3-10). These results may therefore indicate that Ostwald ripening has occurred during sample preparation by DPu, producing a bimodal size distribution. Moreover, as the $Cu_2(OH)_3NO_3$ particles increases in size, they become instable and transform into CuO that continue to grow. It is interesting to note that at variance with the silica and alumina supports (see Introduction), no mixed compound, i.e., no copper titanate formation was detected. Sanker et al [64] showed that in

the case of a parent system, Ni/TiO_2, $NiTiO_3$ was detected by EXAFS after calcination but at temperature higher than 600 °C and only when the samples were prepared by impregnation (not by cation adsorption).

From this discussion, one can now propose an interpretation for the TPR profiles (Figure 3-9). The first TPR peak can be attributed to the reduction of small NPs of $Cu_2(OH)_3NO_3$ while the second one at higher temperature can be attributed to the reduction of large NPs of CuO; this peak becomes predominant as the Cu loading increases.

The number of Cu nucleation sites is limited, thus when the Cu loading increases, the particles of $Cu_2(OH)_3NO_3$ grow on these sites, and increase in size. When the Cu concentration is high enough (>1.6 wt%), $Cu_2(OH)_3NO_3$ becomes instable and transform into CuO that also increase in size. These results are consistent with the different metal particle sizes obtained after reduction at 350 °C, i.e., a progressive increase of the particle size and broadening size distribution with the Cu loading (Figure 3-10). One can conclude that the various particle size ranges observed by TEM are caused by the different Cu loadings and Cu species present on TiO_2 in the as-prepared samples and also to Ostwald ripening.

The catalytic results can now be discussed to the light of these characterization results. Figure 3-12 shows that the sample containing 0.88 wt% Cu, which has the smallest metallic particle size, exhibits the highest catalytic activity. It is interesting to note that the activity is almost 4 times higher (25 μmol s^{-1} g_{Cu}^{-1}) than that of 1.1 wt% Au/TiO_2 catalyst tested in the same conditions [65] (4.5 μmol s^{-1} g_{Au}^{-1}) (or twice as much active if activity is expressed per mol_{metal}), which is also a highly selective catalyst at full conversion of butadiene. Note that compared to Pd, the reference catalyst in industry, copper is less active, but its cost is also much lower and its selectivity to butenes is high at 100% conversion of butadiene. The activity of the Cu/TiO_2 catalysts decreases as the Cu loading and the particle size increase. One can also note that the activity clearly decreases between the 1.55 wt% Cu/TiO_2 sample and the 1.62 wt% one although the loadings are very close (Figure 3-12). As reported before, the 1.55 wt% Cu/TiO_2 sample is green before reduction whereas the 1.62 wt% one is gray (Figure 3-2). Although metal particle sizes have not been determined for these samples, one can explain the different activities by the fact that the green 1.55 wt% sample contains no or less CuO than the 1.62 wt%, and therefore should contain smaller metal particles after reduction, resulting in a noticeable increase in activity. The stability experiment reported in Figure 3-13 shows that the rate of deactivation increases as the Cu loading increases.

According to former works on Cu catalysts [66, 67] oligomerization with the formation of "green oil" is responsible for deactivation. XRD (Figure 3-14) and thermogravimetry comparing the weight loss of the Cu/TiO_2 sample after stability test at 105 °C for 20h with a fresh one (Figure 3-15) confirm these results, i.e., no apparent change in metal particle size and an important weight loss during calcination of the spent catalyst. One can tentatively propose that the higher catalytic stability of the Cu/TiO_2 catalyst containing the smaller particle size may result from the presence of smaller Cu ensembles on which oligomerization reaction takes place. In a way, this interpretation is consistent with a recent study that showed that atomically dispersed Pd on graphene was very stable in selective hydrogenation of butadiene against deactivation compared to Pd nanoparticles [68].

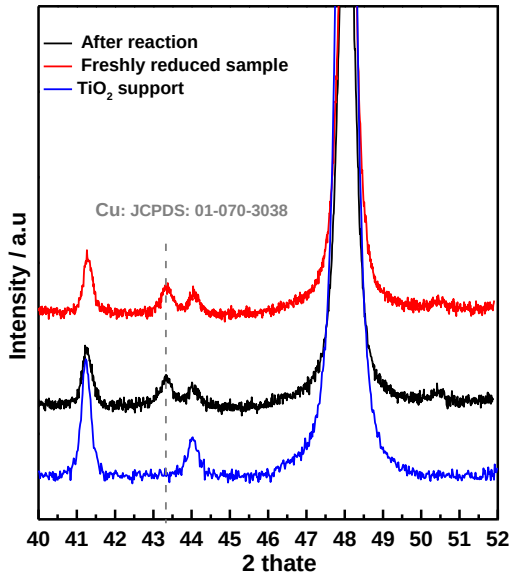

Figure 3-14: XRD of the reduced 2.5 wt% Cu/TiO_2 sample before and after stability test at 90 ^{o}C for 20 h.

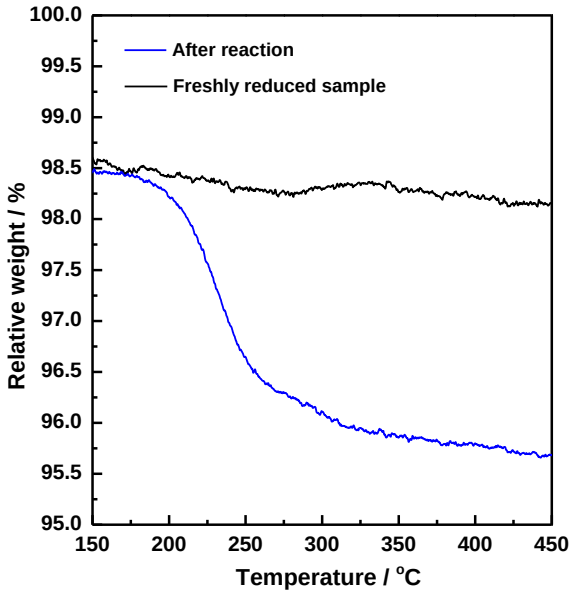

Figure 3-15: TG of DPu the reduced 2.5wt% Cu/TiO_2 sample and after stability test at 105 °C for 20h

Since the large Cu^0 particles result from the presence of CuO in the as-prepared catalysts and since their presence induces lower activity in butadiene hydrogenation, and stronger deactivation, the catalytic results underline the fact that the formation of CuO must be avoided during the deposition-precipitation process in order to achieve high catalytic performance. In order to verify this conclusion, an additional catalytic experiment was performed on the green sample with 2.1 wt% Cu obtained after 3 h of DPu, (Table 3-2). In Figure 3-16, the catalytic performance is compared to that of a gray sample with the same Cu loading (2.05 wt% Cu) but obtained after 20 h of DPu. The results clearly show that the green sample containing smaller Cu particles after reduction is more active than the gray one.

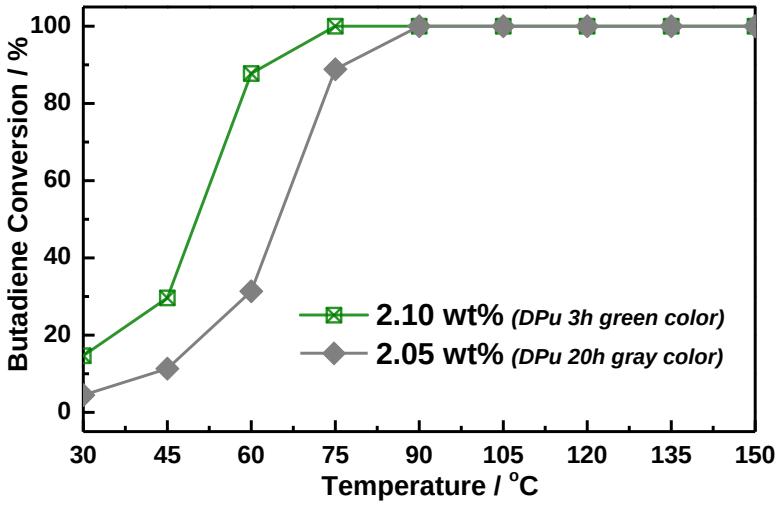

Figure 3-16: Comparison of the evolution of the butadiene conversion between two Cu/TiO_2 samples containing the same Cu loading (2 wt% Cu) but prepared for different durations, 3 h leading to a green sample after DPu and 20 h leading to a gray sample.

3.5 Conclusions

In this contribution, the preparation of Cu/TiO_2 samples (up to 5 wt% Cu) by the method of deposition-precipitation with urea was explored as a function of the Cu loading, DPu time and pH. We observed that the Cu^{2+} complexes in solution start to adsorb on TiO_2 at pH lower than PZC of TiO_2 (< 6) probably because of the presence of some negatively charged Ti – O sites, forming Ti-O-Cu bridges, then most of Cu^{2+} ions are deposited as $Cu_2(OH)_3NO_3$ on TiO_2 surface in the first 2 h of the DPu process. The characterization study led us to propose that the adsorbed Cu^{2+} species act as nucleation sites for the growth of particles of $Cu_2(OH)_3NO_3$ (green samples). As DPu duration proceeds or Cu loading increases, these particles increase in size through a mechanism of Ostwald ripening, then the large $Cu_2(OH)_3NO_3$ transforms into CuO (gray samples) depending on the DPu duration and the final Cu loading, e.g. 2 h for 4.2 wt% Cu/TiO_2 and more than 5 h for 1.6 wt% Cu/TiO_2. The presence of CuO in the as-prepared sample has a great effect on the particle size of metallic Cu after reduction at 350 °C: small particles (<3-5 nm) were obtained in the green samples, which mainly contained $Cu_2(OH)_3NO_3$, whereas large ones (>10 nm) were also present in the gray samples initially containing CuO. Moreover, the study of the Cu/TiO_2 catalytic performance in selective hydrogenation of butadiene in excess of propene revealed that the supported Cu catalysts are able to fully convert butadiene with almost 100% selectivity to butenes at rather mild temperature, and that the catalytic activity and stability are clearly enhanced by decreasing the Cu particle size. It can be concluded that DPu is an

efficient preparation method to produce active Cu catalysts in hydrogenation reaction provided that the formation of CuO is avoided.

4. Monometallic Zn/TiO_2 Catalysts

4.1 Zn loading at different final pHs

During the preparation of 2.5 wt% Zn/TiO_2 sample by DPu, the deposition-precipitation behavior of Zn^{2+} was studied by monitoring the evolution of the Zn loading deposited on TiO_2 as a function of the DPu time and pH (Figure 3-17). It can be seen that as for Cu on titania (Figure 3-3), around 25% of Zn was deposited on TiO_2 surface at pH ~4.5 and that the Zn loading gradually increased with increasing pH or reaction time, with most of Zn^{2+} finally deposited at pH ≤7.0, and a quick increase from 60% to 90% at pH between 5.5 and 6.5. By analogy with Figure 2-3 in Chapter 2 and above in Section 3 with the preparation of Cu/TiO_2 sample by DPu, the deposition of metal complexes mainly happens when the concentration of hydrolysed metal ions reaches the area between its supersolubility (SS) and the supersolubility with support existed in solution ($SS_{support}$) during pH increase. Thus, the sharp increase of Zn loading might correspond to the occurrence of this phenomenon. By comparison with Cu^{2+} (Figure 3-3), Zn^{2+} deposition occurs at higher pH that is in agreement with the theoretical prediction (Figure 2-4) in Chapter 2, that showed that the solubility of $Zn(OH)_2$ (4.1×10^{-17} mol L^{-1}) was higher than that of $Cu(OH)_2$ (2.0×10^{-19} mol L^{-1}) at room temperature [69]. As in the case of the deposition of Cu^{2+}, a large amount of Zn^{2+} is deposited on TiO_2 surface at pH lower than the PZC of TiO_2 (~6), as discussed above for Cu/TiO_2 samples.

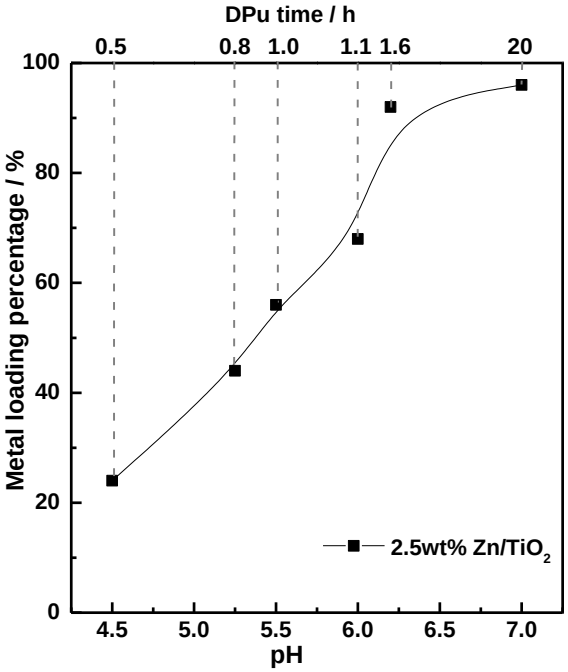

Figure 3-17: Zn loading as a function of pH during DPu preparation

4.2 pH evolution of the Zn^{2+}/TiO_2 mixture solution during DPu

Considering that the pH (OH^- concentration) of the preparation mixture is directly related to the hydrolysis and deposition-precipitation of Zn^{2+}, the pH evolution during the DPu 2.5 wt% Zn/TiO_2 preparation was monitored (Figure 3-18). In Figure 3-18, the pH increased fast in the first 30 min of preparation, i.e., from the initial pH 2 to pH 4.5, because the OH^- ions formed by the urea decomposition neutralized fast the excess of H^+ in the preparation mixture solution. After that, the pH increase slowed down, and it indicates that the consumption of OH^- ions becomes fast. Since the TiO_2 surface is stable in solution (no dissolution), the slower increase of pH could be attributed to the OH^- consumed by the deposition of Zn^{2+} on the TiO_2 surface as it was observed for Cu/TiO_2 preparation (Figure 3-4) in the above section. With extending DPu time, a pH plateau at ~6 was even observed (Figure 3-17), combined to the result of the evolution of the Zn loading versus the pH of preparation solution, it can be proposed that the pH plateaus corresponds to the fast deposition of the Zn^{2+} on the TiO_2 surface.

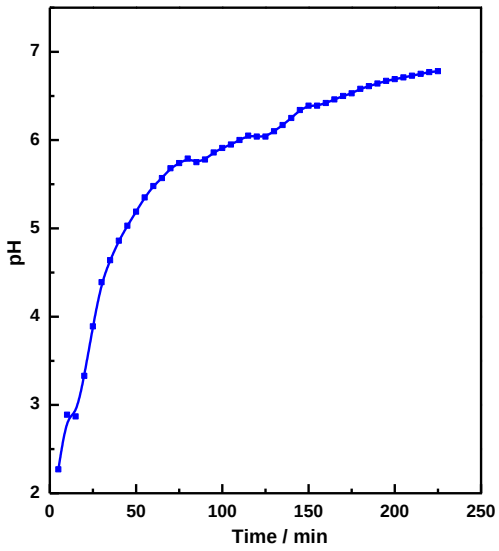

Figure 3-18: pH evolution during 2.5 wt% Zn/TiO_2 preparation by DPu

4.3 Reduction behavior of Zn/TiO_2

The reduction behavior of Zn/TiO_2 was studied by TPR (see Section 3 of Chapter 2). Considering the fact that ZnO is not stable when the reduction temperature becomes higher than 550 ^oC [70-73], and to avoid the contamination of the TPR equipment with volatile Zn, the maximum temperature for the TPR test was set at 550 °C. No visible reduction peak was observed (TPR not shown), which indicates that Zn^{2+} cannot be reduced in this temperature range. Similar result was observed by Kam et al [74] with no ZnO reduction peak up to 400 ^oC, and Turco et al [75] also showed that ZnO seems to be reduced at temperature as high as 650 ^oC.

4.4 Selective hydrogenation of 1,3-butadiene over Zn/TiO_2 catalyst

The catalytic activity of 2.5 wt% Zn/TiO_2 (100 mg, sieve fraction 125-200 μm) in the selective hydrogenation of butadiene was studied following a temperature-programmed procedure (Figure 3-19). Since zinc on TiO_2 does not reduce in the RT-500 °C range, Zn/TiO_2 was activated in the same conditions as Cu/TiO_2, i.e., 350 ^oC. Figure 3-20 shows that Zn/TiO_2, after calcination at 400 ^oC then reduction at 350 ^oC for 2 h, is an inactive catalyst at low temperature (i.e., <180 ^oC) as the butadiene concentration does not change (~3000 ppm) when the reaction temperature increases from 30 ^oC to 180 ^oC. The butadiene concentration only decreases to ~1500 ppm (50% butadiene conversion) when the reaction temperature increases

to 300 °C, meanwhile, there is no butane formed (100% selectivity to butenes) and the conversion of propene to propane is lower than 0.5% (~1500 ppm propane formation). Compared with the 2.5 wt% Cu/TiO_2 catalyst (Figure 3-11), which shows a much higher activity with $T_{100\%}$ at around 75 °C and a high selectivity to butenes after activation at 350 °C, it will be interesting to investigate how the addition of Zn with the preparation of the bimetallic catalyst will modify the catalytic properties of copper (see Chapter 4).

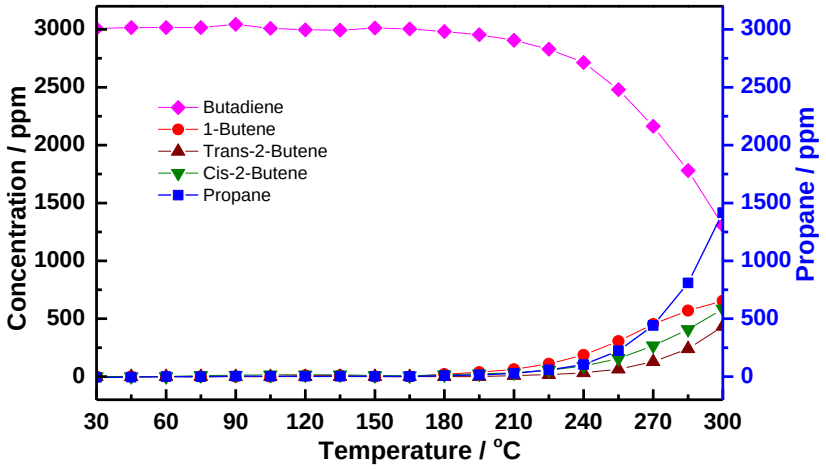

Figure 3-19: Catalytic performances of 2.5 wt% Zn/TiO_2 after calcination at 400 °C then reduction at 350 °C for 2 h

5. Monometallic Ni-based catalysts

Now, we examine the case of supported monometallic nickel catalysts. The possible formation of Ni-Zn alloy was investigated first with a Ni/ZnO sample, which was reduced in a similar way as a former study performed by Derrouiche et al [1], which revealed the formation of Cu-Zn alloy (Cu_3Zn_1 alloy) in Cu/ZnO. As a result, monometallic Ni catalysts supported on TiO_2 and on ZnO are explored in this section. Special attention was paid to select suitable Ni loadings for the study of the catalytic performances and for optimizing the conditions of detection of NiZn alloy in Ni/ZnO sample after reduction at different temperatures. Thus, samples were prepared by DPu with different Ni loadings (5, 2.5, and 0.5 wt%) on TiO_2 and ZnO.

5.1 Monometallic Ni/TiO_2 catalysts

Based on the metal loading selected for the previous TiO_2 supported Cu and Zn study in Section 3.3 and 3.4 (i.e., 2.5 wt%), 2.5 wt% was also selected as Ni loading for this study, as well as a lower Ni loading (0.5 wt%). Table 3-3 shows all of the Ni^{2+} in solution was deposited on TiO_2 by DPu.

Table 3-3: XRF analysis of the Ni loading in the Ni/TiO_2 samples prepared by DPu

Nominal Ni loading	Experimental Ni loading
2.5	**2.3**
0.5	**0.5**

The reduction behavior of the Ni/TiO_2 samples calcined at 400 °C was studied by TPR up to 900 ^oC with a heating rate of 7.5 $^oC\ min^{-1}$, using TiO_2 support as a reference (Figure 3-20). As already shown in the study of Cu/TiO_2 (Figure 3-9), the TPR profile of the TiO_2 support shows some very weak peaks around 520 ^oC, which may be corresponded to the reduction of small amount of superficial Ti^{4+} [76]. The color of TiO_2 initially white turned blue after TPR, this may due to the reduction of part of the Ti^{4+} of the TiO_2 support. Regarding the 2.5 wt% Ni/TiO_2 sample, two reduction peaks can be observed, centered at ~300 ^oC and ~520 ^oC, which is similar to the TPR profile of a 2.5 wt% Ni/TiO_2 sample prepared by adsorption of $Ni(NH_3)_6^{2+}$ reported by Hadjiivanov et al [77]. The first peak can be attributed to the reduction of Ni^{2+} to metallic Ni and the peak at around 520 ^oC to the reduction of Ti^{4+} into Ti^{3+} on the TiO_2 surface [76]. In the case of 0.5 wt% Ni/TiO_2, the first reduction peak due to Ni^{2+} reduction is shifted to higher temperature (450 ^oC), this may be due to the higher proportion of Ni^{2+} directly interacting with TiO_2 in this sample. The second reduction peak is still visible at ~520 ^oC. As a result, a temperature of 350°C was selected for the reduction of 2.5 wt% Ni sample and 450 ^oC for the one of 0.5 wt% Ni/TiO_2 sample.

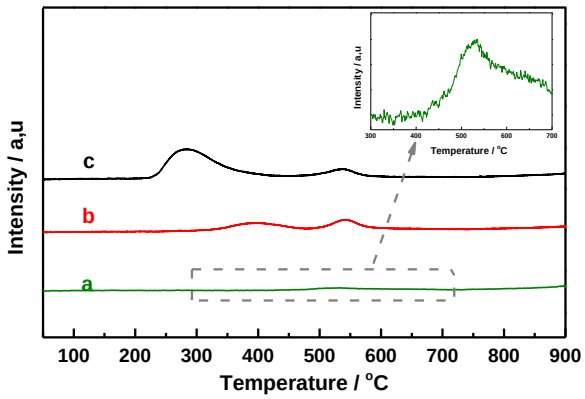

Figure 3-20: TPR of calcined Ni/TiO_2 with different Ni loadings: a, TiO_2 support; b 0.5 wt% and c, 2.5 wt%

Hence, the Ni phase formed after calcination at 400 °C (like for Cu/TiO_2) then reduction at 350 °C for 2.5 wt% Ni/TiO_2 and 450 °C for 0.5 wt% Ni/TiO_2, was checked by XRD (Figure 3-21). Besides the peaks belonging to the TiO_2 support (JCPDS: 01-086-0147), a very weak and broad peak located at ~45.5° (metallic Ni: JCPDS: 00-004-0850) can be observed for the 2.5 wt% Ni/TiO_2 sample. The Ni crystallite size estimated by the Scherrer's equation is around 14 nm. For the 0.5 wt% Ni/TiO_2 sample, the Ni loading is probably too low to observe any Ni phase.

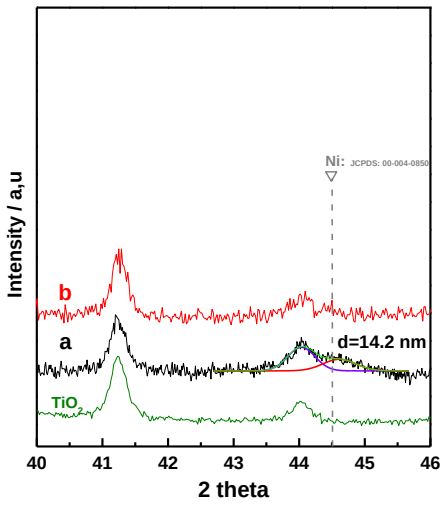

Figure 3-21: XRD of the calcined then reduced Ni/TiO_2 samples with different Ni loadings: a, 2.5 wt%; b, 0.5 wt%

5.1.1 Catalytic performance of 2.5 wt% Ni/TiO_2 sample

The catalytic performance of 2.5 wt% Ni/TiO_2 (sieve fraction 125-200 µm) was evaluated in butadiene/ H_2/ propene mixture at room temperature after sample calcination at 400 °C and reduction at 350 °C for 2 h (C400R350). Firstly, a mixture of 50 mg of catalyst and 50 mg of TiO_2 support (sieve fraction 125-200 µm) was tested at room temperature (Figure 3-22a). As soon as the reactant gas mixture flowed in at RT, the temperature of the reactor increased rapidly from 23 °C to ~ 100 °C as a result of the strong exothermicity of the butadiene/propene hydrogenation reaction, and indicating that the 2.5 wt% Ni/TiO_2 is very active even at room temperature. Note that this phenomenon was not observed with the 2.5 wt% Cu/TiO_2 catalyst. The catalytic data (Figure 3-22a) show that butadiene has been fully converted to butenes and butane, with butane as the main hydrogenation product. Moreover, 28% of the propene was also hydrogenated to propane. This result indicates that the amount of Ni in the catalytic bed must be reduced.

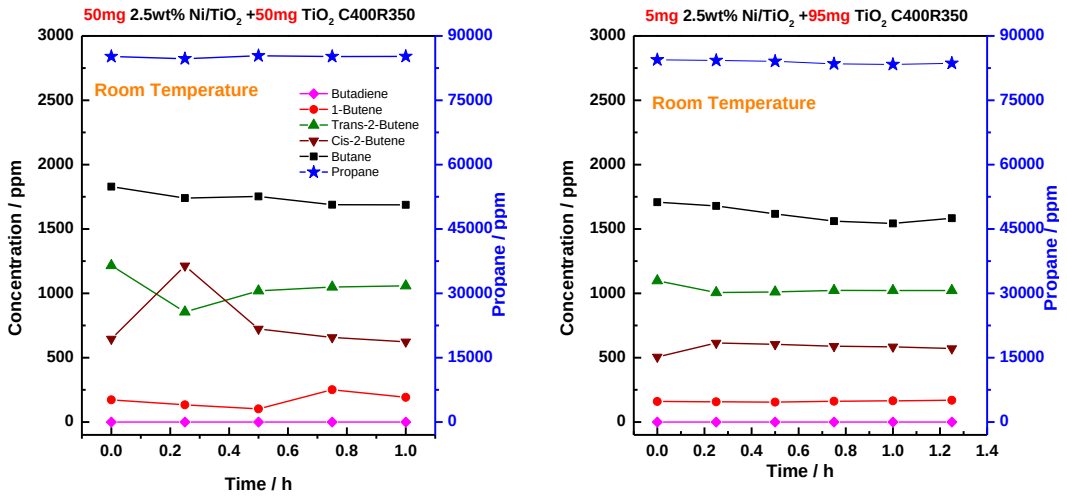

Figure 3-22: Catalytic performance of 2.5 wt% Ni/TiO_2 - TiO_2 mixtures at RT: a, 50 mg catalyst in 50 mg TiO_2; b, 5 mg catalyst in 95 mg TiO_2

The second catalytic test was performed with 100 mg of a mixture containing 5 mg of 2.5 wt% Ni/TiO_2 and 95 mg of TiO_2 (Figure 3-22b). As for the first test, the temperature increased quickly from 26 °C to ~90 °C when the gas mixture was introduced into the reactor at room temperature, and similar catalytic results were obtained.

5.1.2 Catalytic performance of 0.5wt% Ni/TiO_2 sample

The nickel loading was therefore reduced to 0.5 wt%, and the catalytic performances were first tested at RT with a mixture of 10 mg of 0.5 wt% Ni/TiO_2 diluted with 90 mg of TiO_2 after calcination at 400 ^oC and activation at 450 ^oC for 2 h. The temperature of the reactor only slightly increased from 25 to around 30 ^oC when the gas reactants were introduced. Figure 3-23a shows that at this temperature, the sample showed high activity with an initial butadiene conversion close to 100% (butadiene concentration ~100 ppm) and a rather low selectivity to butenes (~80%). However, in the first 6 h of reaction, the butadiene conversion dropped down to ~33% (butadiene concentration ~2000 ppm), then it stabilized to reach a conversion of ~26% (butadiene concentration ~2200 ppm) after 9 other hours of reaction. After 15 h of reaction at room temperature, the temperature of the reactor was increased from room temperature to 115 ^oC with a rate of 1 $^oC\ min^{-1}$. Figure 3-23b shows that the butadiene concentration decreased as temperature increased and a full butadiene conversion ($T_{100\%}$) was achieved around 60 ^oC. At temperature lower than $T_{100\%}$ (Figure 3-24), butadiene was hydrogenated to butenes (~90%) with small amount of alkane formed (~10%) indicating that Ni catalysts are able to provide rather good selectivity to alkenes.

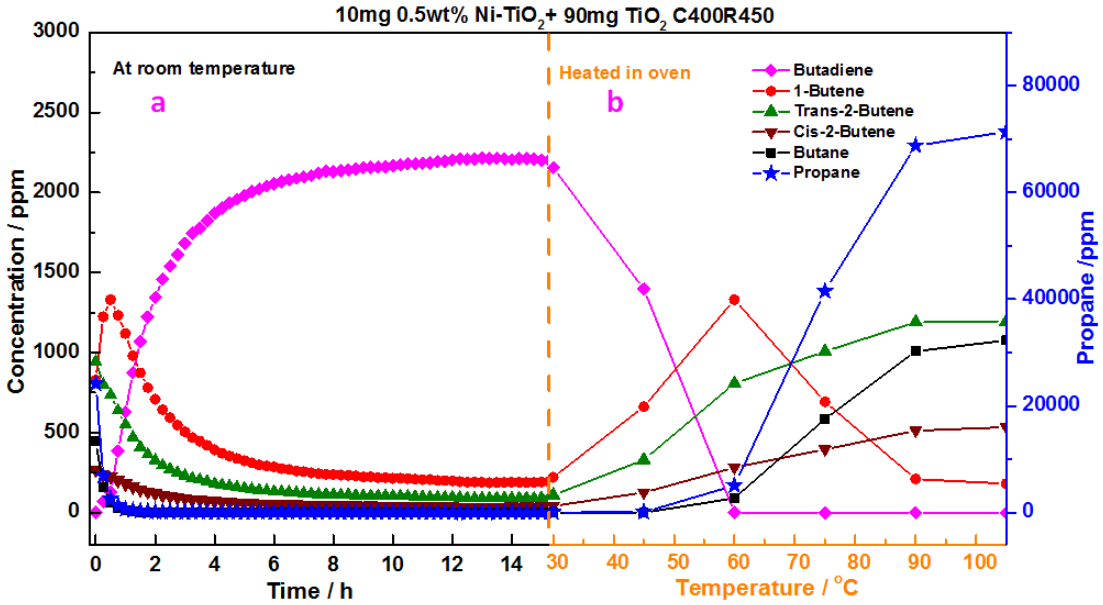

Figure 3-23: catalytic performance of the mixture of 10 mg 0.5 wt% Ni/TiO_2 and 90 mg TiO_2

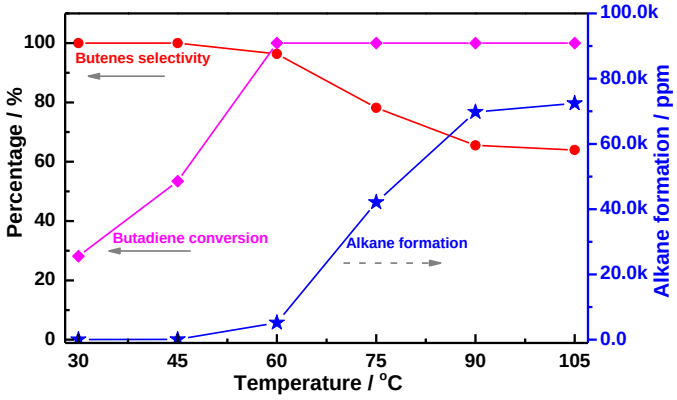

Figure 3-24: Butadiene conversion, butenes selectivity and alkanes formation as a function of temperature for the mixture of 10 mg 0.5 wt% Ni/TiO_2 and 90 mg TiO_2 (extracted from Figure3-23b)

Based on these preliminary results, it can be concluded that monometallic Ni/TiO_2 is very active in hydrogenation of butadiene at low temperature, but it deactivates fast. Once it is partially deactivated, it can provide rather good selectivity to alkenes. The catalyst with 0.5 wt% Ni loading will be more suitable for the evaluation of the catalytic performances of bimetallic $Ni\text{-}Zn/TiO_2$ samples than the one with 2.5 wt% loading. Nevertheless, a $Ni\text{-}Zn/TiO_2$ catalyst containing a higher Ni loading could be used for easier characterization during sample preparation.

5.2 Monometallic Ni/ZnO catalysts

The exploration of the possible formation of Ni-Zn alloy after Ni/ZnO sample reduction was examined with a sample containing ~5 wt % Ni, prepared by DPu, as in the previous study on Cu/ZnO by Derrouiche et al [1]. A 0.5 wt % Ni/ZnO sample was also prepared by DPu, and its catalytic performances (activity, selectivity and stability) were evaluated after reduction at different temperatures.

The metal loadings in these two as-prepared Ni/ZnO samples were measured by XRF (see Section 3 in Chapter 2) (Table 3-4). As in the case of Ni/TiO_2, most of Ni^{2+} has been deposited on the ZnO surface after 20 h of DPu .

Table 3-4: Ni loadings measured by XRF in the as-prepared Ni/ZnO samples

Normal Ni loading	Experimental Ni loading
5.0	**4.8**
0.5	**0.5**

The reduction behavior of Ni^{2+} in the as-prepared and calcined 5 wt % Ni/ZnO samples were studied by temperature programmed reduction with a heating rate of 7.5 $^{o}C\ min^{-1}$ (see Section 3 in Chapter 2). In Figure 3-25, a broad peak centered at ~350 ^{o}C can be observed in the temperature range of 50 to 500 ^{o}C for the as-prepared sample, which is attributed to the reduction of Ni^{2+}. It becomes weaker and broader with a maximum at 450 ^{o}C after sample calcination at 400 ^{o}C for 2 h.

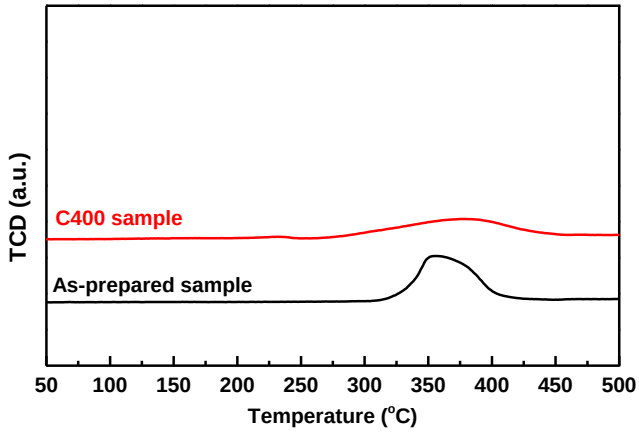

Figure 3-25: TPR of 5 wt% Ni/ZnO: reduction of the calcined and as-prepared samples;

Three reduction temperatures (i.e., 280, 350 and 450 ^{o}C, corresponding to different stage of sample reduction) were first selected to analyze the extent of Ni reduction after a heating rate similar to that used for catalyst activation (i.e., 2 $^{o}C\ min^{-1}$, see Section 4, Chapter 2), and a temperature plateau of 2 h (Figure 3-26). Since the area of the reduction peak is proportional to the amount of H_2 consumed for Ni^{2+} reduction, Figure 3-26 shows that ~90% Ni^{2+} was reduced after reduction at 280 ^{o}C for 2 h and that the rest of Ni^{2+} was fully reduced at around 300 ^{o}C. Indeed, additional H_2 treatments at 350 and 450 ^{o}C did not show substantial H_2 consumption.

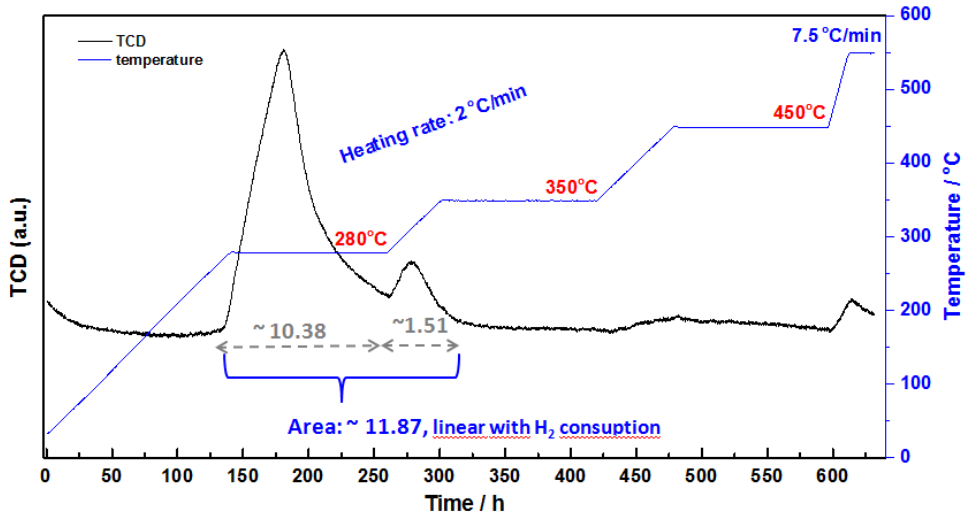

Figure 3-26: TPR of 5 wt% Ni/ZnO: reduction under different conditions during TPR test

Considering that most of Ni^{2+} was reduced at 280 °C for 2 h and that Ni^{2+} is fully reduced at temperature above 300 °C, thus 280, 350 and 450 °C were selected to study the evolution of Ni-phase structure and particle size by XRD as a function of the reduction temperature of the as-prepared and calcined 5 wt% Ni/ZnO samples (Figure 3-27). The diffractogram of ZnO was also presented as a reference. No additional peaks were observed in the as-prepared sample; this means that the Ni compounds are amorphous, probably as hydroxide as identified in some Ni/SiO_2 samples prepared by DPu [33] and in Cu/TiO_2 in Section 3.2. NiO (JCPDS: 71-1179) is present in the calcined Ni/ZnO sample with a broad peak centered at 43.1°, with particle size corresponding to around 5 nm. As reduction temperature increases from 280 to 450 °C, in addition to the ZnO diffraction peaks (JCPDS: 36-1451), the diffractograms of Figure 3-27 show the appearance of three new peaks, 43.5°, 46.5°, 57.7° for both as-prepared and calcined samples. These three peaks show high agreement with the JCPDS card 72-2668, which corresponds to (Ni-Zn) alloy. According to the information of the JCPDS card (i.e., tetragonal cell, a=2.756, c=3.1927 and c/a =1.1585), and to the relationship between the crystal lattice spacing and the composition of Ni-Zn alloy that was summarized in [78], the Ni-Zn alloy seems to correspond to β_1-NiZn alloy with ~50 at% Ni (i.e., Ni_1Zn_1 alloy). The peaks of Ni-Zn alloy become narrower and sharper as reduction temperature increases and the particle sizes calculated from the Scherrer's equation are 3, 10 and 17 nm for the as-prepared sample, and 3, 8 and 14 nm for the calcined sample after reduction at 280, 350 and 450 °C, respectively. The calcination pretreatment seems to induce the formation of slightly smaller Ni-Zn particles. The evolution of the diffractograms with the reduction temperature also shows that the amorphous Ni compounds in as-prepared Ni/ZnO and the NiO in calcined Ni/ZnO directly transformed in NiZn alloy, without any

intermediate formation of metallic Ni. Similar results were found by Spanjers et al [79] who studied the phase composition of 2 wt% Ni/ZnO, prepared by impregnation, by X-ray absorption near-edge spectroscopy (XANES) during *in situ* temperature-programmed reduction with a heating rate of 1.3 ^{o}C min^{-1}. They observed that the proportion of Zn in the Ni-Zn nanoparticles increased with increasing reduction temperature: α-NiZn alloy (Ni_4Zn_1) formed at temperature between 400 and 500 ^{o}C, while it transformed to β_1-NiZn alloy (Ni_1Zn_1) when temperature was higher than 500 ^{o}C. Our results are slightly different since in Figure 3-27, no α-NiZn alloy (Ni_4Zn_1) is observed. It seems that β_1-NiZn alloy (Ni_1Zn_1) phase directly formed, no matter the reduction temperature, and the reduction temperature seems to have no effect on the alloy composition. It is interesting to note that even though the TPR of Zn/TiO_2 sample did not exhibit any reduction peaks below 550 ^{o}C (Figure 3-19), the formation of Ni-Zn alloy indicates that the presence of Ni promote the reduction of some Zn^{2+} at temperature as low as 280 ^{o}C.

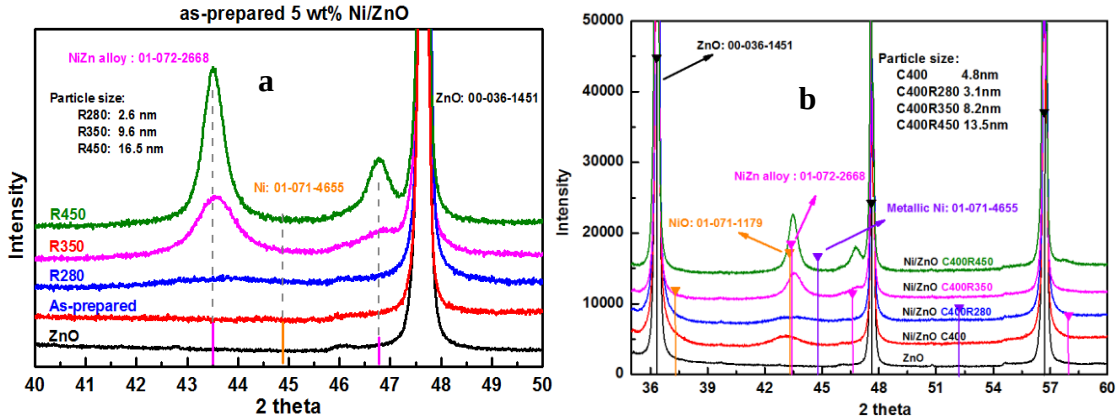

Figure 3-27: XRD of as-prepared (a) and calcined (b) 5 wt% Ni/ZnO sample after reduction at 280 ^{o}C, 350 ^{o}C and 450 ^{o}C for 2 h

The evolution of the nickel phase in the Ni/ZnO with 0.5 wt % Ni loading was also analyzed by XRD after calcination at 400 ^{o}C then reduction at 280, 300, 325, 350 and 450 ^{o}C (Figure 3-28). The results are very different from those obtained with Ni/TiO_2 (Figure 3-21). Even though the Ni loading is low (i.e., 0.5 wt %), NiO (2θ ~43.0^{o}), with crystallite size around 3 nm, can be identified in the calcined sample (Figure 3-28), and the formation of Ni-Zn alloy phase can be observed with a peak at ~43.5^{o} that appears after reduction above 300 ^{o}C. It can also correspond to the Ni-Zn alloy (JCPDS: 72-2668) with Ni:Zn atomic ratio 1:1. According to the Scherrer's equation, the average particle sizes of Ni-Zn alloy in the sample reduced at 300, 325, 350 and 450 ^{o}C are 3, 8, 10 and 11 nm, respectively. No peak was

observed after reduction at 280 °C because either Ni^{2+} is not fully reduced or the particles are too small to be detected by XRD.

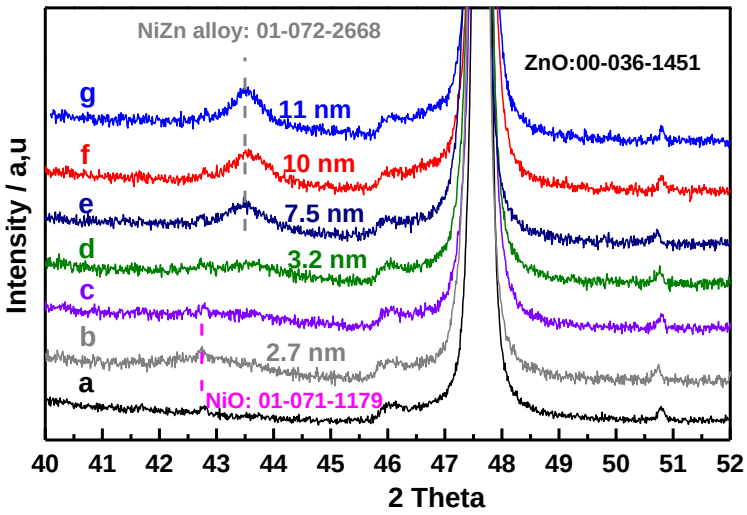

Figure 3-28: XRD of calcined 0.5 wt% Ni/ZnO sample after reduction at different temperature for 2 h: a, ZnO; b, calcined sample; c, reduction at 280 °C; d, reduction at 300 °C; e, reduction at 320 °C; f, reduction at 350 °C; g, reduction at 450 °C;

For the study of the catalytic performances of the Ni/ZnO catalyst, the 0.5 wt% Ni/ZnO sample was employed. Both the as-prepared and the calcined 0.5 wt% Ni/ZnO samples were tested as a mixture of 10 mg of 0.5 wt% Ni/ZnO diluted with 90 mg of ZnO (sieve fraction, 125-200 μm), and the influence of the reduction temperature (i.e., 280, 300, 450 °C) on the catalytic performance was investigated.

Except for the samples reduced at 280 °C, the results in Figure 3-29A show that the calcined catalysts have a lower butadiene 100% conversion temperature ($T_{100\%}$), thus a higher catalytic activity, than the corresponding as-prepared ones. Figure 3-29A also shows that the reduction temperature has a significant effect on $T_{100\%}$, with $T_{100\%}$ close to 70 °C for the samples reduced at 280 °C, and higher than 120 °C for the samples reduced at 450 °C, whatever the starting material. This phenomenon might be explained by the difference of Ni-Zn bimetallic nanoparticle sizes, as smaller particle sizes were obtained in the sample after reduction at lower temperatures (Figure 3-28) and the calcined samples displayed smaller NiZn alloy particle formation after reduction (Figure 3-27). By comparison with the monometallic 0.5 wt% Ni/TiO_2 catalyst reduced at 450 °C, which showed butadiene conversion close to 100% at RT (Figure 3-24), it can be seen that the Ni/TiO_2 catalyst (i.e.,

metallic Ni) has a lower $T_{100\%}$ than Ni/ZnO (i.e., Ni_1Zn_1 alloy), however, the TOFs (turn over frequency) cannot be compared because the Ni particle size in the Ni/TiO_2 catalyst is unknown (and probably much smaller than the NiZn ones in Ni/ZnO since they are not detected by XRD (Figure 3-21)).

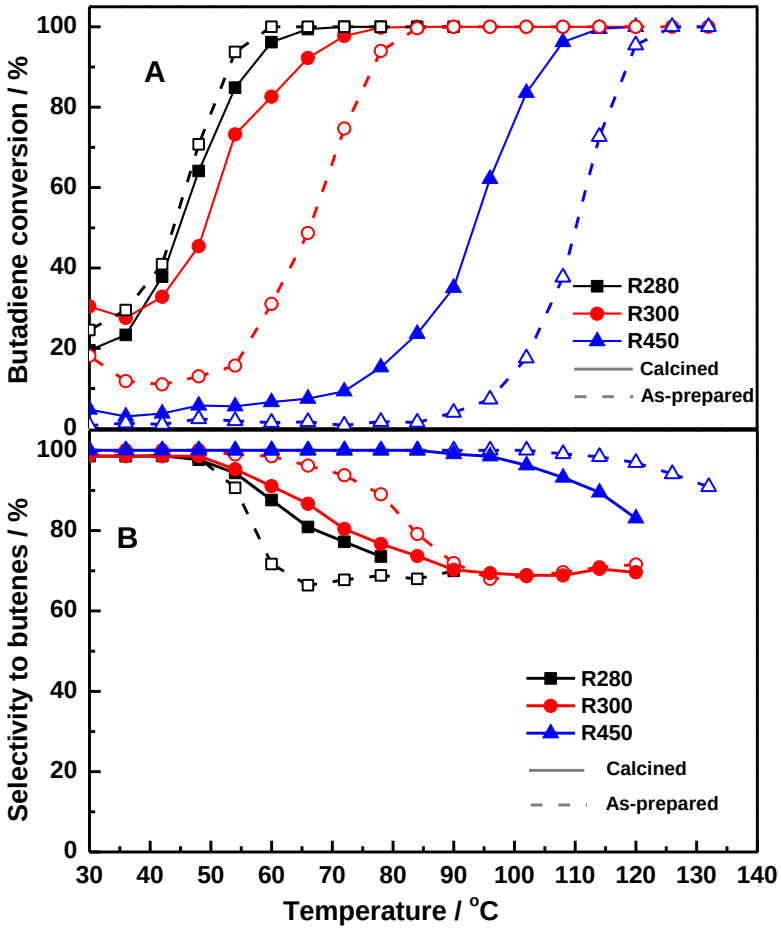

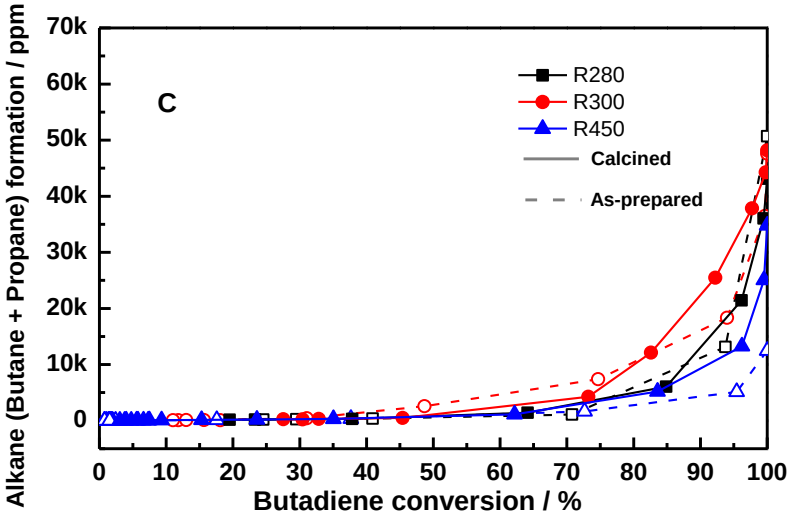

Figure 3-29: Evolution of the butadiene conversion (A) and selectivity to butenes (B) with the temperature and alkanes formation as a function of the butadiene conversion (C) for 0.5 wt% Ni/ZnO sample (10 mg + 90 mg TiO_2) after different thermal treatments

The selectivity to butenes (1-butenes, cis-2-butene and trans-2-butene) and the outlet alkanes (butane and propane) concentration are presented in Figure 3-29B and Figure 3-29C, respectively. Figure 3-29B shows that the selectivity to butenes is high (>90%) for all the samples at reaction temperature lower than 50 °C. It gradually decreases with temperature increases to finally stabilize around 70% at reaction temperatures between 65 °C and 95 °C for the samples reduced at 280 and 300 °C, whereas it keeps decreasing to around 80% for the sample reduced at 450 °C. Selectivities are close to those of the 0.5 wt% Ni/TiO_2 catalyst (i.e., >90% selectivity to butenes at T <$T_{100\%}$, Figure 3-24). From Figure 3-29C, one can note that at high butadiene conversion, the calcined samples provide more alkanes than the as-prepared ones, and that both the as-prepared and calcined catalysts have higher selectivities to alkanes after reduction at 300 °C than at 280 °C and 450 °C.

After reduction at various temperatures (i.e., 280, 300 and 450 °C), the catalytic stability of calcined samples was monitored at specific reaction temperatures corresponding to initial butadiene conversion around 80% for 20 h. Figure 3-30 shows that for all of the samples, the butadiene conversion decreases quickly from ~80% to less than 10% in the first few hours of reaction and that the increase of the reduction temperature results in a decrease of the catalytic stability. Combined with the XRD results (Figure 3-28), the lower stability of Ni/ZnO catalysts as reduction temperature increased may be caused by the increasing Ni-Zn alloy particle size, i.e., the decreasing proportion of surface Ni.

The comparison with the 0.5 wt% Ni/TiO_2 catalyst activated at 450 ^oC for 2 h (Figure 3-24), which showed that butadiene conversion decreased from 100% to ~26% after 8 h of reaction at room temperature, shows that the Ni/ZnO catalyst reduced at the same temperature is less stable as the butadiene conversion decreased sharply from 73% to ~6% in less than 4 h of reaction at 65 ^oC (Figure 3-30). This may indicate that Ni-Zn alloy-based catalysts have lower stability than monometallic Ni catalysts. Spanjers et al [79] also found that by comparison with Ni/SiO_2, the presence of ZnO in Ni/ZnO catalyst hinders the dissociation of H_2 on the β_1-NiZn alloy (Ni_1Zn_1) surface , thereby favors acetylene oligomerization and over hydrogenation, but they concluded that this is due to the presence of ZnO since they reported that the adsorption energies of H on Ni (111) and β_1-NiZn (101) are identical, 0.46 and 0.47 eV, respectively. Even though the authors did not carry stability tests, the possibility of oligomers formation (i.e., green oil or foulant) from the acetylene oligomerization could lead to the catalyst deactivation as oligomer formation is considered as an important cause of deactivation in the case of selective hydrogenation of polyunsaturated compounds [67], thus the oligomerization occurring on the ZnO support may provide an explanation of the lower stability observed for the Ni-Zn alloy in Ni/ZnO catalyst than the monometallic Ni in Ni/TiO_2 sample. Considering the possible negative effect of ZnO on the catalytic performance of supported Ni-Zn alloy, thus it will be better to prepare Ni-Zn supported on another support than ZnO if one would like to study the catalytic stability of supported Ni-Zn alloy

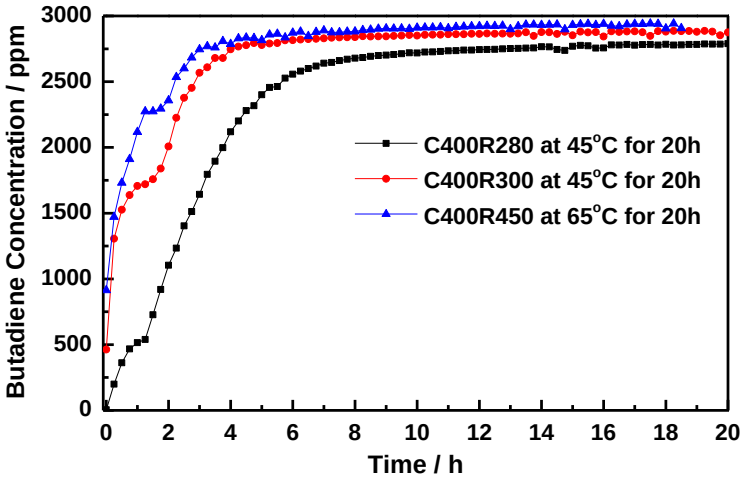

Figure 3-30: Evolution of the butadiene concentration with time on stream for the calcined 0.5 wt% Ni/ZnO sample (10 mg + 90 mg TiO_2) after reduction at various temperatures

6. Conclusion

In this chapter, the deposition-precipitation behavior of transition metal ions (i.e., Cu, Zn and Ni) on TiO_2 support was studied during deposition-precipitation with urea (DPu) preparation, and the catalytic performances of the resulting supported monometallic catalysts were explored in the selective hydrogenation of butadiene reaction in the presence of an excess of propene. According to the experimental results, it was found that the pH required for completing deposition-precipitation of transition metal ions is 5.7 for Cu(II), which is lower than that for Zn(II) (i.e., 6.3), which is in agreement with the theoretical calculation presented in Chapter 2. The deposition-precipitation behavior of Ni will be introduced in Chapter 5. The TPR results revealed that the temperature of reduction of Cu^{2+} and Ni^{2+} on TiO_2 surface is around 350 ^oC and 450 ^oC, respectively and that Zn^{2+} on TiO_2 does not reduce in the 25-550 °C range.

Zn/TiO_2 sample, after activation at 350 ^oC, is inactive at temperature lower than 180 ^oC and very poorly active at temperature higher than 180 ^oC for selective hydrogenation of butadiene.

For the Cu/TiO_2 catalysts, most of Cu was deposited on TiO_2 surface in the first 3 h of DPu preparation, i.e. at pH lower than the PZC of TiO_2 support (~6.0). The formation of a metallic Cu phase was clearly observed after reduction at 350 ^oC, and the size of the Cu nanoparticles strongly depended on the Cu loading and the preparation time, i.e. on the nature of supported Cu phase, $Cu_2(OH)_3NO_3$ or CuO, which arose from the decomposition of $Cu_2(OH)_3NO_3$ during DPu procedure. The formation of the CuO phase was also favored by high Cu loading. As a result, larger Cu^0 particles (8.5 nm) were obtained after reduction of ~5 wt% Cu/TiO_2 than after reduction of 1.55 wt% Cu/TiO_2 (4.5 nm). The evolution of butadiene conversion during reaction from 30 ^oC to 150 ^oC indicates that metallic Cu has a moderate activity (i.e., $T_{100\%}$ around 75 ^oC for 2.5 wt% Cu/TiO_2) in our reaction conditions, a high selectivity to alkenes, but a very low stability during time on stream at temperature close to $T_{100\%}$.

In the case of Ni-based catalysts, metallic Ni particles were only detected by XRD in Ni/TiO_2 samples with high Ni loading (i.e., 2.5 wt%) after reduction at temperature higher than 350 ^oC, however, Ni-Zn alloy (Ni_1Zn_1 alloy) was detected in the monometallic Ni/ZnO sample after reduction at temperature higher than 280 ^oC, without any metallic Ni formation,

no matter the Ni loading (i.e., 2.5 or 0.5 wt%). Strong exothermicity (i.e., the temperature in the reactor sharply increased from RT to >90 °C) was observed once the reactant gas flowed through the 2.5wt% Ni/TiO_2 catalyst at RT, and butadiene was fully converted with butane as the main product, which indicated that metallic Ni was very active in butadiene selective hydrogenation reaction (and much more active than Cu-based catalysts). Thus, a low Ni loading (i.e., 0.5 wt%) will be selected for the further bimetallic Ni-Zn catalytic study in Chapter 5. The diluted 0.5 wt% Ni/TiO_2 catalyst (50 mg in 50mg TiO_2 support) still showed 100% conversion at RT, but no exothermicity with high selectivity to butenes (>95% at temperature close to $T_{100\%}$). However, the catalysts were not stable, and deactivated fast. The comparison of the catalytic performances of Ni/TiO_2 (i.e., metallic Ni) and Ni/ZnO (i.e., Ni_1Zn_1 alloy) catalysts with 0.5 wt% Ni loading after reduction at 450 °C showed that the catalyst containing metallic Ni had higher activity (un-compared TOF as the particle size of metallic Ni in Ni/TiO_2 is unknown) and selectivity to butenes than catalyst containing Ni_1Zn_1 alloy, which is not in agreement with the results of theoretical calculation by Studt's et al (Figure 1-4 in Chapter 1). Indeed, they predicted that Ni_1Zn_1 alloy should have higher selectivity to alkenes, but lower activity than metallic Ni. Our results also indicate that catalyst containing Ni_1Zn_1 alloy deactivates faster than metallic Ni, possibly for reasons developed in Section 5.2 which question the role of the ZnO support. To make a fair comparison, it will be better to prepare bimetallic Ni-Zn supported on another support than ZnO that has an inert surface. As a result, the study of supported $Ni\text{-}Zn/TiO_2$ will be developed in Chapter 5.

Since Zn/TiO_2 is much less active than Cu/TiO_2 and Ni/TiO_2 catalysts (Table 3-5), one can anticipate that the main active metals in the bimetallic $Cu\text{-}Zn/TiO_2$ and $Ni\text{-}Zn/TiO_2$ catalysts that will be studied in Chapters 4 and 5, respectively, are Cu and Ni, and that Zn will behave as a promoter or a modifier as already shown in this chapter in the study of Ni/ZnO.

Table 3-5: Summary of the reaction conditions and activity for the TiO_2 supported Zn, Cu and Ni

Sample	**Metal loading / wt%**	**Mass for catalytic evaluation / mg**	**Activation temperature / °C**	**Full Butadiene conversion temperature**
Zn/TiO_2	**2.5**	**100**	**350**	**50% conversion at 300 °C**
Cu/TiO_2	**2.5**	**100**	**350**	**~75 °C**
Ni/TiO_2	**0.5**	**10 (diluted in 90 mg TiO_2)**	**450**	**RT**

7. References

1. S.Derrouiche, H. Lauron-Pernot, C. Louis, Chemistry of Materials, 24 (2012) 2282.
2. W.F.Bleam, M.B. McBride, Journal of Colloid and Interface Science, 110 (1986) 335.
3. M.F.Ottaviani, E.M. Ceresa, M. Visca, Journal of Colloid and Interface Science, 108 (1985) 114.
4. C. Ludwig, P.W. Schindler, Journal of Colloid and Interface Science, 169 (1995) 284.
5. J.K.Yang, A.P. Davis, Journal of Colloid and Interface Science, 216 (1999) 77.
6. J.K.Yang, S. M. Lee, Journal of Colloid and Interface Science, 282 (2005) 5.
7. J.K.Yang, S. M. Lee, A.P. Davis, Journal of Colloid and Interface Science, 295 (2006) 14.
8. S.K.Poznyak, V.I.Pergushov, A.I.Kokorin, A.I.Kulak, C.W. Schläpfer, The Journal of Physical Chemistry B, 103 (1999) 1308.
9. M.S.Kim, K. M.Hong, J.G. Chung, Water Research, 37 (2003) 3524.
10. M.A.Barakat, Journal of Colloid and Interface Science, 291 (2005) 345.
11. M.Konstantinou, I. Pashalidis, Colloids and Surfaces A: Physicochemical and Engineering Aspects, 324 (2008) 217.
12. A.Georgaka, N. Spanos, Global Nest J, 12 (2010) 239.
13. Z.Wang, D.Brouri, S.Casale, L.Delannoy, C.Louis, Journal of catalysis, 340 (2016) 95.
14. A.Sandoval, C. Louis, R. Zanella, Applied Catalysis B: Environmental, 140 (2013) 363.
15. L.Delannoy, G.Thrimurthulu, P.S. Reddy, C.Méthivier, J.Nelayah, B.M.Reddy, C.Ricolleau, C.Louis, Phys. Chem. Chem. Phys., 16 (2014) 26514.
16. R.Si, J.Raitano, N.Yi, L.Zhang, S.W. Chan, Maria Flytzani-Stephanopoulos, Catalysis Today, 180 (2012) 68.
17. S.F.Peng, J. J. Ho, Physical Chemistry Chemical Physics, 13 (2011) 20393.
18. V.G.Deshmane, R.Y. Abrokwah, D. Kuila, Journal of Molecular Catalysis A: Chemical, 408 (2015) 202.
19. H.C.Yang, H.Y.Lin, Y.S.Chien,J.C.Sheng Wu, H.H.Wu, Catalysis letters, 131 (2009) 381.

20. M.Behrens, F.Studt, I.Kasatkin, S.Kühl, M.Hävecker, F.Abild-Pedersen, S.Zander, F.Girgsdies, P.Kurr, B.L.Kniep, M.Tovar, R.W.Fischer, J.K.Nørskov, R.Schlögl, Science, 336 (2012) 893.
21. J.Llorca, M.Domínguez, C.Ledesma, R.J. Chimentão, F.Medina, J.Sueiras, I.Angurell, M.Seco, O.Rossell, Journal of catalysis, 258 (2008) 187.
22. O.P.H. Vaughan, G.Kyriakou, N.Macleod, Mi.Tikhov, R.M. Lambert, Journal of catalysis, 236 (2005) 401.
23. R.J. Chimentão, F. Medina, J.L.G. Fierro, J. Llorca, J.E. Sueiras, Y. Cesteros, P. Salagre, Journal of Molecular Catalysis A: Chemical, 274 (2007) 159.
24. S.Pande, A.Saha, S.Jana, S.Sarkar, M.Basu, M.Pradhan, A.K.Sinha, S.Saha, A.Pal, T.Pal, Organic letters, 10 (2008) 5179.
25. Q.Jia, D.Zhao, B.Tang, N.Zhao, H.Li, Y.Sang, N.Bao, X.Zhang, X.Xu, H.Liu, Journal of Materials Chemistry A, 2 (2014) 16292.
26. F.Liao, Y.Huang, J.Ge, W.Zheng, K.Tedsree, P.Collier, X.Hong, S.C.Tsang, Angewandte Chemie International Edition, 50 (2011) 2162.
27. B.M. Nagaraja, A.H. Padmasri, B. David Raju, K.S. Rama Rao, Journal of Molecular Catalysis A: Chemical, 265 (2007) 90.
28. J.Phillipson, P. Wells, G. Wilson, Journal of the Chemical Society A: Inorganic, Physical, Theoretical, 1969, 1351.
29. E.Nishimura, Y. Inoue, I. Yasumori, Bulletin of the Chemical Society of Japan, 48 (1975) 803.
30. R.Koeppel, J.T.Wehrli, M.S.Wainwright, D.L.Trimma, N.W.Cant, Applied Catalysis A: General, 120 (1994) 163.
31. N.J.Ossipoff, N.W. Cant, Journal of catalysis, 148 (1994) 125.
32. L.Trouillet, T.Toupance, F.Villain, C.Louis, Physical Chemistry Chemical Physics, 2 (2000) 2005.
33. P.Burattin, M. Che, C. Louis, The Journal of Physical Chemistry B, 102 (1998) 2722.
34. M.K. van der Lee, A. Jos van Dillen, J.H. Bitter, K.P. de Jong, Journal of the American Chemical Society, 127 (2005) 13573.
35. C.Louis, *Deposition-precipitation synthesis of supported metal catalysts.* CATALYST PREPARATION, Science and Engineering, 2007.
36. J. Park, J.R. Regalbuto, Journal of colloid and interface science, 175 (1995) 239.
37. D.C.Pereira, D.L.A.d. Faria, V.R. Constantino, Journal of the Brazilian Chemical Society, 17 (2006) 1651.

38. S.A.Kondrat, P.J.Smith, P.P.Wells, P.A.Chater, J.H.Carter, D.J.Morgan, E.M.Fiordaliso, J.B.Wagner, T.E. Davies, L.Lu, J.K.Bartley, S.H.Taylor, M.S.Spencer, C.J.Kiely, G.J.Kelly, C.W.Park, M.J.Rosseinsky, G.J.Hutchings, Nature, 531 (2016) 83.
39. N.L.Dias Filho, Microchimica Acta, 130 (1999) 233.
40. T.Toupance, M. Kermarec, C. Louis, The Journal of Physical Chemistry B, 104 (2000) 965.
41. M.Liu, X.Qiu, M.Miyauchi, K.Hashimoto, Chemistry of Materials, 23 (2011) 5282.
42. H.Irie, S.Miura, K.Kamiya, K.Hashimoto, Chemical Physics Letters, 457 (2008) 202.
43. H.Irie, K.Kamiya, T.Shibanuma, S.Miura, D.A. Tryk, T.Yokoyama,K.Hashimoto, The Journal of Physical Chemistry C, 113 (2009) 10761.
44. I. Georgiadou, Ch. Papadopoulou, H. K. Matralis, G. A. Voyiatzis, A. Lycourghiotis, Ch. Kordulis, The Journal of Physical Chemistry B, 102 (1998) 8459.
45. B.Choudhury, M. Dey, A. Choudhury, International Nano Letters, 3 (2013) 1.
46. A.Petalaa, E.Ioannidoua, A.Georgakab, K.Bourikasb, D.I. Kondarides, Applied Catalysis B: Environmental, 178 (2015).
47. P.Platanitis, G.D. Panagiotou, K.Bourikas, C.Kordulis, J.L.G. Fierro, A.Lycourghiotis, Journal of Molecular Catalysis A: Chemical, 412 (2016) 1.
48. J.Y. Kim, J.A. Rodriguez, J.C. Hanson, A.I. Frenkel, P.L. Lee, Journal of the American Chemical Society, 125 (2003) 10684.
49. W.P.Dow, Y. P. Wang, T. J. Huang, Journal of catalysis, 160 (1996) 155.
50. G.Fierro, M.L.Jacono, M.Inversi, P.Porta, F.Cioci, R.Lavecchia, Applied Catalysis A: General, 137 (1996) 327.
51. J.N.Nian, S.A.Chen, C.C.Tsai, H.Teng, The Journal of Physical Chemistry B, 110 (2006) 25817.
52. F.S.Delk II, A. Vāvere, Journal of catalysis, 85 (1984) 380.
53. X.F.Yu, N.Z.Wu, Y.C.Xie, Y.Q. Tang, Journal of Materials Chemistry, 10 (2000) 1629.
54. G.Fierro, L.Lojacono, M.Inversi, P.Porta, R.Lavecchia, F.Cioci, Journal of catalysis, 148 (1994) 709.
55. K.Bourikas, C. Kordulis, A. Lycourghiotis, Chemical reviews, 114 (2014) 9754.
56. D.T.Cromer, K. Herrington, Journal of the American Chemical Society, 77 (1955) 4708.

57. G.D.Panagiotou, T.Petsi, K.Bourikas, C.S.Garoufalis, A.Tsevis, N.Spanos, C.Kordulis, A.Lycourghiotis, Advances in colloid and interface science, 142 (2008) 20.
58. L.Pauling, Journal of the American Chemical Society, 51 (1929) 1010.
59. C.J.G. Van Der Grift, P.A. Elberse, A. Mulder, J.W. Geus, Applied Catalysis, 59 (1990) 275.
60. J.A. van Dillen, J.W.G., L.A Hermans, J. van der Meijden, In "Proceedings of the 6th International Congress on Catalysis" London, 1976.
61. G. C. Bond, P.B.W., F.C. Tompkins, Ed., The Chemical Society: London, 1977: p. P 677.
62. J.W.E. Coenen, , *Reduction of Silica Supported Nickel Catalysts*, in *Studies in Surface Science and Catalysis*, P.G.P.J. B. Delmon and G. Poncelet, Editors. 1979, Elsevier. p. 89-111.
63. P.Burattin, M. Che, C. Louis, The Journal of Physical Chemistry B, 101 (1997) 7060.
64. C. RamachandraáRao, Journal of Materials Chemistry, 1 (1991) 299.
65. A.Hugon, L. Delannoy, C. Louis, Gold Bulletin, 41 (2008) 127.
66. N.J.Ossipoff, N. Cant, Journal of Catalysis, 148 (1994) 125.
67. M.R. Stammbach, D.J. Thomas, D.L. Trimm, M.S. Wainwright, Applied Catalysis, 58 (1990) 209.
68. H.Yan, H.Cheng, H.Yi, Y.Lin, T.Yao, C.Wang, J.Li, S.Wei,J.Lu, Journal of the American Chemical Society, 137 (2015) 10484.
69. J.Bjerrum, *Stability constants of metal-ion complexes*. 1964: The Chemical Society.
70. T.Imoto, Y.Harano, Y.Nishi, S.Masuda, Bulletin of the Chemical Society of Japan, 37 (1964) 441.
71. S.Lew, A.F. Sarofim, M. Flytzani-Stephanopoulos, Chemical Engineering Science, 47 (1992) 1421.
72. M.Liang, W. Kang, K. Xie, Journal of Natural Gas Chemistry, 18 (2009) 110.
73. M.A. Valenzuela, P. Bosch, J. Jiménez-Becerrill, O. Quiroz, A.I. Páez, Journal of Photochemistry and Photobiology A: Chemistry, 148 (2002) 177.
74. R.Kama, C.Selomulyaa, R.Amalb, J.Scott, Journal of Catalysis, 273 (2010) 73.
75. M.Turco, G.Bagnasco, U.Costantino, F.Marmottini, T.Montanari, G.Ramis, G.Busca, Journal of Catalysis, 28 (2004) 43.
76. J.van de Loosdrecht, A.M.van der Kraan, A.J.van Dillen, J.W.Geus, Journal of Catalysis, 170 (1997) 217.

77. K.Hadjiivanov, M.Mihaylov, N.Abadjieva, D.Klissurski, J. Chem. Soc., Faraday Trans., 94 (1998) 3711.
78. W.Pearson, W. Pearson, *An Alphabetical Index of Work on Metals and Alloys.* A Handbook of Lattice Spacings and Structures of Metals and Alloys, 1958: p. 634.
79. C.S.Spanjers, R.S.Sim, N.P.Sturgis, B.Kabius, R.M.Rioux, ACS Catalysis, 5 (2015) 3304.

Chapter 4: Novel Non-Noble Bimetallic Cu-Zn/TiO_2 Catalysts for Selective Hydrogenation of Butadiene

Chapter 4: Novel Non-Noble Bimetallic Cu-Zn/TiO_2 Catalysts for Selective Hydrogenation of Butadiene

1. Introduction

According to the study of monometallic Cu/TiO_2 catalysts for the selective hydrogenation of butadiene in Chapter 3, metallic Cu shows high selectivity to alkenes (i.e., ~100% to alkenes at T~$T_{100\%}$), moderate activity (compared to Pd-based catalysts), but low catalytic stability. Thus, in order to make Cu-based catalysts become suitable alternatives to noble metal catalysts (e.g., Pd-based catalysts) in the selective hydrogenation of unsaturated hydrocarbons, the catalytic stability of metallic Cu has to be improved. Based on previous studies on palladium-based bimetallic catalysts, bimetallic Pd-Ag catalysts show higher catalytic activity, selectivity to alkenes and stability than monometallic Pd catalyst [1-7], the introduction of a second metal to metallic Cu could be an attractive path to promote the catalyst stability in selective hydrogenation. It has also been found that alloying copper with gold (in bimetallic Au_1Cu_3 catalyst) resulted in a more stable catalyst than monometallic Cu and a more active catalyst than monometallic gold [8].

On the other hand, using density functional theory (DFT) calculation, Studt et al [9] predicted that Cu-Zn alloy could have a higher selectivity than metallic Cu in acetylene hydrogenation. Moreover, although the promotional role of Zn on the catalytic activity and selectivity of supported Cu catalyst has been studied in catalytic reactions such as methanol synthesis [10-13], water-gas shift reaction [14] and methanol steam reforming [15], the effect of alloying Cu with Zn on the catalytic stability of Cu has not been experimentally verified up to now, especially, in the reaction of selective hydrogenation of alkynes and alkadienes. As a result, it is worth to investigate whether adding Zn to Cu will improve the catalytic stability during reaction. Thus, the aim of this chapter is to prepare supported bimetallic Cu-Zn catalysts with the goal of trying to obtain well dispersed Cu-Zn nanoalloy particles, to characterize the metal particles and to evaluate their catalytic performance in the selective hydrogenation of butadiene.

Regarding the synthesis of Cu-Zn nanoalloy, the alloy phase diagram of bulk Cu-Zn system (Figure 4-1) has to be first examined. Figure 4-1 shows that the phase of the CuZn alloy changes from α to η (7 types of alloy phases) according to the amount of Zn in the

bimetallic Cu-Zn system, e.g., α-CuZn phase when the Zn content is lower than 38.95 wt%, while η-CuZn phase when the Zn content is higher than 97.25 wt%. Since the Zn content in the bimetallic Cu-Zn system plays a key role on the nature of Cu-Zn alloy phase, it will be interesting to vary the Zn loading in the supported bimetallic Cu-Zn catalysts and study its influence on their catalytic performances. Besides that, the low melting temperature of metallic Zn (~420 ^{o}C; boiling point: ~907^{o}C) also reminds us to be aware of the selection of the temperature for sample reduction, to avoid the risk of Zn evaporation, which may cause a change in the Zn content, and finally affects the CuZn alloy phase formation.

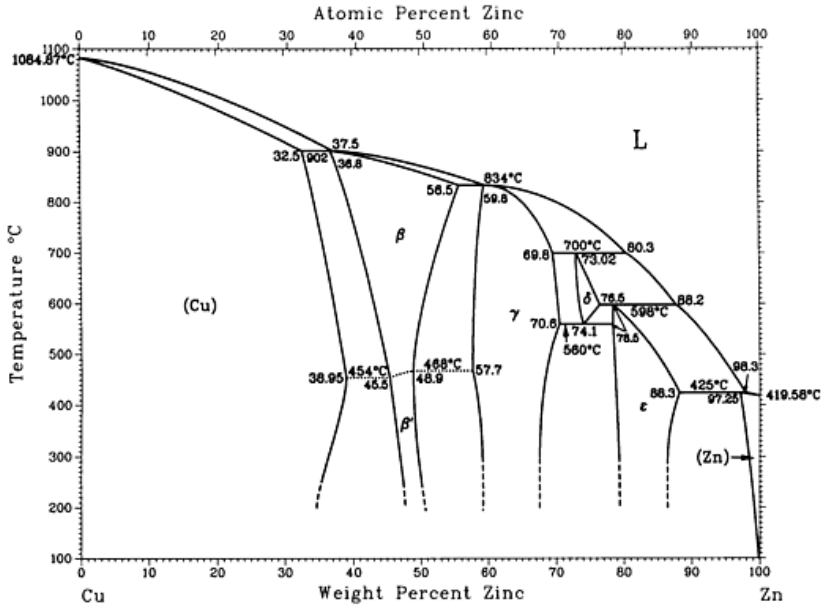

Cu-Zn crystallographic data

Phase	Composition, wt% Zn	Pearson symbol	Space group
α or (Cu)	0 to 38.95	*cF*4	$Fm\overline{3}m$
β	36.8 to 56.5	*cI*2	$Im\overline{3}m$
β_1	45.5 to 50.7	*cP*2	$Pm\overline{3}m$
γ	57.7 to 70.6	*cI*52	$I\overline{4}3m$
δ	73.02 to 76.5	*hP*3	$P\overline{6}$
ε	78.5 to 88.3	*hP*2	$P6_3/mmc$
η or (Zn)	97.25 to 100	*hP*2	$P6_3/mmc$

Figure 4-1: Alloy phase diagram of Cu-Zn system (left), Cu-Zn crystallographic data (right) [16]

In this chapter, bimetallic Cu-Zn catalysts are for the first time studied in a reaction of hydrogenation, here in that of selective hydrogenation of butadiene in the presence of propene. The Cu-Zn/TiO_2 catalysts with CuZn ratios of 3:1 and 1:1 were prepared by the same method of deposition-precipitation with urea (DPu) as Cu/TiO_2 (Chapter 3), i.e., by co-DPu and by another method of deposition-precipitation at fixed pH (DP8) for reasons that will be explained later. Note that specific attention is paid to the characterization of the composition of Cu-Zn particles, which is an important aspect for the study of bimetallic catalysts. This chapter will describe:

- The deposition behavior of Cu and Zn on titania as a function of pH and time;

- The characterization of Cu-Zn nanoalloy after sample calcination and reduction by different techniques, such as XRF, XRD, XPS, and STEM-HAADF coupled with EDS.

- The effect of the addition of Zn to Cu/TiO_2 catalyst on the catalytic performance, including activity, selectivity to alkenes and stability.

- The influence of the catalyst preparation method (i.e., DPu and DP8) on the nanoparticle size, dispersion and catalytic performance.

2. Catalysts preparation

Monometallic Cu/TiO_2 and Zn/TiO_2 and bimetallic $Cu\text{-}Zn/TiO_2$ catalysts were prepared using the method of DPu procedure described elsewhere [17] and deposition-precipitation at fixed pH (i.e. 8). Briefly, for the DPu procedure, 3 g of support (TiO_2 P25 Evonik) dispersed into 300 ml distilled water were mixed with the appropriate amount of $Cu(NO_3)_2 \bullet 3H_2O$ and/or $Zn(NO_3)_2 \bullet 6H_2O$ precursors in order to achieve the desired nominal copper and/or zinc loading with Cu:Zn atomic ratios of 3:1 and 1:1. Urea was added to achieve a urea to metal molar ratio of ca. 100. The mixture was kept at 80 °C in a closed reactor for 20 h under continuous stirring. The solid was separated from the liquid by centrifugation and subsequently washed with distilled water and centrifuged again (three times) (sample called DPu).

DP8 preparation was performed as follows. A suspension of 3 g TiO_2 support in 250 ml distilled water with pH adjusted to 8 using NaOH (0.5 M) was introduced into a glass reactor at room temperature. A 50 ml distilled water containing $Cu(NO_3)_2 \cdot 3H_2O$ and/or $Zn(NO_3)_2 \cdot 6H_2O$ was injected into the TiO_2 suspension slowly (~2 ml min^{-1}), then the mixture was stirred for 2 h. The pH of the solution was kept constant at pH around 8 by gradually injecting 0.5 M NaOH solution throughout the whole preparation procedure. The solid was then collected by centrifugation and subsequently washed with distilled water and centrifuged again (three times) (sample called DP8).

All of the samples were further dried under vacuum at room temperature for 24 h (as-prepared sample).

Monometallic Cu/TiO_2 and Zn/TiO_2 samples were prepared with a 2.5 wt% nominal metal loading by both methods. Bimetallic CuZn 3:1 and $1:1/TiO_2$ catalysts were prepared to achieve 2.5 wt% Cu and 0.8 wt% Zn and 2.5 wt% Cu and 2.5 wt% Zn, respectively. Before characterization or reaction, the catalysts were calcined at 400 °C for 2 h with a temperature ramp of 5 °C min^{-1}, under flowing air (100 mL min^{-1}), and reduced at 350 °C for 2 h (temperature ramp of 2 °C min^{-1}) under flowing H_2 (100 mL min^{-1}) .

3. Results and discussion

3.1 XRF study of metals deposition-precipitation behavior

The evolution of the metal loadings as a function of pH/time for a representative DPu and DP8 sample (nominal 2.5 wt% Cu and Zn loadings, Cu/Zn=1) was studied by extracting the Cu-Zn/TiO_2 solids from the suspensions at different pHs/time. The metal loadings in the as-prepared samples were determined by XRF and presented in Figure 4-2.

It appears that the deposition-precipitation of copper and zinc is not coincident in the case of the DPu process (Figure 4-2A) as copper is deposited first on TiO_2 surface and almost completely at pH around 5, whereas zinc starts to deposit at pH above 5 to finally reach complete deposition at pH around 7.5. This was also previously observed in the case of homogeneous precipitation of ternary $Cu/ZnO/Al_2O_3$ using urea as the precipitating agent [18], showing that the precipitation of Cu(II) and Zn(II) proceeded stepwise, with Cu(II) hydrolysed first then Zn(II) during the pH increase, and the final compound in the as-prepared samples consisted mainly of aurichalcite, $(Cu,Zn)_5(CO_3)_2(OH)_6$. The formation of the latter compound resulted from the dissolution-reprecipitation of amorphous $Cu(OH)_2$ assisted by Zn(II) [18]. Considering the principle of DPu method described in the literature [19-22], the solubility difference between copper ($log^*K_s^0 = 8.85$) [23-25] and zinc hydroxide ($log^*K_s^0 = 12.0$) [23, 24] could be responsible for the sequential deposition-precipitation behaviour of Cu^{2+} and Zn^{2+}. However, because of the low metal loadings employed in this work, and maybe also because the compound was amorphous, it was not possible to identify the phase(s) present at the end of the preparation process by XRD.

Consequently, a pH above 7.5 is required to simultaneously precipitate/deposit copper and zinc. This is confirmed by the results obtained for the sample prepared at pH ~8 (DP8)

(Figure 4-2B), which show that the major part of both metals is deposited concurrently within the first hour of the process.

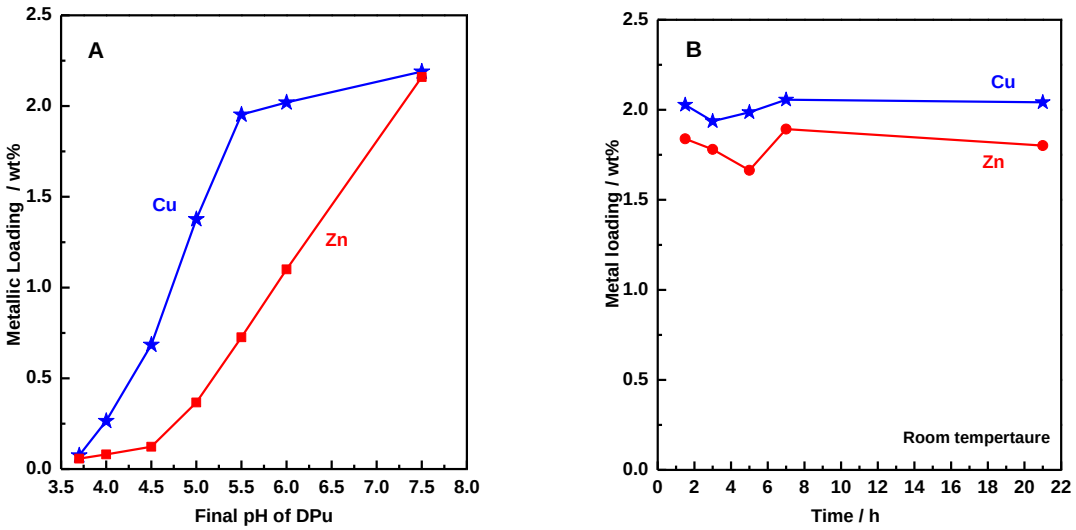

Figure 4-2: Evolution of the Cu and Zn loadings on titania versus pH during the DPu (A) and versus time during the DP8 (B) preparation procedure. Nominal loadings: 2.5 wt% Cu and 2.5 wt% Zn

The final metal loadings in the catalysts prepared by DPu and DP8 are presented in Table 4-1. The experimental Cu and Zn loadings are closed to the nominal ones, indicating that the deposition yields reached values above 80%. Moreover, the Cu/Zn atomic ratios are also closed to the ones expected for all the samples.

Table 4-1: Final metal loading in the Cu-Zn/TiO_2 sample prepared by DPu and DP8

Theoretical values			**Experimental values**					
Cu : Zn ratios	**Loading (wt%)**		**DPu**		**DP8**		**DPu Cu : Zn ratios**	**DP8 Cu : Zn Ratios**
	Cu	**Zn**	**Cu**	**Zn**	**Cu**	**Zn**		
1 : -	**2.5**	**-**	**2.2**	**-**	**2.2**	**-**	**1 : -**	**1 : -**
3 :1	**2.5**	**0.8**	**2.0**	**0.7**	**2.3**	**0.8**	**2.9 :1**	**2.9 :1**
1 :1	**2.5**	**2.5**	**2.0**	**1.9**	**2.1**	**2.0**	**1.1 :1**	**1.1 :1**
- : 1	**-**	**2.5**	**-**	**2.1**	**-**	**2.1**	**- : 1**	**- : 1**

3.2 UV-Visible study of calcined Cu-Zn/TiO_2 catalysts

The UV-Visible spectra obtained for the calcined DPu and DP8 samples are presented in Figure 4-3A, B. The contribution of the support was removed by using TiO_2 as the baseline

for the UV-visible spectra. The Zn/TiO_2 spectrum shows an absorption band with a maximum at 370 nm (spectrum 5 in Figures 4-3A), which is characteristic of ZnO whose band gap is at 3.35 eV [26]. However, this band cannot be observed in the DPu or DP8 CuZn 3:1 and 1:1/TiO_2 samples (spectra 2 and 3 in Figures 4-3A, B) which may mean that these samples do not contain bulk ZnO. The spectra of the DPu and DP8 Cu/TiO_2 (spectrum 1 in Figures 4-3A and B) show two bands: one is at ~430 nm, previously observed for Cu/TiO_2 samples [27] and attributed to the interfacial charge transfer (IFCT) from the O_{2p} valence band of TiO_2 to M^{x+} ions, such as Cu^{2+} [28-30], V^{5+} [31], Mo^{2+} [32], Fe^{3+} [33]. Another broad band is visible in the 600-1000 nm region and could be assigned to the Cu(II) d-d transition band [34-36]. These two bands are visible in all the Cu/TiO_2 and Cu-Zn/TiO_2 samples, whatever the preparation method. Moreover, in the DPu samples, there is an additional band in the range 450-800 nm that can be assigned to the presence of CuO [17, 27, 37].

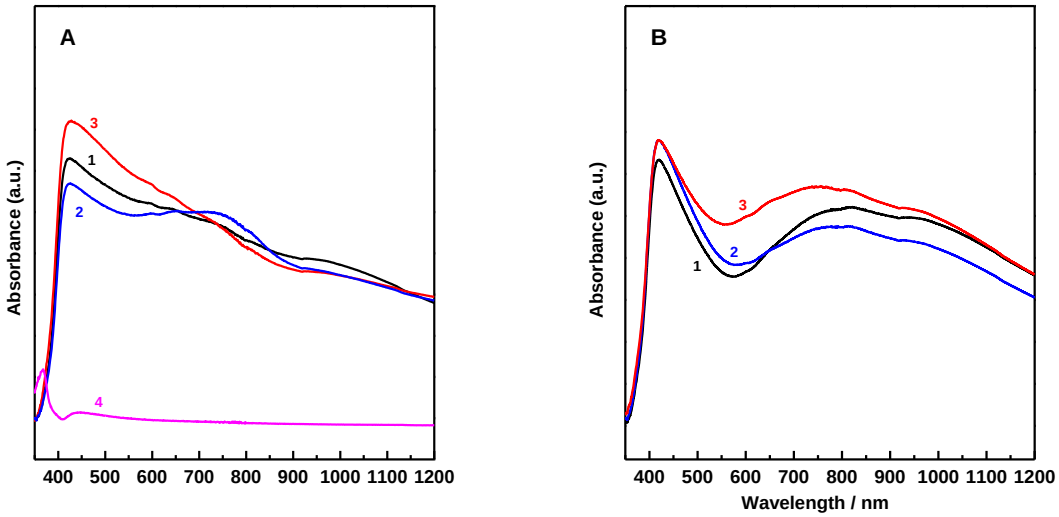

Figure 4-3: UV-visible spectra of the calcined DPu (A) and DP8 (B) samples: 1, Cu/TiO_2; 2, CuZn 3:1/TiO_2; 3, CuZn 1:1/TiO_2; 4, DPu Zn/TiO_2 in (A)

3.3 Study of the thermal stability of Zn under H_2 atmosphere

Considering that the Zn content in the bimetallic Cu-Zn system strongly affects the final Cu-Zn alloy phase formation, and combined to the low melting temperature for metallic Zn (420 °C, Figure 4-1, left), it is necessary to study the thermal stability of metallic Zn in H_2 atmosphere, using XRF technique, before the selection of reduction temperature for the bimetallic Cu-Zn/TiO_2 samples. Here, the DPu and DP8 2.5wt% CuZn 1:1/TiO_2 were used as examples. After reduction at 280, 350 and 550 ^oC for 2 h, the Zn loadings in the samples were

analyzed by XRF and summarized in Table 4-2. It was found that Zn loadings in both catalysts after reduction at 280 and 350 ^{o}C stay around ~2.0 wt%, which were similar to that in the as-prepared and calcined samples, however, they decreased to ~0.4 wt% when the reduction temperature increased to 550 ^{o}C. Meanwhile, it was also observed that the inner wall of the rector at the outlet of the oven turned gray after sample reduction at 550 ^{o}C. A similar phenomenon of Zn deposition was observed by Yao et al [38] at the outlet of an oven in a reactor opened to air during thermal evaporation of pure metallic Zn at 1100 ^{o}C.

Based on this result, it can be concluded that it is compulsory to carry out catalyst reduction at temperature lower than 550 ^{o}C.

Table 4-2: Cu, Zn loading of CuZn 1:1/TiO_2 prepared by DPu and DP8 after drying and different thermal treatments

CuZn1:1/TiO_2		**Dry RT (wt%)**	**Dry RT - C400 (wt%)**	**Dry RT - C400 R280 (wt %)**	**Dry RT - C400 R350 (wt %)**	**Dry RT - C400 R550 (wt %)**
DPu	**Cu**	**2.19**	**2.17**	**2.18**	**2.16**	**2.23**
	Zn	**2.16**	**2.16**	**2.17**	**2.12**	**0.44**
DP at pH=8	**Cu**	**2.18**	**2.19**	**2.17**	**2.16**	**2.27**
	Zn	**1.93**	**1.91**	**1.92**	**1.89**	**0.46**

3.4 Reduction behavior of calcined Cu-Zn/TiO_2 catalysts

Temperature programmed reduction under H_2 (TPR-H_2) was performed on the calcined DPu and DP8 samples and the results are presented in Figure 4-4. Firstly, the calcined DPu Zn/TiO_2 sample (2.5 wt% Zn) does not exhibit any reduction peak up to 550 °C, which agrees with previous articles [39, 40] that reported that bulk ZnO reduction occurs at temperature as high as 650 ^{o}C [41-44]. Note that the TPR in this study was stopped at 550 °C to avoid the contamination of the TPR equipment by the volatile Zn^0. The copper species in the monometallic Cu/TiO_2 DPu and DP8 samples are reduced below 200 °C. In both cases, two close reduction peaks are visible, and could correspond to the reduction of Cu (II) species highly dispersed onto the support for the low temperature peak and to CuO for the high temperature one, respectively [27, 45]. In the case of the bimetallic Cu-Zn/TiO_2 samples, a general feature is that the temperature of the maximum of the reduction peaks increases with the introduction of Zn, whatever the preparation method. This was previously observed by Shi et al [46] in the case of Cu-Zn/SiO_2 samples and could be ascribed to the interaction between the two metals. According to thermodynamic calculations performed by Jung et al [47], part

of ZnO could be reduced by forming alloy with Cu in the temperature range 250-350 °C in CO or methanol environment. A schematic model of the Cu-Zn alloy formation in the temperature range 120-600 °C in CO/H_2 gas mixture was proposed by Grunwaldt et al [48]. But in none of these papers, the structure of Cu-Zn alloy was identified. Derrouiche et al [17] showed that Cu_3Zn alloy was obtained after reduction of Cu/ZnO at 350 °C. Based on the TPR data and the study of Derrouiche et al [17], the temperature of 350 °C was selected for the sample reduction in this study to favor alloy formation.

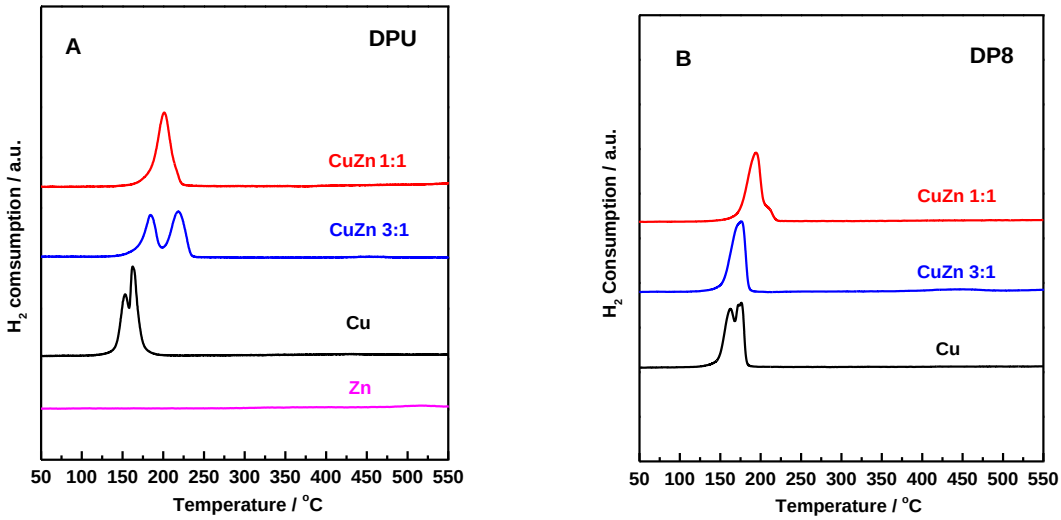

Figure 4-4: TPR of calcined copper, zinc and copper-zinc catalysts supported on TiO_2: A, DPu samples; B, DP8 samples; TPR of calcined DPu Zn/TiO_2 is also presented.

3.5 XRD study of calcined and reduced Cu-Zn/TiO_2 catalysts

The X-ray diffraction patterns of the DPu and DP8 samples calcined then reduced at 350 °C are presented in Figure 4-5. Metallic copper (JCPDS# 70-3038) is detected in the monometallic DPu Cu/TiO_2 sample, indicating that Cu^0 was not fully reoxidized in air. The formation of a Cu_3Zn alloy (JCPDS# 65-6567) is revealed in the DPu CuZn 1:1/TiO_2 sample (Figure 4-5A). For the DPu CuZn 3:1/TiO_2 sample, a peak located between metallic Cu and Cu_3Zn alloy (Figure 4-5A) is clearly observed. From the crystal lattice (i.e. 3.6403 Å) calculated using the Bragg's law, the composition of this "intermediate" Cu-Zn alloy (i.e. $Cu_{0.9}Zn_{0.1}$) could be estimated according to the Vegard's law. Moreover, Pearson et al. [49] confirmed that the crystal lattice distance varies linearly with the Cu-Zn alloy composition when the Zn content is lower than 40% in the alloy particle. The crystallite sizes evaluated using Scherrer's equation are 20, 25 and 18 nm for the DPu Cu, CuZn 3:1/TiO_2 and CuZn

1:1/TiO_2, respectively. In the case of the DP8 catalysts (Figure 4-5B), no diffraction peak of metallic Cu or Cu-Zn alloy was observed, whatever the sample, which indicates the presence of small crystallites.

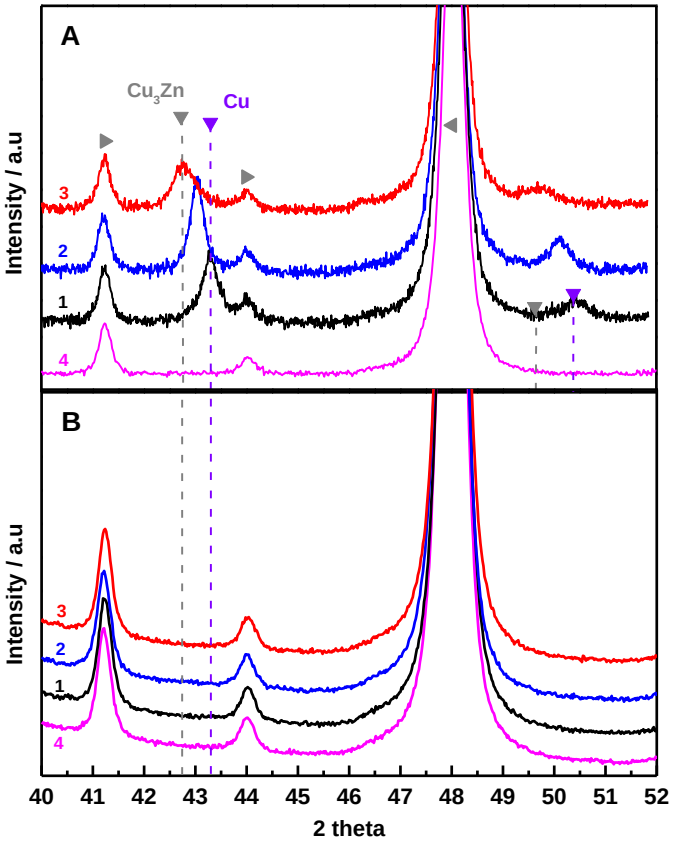

Figure 4-5: XRD diagrams of the calcined-reduced DPu (A) and DP8 (B) samples: 1, Cu/TiO_2; 2, CuZn 3:1/TiO_2; 3, CuZn 1:1/TiO_2 and 4, bare TiO_2 support. ► Anatase TiO_2 (JCPDS: 01-084-1286); ◄ Rutile TiO_2 (JCPDS: 01-086-0147); Cu_3Zn alloy peak position from JCPDS: 03-065-6567; metallic Cu peak position from JCPDS: 01-070-3038.

3.6 UV-Visible study of calcined then reduced Cu-Zn/TiO_2 catalysts

The UV-Visible spectra of the DPu and DP8 samples after calcination at 400 ^oC then reduction at 350 ^oC are shown in Figures 4-6A,B. A broad band centred at 710 nm is observed in the Cu/TiO_2 sample (spectra 1), whatever the preparation method. It belongs to the Cu(II) d-d transition. Moreover, combined with the XRD of reduced DPu Cu/TiO_2 that indicated the presence of Cu^0 in the sample, it can be concluded that part of metallic Cu has been reoxidized in air, which is in agreement with a former study [8]. After adding Zn in DPu and DP8 Cu-Zn samples, the absorption band appears at lower wavelength (spectra 2 and 3 in Figures 4-6A,B). The band at 590 nm for the CuZn 1:1 sample may correspond to the

plasmon band of metallic Cu modified by the presence of Zn since Cu^0 plasmon band is expected around 570 nm [50-52] (spectra 2 and 3 in Figures 4-6A,B). This result suggests that the addition of Zn to Cu prevents metallic Cu from deep oxidation in air owing to the probable formation of Cu-Zn alloys.

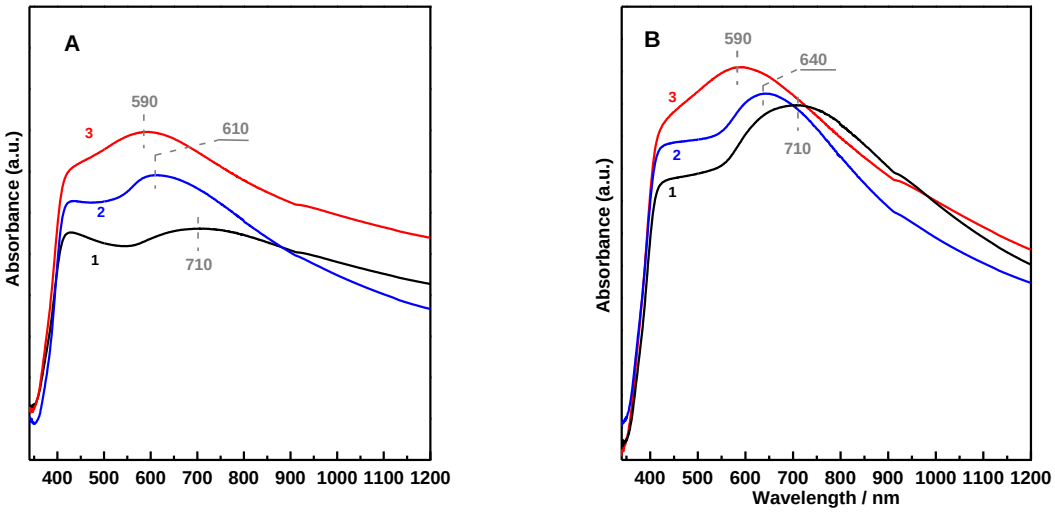

Figure 4-6: UV-visible spectra of the calcined-reduced DPu (A) and DP8 (B) samples: 1, Cu/TiO_2; 2, CuZn 3:1/TiO_2; 3, CuZn 1:1/TiO_2;

3.7 STEM-HAADF study of calcined Cu-Zn/TiO_2 catalysts

STEM-HAADF was performed on the different samples after calcination at 400 ^oC then reduction at 350 ^oC, and the resulting images and the particle size distribution are presented in Figure 4-7. Small particles are visible in the Cu and Cu-Zn DPu samples (Figure 4-7a-c). The estimated average particle sizes are 3, 2.1 and 1.8 nm for DPu Cu/TiO_2, CuZn 3:1/TiO_2 and CuZn 1:1 /TiO_2 samples (Table 4-3), respectively. These results are in contradiction with the much larger sizes previously estimated from the XRD diagrams of Cu/TiO_2, CuZn 3:1/TiO_2 and CuZn 1:1/TiO_2 (Figure 4-5A). This would mean that the DPu samples contain heterogeneous particle size distribution with the presence of small and large particles. The images obtained for the DP8 Cu and CuZn 1:1/TiO_2 samples are shown in Figure 4-7d, e. The visible particles are well dispersed with narrow particle size dispersion and average size of 1.9 and 2.1 nm for Cu and CuZn 1:1/TiO_2, respectively. Only few large particles (~5 nm) were observed in the STEM-HAADF images. As no diffraction peak of metallic Cu and Cu-Zn alloy was visible in the XRD data (Figure 4-5B), it can be deduced

that the metallic Cu or Cu-Zn alloy particles in the DP8 samples have rather small and uniform size.

3.8 EDS study of calcined Cu-Zn/TiO_2 catalysts

The EDS measurements were performed on particles with size range below 5 nm, and the results presented in Figure 4-8a-c show that the small particles visible in the TEM images of DPu samples are Cu in Cu/TiO_2, and Cu-Zn alloys in the CuZn 3:1 and CuZn 1:1/TiO_2 samples. Interestingly, the EDS analysis of DPu CuZn 3:1/TiO_2 (Figure 4-8b) shows that there is a clear localization of the Cu element in the nanoparticles, while, the Zn element seems to be present both in the nanoparticle and around it. Moreover, the EDS spectra shows that the concentration ratios (C_{Cu}/C_{Zn}) for a dozen particles in this sample are in the range from 4 to 16 with an average value close to 9, which agrees with the Cu-Zn alloy composition estimated by XRD ($Cu_{0.9}Zn_{0.1}$). The C_{Cu}/C_{Zn} ratios are in the range from 2 to 4 in a dozen particles of the DPu CuZn 1:1/TiO_2 sample (Figure 4-8c), resulting in an average ratio around 3 in accordance with the Cu_3Zn alloy evidenced by XRD. At this point, we can conclude that the small particles observed by STEM-HAADF in the bimetallic DPu samples possess on average the same composition as the one evidenced by XRD ($Cu_{0.9}Zn_{0.1}$ for CuZn 3:1/TiO_2 and Cu_3Zn alloy for CuZn 1:1/TiO_2). For DP8 samples, the Zn element cannot be detected in the very small particles (~2 nm) of DP8 CuZn 1:1/TiO_2 sample (Figure 4-8e). However, one larger particle (~5 nm) in DP8 CuZn 1:1/TiO_2 sample was examined by EDS (Figure 4-8f) resulting in a C_{Cu}/C_{Zn} ratio around 5. At this stage, we can only assume that the small particles in DP8 Cu-Zn/TiO_2 samples are bimetallic Cu-Zn particles although their composition, which can be variable, could not be determined.

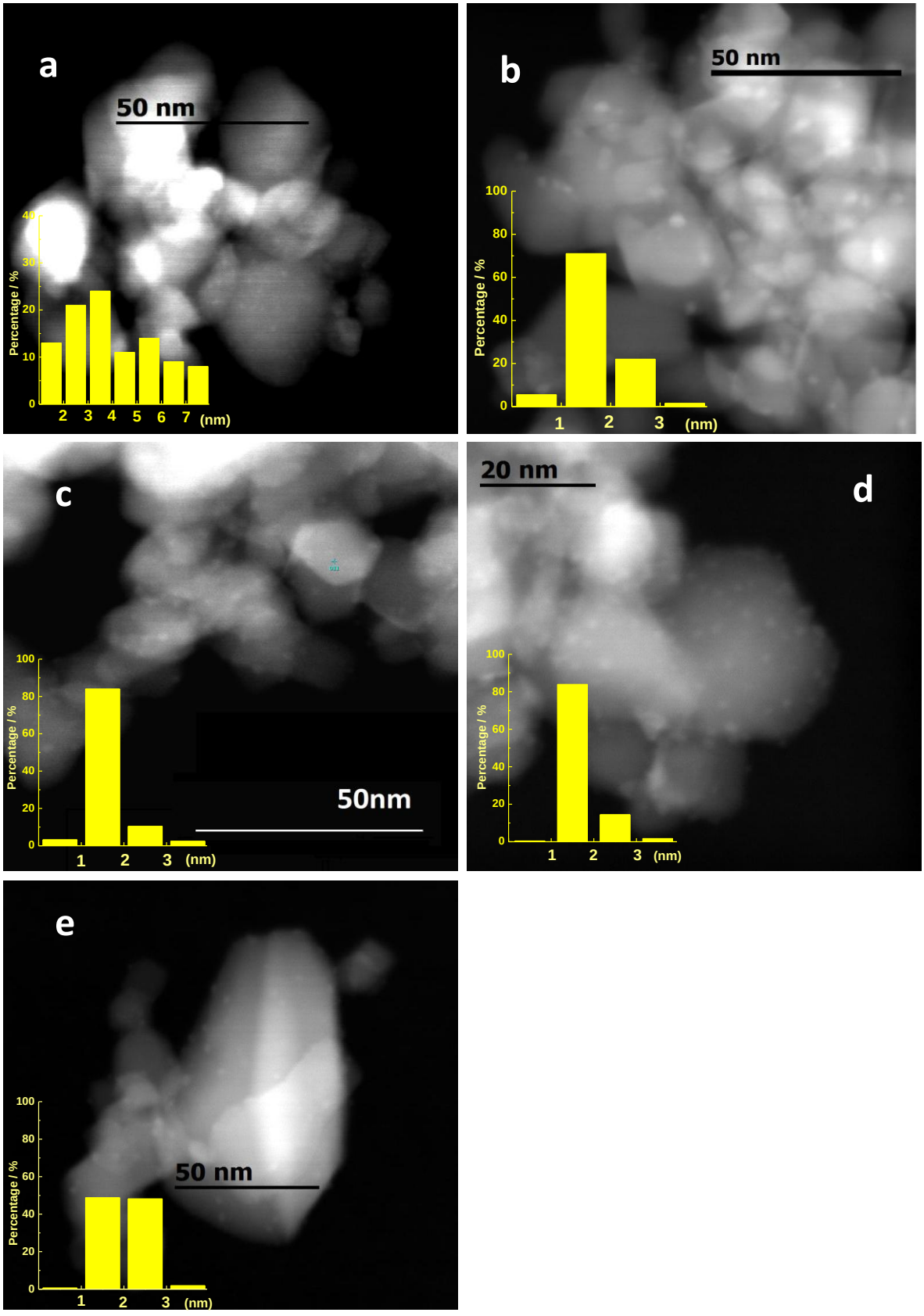

Figure 4-7: STEM-HAADF images of the calcined-reduced DPu and DP8 samples with the particle size distribution: a, DPu Cu/TiO_2; b, DPu CuZn 3:1/TiO_2; c, DPu CuZn 1:1/TiO_2; d, DP8 Cu/TiO_2; e, DP8 CuZn 1:1/TiO_2

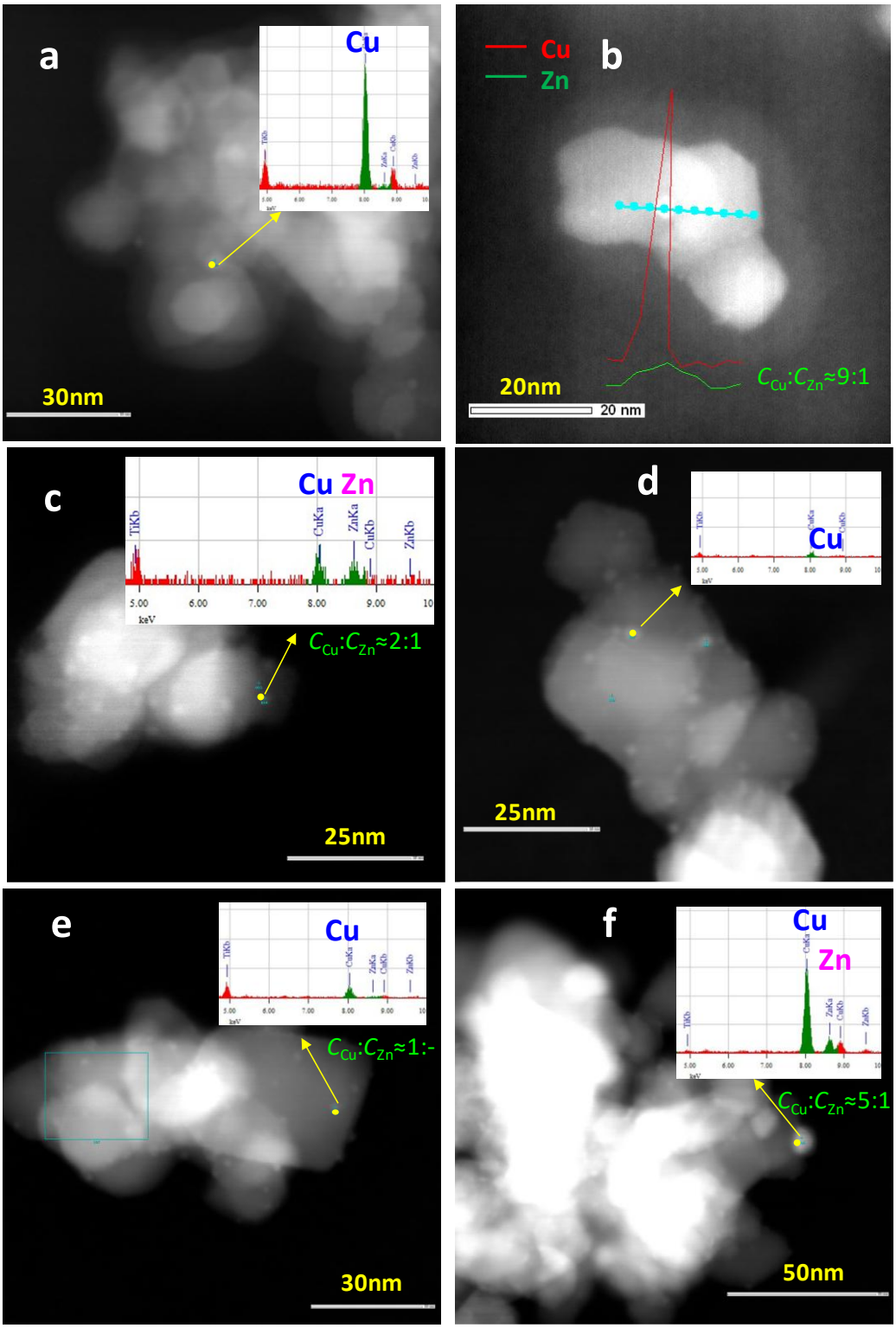

Figure 4-8: EDS analysis of some particles in the calcined-reduced DPu and DP8 samples: a, DPu Cu/TiO_2; b, DPu CuZn 3:1/TiO_2; c, DPu CuZn 1:1/TiO_2; d, DP8 Cu/TiO_2; e, DP8 CuZn 1:1/TiO_2; f, large particle analysis in DP8 CuZn 1:1/TiO_2

3.9 XPS of ex-situ calcined then reduced mono Cu/TiO_2 and bimetallic $Cu\text{-}Zn/TiO_2$ catalysts

After reduction under H_2 at 350 ^oC for 2 h, the oxidation state of supported Cu and Zn were studied by XPS after that the samples were transferred in air into the XPS equipment. The XPS spectra shown in Figure 4-9A indeed show the partial re-oxidation of copper during air exposure, since peaks of Cu^{2+} (BE~934.0 ± 0.2 eV) and of Cu^0 (BE~932.0 ± 0.2 eV) are present for DPu Cu/TiO_2 and CuZn 1:1/TiO_2 samples. Moreover, it is found that the XPS intensity ratio of Cu^{2+} to Cu^0 (I_{Cu2+}/I_{Cu0}) in CuZn 1:1/TiO_2 sample is higher than that in the Cu/TiO_2 sample, this could mean that metallic Cu in the CuZn 1:1/TiO_2 sample (Cu_3Zn alloy phase) is less stable upon air exposure than that in the Cu/TiO_2 sample (Cu phase), which is not consistent with the UV-visible results (Figure 4-3C, D). However, these differences can also result from different time of exposure to air for the CuZn 1:1/TiO_2 and Cu/TiO_2 samples before XPS characterization, as they were reduced in H_2 sequentially with a gap of time longer than 24 h. Regarding the oxidation state of Zn, the Auger spectrum of Zn LMM (Figure 4-9B) indicates that both Zn^{2+} (~498.1 ± 0.2 eV) and metallic Zn^0 (~495.0 ± 0.5 eV) are present in DPu bimetallic CuZn 1:1/TiO_2 sample with $I_{Zn2+} >> I_{Zn0}$. It is known that Zn^{2+} is the main oxidation state for Zn in the reduced bimetallic CuZn 1:1/TiO_2 as only 1/3 of Zn present in the sample is involved in the Cu_3Zn alloy phase formed in this sample, thus 2/3 of Zn remains on TiO_2, and TPR showed that Zn on TiO_2 does not reduce at 350 °C (TPR of Zn/TiO_2 in Figure 4-4A). In addition, it is possible that at least part of the metallic Zn alloyed with Cu was re-oxidized after air exposure. The fact that contributions of metallic Cu and metallic Zn could be observed in spite of the air contact is in accord with the XRD and EDS analyses that revealed the presence of bimetallic particles after reduction under H_2 at 350 °C.

Moreover, the effect of the addition of Zn to Cu on the electronic property of metallic Cu can be studied by the analysis of the binding energies (BE) of XPS Cu2p and Auger of Zn LMM peaks in the monometallic Cu/TiO_2 and bimetallic CuZn 1:1/TiO_2 samples (Figure 4-9). The binding energy of metallic Cu in DPu mono Cu/TiO_2 (~932.0 ± 0.2 eV) is similar to the BE (~931.9 ± 0.2 eV) in the CuZn 1:1/TiO_2 sample. The binding energy of metallic Zn^0 in the DPu CuZn 1:1/TiO_2 shows a weak peak located at ~495.0 ± 0.5 eV, which does not show big difference from the standard value (494.6 eV). As a result, even though DFT calculation performed by Wiame et al [53] proposed the existence of a charge transfer between the Cu and Zn atoms in $Cu_{0.7}Zn_{0.3}$ brass with a calculated charge of - 0.07 e on Cu

atoms and of + 0.19 e on Zn atoms, the difference observed for the XPS Cu2p peak and the Auger Zn LMM peak are too small to allow us to conclude that a charge transfer exists between Cu and Zn in DPu CuZn 1:1/TiO_2 sample.

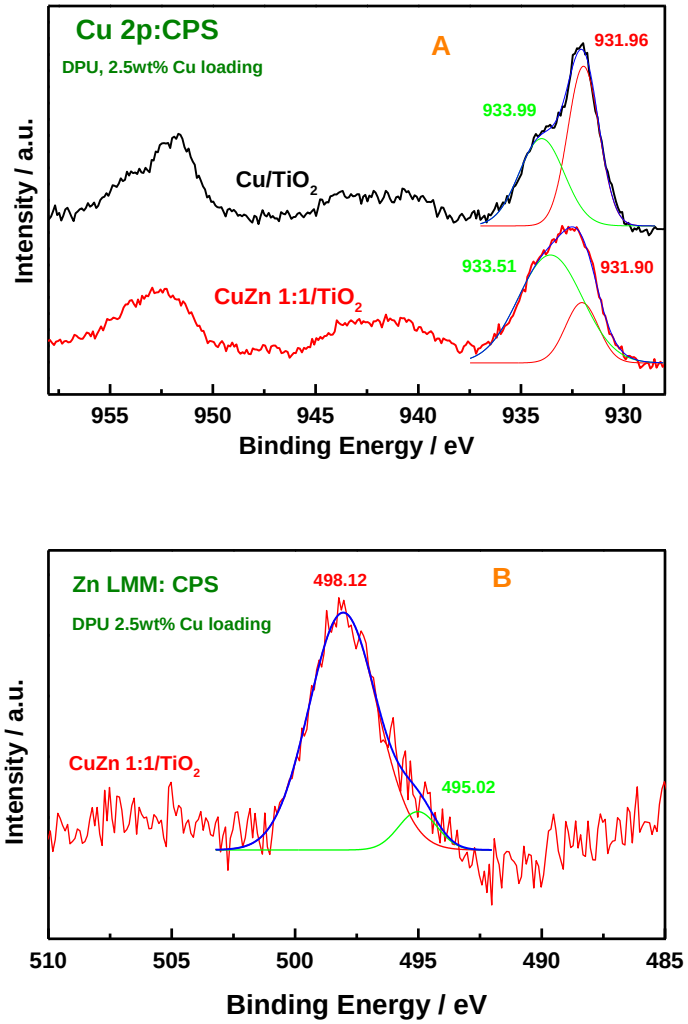

Figure 4-9: A, XPS of Cu 2p level for ex-situ calcined then reduced DPu 2.5wt% Cu, Cu/TiO_2 and CuZn 1:1/TiO_2; B, Auger spectrum of Zn LMM in CuZn 1:1/TiO_2.

4. Catalytic results – Butadiene selective hydrogenation

The catalytic performances of the DPu and DP8 samples are depicted in Figure 4-10 for the temperature programmed reaction (TP-Reaction).

Table 4-3: Catalytic properties of DPu and DP8 samples

Method	Catalyst	Average metal particle size (nm, based on TEM)	Dispersion (based on TEM)	Activity at 60 °C ($\mu mol_{butadiene}$ s^{-1} g_{Cu})	TOF at 60°C ($\times 10^{-4}$ s^{-1} based on TEM)	1-butene : Trans-2-butene : Cis-2-butene at 20-30% butadiene conversion (%)
DPu	Cu	3	0.35	27.1	49.8	83 : 7 : 10
	CuZn 3:1	2.1	0.5	4.2	6	88 : 6 : 6
	CuZn 1:1	1.8	0.58	1	1.5	76 : 5 : 18
DP8	Cu	1.9	0.55	27.8	32.4	87 : 5 : 8
	CuZn 3:1	-	-	9.2	-	89 : 3 : 8
	CuZn 1:1	2.1	0.5	2.9	4.9	80 : 8 : 12

The monometallic Cu/TiO_2 catalysts are the most active, with a temperature of full conversion of butadiene ($T_{100\%}$) of 75 °C, whatever the preparation method, whereas the Zn/TiO_2 catalyst does not present any activity in the temperature range 30-150 °C (Figure 4-10A). The introduction of zinc induces a decrease in the activity with respect to the Cu catalysts, i.e., a higher $T_{100\%}$ (up to 120 °C for DPu CuZn 1:1/TiO_2), which increases with the Zn loading. The DP8 Cu-Zn/TiO_2 samples present higher activity than the corresponding DPu catalysts. This can be explained by the smaller particle sizes observed by XRD and STEM-HAADF for the DP8 catalysts compared to the bimodal size distribution in DPu ones. The activity ($\mu mol_{butadiene}$ s^{-1} g_{Cu}^{-1}) and TOF (s^{-1}) of DPu and DP8 samples at 60 °C reported in Table 4-3 confirm the trends previously described. Note that the TOF values were calculated from the average particle sizes estimated from STEM-HAADF, which does not take into account the bimodal size distribution existing for DPu samples. This results in an underestimation of the TOF for the latter catalysts. Nevertheless, the difference in catalytic performances between the DPu and DP8 samples shows that the catalysts with smaller and more homogeneous particle sizes result in higher activity, which clearly reflects a size effect. This may be assigned to the presence of higher proportion of low coordination sites (corners and edges) for lower particles sizes which are considered as the active sites for H_2 dissociation for Au, Ag or Cu metal particles as underlined in a recent review [54].

Concerning the selectivities, the alkenes (butenes and propene, which have similar reactivity) conversion into alkanes (butane and propane) is still low (below 2%) on the all range of temperature (30-150 °C) for the DPu and DP8 Cu/TiO_2 samples (Figure 4-10C). Whatever the preparation method, the bimetallic catalysts are fully selective to alkenes at temperatures below $T_{100\%}$ (Figure 4-10B, C), and less than 1% of alkenes are converted into alkanes at $T_{100\%}$ for all the Cu-Zn/TiO_2 catalysts. The selectivities to the various butene isomers for the DPu and DP8 samples are summarized in Table 4-3 at butadiene conversion of 20 to 30% and shows similar butenes distribution with 1-butene as the main product. In contrast with the monometallic Cu samples, the conversion of alkenes to alkanes on Cu-Zn bimetallic catalysts increases with temperature. The high selectivity of the Cu/TiO_2 catalysts to alkenes on the whole range of temperature (Figure 4-10B, C) might be related to a gradual deactivation of the samples during the slow heating ramp, as discussed later.

The catalytic stability was studied either at $T_{100\%}$ of each sample (Figure 4-11A) or at the same temperature (105 ^{o}C) for all the catalysts (Figure 4-11B). In both cases, a rapid loss of activity is observed for the Cu/TiO_2 catalysts, whatever the preparation method, with a decrease in conversion of about 85 to 95% during the first 5 hours of reaction. The presence of Zn in the catalysts induces a clear improvement of the stability, with slower rates of deactivation for the CuZn 3:1/TiO_2 and CuZn 1:1/TiO_2 samples. Moreover, the higher the Zn loading, the slower the deactivation of the bimetallic DPu and DP8 catalysts; the DPu and DP8 CuZn 1:1/TiO_2 catalysts maintain high butadiene conversion (above 70%) after 20 h at $T_{100\%}$, and the DP8 Cu-Zn/TiO_2 samples exhibit a lower deactivation slope than the DPu samples (Figure 4-11A). When compared at the same reaction temperature of 105 °C (Figure 4-11B), the DP8 CuZn 1:1/TiO_2 shows the highest stability, the DPu CuZn 1:1/TiO_2 deactivates at a slower rate than the DP8 and DPu CuZn 3:1/TiO_2 (Figure 4-11B).

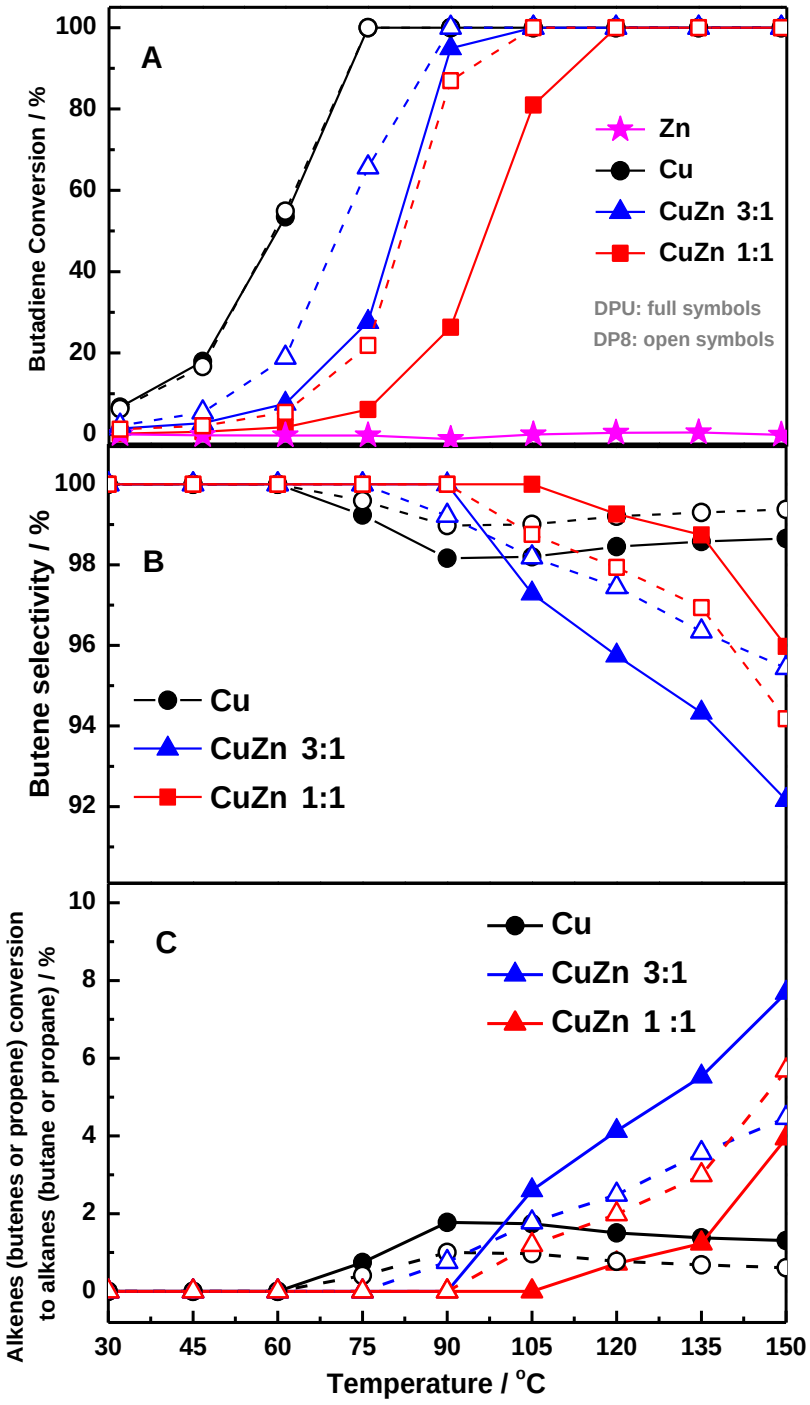

Figure 4-10: Evolution of the butadiene conversion (A), the selectivity to butenes (1-butene + cis-2-butene + trans-2-butene) (B) and the alkenes conversion to alkanes (butane and propane) (C) as a function of the reaction temperature for reduced monometallic Cu/TiO_2, Zn/TiO_2 and bimetallic $Cu\text{-}Zn/TiO_2$ samples prepared by different methods (100 mg of catalyst). (Full symbols for DPu samples, open symbols for DP8 samples)

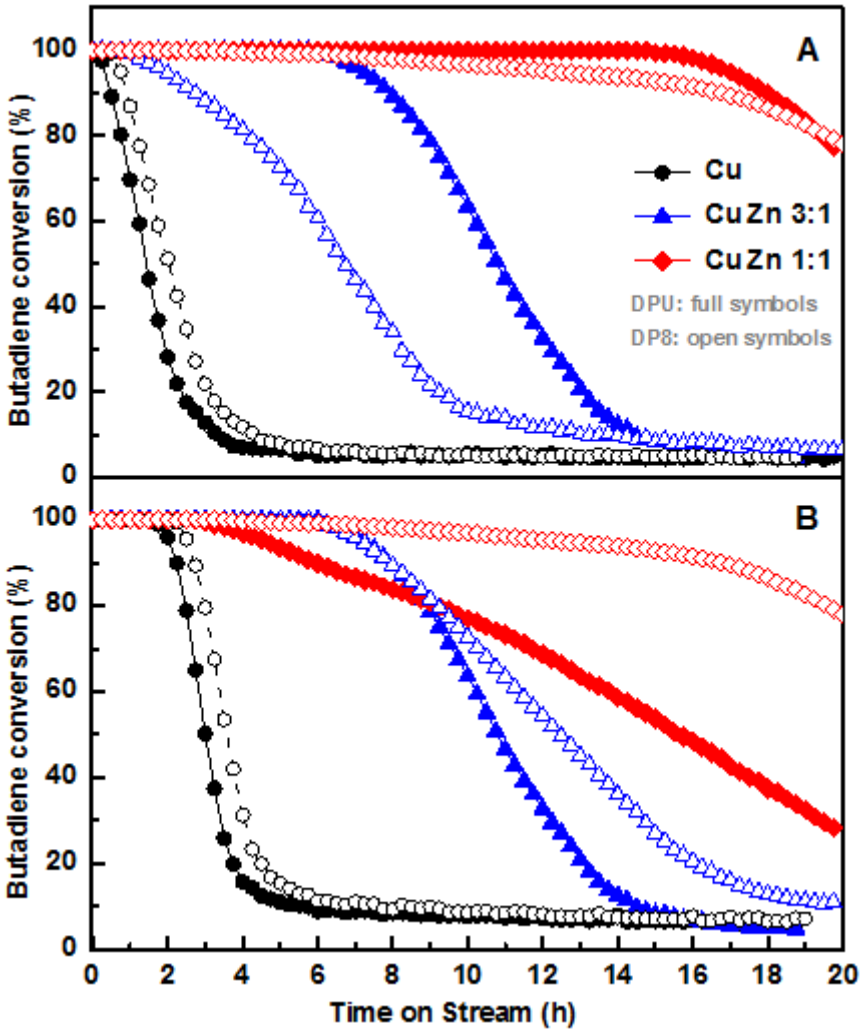

Figure 4-11: Evolution of the conversion of butadiene with time on stream (A) at $T_{100\%}$ (75 °C for DPu and DP8 Cu/TiO_2, 90 °C for DP8 CuZn 3:1/TiO_2, 105 °C for DPu CuZn 3:1/TiO_2 and DP8 CuZn 1:1/TiO_2 and 120 °C for DPu CuZn 1:1/TiO_2) and (B) at 105 °C for the various DPu and DP8 catalysts. (Full symbols for DPu samples, open symbols for DP8 samples)

It has been previously reported that copper catalysts suffer from strong deactivation during reactions of alkyne and alkadiene hydrogenation because of the formation of oligomeric compounds (green oil) [8, 55-58] at moderate reaction temperature. For instance, the formation of large amount of coke and oligomeric compounds was observed in Cu/Al_2O_3 catalyst exposed to acetylene/H_2 mixture at 250 °C [59]. In our reaction conditions, the deactivation of the Cu/TiO_2 catalyst occurs either in the presence or in the absence of propene (30%) in the reaction feed, although with a slightly slower rate in the absence of propene (not shown). This seems to indicate that both reactants, butadiene and propene, are involved in the deactivation process. It was found above that the addition of zinc strongly improves the stability of the copper based catalysts in butadiene hydrogenation. Enhanced activity for supported composite Cu-ZnO catalysts has been widely reported for methanol synthesis,

methanol steam reforming and water-gas shift reactions by comparison with Cu supported on Al_2O_3 [13, 14, 60, 61]. Among several explanations, the formation of a Cu-Zn alloy was frequently claimed as a possible cause for the enhancement of activity [11, 13, 61, 62]. Moreover, in the case of Al_2O_3-supported Pd catalysts, the introduction of Zn was reported to limit carbonaceous formation during selective hydrogenation of acetylene [63]. However, the beneficial effect of Zn was ascribed to the reduction of the number of acidic sites on the alumina surface by the presence of ZnO rather than to the formation of a Pd-Zn alloy. It is worth to mention that the composition of the Cu-Zn alloys determined by XRD and EDS reveals that only a fraction of zinc was alloyed with copper, implying that an another fraction was still present on the support surface under an unidentified form, as the presence of ZnO was not evidenced.

The thermogravimetric (TG) analysis of the samples after stability test at 105 ^{o}C for 20 h was performed under air up to 450°C. Figure 4-12 shows a weight loss in all of the samples, but it is weaker on the Cu-Zn/TiO_2 samples than on monometallic Cu/TiO_2. Around 2.5%, 1.25% and 0.47% mass was lost for the DPu Cu/TiO_2, CuZn 3:1/TiO_2 and CuZn 1:1/TiO_2 samples and 2.6%, 1.75% and 0.5% mass for the DP8 Cu/TiO_2, CuZn 3:1/TiO_2 and CuZn 1:1/TiO_2 samples, respectively. The loss weight mainly occurs between 200 and 350 °C, in the same temperature range as the one observed after selective hydrogenation of acetylene over Cu/SiO_2 [64]. In the latter study, the weight loss was mainly attributed to the oxidation or decomposition of the foulant or green oil i.e., C6 to C10 olefinic and aromatic compounds that accumulated on the catalytic surface during hydrogenation run, while the weight change from the oxidation of copper becomes negligible. Even though the bimetallic catalysts have relative smaller (DPu samples) or similar particle size (DP8 samples) to the corresponding metallic Cu based samples (bimodal size distribution in the DPu sample, and uniform small particle size in DP8 sample), the formation of Cu-Zn alloy particles seem to limit the formation of the oligomers resulting in higher catalytic stability than metallic Cu.

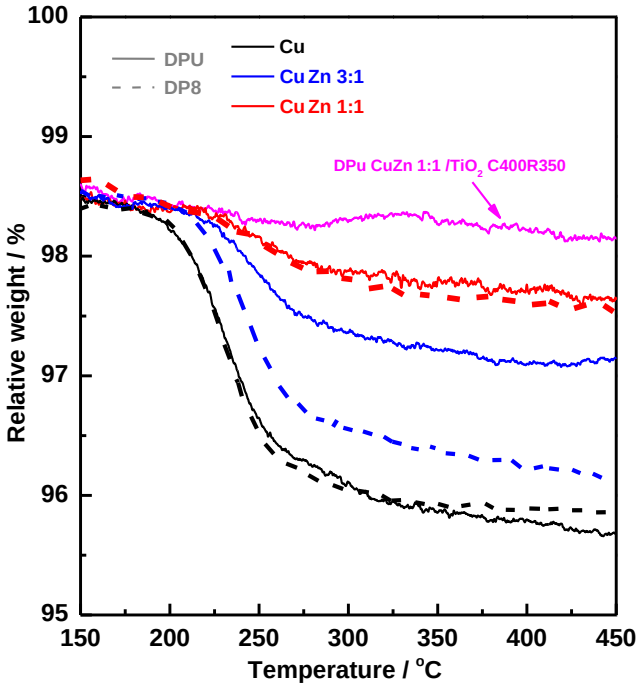

Figure 4-12: TG analysis of the DPu and DP8 samples after 20 h stability test at 105 °C. The freshly reduced DPu CuZn 1:1/TiO_2 was taken as a reference.

In the case of the supported Cu-Zn catalysts, with Cu atoms replaced by Zn ones, the formation of Cu-Zn alloy might change the surface geometry of Cu crystal resulting in a decrease of the Cu surface ensemble. Jung et al [47] observed that the copper surface area decreased after alloying with zinc. Since the Zn/TiO_2 catalyst has no activity in the reaction condition, it is reasonable that the introduction of Zn leads to a decrease in the catalytic activity. Besides that, the change in the surface composition could also induce changes in the adsorption mode or strength of the reactants and/or products of the reaction and thus in the formation of the oligomers species responsible for the deactivation. Indeed, it was recently shown that the incorporation of Zn into Ni catalysts to form Ni-Zn alloy resulted in a reduction in carbon-carbon bond formation (oligomerization reaction) during the hydrogenation of acetylene [65]. This was assigned to a decrease in the adsorption energy and resultant coverage of acetylene on Ni-Zn catalysts [65]. The positive role of Zn was also ascribed, in modeling studies [9], to changes in adsorption properties of the reactants resulting from changes in the electronic properties of Ni in the surface by alloying with Zn. The same effect might apply to the case of the Cu-Zn system, although the XPS results for the ex-situ reduced Cu-Zn/TiO_2 sample (Figure 4-9) did not clearly evidence any electronic modification

of Cu by the existing Zn in the sample, contrary to what was proposed in a recent article based on DFT calculations, referring to the existence of a charge transfer between the Cu and Zn atoms in $Cu_{0.7}Zn_{0.3}$ alloy [53].

In the case of bimetallic Cu-Ni systems, DFT calculations showed that the isolated Cu-Ni sites showed larger coupling barriers for C-C bond formation than for pure Ni or Cu, which allowed improving the resistance to oligomers formation during propyne hydrogenation [66]. The isolation of the active sites was also proposed to play an important role for avoiding undesired side reactions for other intermetallic compounds, such as oligomerization, which requires a sufficiently short distance between the coadsorbed hydrocarbon molecules [67]. A similar geometric effect might take place in the case of our bimetallic Cu-Zn catalysts.

Apart from the fraction of zinc that is alloyed with copper may inhibit green oil formation and deactivation, the residual zinc on the TiO_2 surface may also modify the acidic properties of the support surface. The acidic surface site concentrations on the DPu samples were evaluated by NH_3-TPD experiments. The amount of NH_3 that desorbed from TiO_2 surface was monitored by mass spectrometry with the results shown in Figure 4-13A. The acidic site concentration on the bare TiO_2 support surface is 0.36 $mmol_{NH3}\, g_{sample}^{-1}$ (Figure 4-13B). It decreased to 0.26 $mmol_{NH3}\, g_{sample}^{-1}$, when 2.5 wt% Cu was deposited on its surface, and it is still decreasing when Zn was present into the samples, 0.22 and 0.18 $mmol_{NH3}\, g_{sample}^{-1}$ for the CuZn 3:1/TiO_2 and CuZn 1:1/TiO_2 samples, respectively. As the acidic sites on the support surface could adsorb hydrocarbons and provoke not only isomerisation but also transformation into coke or C_2-C_6 hydrocarbons from cracking and disproportionation reactions [68, 69], the decrease in the number of acidic sites on TiO_2 surface could also account for the more stable catalytic performances of Cu-Zn/TiO_2 samples.

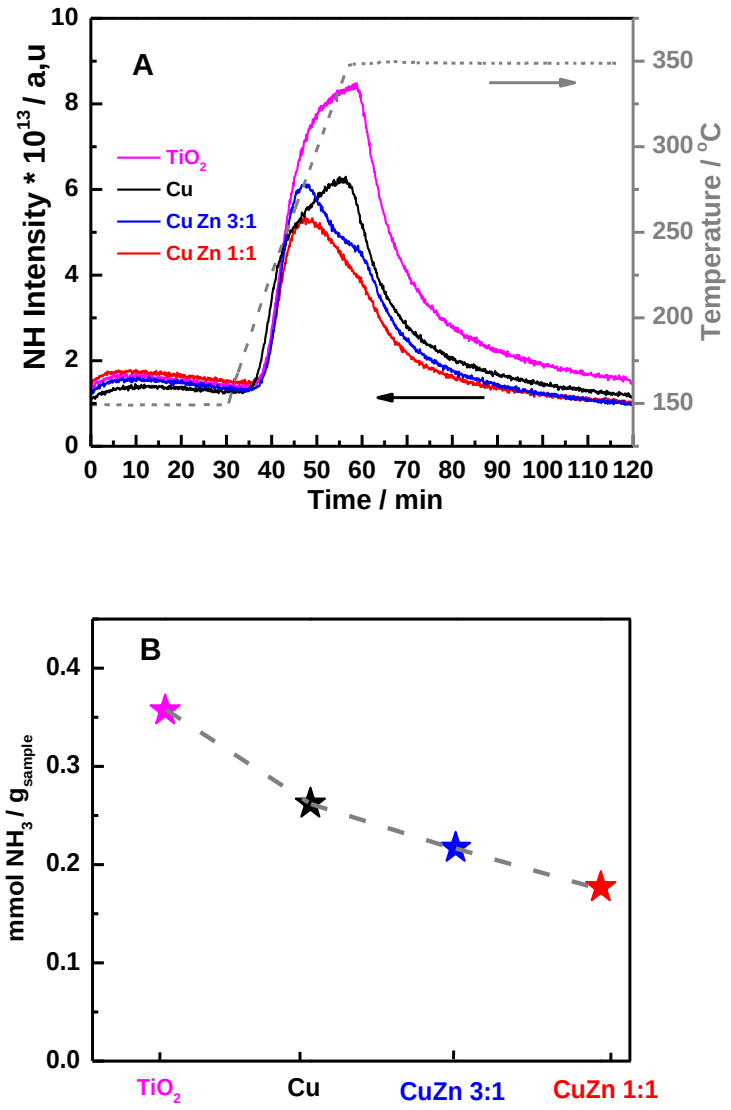

Figure 4-13: NH_3 temperature programmed desorption (TPD) profiles for the bare TiO_2 support and the DPu Cu, CuZn 3:1 and CuZn 1:1/TiO_2 samples after calcination at 400 °C and reduction at 350 °C: (A) mass spectrometer signal intensity of NH fragment (m/z=15) and (B) amount of NH_3 desorbed calculated from the mass spectrometer results.

During the stability test at 105°C, a peculiar behaviour was noticed for the DPu and DP8 CuZn 1:1/TiO_2 catalysts. While a continuous decrease was observed for the butadiene conversion with time on stream, the propene conversion after a progressive decrease during the first hours of reaction increased again between 8 and 15 hours of reaction for DPu and DP8 CuZn 1:1/TiO_2, respectively (Figure 4-14). Then, the propene conversion passed through a maximum before starting to decrease again. Such a behaviour was not observed for the Cu/TiO_2 and CuZn 3:1/TiO_2 catalysts up to 20 h of reaction, whatever the preparation method. In order to interpret such a behaviour, the DPu CuZn 1:1/TiO_2 was characterized

after different reaction times at 105 °C using XRD. From the diffractograms, it is found that a change in the copper-zinc alloy composition from Cu_3Zn after reduction at 350 °C (brown line) towards $Cu_{0.7}Zn_{0.3}$ (JCPDS file 03-065-9062) after reaction at 105 °C (pink line) occurred (Figure 4-15A). The transformation of the copper-zinc alloy starts after 8 hours of reaction, as attested by the shift of the position of the alloy peak compared to the initial Cu_3Zn phase (blue line), and seems to be complete after 12 hours of reaction i.e., at the reaction time corresponding to the maximum of propene conversion (Figure 4-14, blue line). It is worth to note that the Cu_3Zn phase is preserved after exposure to H_2 at 105 °C for 12 h (red line in Figure 4-15A), underling the fact that hydrocarbons (butadiene and/or propene) reactants or products are required to generate the change in the alloy composition. The change in composition corresponds either to enrichment in Zn or to depletion in Cu of the alloy (Cu/Zn atomic ratio decreasing from 3 to about 2.3). An additional experiment was performed on a DPu CuZn 1:1/TiO_2 after calcination then reduction at 280 ^oC instead of 350 ^oC. In this case, metallic Cu was formed after reduction as attested by XRD (Figure 4-15B), but after reaction at 105 ^oC for 20 h, a slight shift of the main (111) peak of Cu^o from 43.24 to 43.09° was observed, which could indicate that the Zn diffusion into the Cu lattice occurred under the reaction atmosphere (Figure 4-15B). This observation would support the assumption of an enrichment in Zn of the Cu_3Zn alloy rather than a depletion in Cu during the reaction of the sample reduced at 350 °C.

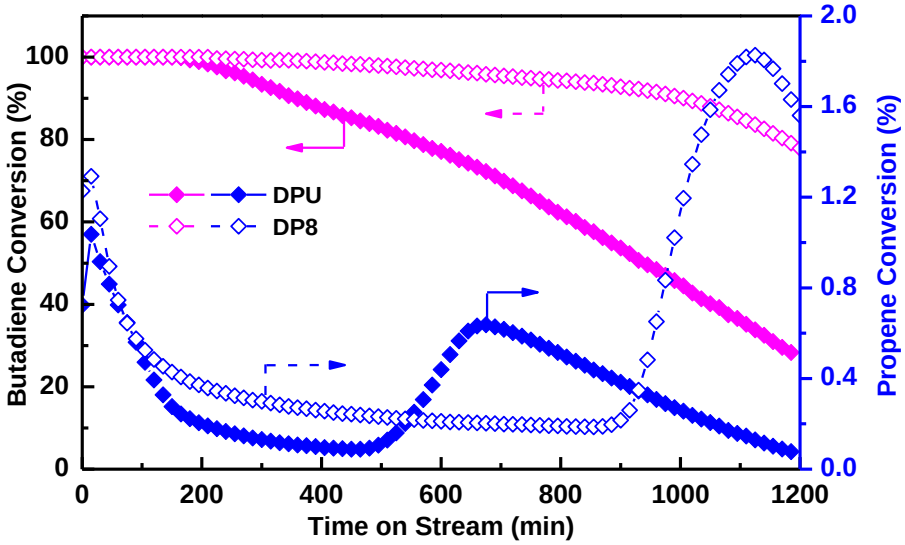

Figure 4-14: Evolution of the conversion of butadiene and propene with time on stream at 105 °C for the DPu and DP8 CuZn 1:1/TiO_2 catalysts.

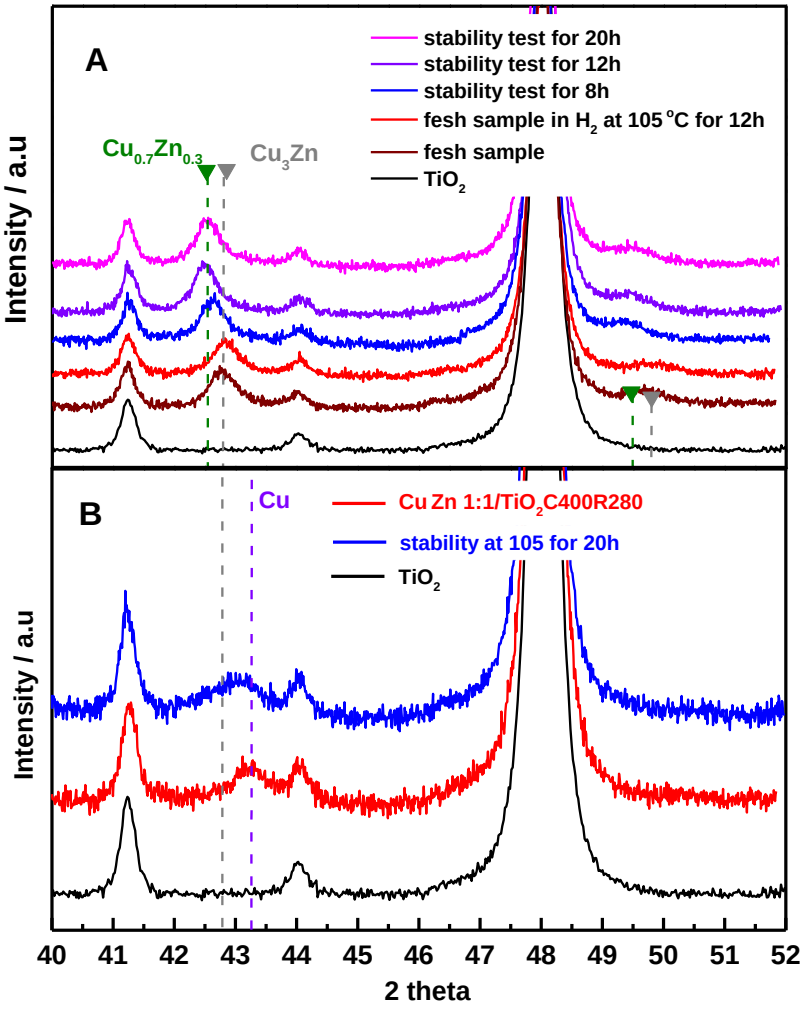

Figure 4-15: XRD diagrams of (A) the DPu CuZn 1:1/TiO_2 catalyst after calcination then reduction at 350 °C (labeled fresh sample) and after various stages of the reaction at 105 °C; $Cu_{0.7}Zn_{0.3}$ alloy peak position from JCPDS: 03-065-9062; (B) the DPu CuZn 1:1/TiO_2 catalyst after calcination then reduction at 280 °C and stability test at 105 °C for 20h.

Besides that, an additional regeneration experiment was also proposed for the bimetallic Cu-Zn/TiO_2 samples, with using a used DP8 CuZn 1:1/TiO_2 sample as an example. The regeneration procedural as follows: after catalytic stability test at 105 ^{o}C for 20 h, the catalysts are regenerated by in situ calcination at 400 ^{o}C for 2 h with heating rate 5 ^{o}C min^{-1} then in situ reduction at 350 ^{o}C for 2 h with heating rate 2 ^{o}C min^{-1}. After this thermal treatment, the catalytic stability at 105 ^{o}C was performed on the used DP8 CuZn 1:1 catalyst. In Figure 4-16, the initial butadiene conversion is around 90%. The catalyst deactivates in the first 8 h of reaction (butadiene conversion decreased to ~68%), then re-activates in the following 27 h (butadiene conversion went back to ~90%). After that, the catalytic activity decreases again to 72% at the end of this experiment (65 h).

Compare with the catalytic performance of fresh DP8 CuZn 1:1/TiO_2 (Figure 4-14), the regenerated catalyst shows slightly lower initial catalytic activity (butadiene conversion ~90%, instead of 100%). Besides that, similar to the fresh DP8 CuZn 1:1/TiO_2, the concentration of each product (e.g., propane) evolves during the stability test, which underlines again the dynamic character of the bimetallic CuZn system. These results might not indicate that the CuZn bimetallic catalysts are suitable for direct application in purification of alkene streams but the aim of this work is first and foremost fundamental and explorative and is only intended to demonstrate the potential for using base metals for such applications. Besides that, the dynamic of bimetallic Cu-Zn system during catalytic reaction also indicates that such Cu-Zn bimetallic systems are complex, with several possible phases and compositions existing or co-existing, thus, extensive additional studies are clearly required to foresee any possible long-term catalytic implementation.

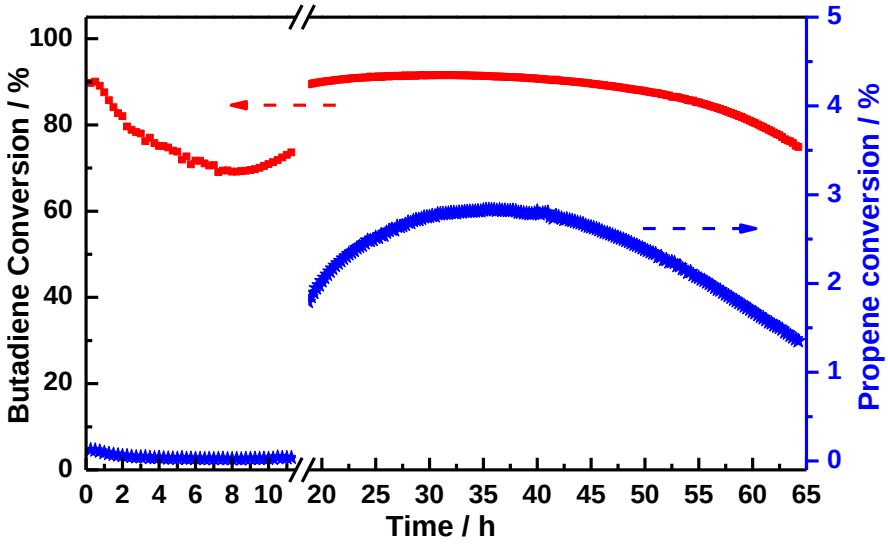

Figure 4-16: catalytic stability test of the regenerated DP8 CuZn 1:1/TiO_2C400R350 at 105 ^{o}C for 65 h.

5. Conclusion

In this contribution, TiO_2-supported bimetallic Cu-Zn catalysts prepared by deposition precipitation with urea and deposition-precipitation at pH≈8, were studied in selective hydrogenation of butadiene. The formation of monometallic copper and copper-zinc alloy nanoparticles was evaluated by XRD and STEM-HAADF coupled with EDS analysis, two different particle size ranges (~3 nm and >15 nm) were found in the DPu samples, while

smaller particles with uniform particle size (~2 nm) were obtained using the deposition-precipitation at fixed pH method. Cu_3Zn alloy and a Cu-rich alloy ($Cu_{0.9}Zn_{0.1}$) were formed in DPu CuZn 1:1/TiO_2 and CuZn 3:1/TiO_2 samples, respectively, indicating also that part of the Zn present in the samples was not involved in the formation of alloys. The performances of the bimetallic Cu-Zn/TiO_2 catalysts in the selectivity hydrogenation of butadiene demonstrated that such non-noble systems have high potential for this type of reaction as they present only slightly lower activity at moderate temperature, similar selectivity to alkenes and enhanced stability compared to monometallic Cu/TiO_2. Besides that, the DP8 Cu-Zn samples show similar selectivities to alkenes but higher activity and more stable catalytic performances than the DPu Cu-Zn ones, which could result from the presence of smaller Cu-Zn bimetallic particles with uniformed particle sizes in DP8 samples. A decrease of the size of the Cu ensemble at the surface of the nanoparticles due to alloying with zinc and of the acidic properties of the TiO_2 surface by the residual zinc seems to result in the lowering of the fouling by carbonaceous species, leading to higher stability of the bimetallic catalysts.

Interestingly, the dynamic behavior of the Cu-Zn alloy structure was evidenced by a change in the composition of the alloyed phase during the selective butadiene hydrogenation reaction, from Cu_3Zn to $Cu_{0.7}Zn_{0.3}$ alloy for the DPu CuZn 1:1/TiO_2 sample.

This explorative study is intended to demonstrate the potential for using base metals for application in selective hydrogenation reaction. The various results presented in this work show that such systems composed of bimetallic nanoparticles are complex, with several possible phases and compositions co-existing and evolving under reaction conditions. Thus, extensive additional studies are clearly required to foresee any possible long-term catalytic implementation.

6. References

1. J.W.Hightower, B.Furlong, A.Sarkany, L.Guczi, Studies in Surface Science and Catalysis, 75 (1993) 2305.
2. A.Sarkany, Applied Catalysis A: General, 165 (1997) 87.
3. I.Y.Ahn, J.H.Lee, S.K.Kim, S.H.Moon, Applied Catalysis A: General, 360 (2009) 38.
4. W. J.Kim, S.H. Moon, Catalysis Today, 185 (2012) 2.
5. Q.Zhanga, J.Li, X.Liu, Q.Zhu, Applied Catalysis A: General, 197 (2000) 221.
6. A.Pachulski, R. Schödel, P. Claus, Applied Catalysis A: General, 400 (2011) 14.
7. Y.Han, D.Peng, Z.Xu, H.Wan, S.Zheng, D.Zhu, Chemical Communications, 49 (2013) 8350.
8. L.Delannoy, G.Thrimurthulu, P.S. Reddy, C.Méthivier, J.Nelayah, B.M.Reddy, C.Ricolleau, C.Louis, Phys. Chem. Chem. Phys., 16 (2014) 26514.
9. F.Studt, F.Abild-Pedersen, T.Bligaard, R.Z. Sørensen, C.H. Christensen, J.K. Nørskov, Science, 320 (2008) 1320.
10. Y.Choi, K.Futagami, T.Fujitani, J.Nakamura, Applied Catalysis A: General, 208 (2001) 163.
11. J.Nakamura, T.Uchijima, Y.Kanai, T. Fujitani, Catalysis Today, 28 (1996) 223.
12. Y. Kanai, T. Watanabe, T. Fujitani, T. Uchijima, J. Nakamura, Catalysis letters, 38 (1996) 157.
13. M.Behrens, F.Studt, I.Kasatkin, S.Kühl, M.Hävecker, F.Abild-Pedersen, S.Zande, F.Girgsdies, P.Kurr, B.L.Kniep, M.Tovar, R.W. Fischer, J.K. Nørskov, R.Schlögl, Science, 336 (2012) 893.
14. T.Shishido, M.Yamamoto, D.Li, Y.Tian, H.Morioka, M.Honda, T.Sano, K.Takehir Applied Catalysis A: General, 303 (2006) 62.
15. M. Turcoa, G. Bagnascoa, U. Costantinob, F. Marmottinib, T. Montanaric, G. Ramisc, G. Buscac, Journal of catalysis, 228 (2004) 43.
16. Handbook, A., *Volume 3: Alloy phase diagrams.* ASM international, 1992: p. p.780.
17. S.Derrouiche, H. Lauron-Pernot, C. Louis, Chemistry of Materials, 24 (2012) 2282.
18. I.Atake, K.Nishida, D.Li, T.Shishido, Y.Oumi, T.Sano, K.Takehir, Journal of Molecular Catalysis A: Chemical, 275 (2007) 130.
19. J.A. van Dillen, J.W.G., L.A Hermans, J. van der Meijden, In "Proceedings of the 6th International Congress on Catalysis" London, 1976.

20. G. C. Bond, P.B.W., F.C. Tompkins, Ed., The Chemical Society: London, 1977: p. P 677.
21. J.W.E.Coenen, *Reduction of Silica Supported Nickel Catalysts*, in *Studies in Surface Science and Catalysis*, P.G.P.J. B. Delmon and G. Poncelet, Editors. 1979, Elsevier. p. 89-111.
22. C.Louis, *Deposition-Precipitation Synthesis of Supported Metal Catalysts.* ChemInform, 38 (2007).
23. J.Kragten, *Atlas of metal—ligand equilibria in aqueous solution*, 1979, Pergamon.
24. C.F. Baes, R.E. Mesmer, *The Hydrolysis of cations*. 1976: Wiley.
25. Y.I.Sal'nikov, Y.V. Sidorov, K.A. Burkov, Russian Journal of Applied Chemistry, 81 (2008) 1296.
26. C.Chouillet, F.Villain, M.Kermarec, H.Lauron-Pernot, C.Louis, The Journal of Physical Chemistry B, 107 (2003) 3565.
27. Z.Wang, D.Brouri, S.Casale, L.Delannoy, C.Louis. Journal of catalysis, 340 (2016) 95.
28. H.Iriea, S.Miura, K.Kamiya, K.Hashimoto, Chemical Physics Letters, 457 (2008) 202.
29. H.Irie, K.Kamiya, T.Shibanuma, S.Miura, D.A.Tryk, T.Yokoyama, K.Hashimoto, The Journal of Physical Chemistry C,113 (2009) 10761.
30. M.Liu, X.Qiu, M.Miyauchi, K.Hashimoto, Chemistry of Materials, 23 (2011) 5282.
31. I. Georgiadou, Ch. Papadopoulou, H. K. Matralis, G. A. Voyiatzis, A. Lycourghiotis, Ch. Kordulis, The Journal of Physical Chemistry B, 102 (1998) 8459.
32. P.Platanitis, G.D.Panagiotou, K.Bourikas, C.Kordulis, J.L.G. Fierro, A.Lycourghiotis, Journal of Molecular Catalysis A: Chemical, 412 (2016) 1.
33. H.Yu, H.Irie, Y.Shimodaira, Y.Hosogi, Y.Kuroda, M.Miyauchi, K.Hashimoto, The Journal of Physical Chemistry C, 114 (2010) 16481.
34. N.L.Dias Filho, Microchimica Acta, 130 (1999) 233.
35. T.Toupance, M. Kermarec, C. Louis, The Journal of Physical Chemistry B, 104 (2000) 965.
36. H.Praliaud, S.Mikhailenko, Z.Chajar, M.Primet, Applied Catalysis B: Environmental, 16 (1998) 359.
37. S.Derrouiche, H. Lauron-Pernot, C. Louis, Chemistry of Materials,24 (2012) 2282.
38. B.Yao, Y. Chan, N. Wang, Applied Physics Letters, 81 (2002) 757.
39. R.Kam, C.Selomulya, R.Amal, J.Scott, Journal of catalysis, 273 (2010) 73.

40. F.Arena, K.Barbera, G.Italiano, G.Bonura, L.Spadaro, F.Frusteri, Journal of catalysis, 249 (2007) 185.
41. T.Imoto, Y.Harano, Y.Nishi, S.Masuda, Bulletin of the Chemical Society of Japan, 37 (1964) 441.
42. S.Lew, A.F. Sarofim, M. Flytzani-Stephanopoulos, Chemical Engineering Science, 47 (1992) 1421.
43. M.Liang, W. Kang, K. Xie, Journal of Natural Gas Chemistry, 18 (2009) 110.
44. M.A. Valenzuelaa, P. Boschb, J. Jiménez-Becerrillc, O. Quiroza, A.I. Páez, Journal of Photochemistry and Photobiology A: Chemistry, 148 (2002) 177.
45. C.S.Chen, J.H.You, J.H.Lin, Y.Y.Chen, Catalysis Communications, 9 (2008) 2381.
46. X.Shi, Bull Korean Chem Soc, 35 (2014) 141.
47. K.D.Jung, O. S. Joo, S. H. Han, Catalysis letters, 68 (2000) 49.
48. J.-D.Grunwaldt, A.M.Molenbroek, N.-Y.Topsoe, H.Tposoe, B.S.Clausen, Journal of catalysis, 194 (2000) 452.
49. Pearson, W.B., *A handbook of lattice spacings and structures of metals and alloys*. 1967. p.601.
50. H.H.Huang, F.Q.Yan, Y.M.Kek, C.H.Chew, G.Q.Xu, W.Ji, P.S.Oh, S.H.Tang, Langmuir, 13 (1997) 172.
51. G.G.Condorelli, L.L.Costanzo, I.L.Fragalà, S.Giuffrida, G.Ventimiglia, Journal of Materials Chemistry, 13 (2003) 2409.
52. K.L. Kelly, K. Yamashita, The Journal of Physical Chemistry B, 110 (2006) 7743.
53. F.Wiame, M.M.Islam, B.Salgın, J.Świątowska, D.Costa, B.Diawara, V.Maurice, P.Marcus, Surface Science, 644 (2016) 148.
54. G.Vilé, D.Albani, N.Almora-Barrios, N.Lopez, J.Perez-Ramirez, ChemCatChem, 8 (2016) 21.
55. R.A.Koeppel, J.T.Wehrli, M.S.Wainwright, D.L.Trimma, N.W.Cant, Applied Catalysis A: General, 120 (1994) 163.
56. J.T. Wehrli, D.J. Thomas, M.S. Wainwright, D.L. Trimm, Applied Catalysis, 66(1990) 199.
57. N.J.Ossipoff, N.W. Cant, Journal of catalysis, 148 (1994) 125.
58. B.Bridier,D.Karhanek, J.Perez-Ramirez, N.lopez, ChemCatChem, 4 (2012) 1420.
59. G.Kyriakou, J.Kim, M.S.Tikhov, N.Macleod, R.M. Lambert, The Journal of Physical Chemistry B, 109 (2005) 10952.

60. D.Jingfa, S.Qi, Z. Yulong, C. Songying, W.Dong, Applied Catalysis A: General, 139 (1996) 75.
61. K.V.Bussche, G. Froment, Journal of catalysis, 161 (1996) 1.
62. T. Fujitani, J. Nakamura, Applied Catalysis A: General, 191 (2000) 111.
63. S.Chinayon, O.Mekasuwandumrong, P.Praserthdam, J.Panpranot, Catalysis Communications, 9 (2008) 2297.
64. M.R. Stammbach, D.J. Thomas, D.L. Trimm, M.S. Wainwright, Applied Catalysis, 58 (1990) 209.
65. C.S. Spanjers, J.T.Held, M.J.Jones, D.D.Stanley, R.S. Sim, M.J.Janik, R. M.Rioux, Journal of catalysis, 316 (2014) 164.
66. B.Bridier, N. López, J. Pérez-Ramírez, Dalton Transactions, 39 (2010) 8412.
67. M.Krajčí, J. Hafner, ChemCatChem, 8 (2016) 34.
68. P.Berteau, S. Ceckiewicz, B. Delmon, Applied Catalysis, 31 (1987) 361.
69. M.D.Argyle, C.H. Bartholomew, Catalysts, 5 (2015) 145.

Chapter 5: Synthesis of TiO_2 supported Ni-Zn bimetallic catalyst for selective hydrogenation of 1,3-butadiene in the presence of an excess of propene

Chapter 5: Synthesis of TiO_2 supported Ni-Zn bimetallic catalyst for selective hydrogenation of 1,3-butadiene in the presence of an excess of propene

1. Introduction

Through density functional theory calculations (DFT), Studt et al [1] predicted that Ni-Zn systems could be an interesting alternative to palladium ones. In addition, they also showed experimentally that the addition of Zn to $Ni/MgAl_2O_4$ resulted in a lower ethane formation than in monometallic $Ni/MgAl_2O_4$ during selective hydrogenation of acetylene, but the paper does not contain any information about the possible Ni-Zn alloy formation and the Ni-Zn catalysts stability. On the other hand, Spanjers et al [2] studied bulk intermetallic Ni-Zn compounds (Ni_4Zn, Ni_1Zn_1 and Ni_5Zn_{21} alloys) for selective acetylene hydrogenation in excess of ethylene, and also found that zinc inclusion into nickel catalysts could reduce the oligomerization reaction that resulted in a higher ethylene selectivity, but no catalytic activity and stability were reported in the paper. Thus, the type of supported Ni-Zn nanoalloy formed after reduction and the catalytic properties of supported Ni-Zn nanoalloy for alkyne or alkadiene selective hydrogenation need to be further studied.

The study of the catalytic properties of the 0.5 wt% Ni/TiO_2 catalysts in Section 5 of Chapter 3 indicated that metallic Ni is very active with 100% butadiene conversion at RT even after catalyst dilution, rather highly selective to butenes (Figure 3-23, in Chapter 3), but low catalytic stability for butadiene selective hydrogenation. In comparison with Ni/TiO_2 (i.e., metallic Ni), 0.5 wt% Ni/ZnO catalysts, which formed Ni_1Zn_1 alloy particles after reduction at temperature higher than 280 ^oC, showed lower activity (higher $T_{100\%}$, but the particle size were also clearly much larger), similar selectivity to butenes and still lower stability. Similarly, another work on ZnO and SiO_2 supported Ni catalysts performed by Spanjers et al [3] for selective acetylene hydrogenation in excess of ethylene reaction also showed that Ni/ZnO catalysts containing supported Ni_4Zn_1 alloy and Ni_1Zn_1 alloy after sample reduction displayed a lower activity and selectivity to ethylene than Ni/SiO_2 (metallic Ni). These results are in disagreement with the results of the calculations performed by Studt et al. [1] mentioned above. Moreover, in the study about ZnO and SiO_2 supported Ni catalysts, Spanjers et al attributed the low activity and selectivity to ethylene of ZnO supported Ni-Zn

alloy to the oligomerization reaction occurring on the ZnO support and concluded that ZnO support has negative effect on ethylene selectivity. Thus, to go further in the study of the catalytic performance of supported Ni-Zn bimetallic catalysts, it was worth and reasonable to prepare bimetallic Ni-Zn catalysts supported on another oxide that ZnO. TiO_2 was chosen as it has a chemically inert surface [4].

Figure 5-1 shows the alloy phase diagram of bulk Ni-Zn system. There are four main Ni-Zn alloy phases, i.e., β, β_1, γ and δ. The β and β_1 phases are predominant when the Zn weight percentage is around 50% (Ni:Zn atomic ratio ~1:1), while, the γ phase appears at Zn content above 72%, and it changes to δ phase when the Zn weight percentage becomes higher than 90% in the bimetallic particles. The Ni:Zn ratio presented in the Ni-Zn alloy phase in Figure 5-1 suggests that it is better to study bimetallic Ni-Zn catalysts with initial Ni:Zn ratio lower than 1:1. Besides that, according to our Ni/ZnO study reported in Chapter 3, the XRD diagram of 5 wt% Ni/ZnO reduced at 350 °C (Figure 3-27) indicated that β_1-NiZn alloy (Ni_1Zn_1 alloy) was the main bimetallic phase present in the sample.

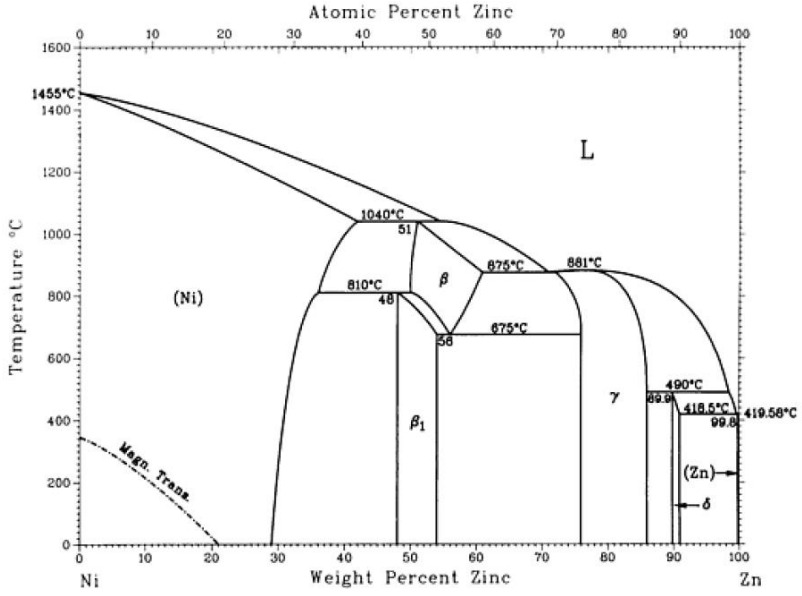

Ni-Zn crystallographic data

Phase	Composition, wt% Zn	Pearson symbol	Space group
(Ni)	0 to 41.9	*cF*4	$Fm\bar{3}m$
β	50.0 to 60.9	*cP*2	$Pm\bar{3}m$
β_1	48.0 to 54.5	*tP*2	*P*4/*mmm*
γ[a]	72 to 86	*cI*52	$I\bar{4}3m$
δ	~90	*mC*6	*C*2/*m*
(Zn)	**100**	***hP*2**	$P6_3/mmc$

Figure 5-1: Alloy phase diagram of Ni-Zn system (left), Ni-Zn crystallographic data (right) [5]

In this chapter, TiO_2 supported bimetallic NiZn catalysts with NiZn ratio of 1:0, 1:1, 1:3 and 1:5 were prepared by deposition-precipitation with urea (DPu) and deposition-precipitation at fixed pH (DP8) as in the case of Cu-Zn/TiO_2 in Chapter 4 (see also Section 2 of Chapter 2), and the catalytic performances (including activity, selectivity and stability)

were evaluated in the selective hydrogenation of butadiene in the presence of an excess of propene. Specific attention was paid to the characterization of the composition of Ni-Zn nanoalloy particles. This chapter will describe:

- The deposition behavior of Ni and Zn on titania as a function of pH and time during bimetallic Ni-Zn preparation by DPu and DP8;
- The effect of the addition of Zn on the reduction behavior of supported Ni;
- The characterization of Ni-Zn nanoalloy after sample calcination and reduction by XRD and STEM-HAADF coupled with EDS techniques;
- The influence of alloying Ni with Zn on the catalytic activity, selectivity and stability performances for the butadiene selective hydrogenation reaction;

2. Catalysts preparation

Monometallic Ni/TiO_2 and bimetallic $Ni\text{-}Zn/TiO_2$ catalysts were prepared using the method of deposition-precipitation with urea (DPu) as described in Section 2 of Chapter 2, so as to reach a nickel loading of 0.5 or 2.5 wt%. Briefly, after filling a double wall reactor with 300 ml distilled water, then adding 3 g of supports (TiO_2 P25 Evonik, 50 $m^2\ g^{-1}$), the reactor was heated to 80 ^oC by water heating system. Then, the appropriate amount of $Ni(NO_3)_2 \cdot 6H_2O$ and/or $Zn(NO_3)_2 \cdot 6H_2O$ precursors were added into the reactor to achieve the desired nominal nickel and zinc loadings (i.e., 0.5 or 2.5 wt% Ni loading with Ni:Zn atomic ratios of 1:0, 1:1, 1:3 and 1:5). Meanwhile, urea was added to achieve a urea to metal molar ratio of ca. 100. After that, the mixture was kept at 80 °C in a closed reactor for 20 h under continuous stirring. Finally, the solid samples were separated from the liquid by centrifugation and subsequently washed with distilled water and centrifuged (three times). All of the samples were further dried under vacuum at room temperature (RT) for 24 h (as-prepared sample).

The procedure for sample preparation by deposition-precipitation at a fixed pH of 8 (see Section 3 of Chapter 2) is as follows: 3 g of TiO_2 support was dispersed into 250 mL distilled water in beaker at room temperature, and the pH of TiO_2 suspension was adjusted to ~8 using 0.5 M NaOH solution. A 50 mL aqueous solution containing appropriate amounts of $Ni(NO_3)_2 \cdot 6H_2O$ and/or $Zn(NO_3)_2 \cdot 6H_2O$ precursors, corresponding to 0.5 or 2.5 wt% Ni loading with the desired Ni:Zn atomic ratio of 1:0, 1:1 and 1:3, was added into the TiO_2 solution in 30 min. During the injection of the Ni/Zn aqueous solution, the pH of the mixture

was kept at ~8 by addition of 0.5 M NaOH solution. After stirring for 4 h, the solid samples were collected by centrifugation and subsequently washed with distilled water and centrifuged (three times) and dried under vacuum at room temperature (RT) for 24 h.

The kinetics of Ni^{2+} and Zn^{2+} deposition during sample preparation by DPu and DP8 were studied by extracting the solid powder from 30-40 mL of suspension out of the reactor at different pHs (DPu) or time (DP8) during the preparation followed by washing, centrifugation and drying under vacuum at RT.

Before characterization or catalytic reaction, the catalysts were calcined at 400 °C for 2 h after sample heating with a rate of 5 °C min^{-1}, under flowing air (100 mL min^{-1}) then reduced at a plateau of 450 °C for 2 h with a heating rate of 3 °C min^{-1}, under flowing pure H_2 (100 mL min^{-1}).

3. Results and discussion

3.1 Deposition behaviour of Ni^{2+} and Zn^{2+} onto TiO_2 during sample preparation

During DPu preparation of Ni-Zn/TiO_2 with a nominal loading of 2.5 wt% Ni and 2.5 wt% Zn, i.e., a Ni:Zn ratio =1:1, the pH of the suspension increases gradually and uniformly at 80 ^oC as the result of urea decomposition [6]. As a consequence, the evolution of the nickel and zinc loadings with pHs was explored for nominal metals loadings of 2.5 wt%. Figure 5-2A shows that Zn^{2+} ions deposition occurs at pH lower than for Ni^{2+} ions. Zn^{2+} deposition mainly occurs at pH between 4.5 and 6.5, while the Ni^{2+} deposition seems to start at pH around 5.5 and to become significant at pH above 6.0. This sequential deposition could be explained by the lower solubility of $Zn(OH)_2$ (4.1×10^{-17}) than that of $Ni(OH)_2$ (5.5×10^{-16}) at room temperature [7].

For the sample prepared by deposition-precipitation at pH 8 at room temperature, Figure 5-2B shows that Ni and Zn ions were simultaneously deposited on the TiO_2 surface. The Ni and Zn loadings on TiO_2 were around 1.8 wt% for each, after 30 min of stirring, which may correspond to the limitation of the adsorption capacity of TiO_2 surface. Based on the density of $TiO^{-0.35}$ (i.e., ~5.5 site nm^{-2}) and $Ti_2O^{-0.6}$ (i.e., ~0.5 site nm^{-2}) at pH = 8 , given by Panagiotou et al [8], one can calculate that the total amount of negatively charged sites (i.e., 9×10^{20} in 3 g TiO_2) roughly corresponds to the loading of 1.8 wt% Ni and Zn ions. Then the

metal loadings increase during the following 3 h stirring may result from the deposition and nucleation growth. Finally, the metal loadings almost remain constant with extending reaction time in solution from 4 h to 20 h.

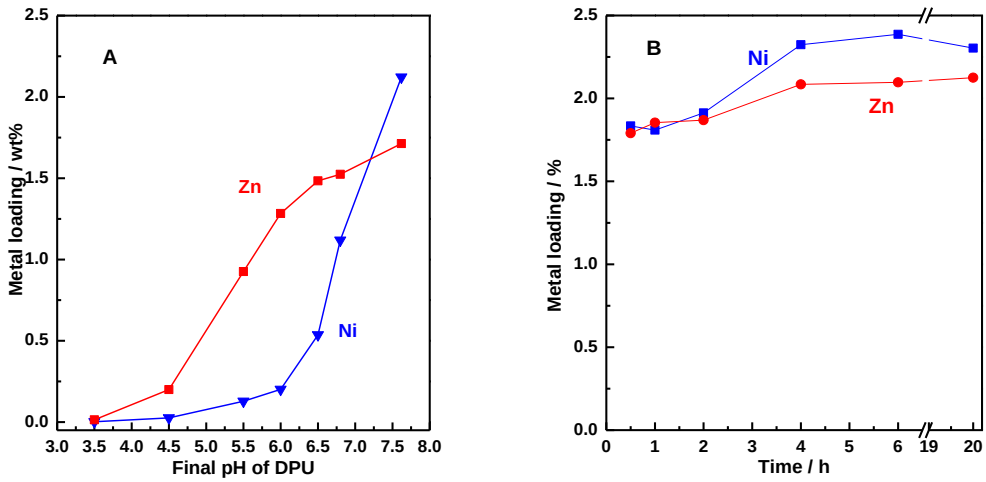

Figure 5-2: Preparation of Ni-Zn/TiO_2 catalysts with Ni:Zn ratio =1:1 and nominal loadings: 2.5 wt% Ni and 2.5 wt% Zn: Evolution of the Ni and Zn loadings on titania versus pH during the DPu (A) and versus time during DP8 (B).

Considering the high catalytic activity of metallic Ni for the selective hydrogenation of butadiene, the Ni loading had to be lowered to 0.5 wt% in the catalysts for the catalytic tests. The metals loadings in the as-prepared Ni and Ni-Zn samples are summarized in Table 5-1, which shows that the final Ni loadings are close to the nominal ones. One can note that the Zn loadings were always lower than the nominal ones in both types of preparation, as also shown in Figure 5-2 for higher metal loadings. This might result from a systematic error arising from the XRF analyses as the membrane used in the sample holder for XRF analysis contains some zinc element.

Table 5-1: final metal loading in the Ni-Zn/TiO_2 samples with 0.5wt% nominal Ni loading prepared by DPu and DP8

Theoretical values			Experimental values					
Ni : Zn ratios	Normal loading / wt%		DPu		DP8		DPu	DP8
	Zn	Ni	Zn	Ni	Zn	Ni	Ni : Zn ratios	Ni : Zn ratios
1:0	-	0.5	-	0.54	-	0.56	-	-
1 :1	0.5	0.5	0.4	0.5	-	-	1 :0.8	-
1 :3	1.5	0.5	1.2	0.5	1.2	0.54	1 :2.4	1 :2.2
1 :5	2.5	0.5	2.0	0.55	-	-	1 :3.7	-

3.2 TPR of calcined 0.5wt% Ni-Zn/TiO_2 samples

The temperature chosen for the reduction of calcined Ni-Zn/TiO_2 derived from the results of temperature programmed reduction under H_2 (TPR-H_2) presented in Figure 5-3. For comparison, TPR of calcined DPu 0.5 wt% Zn/TiO_2 was also included in Figure 5-3 and shows no reduction peaks in the range 50-550 °C. The maximum temperature for TPR was set at 550 °C to avoid the contamination of the TPR equipment with volatile Zn^o [9-12]. For the DPu Ni/TiO_2 sample, two reduction peaks can be observed at ~400 ^oC and ~530 ^oC, similar to the previous TPR results on Ni/TiO_2 samples prepared by $[Ni(NH_3)_6]^{2+}$ adsorption [13]. In the case of DPu Ni-Zn/TiO_2 samples, the reduction temperatures shift to higher values with increasing Zn loading, leaving only the low reduction temperature peak visible. However, it seems that the increase of the reduction temperature of supported Ni^{2+} was not proportional to the amount of Zn in the sample as it decreased back to ~350 ^oC when ZnO was used as support (see Figure 3-26 in Chapter 3). To verify whether all the Ni^{2+} ions were reduced in the low reduction temperature range, the percentage of Ni^{2+} reduction in the first reduction peak of the sample was calculated by using the TPR of pristine NiO as a reference and the results are summarized in Table 5-2. It can be seen that almost all the Ni^{2+} species were reduced to metallic Ni in the first reduction temperature range. As a consequence, the high temperature range for Ni/TiO_2 probably corresponds to the reduction of TiO_2 support, and a similar result was observed by Geus et al [14] who found that the total hydrogen consumption was larger than necessary for full reduction of nickel ions by calculation when they carried TPR on Ni/TiO_2 sample up to 900 ^oC. The same trends can be observed for the DP8 samples, but they show higher reduction temperature (of about 50 °C) than the corresponding DPu ones. Based on Figure 5-3, a temperature of 450 ^oC with a 2 h-plateau at 450 ^oC was selected for sample reduction and activation before characterisation or catalytic reaction.

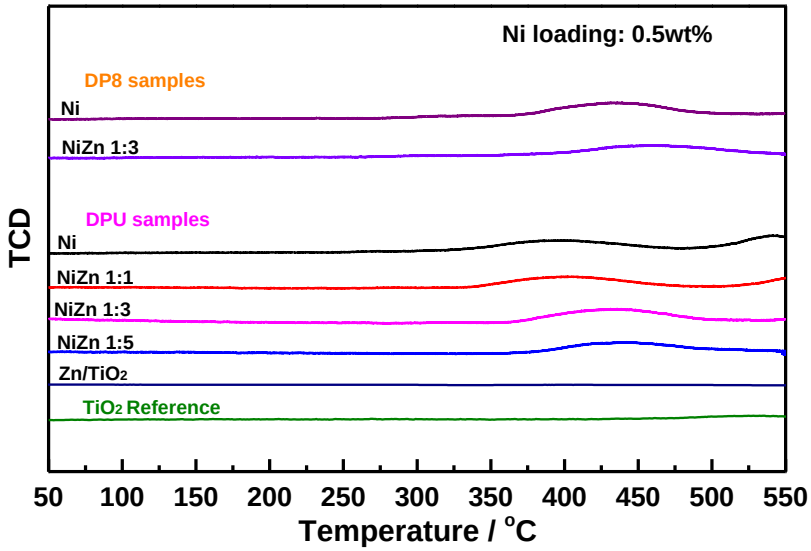

Figure 5-3: TPR of calcined nickel, zinc and nickel-zinc catalysts supported on TiO_2 prepared by DPu and DP8 method.

Table 5-2: Percentage of reduced Ni^{2+} calculated from the TPR

	Sample	Sample weight for TPR / mg	NiO weight / mg	integral area from TPR data	Reduced NiO calculated from TPR / mg	Percentage of reduced Ni^{2+}
Reference	**NiO**	**112.5**	**112.5**	**647.6**	**112.5**	**100%**
DPu	**Ni**	**113.5**	**0.78**	**3.72**	**0.65**	**83%**
	NiZn 1:1	**114.5**	**0.72**	**3.91**	**0.68**	**94.3%**
	NiZn 1:3	**110.6**	**0.70**	**4.47**	**0.78**	**111%**
	NiZn 1:5	**101.1**	**0.71**	**3.94**	**0.68**	**96.8%**
DP8	**Ni**	**103.3**	**0.71**	**4.30**	**0.75**	**105.3%**
	NiZn 1:3	**103.7**	**0.74**	**4.03**	**0.70**	**95%**

3.3 Thermal stability of Zn under H_2 atmosphere

Considering the fact that 450 °C is higher than the melting temperature of metallic Zn (~420 °C, see Figure 5-1), and that Zn content in the Ni-Zn alloy system influences the type of Ni-Zn alloy phase formation (Figure 5-1) after reduction, thus Zn loading in the sample was analyzed after sample reduction at 450 °C. Here, DPu NiZn/TiO_2 (2.5 wt% Ni) samples with NiZn ratios 1:3 and 1:5 were used as examples to study the zinc thermal stability after sample

reduction at 450 °C (Table 5-3). It can be seen that Zn is stable after sample reduction at 450 °C for 2 h.

Table 5-3: Zn loading in Ni-Zn/TiO_2 samples after calcination then reduction

DPu Sample	Nominal metal loading / wt%		As-prepared / wt%		C400R450 [a] /wt%	
NiZn 1:3	**2.5**	**7.5**	**2.1**	**5.7**	**2.2**	**5.7**
NiZn 1:5	**2.5**	**10**	**2.4**	**9.9**	**2.5**	**10.1**

a: C400R450: calcination at 400 °C then reduction at 450 °C for 2 h

3.4 XRD of calcined then reduced 0.5wt% Ni-Zn/TiO_2 samples

Figure 5-4 shows the XRD diagrams of DPu and DP8 0.5 wt% Ni-Zn/TiO_2 samples after calcination at 400 °C then reduction at 450 °C, as well as the one of the TiO_2 support as a reference. Only two samples, DPu Ni:Zn 1:5/TiO_2 and DP8 Ni:Zn 1:3/TiO_2, show an additional peak (~43.3°) to the ones of the support. According to the study of Ni/ZnO with 5 wt% Ni loading in Section 5 of Chapter 3, this peak could be assigned to the one of Ni-Zn alloy (~43.3° JCPDS card: # 72-2668), which correspond to β_1-NiZn alloy with ~50 at% Ni (i.e., Ni_1Zn_1 alloy) [15]. Using the Scherrer's equation, the Ni-Zn alloy crystallite sizes were estimated at 5.8 nm for the DPu Ni:Zn 1:5/TiO_2 and 8.7 nm for DP8 Ni:Zn 1:3/TiO_2. For the other Ni-Zn/TiO_2 samples, the crystallite size of metallic Ni or Ni-Zn alloy may be too small to be detected by XRD, or it could overlap with the broad TiO_2 peak at ~44°. Thus, the exact composition of the Ni-Zn alloy phase on the TiO_2 surface needs to be further identified.

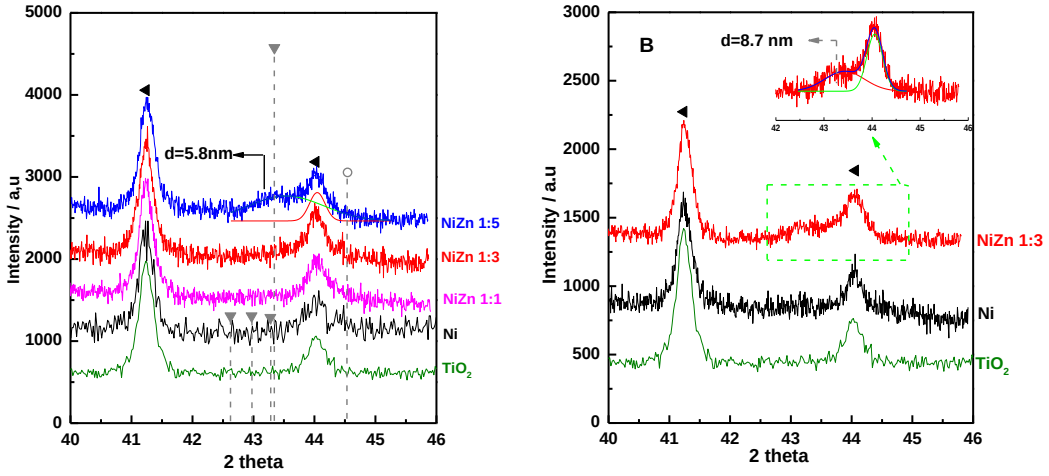

Figure 5-4: XRD diagrams of the calcined-reduced DPu (A) and DP8 (B) samples: 1, Ni/TiO_2; 2, NiZn 1:1/TiO_2; 3, NiZn 3:1/TiO_2 and 4, NiZn 5:1/TiO_2 and 5, bare TiO_2 support. ◀ Rutile TiO_2 (JCPDS: 01-086-0147); ▼NiZn alloy peak position from JCPDS: 01-072-2668; ○ metallic Ni peak position from JCPDS: 00-004-0850

3.5 STEM-HAADF coupled with EDS

The metal nanoparticles in the DPu and DP8 samples were imaged by STEM-HAADF after calcination at 400 ^{o}C then reduction at 450 ^{o}C (Figure 5-5). The average particle size deduced from the particle size distribution was also included in Table 5-4. For DPu 0.5 wt% Ni/TiO_2 sample (Figure 5-5A), small particles were visible with average particle size of ~3.7 nm. The metallic particle size increases when Zn is present in the samples. The average particle sizes are 3.8, 4.9 and 5.3 nm for the DPu Ni-Zn/TiO_2 with Ni:Zn 1:1, 1:3 and 1:5 samples, respectively. Besides the effect of alloying Ni with Zn on the particle size, the addition of Zn also broadens the size distribution in the DPu Ni-Zn/TiO_2 samples, from 1 to 6 nm for Ni:Zn 1:1 and from 1 to 9 nm for Ni:Zn 1:5 sample. The same phenomenon was also observed for the DP8 Ni:Zn 1:3/TiO_2 (6.5 nm) compared to DP8 Ni/TiO_2 (4.8 nm), and it seems that the DP8 method brings larger particle size after sample reduction than the DPu method.

Since Ni-Zn alloy formation was verified by XRD only for the DPu Ni:Zn 1:5/TiO_2 and DP8 Ni:Zn 1:3/TiO_2 samples, STEM-HAADF coupled with Energy Dispersive X-ray spectrometry (EDS) was performed on a series of individual particles in several bimetallic Ni-Zn/TiO_2 samples to determine the Ni:Zn atomic ratios as a function of the nanoparticle size and the Ni:Zn distribution. The results in Figure 5-6 first show that Ni-Zn alloys (or intermetallic Ni-Zn compounds) are formed in all the DPu and DP8 samples studied, and that the average Ni:Zn atomic ratios decrease with increasing Zn loading (from 12:1 in DPu Ni:Zn 1:1/TiO_2 to 1.8:1 in the DPu Ni:Zn 1:5/TiO_2 sample, Table 5-4). The preparation method does not seem to have an influence on the Ni:Zn atomic ratio as similar Ni:Zn atomic ratios were observed in DPu and DP8 Ni:Zn 1:1/TiO_2 samples (Table 5-4). It is worth to note that the composition of the Ni-Zn nanoparticles determined by EDS (Table 5-4) reveals that only a fraction of zinc present in the various samples was alloyed with nickel, implying that another fraction was still present on the support surface under an unidentified form, as the presence of ZnO was not evidenced by XRD (Figure 5-7). Figure 5-6 also shows that the Ni:Zn atomic ratio increases with the decrease of particle size for all the samples, however the lower amount of Zn content in the smaller particles (< 3 nm) may result in a lower accuracy of EDS analysis. Moreover, the EDS analysis reveals that the Ni:Zn atomic ratio (1.1:1) is close to 1 for the larger nanoparticles for DPu Ni:Zn 1:5/TiO_2 (~6 nm) and DP8 Ni:Zn 1:3/TiO_2 (~9

nm), which is in agreement with the presence of the β_1-NiZn (Ni_1Zn_1) alloy phase with ~50 at% Ni identified by XRD.

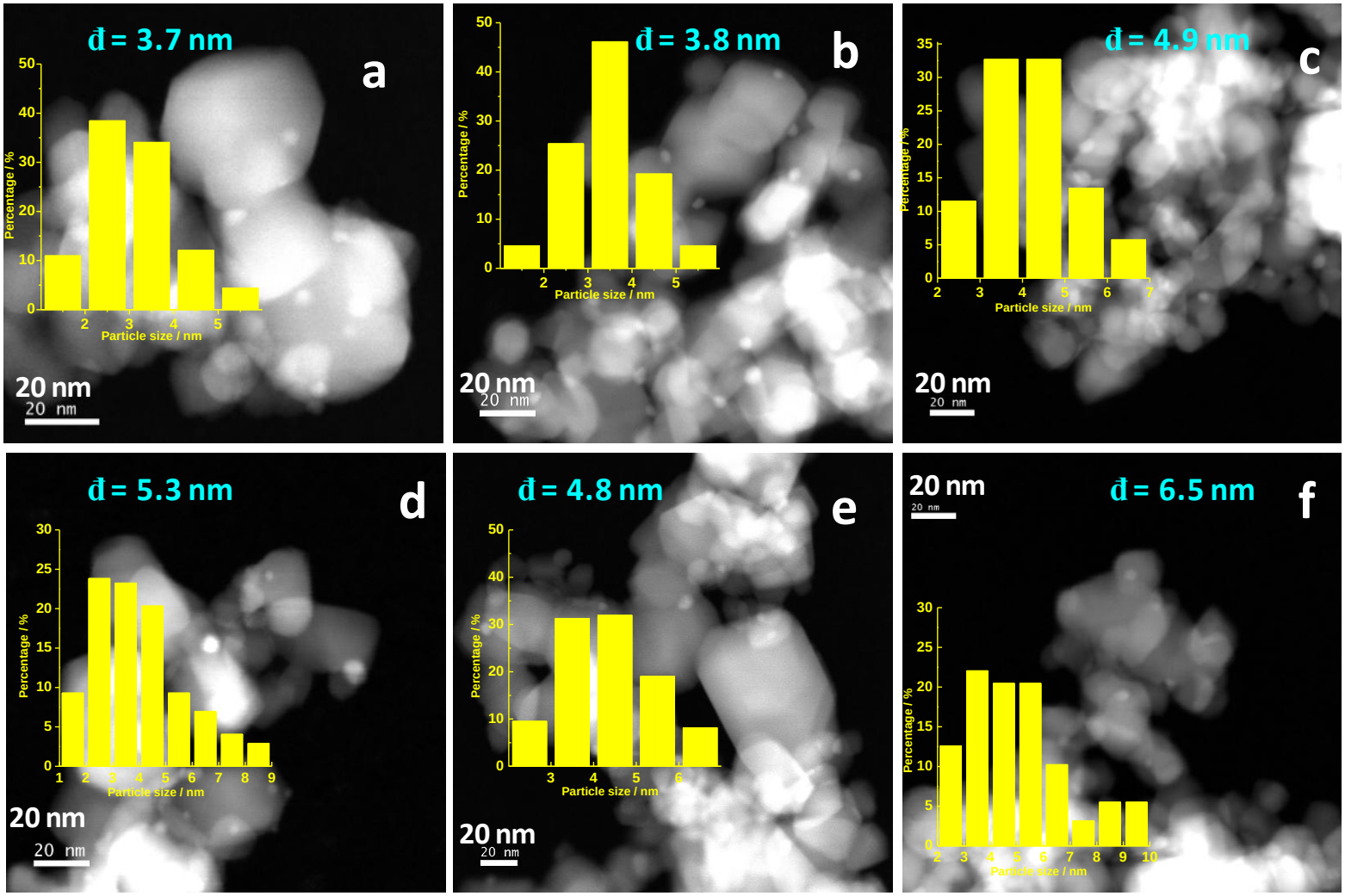

Figure 5-5: STEM-HAADF images of the calcined-reduced DPu and DP8 samples with the particle size distribution: a, DPu Ni/TiO_2; b, DPu NiZn 1:1/TiO_2; c, DPu NiZn 1:3/TiO_2; d, DPu NiZn 1:5/TiO_2; e, DP8 Ni/TiO_2; f, DP8 NiZn 1:3/TiO_2

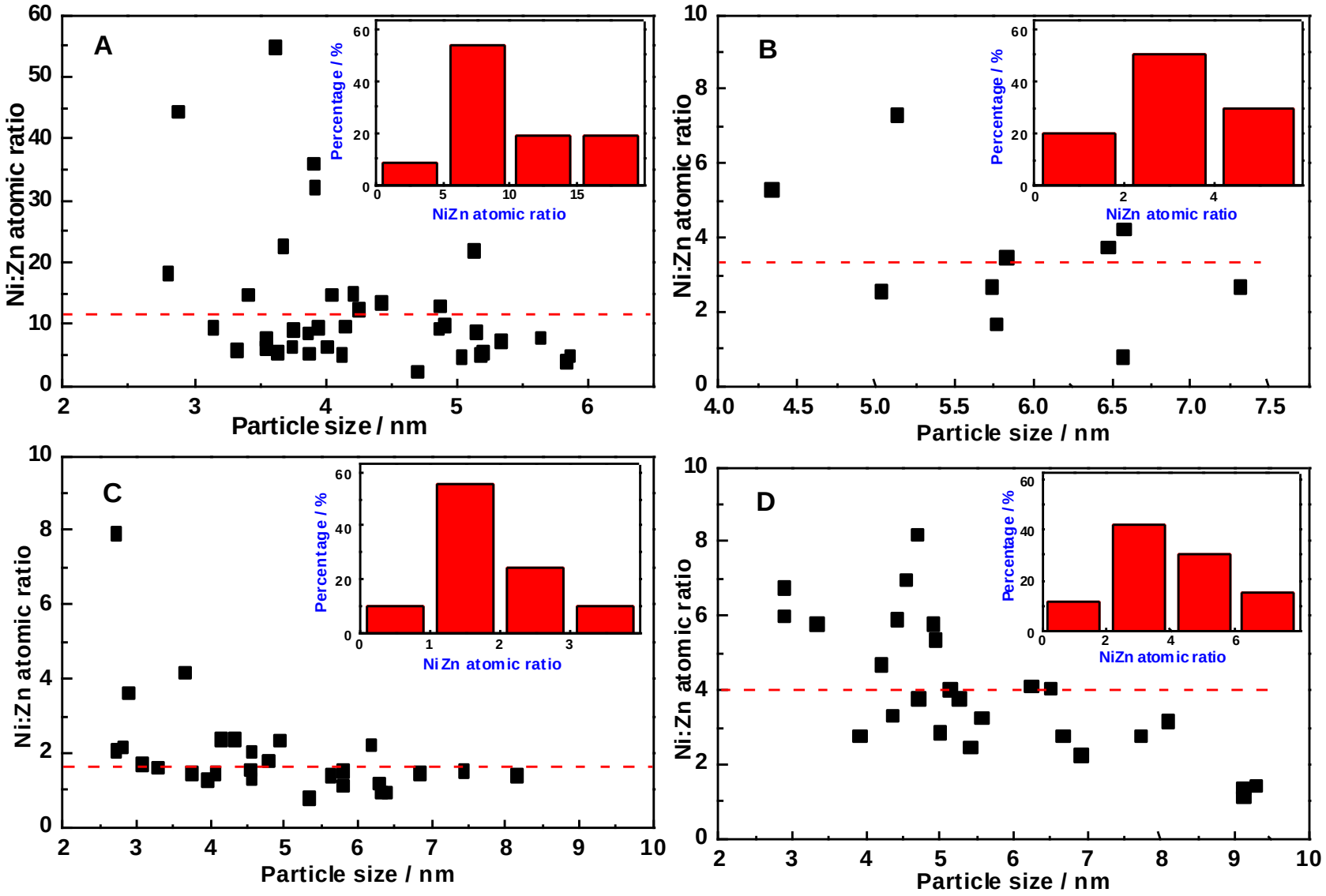

Figure 5-6: EDS analysis of some particles in the calcined-reduced DPu and DP8 samples: A, DPu NiZn 1:1/TiO_2; B, DPu NiZn 1:3/TiO_2; C, DPu NiZn 1:5/TiO_2; D, DP8 NiZn 1:3/TiO_2;

Table 5-4: summary of the composition, particle size of the supported NiZn nanoalloys, of the catalytic performance and of TGA after catalytic stability

Sample	Average Ni:Zn ratio in the nanoparticles (from EDS)	Average metal particle size (nm, based on TEM)	Ni metal dispersion (based on TEM)	Activity at 20 °C ($\times 10^{-4}$ $mol_{butadiene}$ s^{-1} g_{metal}^{-1})	TOF at 20 °C (s^{-1}) (based on TEM)	Alkane formation at ~80% butadiene conversion (ppm)		Decrease of butadiene conversion in 20 h reaction (%)	Weight loss in the TGA results (wt%)	Integral area of the peak in the MS results (a. u. $\times 10^{-12}$)
						Butane	Propane			
DPu Ni	-	3.7	0.27	16.9	0.36	27	596	88	1.37	762.8
DPu NiZn 1:1	12:1	3.8	0.25	9.4	0.22	99	2594	44	1.30	369.9
DPu NiZn 1:3	3.3:1	4.9	0.16	10.4	0.38	165	5094	38	1.27	311.3
DPu NiZn 1:5	1.8:1	5.3	0.12	4.2	0.20	101	3877	58	1.23	211.1
DP8 Ni	-	4.8	0.21	15.4	0.42	57	1507	75	-	-
DP8 NiZn 1:3	4:1	6.5	0.13	5.7	0.27	78	2361	38	-	-
TiO_2	-	10-50	-	-	-	-	-	-	1.19	249.7

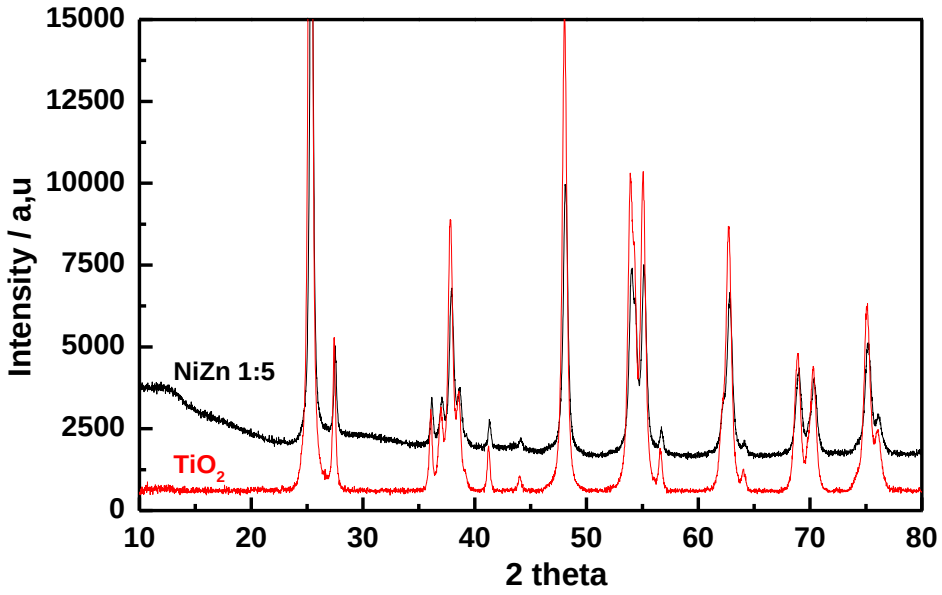

Figure 5-7: XRD of calcined DPu NiZn 1:5/TiO_2 sample.

3.6 Selective hydrogenation of Butadiene in an excess of propene

3.6.1 Activity and selectivity

The catalytic performances of the DPu and DP8 samples were evaluated in the selective hydrogenation of butadiene in the presence of an excess of propene. Two sets of experiments were performed: temperature programmed reaction and isothermal reaction.

Figure 5-8 shows the evolution of the catalytic activity and selectivity to butenes during temperature programmed reaction. Note that Zn/TiO_2 does not present any activity in the temperature range 30-150 ^{o}C (not shown).

Monometallic Ni/TiO_2 presents a lowest temperature corresponding to full conversion of butadiene, $T_{100\%}$ around 35 ^{o}C, for both preparation methods (Figure 5-8A). The introduction of increasing amounts of Zn in the DPu samples leads to an increase of the $T_{100\%}$, i.e., 45 ^{o}C for Ni:Zn 1:1 or 1:3 and 50 ^{o}C for Ni:Zn 1:5. The catalytic activities ($mol_{butadiene}\ s^{-1}\ g_{Ni}^{-1}$) and turn over frequencies (TOF, s^{-1}) were calculated at 20 ^{o}C and are gathered in Table 5-4. The particle sizes applied for the TOF calculation were the average ones estimated from STEM-HAADF. For the DPu bimetallic samples, DPu Ni-Zn/TiO_2 with Ni:Zn atomic ratio 1:3 (containing nanoparticles with an average Ni:Zn atomic ratio 3.3:1) shows the highest

catalytic activity (TOF), similar to monometallic Ni and higher than Ni-Zn/TiO_2 catalysts with Ni:Zn ratio 1:1 and 1:5. These results are in agreement with the calculation prediction from Studt et al [1], e.g., which showed that Ni_3Zn_1 alloy was expected to be more active than monometallic Ni, Ni_1Zn_1 alloy and Ni_1Zn_3 alloy. In the case of DP8 samples, the Ni:Zn 1:3/TiO_2 (average Ni:Zn EDS ratio close to 4) catalyst shows slightly higher $T_{100\%}$ and is less active than the monometallic Ni/TiO_2 catalyst, and it also show lower activity than that of DPu Ni:Zn 1:3/TiO_2. The lower catalytic activity of DP8 catalysts might be caused by the rather larger particle size (Table 5-4). Moreover, it is also found that Ni-Zn/TiO_2 samples, whatever the Ni:Zn atomic ratio, have higher catalytic activity than Ni/ZnO after reduction at 450 ^oC for 2 h, which showed a catalytic activity ~1×10^{-4} $mol_{butadiene}$ s^{-1} g_{Ni}^{-1} and TOF of 0.14 s^{-1}. The lower activity of the Zn-containing catalysts compared to Ni counterparts is in line with what was previously observed for Ni-Zn systems in selective hydrogenation reactions [2, 16]. For acetylene hydrogenation, such a decrease in activity was ascribed to the decrease of the acetylene adsorption energy on the Ni-Zn intermetallic compounds [2], which would result from the substitution of Ni atoms by Zn ones at the surface of the bimetallic nanoparticles. It has been confirmed by Bond et al [17] that alkynes and diolefins chemisorption on Ni have a comparable strength as on Pd. Ni substitution by a second metal, Zn in [1] and Pt in [18], was proposed to modify the electronic properties of surface Ni atoms and thus the strength of adsorption of reactants [17]. It was also proposed recently that Zn atoms prefer to replace the Ni atoms at low coordination sites (corners, edges or defects) of the particles surface [19, 20]. As the low coordination Ni sites are expected to bind unsaturated compounds more strongly than more coordinated sites [21], their replacement by Zn atoms could also contribute to the lower activity of bimetallic samples.

For this kind of reaction of semi-hydrogenation of poly-unsaturated hydrocarbons in the presence of an excess of alkene, the catalytic selectivity can be considered either from the side of the selectivity to butenes (Figure 5-8B) or from the side of the concentration of alkane (butane and propane) formed (Figure 5-8C). Figure 5-8B shows that all the catalysts exhibit a progressive decrease of the selectivity to butenes as the reaction temperature increases and before $T_{100\%}$ is reached, which is similar to what was observed for Ni/ZnO catalyst (Figure 3-29 in Chapter 3). This trend is more pronounced for the Ni-Zn/TiO_2 samples, which means that they are less selective to butenes than the Ni ones. For instance, at butadiene conversion close to 100%, DPu Ni:Zn 1:5 and 1:1/TiO_2 appear less selective to butenes (Figure 5-8B) and shows clearly more alkanes formed (Figure 5-8C) than DPu Ni/TiO_2. This result is rather

surprising as the corresponding bimetallic Ni-Zn samples present lower activity in butadiene hydrogenation than the monometallic Ni/TiO_2 catalysts (Figure 5-8A) and one would have expected that a decrease in activity would have resulted in an increase in selectivity to alkenes. However, considering the fact that the calculation performed by Studt et al [1] also showed that lower selectivity to ethylene were expected for Ni_3Zn_1 alloy than for monometallic Ni or bimetallic Ni_1Zn_1 or Ni_1Zn_3 systems (the selectivity to alkenes for Ni-Zn alloys decreases as follows: Ni_1Zn_3 alloy > Ni_1Zn_1 alloy > Ni > Ni_3Zn_1 alloy), and that the average Ni:Zn atomic ratios estimated by EDS are in the range from 12 to 2 for the bimetallic catalysts (Table 5-4), the high Ni:Zn ratios may explain the lower observed selectivity to alkenes than monometallic Ni. Indeed, the DPu Ni:Zn 1:5 catalyst, which contains Ni-Zn nanoalloy particles with average Ni:Zn atomic ratio close to 2, shows higher selectivity to alkenes than the other DPu Ni-Zn catalysts at high conversion (Figure 5-8C).

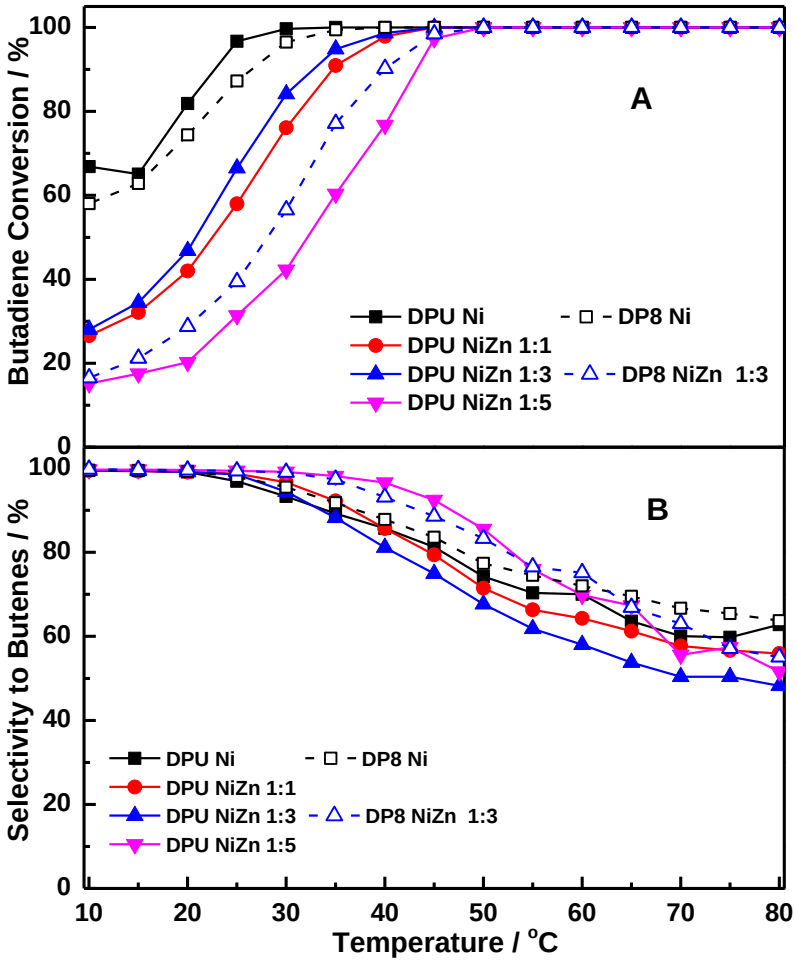

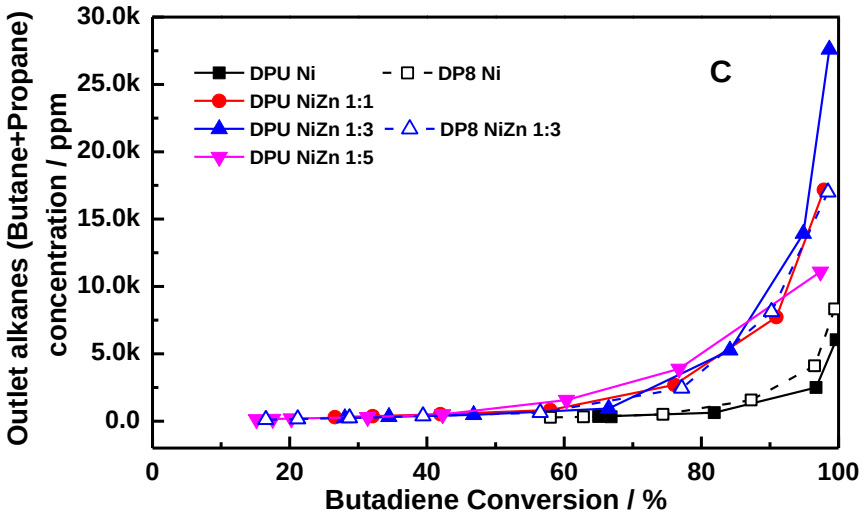

Figure 5-8: Evolution of the butadiene conversion (A), the selectivity to butenes (1-butene + cis-2-butene + trans-2-butene) (B) as a function of the reaction temperature for the reduced monometallic Ni/TiO_2, and bimetallic Ni-Zn/TiO_2 catalysts prepared by different methods (10 mg of catalyst diluted with 90 mg TiO_2), outlet alkanes concentration as a function of butadiene conversion (C). (Full symbols for DPu samples, open symbols for DP8 samples)

3.6.2 Stability and regeneration

The catalytic stability of DPu and DP8 samples was compared from a similar initial butadiene conversion (80-90%) at different reaction temperatures for 20 h (Figure 5-9 and Table 5-4). For monometallic Ni catalysts, the butadiene conversion decreases rapidly to below 10% during the first 12 h, whatever the preparation method. In the case of bimetallic Ni-Zn/TiO_2 catalysts, a higher stability is observed, especially for the Ni:Zn atomic ratios of 1:3 and 1:5. For instance, the DPu Ni:Zn 1:3 sample present only 38% butadiene conversion decrease during 20 h reaction (Table 5-4). The sample preparation method seems to have no significant effect on the catalytic stability as the deactivation behaviours of monometallic Ni and Ni:Zn 1:3/TiO_2 catalysts prepared by DPu and DP8 are similar. Moreover, the TiO_2 supported Ni-Zn alloy has superior stability than that formed on ZnO, which deactivated rapidly from ~80% to lower than 10% after 4 h of reaction (Figure 3-30 in Chapter 3).

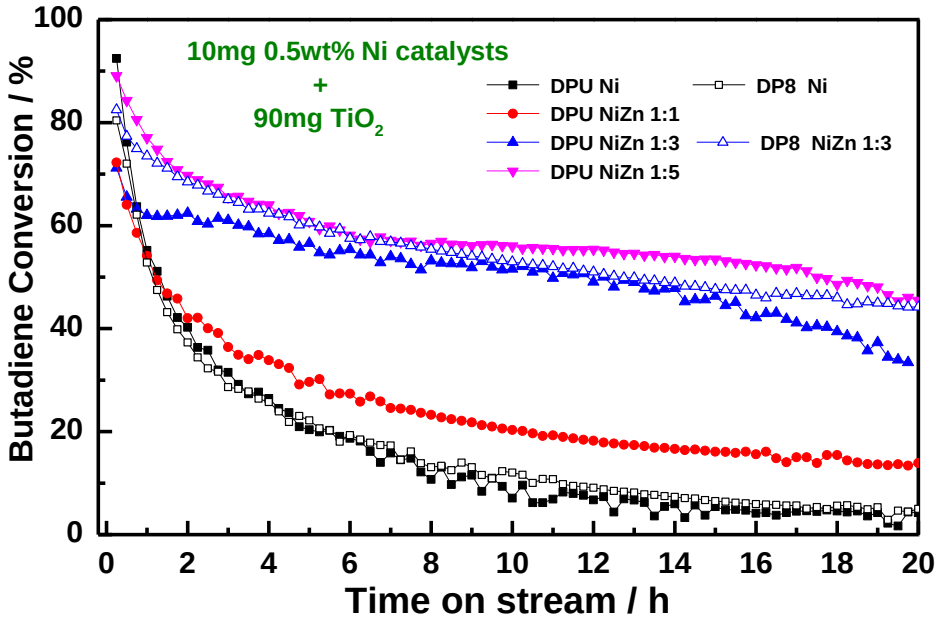

Figure 5-9: Evolution of the conversion of butadiene with time on stream from an initial conversion ~80% for 20 h at a given reaction temperature: 15 °C for DPu and DP8 Ni, 25 °C for DPu NiZn 1:1 and 3:1, 35 °C for DPu NiZn 5:1 and 30 °C for DP8 NiZn 3:1). (10 mg of catalyst diluted with 90 mg TiO_2) (Full symbols for DPu samples, open symbols for DP8 samples)

Catalysts deactivation can result from several causes involving various chemical, thermal and mechanical phenomenon (i.e., poisoning, fouling, thermal degradation, vapour formation, vapour-solid and solid-solid reactions, and attrition/crushing) [22]. In the case of selective hydrogenation of polyunsaturated compounds, an important cause of deactivation is the formation of foulant (green oil) blocking the active sites at the surface of the catalyst [23].

To check this hypothesis, the samples were submitted to a regeneration treatment by calcination. Before, the temperature of decomposition and the amount of carbonaceous deposit on the catalysts surface after stability test was quantified by thermogravimetric analyses (TGA) performed under air flow and coupled with mass spectrometry (MS) (Figure 5-10). Considering the fact that the catalyst-TiO_2 mixtures used for the stability tests (Figure 5-9) contained very small amount of Ni (only 0.05 mg of Ni in 100 mg of catalyst/TiO_2 mixture), undiluted DPu Ni/TiO_2 and Ni-Zn/TiO_2 catalysts (without mixing with the TiO_2 support) were employed after stability test at 25 °C for 20 h to clearly observe the variations in the weight loss and in the formation of CO_2. A reference analysis was also performed on the bare TiO_2 support, which was calcined then reduced at 450 °C for 2 h and exposed to the

reactant gas mixture at 25 °C for 20 h. In Figure 5-10A, a decrease in the weight of the TiO_2 support (~1.2 wt%), can be observed in the temperature range between 150 and 500 °C, combined to CO_2 formation detected by MS in the same temperature range (Figure 5-10B). It can be assigned to the removal of butadiene/propene adsorbed on TiO_2 support as TiO_2 has no activity at low temperature. Regarding the Ni containing catalysts, even though the weight losses in the monometallic Ni and bimetallic Ni-Zn catalysts are similar during the TGA measurement (Table 5-4), differences in CO_2 formation can be clearly observed by the analysis of the outlet gas from TGA by MS (Figure 5-10B). It can be seen that the monometallic Ni sample presents the largest CO_2 formation while the addition of Zn strongly decreases the CO_2 release (Table 5-4), which indicates that the Zn inclusion limits the carbonaceous deposition on the catalysts surface, resulting in an enhanced stability.

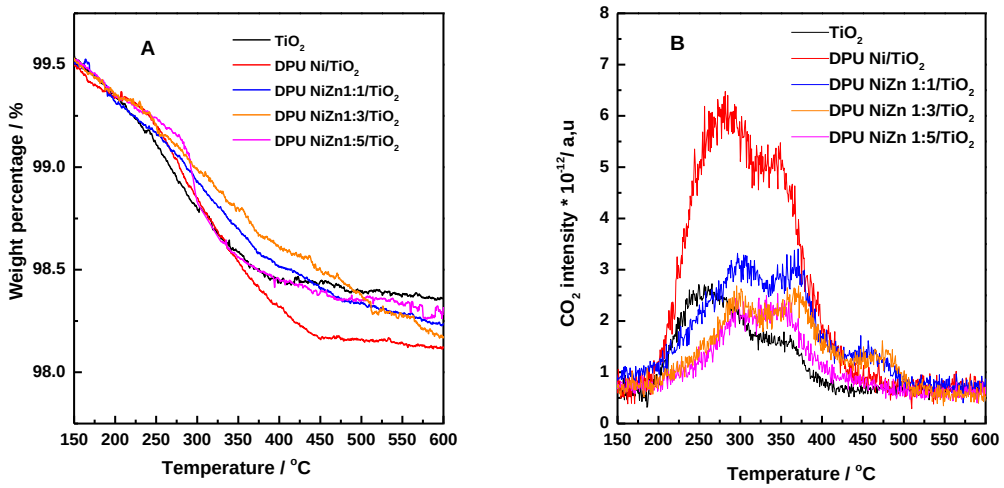

Figure 5-10: Thermogravimetric analyses (A) performed in air coupled with mass spectrometry (B) of TiO_2 support and undiluted DPu samples after 20 h of stability test at 25 °C. TiO_2 was previously calcined then reduced at 450 °C and exposed to reactant gas mixture for 20h at 25 °C.

A positive effect of Zn addition to Ni containing catalysts has been previously observed for ethanol steam reforming, as it resulted in a decrease in the formation of carbonaceous deposit responsible for the catalysts deactivation [24]. The enhanced stability was ascribed to the formation of Ni-Zn alloy, resulting in the dilution of large ensembles of Ni metal atoms by Zn atoms, which led to the inhibition of carbon deposition [24]. In the case of selective hydrogenation of acetylene in the presence of ethylene over bulk intermetallic Ni-Zn compounds [2], the formation of Ni-Zn alloys resulted in a decrease in the oligomer formation, enhancing the selectivity to ethylene. The lower acetylene adsorption energy,

which was estimated from DFT calculations, on the alloys surface compared to pure Ni surface was considered as the primary cause for the decrease of the rate of carbon-carbon formation. However, the related experiments were performed in a batch reactor and catalystic stability was not studied. In the case of bimetallic Cu-Ni systems and propyne hydrogenation [25], DFT calculations indicated that isolated Cu-Ni sites showed larger coupling barriers for C-C bond formation than pure Ni or Cu sites, which allowed improving the resistance to oligomers formation. As for other intermetallic compounds such as Ga-Pd for selective acetylene hydrogenation [26], the isolation of the active Pd sites was also proposed to play an important role for avoiding undesired side reactions, such as oligomerization, which requires a sufficiently short distance between the co-adsorbed hydrocarbon molecules. Moreover, the replacement of Ni atoms by Zn ones at specific positions of the nanoparticles can also contribute to the lower deactivation observed. Indeed, as previously mentioned in Section 3.6.1, DFT calculations reported that Zn preferentially occupied low coordination sites (corners) in bimetallic Ni-Zn particles [19, 20]. As these sites are considered to be active for C-C bond breaking and thus could lead to the formation of carbonaceous compounds [27], the preferential substitution of low coordination Ni sites by Zn could also limit the formation of such poisoning species. A lower formation of carbonaceous compounds was also observed on a Zn modified Ni/Al_2O_3 catalysts during selective hydrogenation of acetylene [28], however, the authors ascribed this phenomenon to a higher Ni phase dispersion in the zinc aluminate phase formed in ternary Ni-Zn-Al catalyst and to a decrease in the number of surface acid sites compared to Ni/Al_2O_3 rather than to the formation of an intermetallic NiZn phase. The EDS analyses (Table 5-4) indicate that a part of Zn is present on the TiO_2 surface and not alloyed with Ni. These residual zinc species could thus modify the acidic properties of the support surface. Indeed, acid sites can promote the adsorption of hydrocarbons and provoke not only isomerisation but also transformation into coke or C2-C6 hydrocarbons from cracking and disproportionation reactions [22, 29]. The presence of Zn species may thus lower the number of such acid sites, as previously proposed for $Cu-Zn/TiO_2$ catalysts in the same reaction [30].

Although being more stable than monometallic Ni/TiO_2 catalysts, the bimetallic Ni-Zn samples suffer from a progressive deactivation with time of reaction. In order to further explore the possibility to reactivate such catalysts, the two Ni:Zn 1:3 $/TiO_2$ catalysts prepared by DPu and DP8, were tested for a longer time on stream (~65 h, to reach a final butadiene conversion below 20%) then the catalysts were attemptly *in situ* regenerated by calcination at

500 ^{o}C then reduction at 450 ^{o}C for 2 h, according to the same procedure as for activation. The catalytic performances were then evaluated during a second run for 20 h (Figure 5-11). The results show that the regeneration treatment at 500 ^{o}C under air cannot allow the recovery of the initial catalytic performances of Ni-Zn catalysts, the butadiene conversion is even lower than the one recorded at the end of the first run. In order to explain this observation, the cristallites size after regeneration and the formation of carbonaceous species accumulated on the catalyst surface were estimated by XRD (Figure 5-12) and Raman spectroscopy (Figure 5-13), respectively. It can be seen that the cristallite size of bimetallic Ni-Zn alloy appears to only slightly increase after regeneration as a very weak additional broad peak assigned to β_1-NiZn alloy (Ni_1Zn_1) (JCPDS:01-072-2668) is visible in the regenerated catalyst. The presence of carbonaceous deposit was identified by Raman spectroscopy (i.e., bands at 1300 cm^{-1} and 1581 cm^{-1} , assigned to the C-C single bonds between sp^3-hybridized carbon atoms in the cubic structure (D band) and to the 'in plane' displacement of carbons strongly coupled in the hexagonal sheets (G band) [31], respectively) after stability test but these species seems to have been removed after the regeneration treatment at 500 ^{o}C. Considering the fact that the catalytic performances cannot be recovered after this oxidative treatment, an additional TGA-MS experiment was performed on the regenerated DPu Ni:Zn 1:3/TiO_2 sample (Figure 5-14), which shows an only slight weight loss (~0.6 wt%) in parallel to very low CO_2 formation in the temperature range 150 and 600 ^{o}C. All these characterizations indicate that particle growth or deposition of carbonaceous species on the catalysts surface can not be considered as the main reason for the observed irreversible deactivation. Thus, additional unknown causes are at the origin of the deactivation phenomenon and further investigations are required to solve this issue.

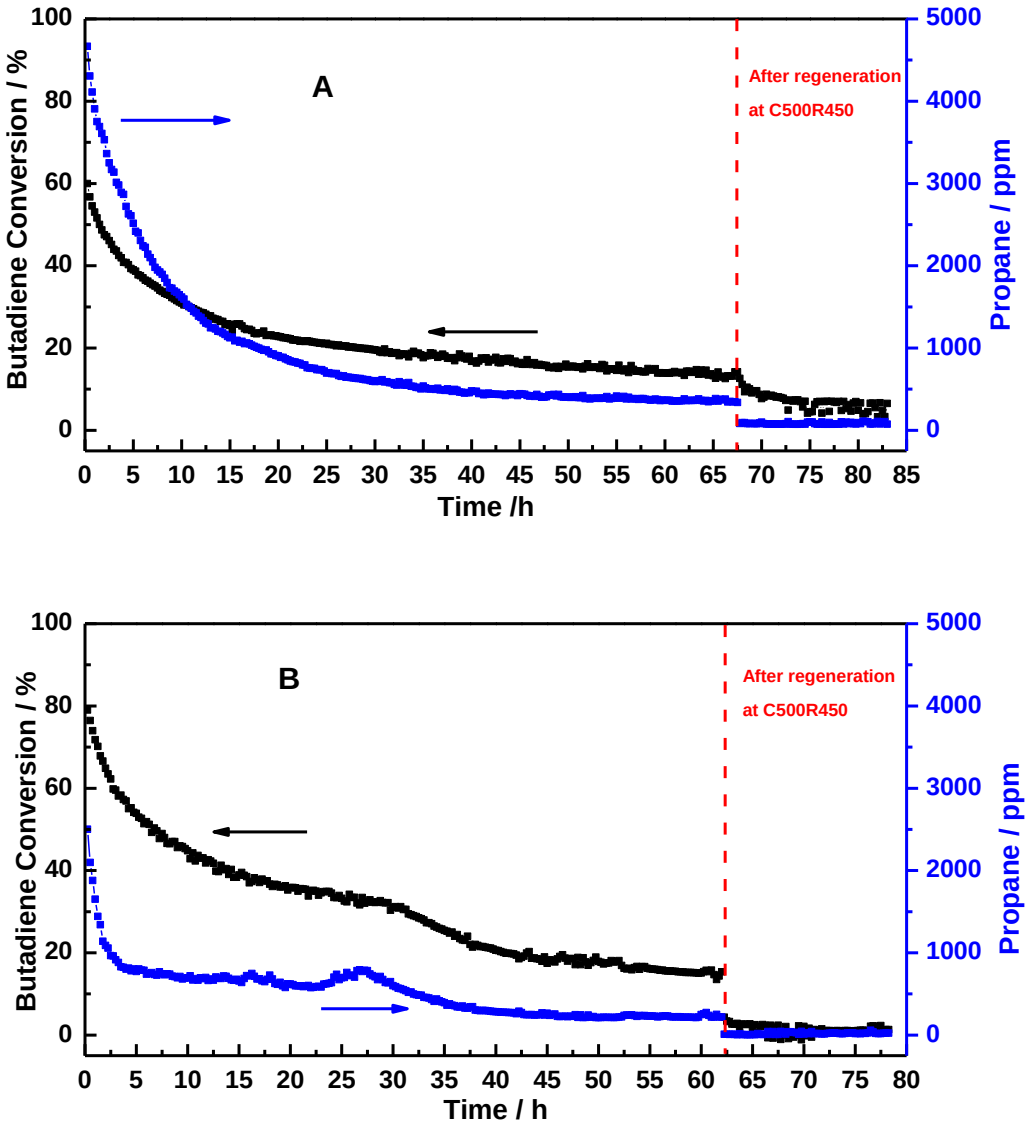

Figure 5-11: Evolution of the conversion of butadiene with time on stream for ~65 h and after catalyst regeneration by calcination at 500 °C then reduction at 450 °C. (A): 25 °C for DPu NiZn and 1:3/TiO_2, (B): 30 °C for DP8 NiZn 1:3/TiO_2 (10 mg of catalyst diluted with 90 mg TiO_2)

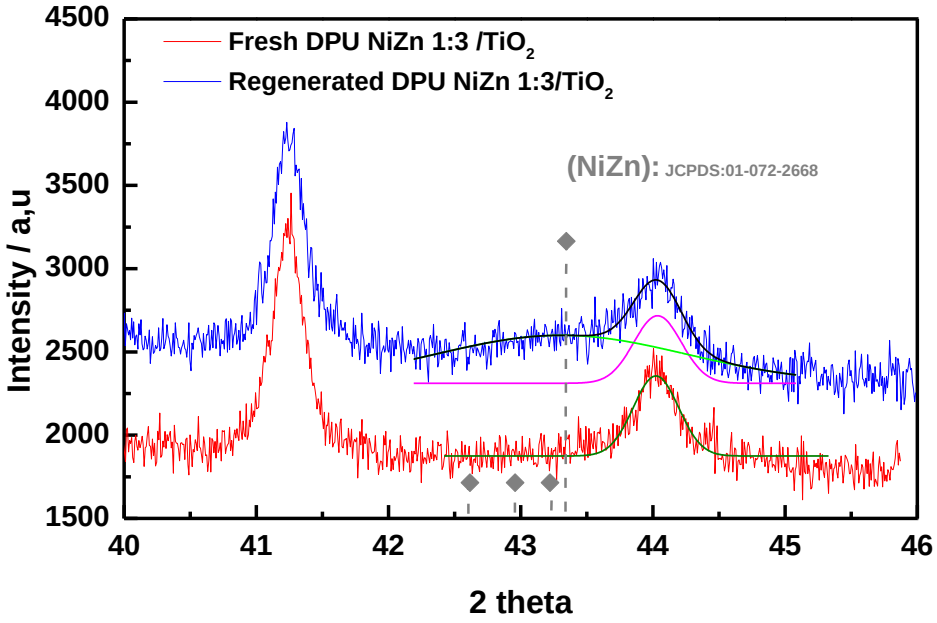

Figure 5-12: XRD of the freshly calcined 0.5wt% NiZn 1:3/TiO_2 and the regenerated 0.5wt% NiZn 1:3/TiO_2 sample after reduction at 450 ^oC for 2 h.

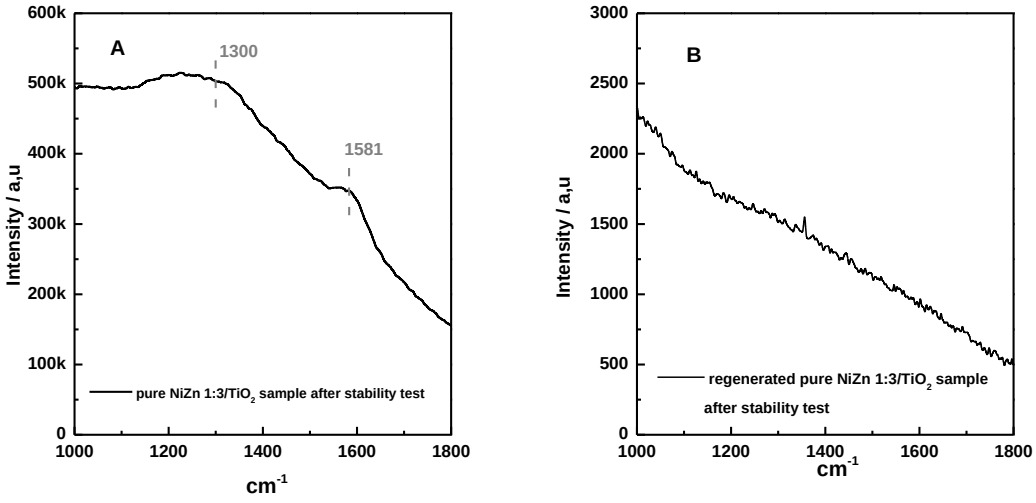

Figure 5-13: Raman spectra of the 0.5wt% NiZn 1:3/TiO_2 after stability test at 25oC for 20h (a) and after regeneration at 500 ^oC for 2 h (b).

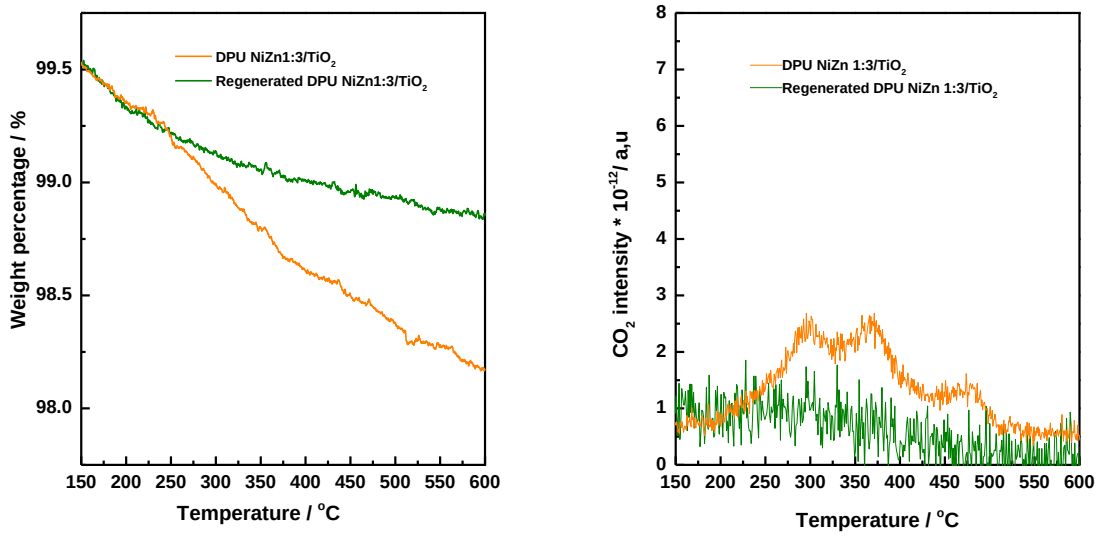

Figure 5-14: Thermogravimetric analyses (A) coupled with mass spectrometry (B) analysis of the undiluted DPu NiZn 1:3/TiO_2 sample after catalytic stability test and regeneration at 500 ^{o}C.

4. Conclusion

TiO_2-supported monometallic Ni and bimetallic Ni-Zn with various Ni:Zn ratios (i.e., 1:1, 1:3, 1:5) were prepared by deposition-precipitation with urea (DPu) and deposition-precipitation at fixed pH (DP8). It has been found that Zn^{2+} deposition occurred first then followed by the one of Ni^{2+} on TiO_2 surface during DPu preparation, and simultaneously during DP8. After calcination at 400 ^{o}C then reduction at 450 ^{o}C for 2 h, the formation of bimetallic Ni-Zn nanoparticles was evidenced by XRD and STEM-HAADF coupled with EDS analysis. The Ni:Zn atomic ratio in Ni-Zn alloyed nanoparticles decreases with the increase of Zn loading in DPu and DP8 samples, and the alloying of Ni with Zn leads to an increase of the average nanoparticle size. The catalytic results showed that Ni has high catalytic activity in the selective butadiene hydrogenation reaction, and that alloying Ni with Zn slightly decreased the activity and, more surprisingly, the selectivity to alkenes, which is not in full agreement with the theoretical prediction by Studt et al. However, the bimetallic Ni-Zn/TiO_2 catalysts displayed much higher stability under isothermal reaction than Ni/TiO_2, which deactivated rapidly in the first few hours of reaction. The DP8 Ni:Zn sample showed slightly higher $T_{100\%}$ and selectivity to butenes, but similar stability than the corresponding DPu sample. The higher stability of bimetallic Ni-Zn/TiO_2 catalysts, compared to monometallic Ni/TiO_2, was ascribed to the formation of a lower amount of carbonaceous

species during reaction, as revealed by TGA analyses. However, even though most of the carbonaceous deposited on the catalytic surface can be eliminated by an *in situ* oxidative treatment, the initial catalytic activity cannot be recovered.

5. Reference

1. F.Studt, F.Abild-Pedersen, T.Bligaard, R.Z.Sørensen, C.H.Christensen, J.K. Nørskov. Science, 320 (2008) 1320.
2. C.S.Spanjers, J.T.Held, M.J.Jones, D.D.Stanley, R.S.Sim, M.J.Janik, R.M.Rioux Journal of Catalysis, 316 (2014) 164.
3. C.S. Spanjers, R.S.Sim, N.P.Sturgis, B.Kabius, R.M.Rioux, ACS Catalysis, 5 (2015) 3304.
4. K.Bourikas, C. Kordulis, A. Lycourghiotis, Chemical reviews, 114 (2014) 9754.
5. Handbook, A., *Volume 3: Alloy phase diagrams.* ASM international, 1992: p. p.780.
6. C.Louis, *Deposition-Precipitation Synthesis of Supported Metal Catalysts.* ChemInform, 2007. **38**(20).
7. J.Bjerrum, *Stability constants of metal-ion complexes*. 1964: The Chemical Society.
8. G.D.Panagiotou, T.Petsi, K.Bourikas, C.S.Garoufalis, A.Tsevis, N.Spanos, C.Kordulisa, A.Lycourghiotis, Advances in colloid and interface science, 142 (2008) 20.
9. T.Imoto, Y.Harano, Y.Nishi, S.Masuda, Bulletin of the Chemical Society of Japan, 37 (1964) 441.
10. S.Lew, A.F. Sarofim, M. Flytzani-Stephanopoulos, Chemical Engineering Science, 47 (1992) 1421.
11. M.Liang, W.Kang, K.Xie, Journal of Natural Gas Chemistry, 18 (2009) 110.
12. M.A.Valenzuela, P.Bosch, J.Jiménez-Becerrill, O.Quiroz, A.I. Páez, Journal of Photochemistry and Photobiology A: Chemistry, 148 (2002) 177.
13. K.Hadjiivanov, M.Mihaylov, N.Abadjieva, D.Klissurski, J. Chem. Soc., Faraday Trans., 94 (1998) 3711.
14. J.van de Loosdrecht, A.M.van der Kraan, A.J van Dillen, J.W.Geus, Journal of Catalysis, 170 (1997) 217.
15. W. Pearson, W. Pearson, *An Alphabetical Index of Work on Metals and Alloys.* A Handbook of Lattice Spacings and Structures of Metals and Alloys, 1958: p. 634.
16. D.L.Trimm, N.W. Cant, I.O. Liu, Catalysis today, 178 (2011) 181.
17. G.Bond, Discussions of the Faraday Society, 41 (1966) 200.
18. B.Hammer, J.K. Nørskov, Advances in catalysis, 45 (2000) 71.

19. A.H. Al-ShaikhAli, A.Jedidi, L.Cavallo, K.Takanabe, Chemical Communications, 51 (2015) 12931.
20. A.H. Al-ShaikhAli, A.Jedidi, D.H.Anjum, L.Cavallo, K.Takanabe, ACS Catalysis, 3 (2017) 1592.
21. R.T.Vang, K.Honkala, S.Dahl, E.K.Vestergaard, J.Schnadt, E.Lægsgaard, B.S. Clausen, J.K.Nørskov, F.Besenbacher, Nature materials, 4 (2005) 160.
22. M.D.Argyle, C.H. Bartholomew, Catalysts, 5 (2015) 145.
23. M.R. Stammbach, D.J. Thomas, D.L. Trimm, M.S. Wainwright, Applied Catalysis, 58 (1990) 209.
24. C.Anjaneyulu, L.O.O.da Costa, M.C.Ribeiro, R.C.Rabelo-Neto, L.V.Mattos, A.Venugopal, F.B.Noronha, Applied Catalysis A: General, 519 (2016) 85.
25. B.Bridier, N. López, J. Pérez-Ramírez, Dalton Transactions, 39 (2010) 8412.
26. M.Krajčí, J. Hafner, ChemCatChem, 8 (2016) 34.
27. J.T. Wehrli, D.J. Thomas, M.S. WainwrightD.L. Trimm, Applied Catalysis, 70 (1991) 253.
28. J.C.Rodrıguez, A.J.March, A.Borgna, A.Monzon, Journal of Catalysis, 171 (1997) 268.
29. P.Berteau, S. Ceckiewicz, B. Delmon, Applied Catalysis, 31 (1987) 361.
30. Z.Wang, G.Wang, C.Louis, L.Delannoy, Journal of Catalysis, 347 (2017).
31. T.Jawhari, A. Roid, J. Casado, Carbon, 33 (1995) 1561.

Chapter 6: Preliminary explorations of the use of supported bimetallic Fe-based catalysts for selective hydrogenation reaction.

Chapter 6: Preliminary explorations of the use of supported bimetallic Fe-based catalysts for selective hydrogenation reaction

1. Introduction

Recently, an $Al_{13}Fe_4$ bulk alloy was found to have high catalytic performance in selective hydrogenation of butadiene and acetylene. This remarkable behavior was ascribed to the presence of highly stable isolated iron catalytic active sites at the surface of the alloy and to the alteration of the electronic structure of iron by chemical bonding with Al [1, 2]. This study revealed that iron-based bimetallic catalysts have interesting potential for the selective hydrogenation of polyunsaturated hydrocarbons. However, even though Fe-based bimetallic catalysts were explored in various reactions, such as bimetallic Fe-Co and Fe-Ni in the hydrogenation of carbon monoxide [3], bimetallic Fe-Ru in the Fischer–Tröpsch synthesis [4] and bimetallic Fe-Cu in the selective catalytic reduction of NO with NH_3 [5], the study of supported bimetallic Fe-based catalysts in the selective hydrogenation of polyunsaturated hydrocarbons is indeed rare. Thus it is worth to carry out some explorations on the application of supported Fe-based catalysts in such reactions. On the other hand, through density functional theory (DFT) calculations, Studt et al [6] predicted that bimetallic Fe-Zn could be an interesting alternative to palladium-based catalysts for the selective hydrogenation of polyunsaturated hydrocarbons. Thus, in this chapter, a preliminary exploration of Fe-Zn/TiO_2 in terms of catalyst preparation and catalytic evaluation is presented. Based on our previous study showing Ni-Zn alloy formation after reduction of Ni/ZnO at different temperatures (Figure 3-27 in Chapter 3), Fe/ZnO was also prepared to more easily evidence the possible Fe-Zn alloy formation.

The Fe-Zn alloy phase diagram presented in Figure 6-1 shows that no clear boundary of Zn content for separating different Fe-Zn alloy phases, and only two identifiable Fe-Zn alloy phases are described: δ-$FeZn_{10}$ and ζ-$FeZn_{13}$, with Zn content higher than 88.5 wt%. Besides that, a kind of *Fe-Zn solid solution* is formed when Zn content is lower than 46 wt%, and Γ *phase* (Γ_1 or Γ_2) is the main Fe-Zn phase when Zn content increases to 72~85 wt%. According to a previous structure analysis on bulk Fe-Zn alloy by Pearson et al [7], Γ *phase* may be Γ-Fe_3Zn_{10}.

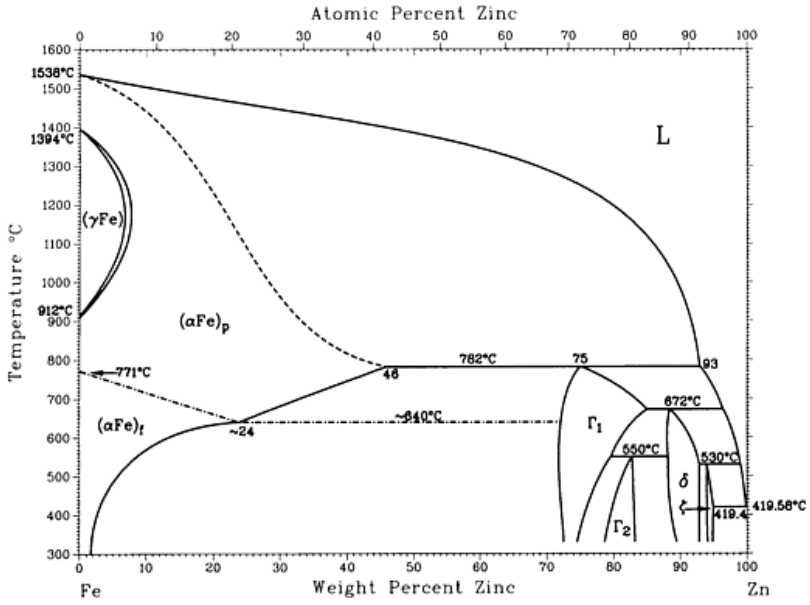

Fe-Zn crystallographic data

Phase	Composition, wt% Zn	Pearson symbol	Space group
(γ_{Fe})	0 to 6.59	*cF*4	$Fm\bar{3}m$
$(\alpha Fe,\delta_{Fe})$	0 to 46	*cI*2	$Im\bar{3}m$
Γ_1	~72 to ~85	*cI*52	$I\bar{4}3m$
Γ_2	0.91 to 83	*cF*408	$F\bar{4}3m$
δ-$FeZn_{10}$	88.5 to 93.0	*hP*555	$P6_3mc$
ζ-$FeZn_{13}$	~94 to 94.8?	*mC*28	$C2/m$
(Zn)	~100	*hP*2	$P6_3/mmc$

Figure 6-1: Alloy phase diagram of Fe-Zn system (left), Fe-Zn crystallographic data (right) [8]

This chapter will describe:

- The reduction behavior of monometallic Fe/ZnO and the possible Fe-Zn alloy formation after sample reduction at different temperatures and the catalytic performance;

- The deposition behavior of iron and zinc ions on titania was monitored as a function of preparation time during bimetallic Fe-Zn preparation.

- The reduction behavior of supported monometallic Fe/TiO_2 and bimetallic $Fe-Zn/TiO_2$ was studied by temperature-programmed reduction (see Section 3 of Chapter 2).

- The evolution of the structure of the iron-based phase in supported monometallic Fe and bimetallic Fe-Zn sample after different thermal treatments was analyzed by XRD (see Section 3 of Chapter 2).

- Finally, the influence of addition of Zn the catalytic performance of Fe/TiO_2 was evaluated under butadiene/H_2/propene gas mixture (see Section 4 of Chapter 2).

2. Preparation of Fe-based catalysts

Fe/ZnO, Fe/TiO_2 and FeZn 1:1/TiO_2 catalysts with 2.5 wt% Fe loading were prepared by deposition-precipitation with urea with the same duration of 20 h (Experiment I) according

to the following procedure (see Section 2 of Chapter 3): 300 mL of distilled water and 3 g of support (TiO_2 P25 Evonik, 80% anatase and 20% rutile) or ZnO (Kadox) were introduced into a double-wall reactor under N_2 (50 mL min^{-1}) in order to prevent the oxidation of Fe^{2+} ions to Fe^{3+} and the precipitation in solution (shown later) during sample preparation when a Fe(II) precursor was used. The mixture was heated at 80 ^oC. Given amounts of metal precursors (i.e., $FeCl_2 \cdot 4H_2O$ and $Zn(NO_3)_2 \cdot 6H_2O$) were dissolved into the TiO_2 suspension solution in order to achieve the desired Fe:Zn ratio (1:0 and 1:1) with 2.5 wt% Fe loading as a constant. Moreover, the initial pH of the solution depends on the acid-base property of the metal precursors. After addition of a large excess of urea $CO(NH_2)_2$ (Sigma-Aldrich) (i.e. [urea]/[metal] ≥100), the mixture was stirred at 80 ^oC in the closed reactor for 20 h. The solid was separated from the liquid phase by centrifugation and subsequently repeatedly washed with distilled water and centrifuged (three times). Then the samples were dried under vacuum at room temperature for 24 h (so-called as-prepared sample).

The pH evolution during monometallic Fe/TiO_2 and FeZn 1:1/TiO_2 was recorded every 5 min during the first 5 h of DPu (Experiment II) with initial pH of the preparation solution adjusted to ~2 by adding 0.5 M HNO_3, with Fe(II)/urea and urea/TiO_2 as references. In addition, the evolution of the metals loadings in the as-prepared sample as a function of time (Experiment III) was studied during the FeZn 1:1/TiO_2 with 2.5 wt% Fe loading sample preparation (using 3 g of TiO_2 in 300 mL). Two different iron precursors, i.e., $FeCl_2 \cdot 4H_2O$ and $Fe(NO_3)_3 \cdot 9H_2O$, were employed to study the deposition behavior of iron ions. Aliquots of 40 to 50 mL of suspension were withdrawn at different pHs, and treated as above, i.e., centrifuged, washed and dried. Note that, in the following text, Fe(II) was used for the samples prepared by $FeCl_2 \cdot 4H_2O$ precursor and Fe(III) was for $Fe(NO_3)_3 \cdot 9H_2O$.

The final metal loadings achieved for the various samples after 20 h of DPu are summarized in Table 6-1. More than 80% of Fe and Zn were deposited on TiO_2 surface.

Table 6-1: Fe and Zn loadings in the as-prepared Fe-Zn/TiO_2 sample prepared by DPu

DPu Sample	**Normal metal loading / wt%**		**Experimental metal loading / wt%**	
	Fe	**Zn**	**Fe**	**Zn**
Fe(II) /TiO_2	**2.5**	**-**	**2.1**	**-**
Fe(II)Zn 1:1/TiO_2	**2.5**	**2.5**	**2.0**	**2.0**
Fe(II)/ZnO	**2.5**	**-**	**2.1**	**-**

Before characterization or reaction, the catalysts were calcined at 400 °C for 2 h with a temperature ramp of 5 °C min^{-1}, under flowing air (100 mL min^{-1}) (like for the Cu-Zn/TiO_2, Ni-Zn/TiO_2 study), and reduced at 500 °C for 2 h (temperature ramp of 3 °C min^{-1}) under flowing H_2 (100 mL min^{-1}).

3. Monometallic Fe/ZnO catalyst

In this part, 2.5 wt% Fe(II)/ZnO was prepared by DPu method. After calcination at 400 ^{o}C for 2 h, the reduction behaviour of the sample was analysed by TPR. Special attention was mainly paid on the possible formation of Fe-Zn alloy after sample reduction at different temperatures.

3.1 Reduction behaviour of Fe(II)/ZnO catalysts.

Considering the high iron oxide reduction temperature (above 550 ^{o}C) previously observed by Liang et al [9], the TPR experiment was performed on the calcined Fe(II)/ZnO sample with temperature going up to 900 ^{o}C (Figure 6-2). Three reduction peaks (i.e., 525, 570 and 670 ^{o}C) can be observed. As it was mentioned in Section 4 of Chapter 2, ZnO is reduced at temperature as high as 650 ^{o}C [10], thus the broad peak at ~670 ^{o}C is probably due to the reduction of ZnO support. The structure of the iron phase detected by XRD was mainly $ZnFe_2O_4$ in the calcined Fe(II)/ZnO (Figure 6-3), and according to Liang et al [9], bulk $ZnFe_2O_4$ could be first reduced to Fe_3O_4 (~380 ^{o}C) and then to FeO (~560 ^{o}C) and finally to metallic Fe (~640 ^{o}C). Thus the reduction peaks at 525 and 570 ^{o}C might be attributed to the reduction of Fe_3O_4 to FeO and to metallic Fe, respectively. The reduction of $ZnFe_2O_4$ to Fe_3O_4 might occurred at low temperature (i.e., ~450 ^{o}C) as the peak at ~525 ^{o}C can be divided into two peaks with a shoulder around 450 ^{o}C. Thus, considering that ZnO is not stable when the reduction temperature becomes higher than 550 ^{o}C, two reduction temperatures (450 and 500 ^{o}C) were selected for the reduction of calcined Fe/ZnO and the study of the possible Fe-Zn alloy formation.

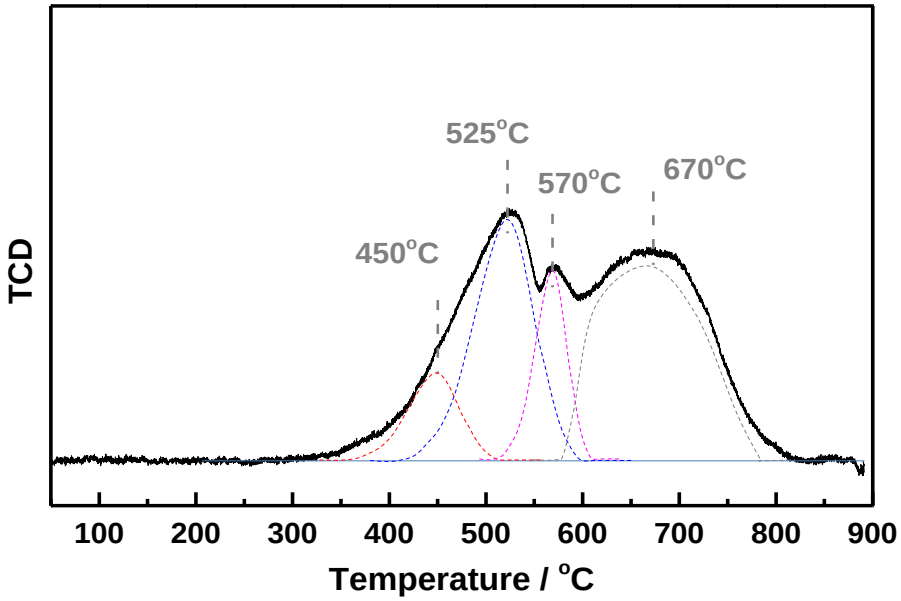

Figure 6-2: TPR of calcined 2.5 wt% Fe/ZnO sample

3.2 Structure evolution of Fe(II)/ZnO after different thermal treatments

The structure of the iron phase on ZnO was analyzed by XRD after different thermal pretreatments (Figure 6-3). It is found that $ZnFe_2O_4$ (JCPDS: #22-1012) is the main compound of iron on the ZnO surface in the as-prepared and calcined samples with particle size around 17 and 15 nm, respectively. After reduction at 450 and 500 °C for 2 h, The $ZnFe_2O_4$ was directly reduced to metallic Fe (Figure 6-3), with particle size estimated by Scherrer's equation of ~16 and 18 nm, respectively, without any Fe-Zn alloy formation. Although the Fe-Zn alloy phase diagram (Figure 6-1) reveals that Fe-Zn alloy should only formed in sample with a high Zn wt%, no Fe-Zn alloy was detected in the reduced 2.5 wt% Fe(II)/ZnO. The bimetallic Fe-Zn nanoparticles, if existing, might be too small to be identified by XRD.

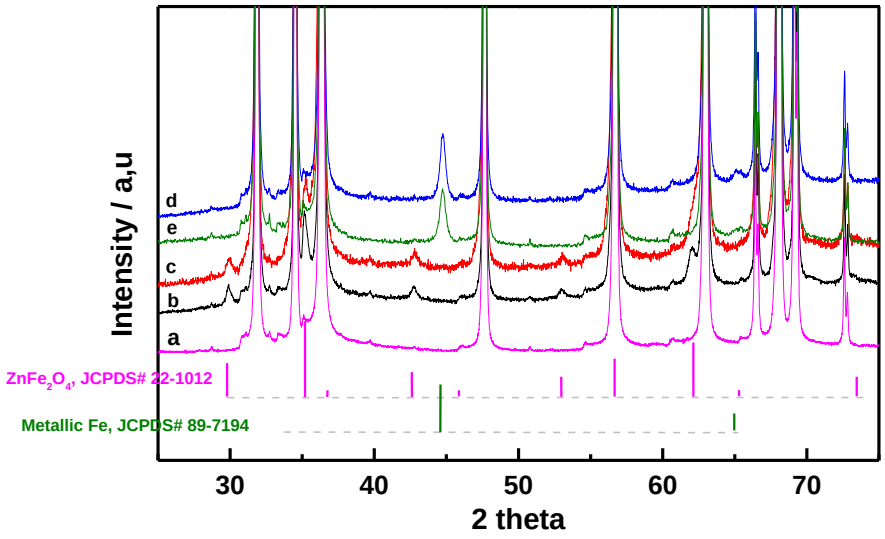

Figure 6-3: XRD of 2.5wt% Fe(II)/ZnO: a, ZnO support; b, as-prepared; c, calcined at 400 ^{o}C; d, calcined then reduced at 450 ^{o}C, e calcined then reduced at 500 ^{o}C

3.3 catalytic performance

The catalytic performance of 100 mg of 2.5 wt% Fe(II)/ZnO after reduction at 450 ^{o}C and 500 ^{o}C was evaluated through temperature programmed reaction (Figure 6-4) and isothermal reaction (Figure 6-5). During the temperature programmed reaction, the temperature for catalytic reaction was increased by 1 ^{o}C min^{-1} with an initial temperature at 30 ^{o}C in oven, then was kept constant for other 20 h once the butadiene conversion reached 100%. Detailed information about the procedural of catalytic test can be checked in Section 4 of Chapter 2.

In Figure 6-4A, Fe(II)/ZnO catalysts shows full butadiene conversion at around 75 ^{o}C, whatever the reduction temperature (450 or 500 ^{o}C). Moreover, both Fe(II)/ZnO catalysts have comparable catalytic activity, which is in agreement with the similar Fe particle sizes estimated from XRD (Figure 6-3).

Similarly to the study on Ni/ZnO (Section 5 of Chapter 3), the catalytic selectivity can be analyzed by checking either the selectivity to butenes (Figure 6-4A) or the alkane (butane and propane) formation (Figure 6-4B). It shows that the catalysts were highly selective to butenes (~100%) at temperature lower than the full butadiene conversion temperature ($T_{100\%}$), no matter the reduction temperature was 450 or 500 ^{o}C. At $T_{100\%}$, the selectivity to butenes of the catalyst reduced at 450 ^{o}C was ~96%, which is slightly higher than the one reduced at 500

°C (i.e., 93%). Figure 6-4B also indicates that the formation of alkane was negligible at low butadiene conversion for both catalysts and the Fe(II)/ZnO reduced at 500 °C formed higher amount of alkanes (~10 kppm) than that reduced at 450 °C (~6 kppm) when butadiene conversion was close to 100%.

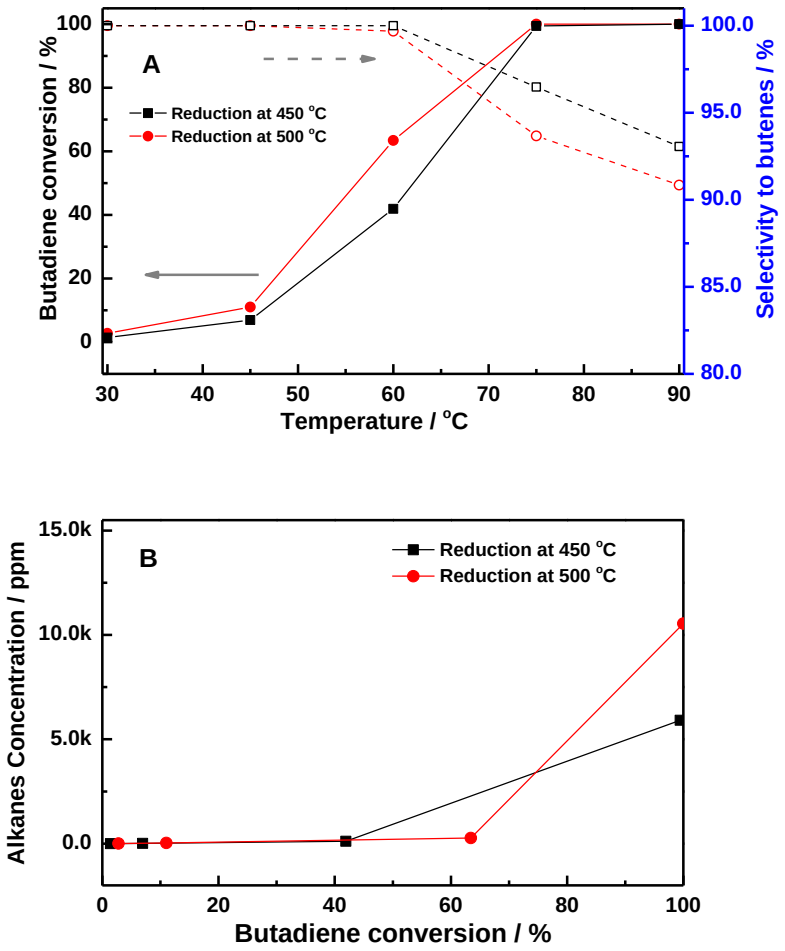

Figure 6-4: Catalytic performance of calcined Fe(II)/ZnO after reduction at 450 and 500 °C: butadiene conversion and selectivity to butenes versus temperature (A); Alkanes formation versus butadiene conversion (B)

After reaching $T_{100\%}$, the catalysts were kept at 90 °C for 20 h (Figure 6-5). It shows that the butadiene conversion decreased sharply from 100% to ~10% after 5 h of reaction for both samples. Moreover, it seems that the catalyst becomes less stable with higher reduction temperature as the butadiene conversion of the catalyst reduced at 500 °C decreased faster than that reduced at 450 °C, similar results were also observed with Ni/ZnO catalysts (Figure 3-30, in Chapter 3). The low catalytic stability could again be attributed to the negative effect

of ZnO that can promote oligomerization on the catalyst surface [11] (see Section 5.2 of Chapter 3).

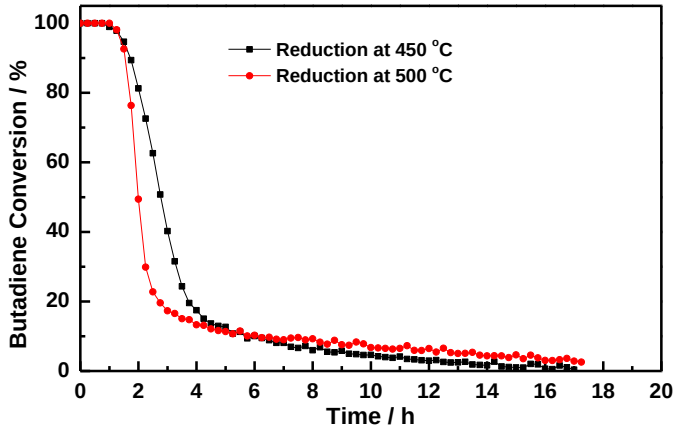

Figure 6-5: Evolution of butadiene conversion with time on steam at 90 °C for Fe(II)/ZnO after reduction at 450 and 500 °C

In summary, the main information arising from this part is that the $ZnFe_2O_4$ phase present in the as-prepared Fe(II)/ZnO sample decomposes into metallic Fe during reduction at 450 °C, without formation of Fe-Zn alloy detectable by XRD whereas it was expected from the Fe-Zn phase diagram that the high Zn content of this sample would lead to the formation of an alloy.

4. Bimetallic Fe-Zn/TiO_2 catalysts

Even though no Fe-Zn alloy was detected in the Fe(II)/ZnO samples after reduction at different temperatures, bimetallic Fe-Zn/TiO_2 was still explored in this part. TiO_2 supported monometallic Fe and bimetallic FeZn 1:1 with 2.5 wt% Fe loading samples were prepared by DPu. Moreover, to confirm the calculation prediction about the different deposition behaviors of Fe^{3+} and Fe^{2+} ions in Figure 2-4 of Chapter 2, $Fe(NO_3)_3$ and $FeCl_2$ were employed as the iron precursors and the iron and zinc loading in the as-prepared sample were studied as a function of DPu time. The reduction behavior of Fe-Zn/TiO_2 catalyst was monitored by temperature-programmed reduction (TPR). The structure evolution of iron-based phase was recorded by X-ray diffraction after different thermal treatments. Finally, the catalytic performance was monitored under butadiene/H_2/propene mixture as a function of temperature and time on stream at constant temperature.

4.1 Fe, Zn loading at different final preparation time with Fe^{2+}/Fe^{3+} precursors

The deposition behavior of iron and zinc ions was studied by analysis of the iron and zinc loading on TiO_2 surface after different preparation time (Figure 6-6). Note that the nominal Fe loading is 2.5 wt% with Fe:Zn loading ratio 1:1. It can be seen that the Fe^{3+} and Fe^{2+} iron precursors lead to totally different iron deposition behaviors: for the preparation with Fe^{3+} precursor, over 80% of Fe^{3+} was precipitated, mainly in solution as phase segregation was clearly observed in the resulting as-prepared samples after drying, at the beginning (i.e., 15 min) of DPu preparation. Then it reached around 93% after 1 h of DPU with no significant change in the following 19 h. Similar deposition-precipitation behavior of Fe(III) was also observed by Geus et al [12], which indicated that $Fe(OH)_3$ precipitation appears when the pH of the solution was higher than 2.0. The situation is different for the Fe^{2+} precursor, which showed that less than 10% Fe^{2+} was deposited on the TiO_2 surface at 15 min of DPu. Then it increased gradually to ~95% in the next 4 h and was kept as a constant in the following 16 h. Additionally, it is also found that the Zn loading evolution with DPu time in these two preparations is similar, which may means that the type of iron precursor has no significant effect on the deposition of Zn ions. Moreover, Figure 6-6B also shows that Zn^{2+} has a similar deposition behavior as Fe^{2+} during DPu preparation. This observation is in agreement with the previous theoretical calculation in Figure 2-4 of Chapter 2, which revealed that the pH for the deposition-precipitation of Fe^{2+} is rather higher than that of Fe^{3+}, but is similar to that of Zn^{2+} on the basis of the solubility of their hydroxides species (see Table 2-1, in Chapter 2). Because of the rapid and uncontrolled precipitation of $Fe(OH)_3$, which mainly occurs in solution, only the samples prepared using Fe(II) precursor ($FeCl_2 \cdot 4H_2O$) will be considered in the following parts of this chapter.

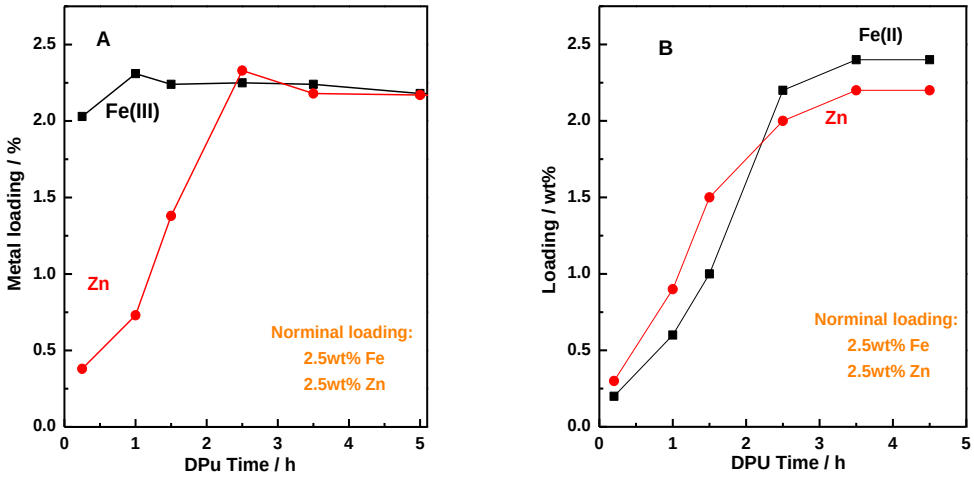

Figure 6-6: Evolution of the Fe and Zn loadings on titania versus time during the DPu preparation procedure: (A) Fe(III)-Zn/TiO_2; (B) Fe(II)-Zn/TiO_2. Nominal loadings: 2.5 wt% Fe and 2.5 wt% Zn

4.3 XRD of the as-prepared and calcined Fe-Zn/TiO_2 catalysts

The structure of the iron-based phase in the as-prepared and calcined Fe-Zn/TiO_2 sample was first characterized by XRD (Figure 6-7). Fe_2O_3 (JCPDS: #33-0664) was formed in the as-prepared and calcined Fe(II)/TiO_2 sample, while, similarly to the Fe(II)/ZnO sample (Figure 6-3), $ZnFe_2O_4$ (JCPDS: #70-6393) was formed in the as-prepared and calcined Fe(II)Zn 1:1/TiO_2. More interesting, the formation of $ZnFe_2O_4$ compound in the as-prepared Fe(II)Zn 1:1/TiO_2 reveals that the interaction between Fe and Zn appears on TiO_2 surface during sample preparation by DPu. Calcination treatment has no significant effect on the structure of the iron-based phase in monometallic Fe/TiO_2 and bimetallic FeZn 1:1/TiO_2 samples. The crystallite size of Fe_2O_3 and $ZnFe_2O_4$ was estimated by the Scherrer's equation at 16 nm 20 nm for the as-prepared and 17 nm and 22 nm for the calcined Fe(II)/TiO_2 and Fe(II)Zn 1:1/TiO_2, respectively.

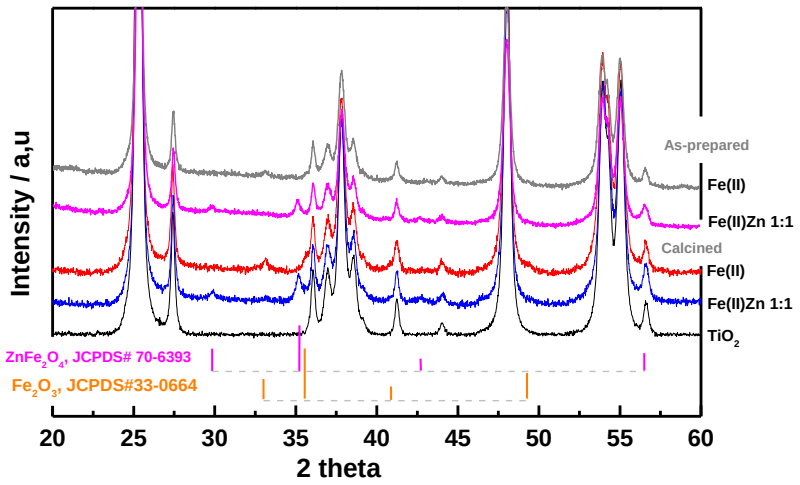

Figure 6-7: XRD of as-prepared and calcined Fe(II)/TiO_2 and Fe(II)-Zn/TiO_2 samples with 2.5wt% Fe

4.4 TPR of Fe-Zn/TiO_2 catalyst

The reduction of calcined TiO_2 supported Fe(II) and Fe(II)Zn 1:1 sample was studied by TPR (Figure 6-8). The Fe(II)/TiO_2 sample shows three reduction peaks at 375, 410 (shoulder) and 490 °C. According to a previous TPR study on the reduction behavior of bulk Fe_2O_3 and $ZnFe_2O_4$ by Liang et al [9], the first reduction peak (~375 ^oC) in Figure 6-8A could correspond to the reduction of Fe_2O_3 to Fe_3O_4, and the last two peaks (~410 and 485^oC) to the reduction of Fe_3O_4 to FeO, and finally to metallic Fe, respectively. Note that the reduction peak appearing at temperature around 900 ^oC is unknow, but might be due to TiO_2 reduction. For the Fe(II)-Zn/TiO_2 sample, which contains $ZnFe_2O_4$, three reduction peaks at 375, 505 and 545 ^oC are observed, which may be caused by the reduction of $ZnFe_2O_4$ to Fe_3O_4, FeO and to metallic Fe, respectively. By comparison with Fe/TiO_2 (Figure 6-8A), the addition of Zn increases the reduction temperature of TiO_2 supported iron species (Figure 6-8B), and similar effect of addition of Zn was also observed for supported copper (Figure 4-4 in Chapter 4) and nickel (Figure 5-3 in Chapter 5). However, this is not consistent with the conclusion of Liang et al [9], which described that the $ZnFe_2O_4$ structure was more easily reduced than that of Fe_2O_3. Considering the fact that ZnO is not stable when the reduction temperature becomes higher than 550 ^oC [13, 14], 500 ^oC was selected for the Fe(II)-based samples activation for the catalytic tests.

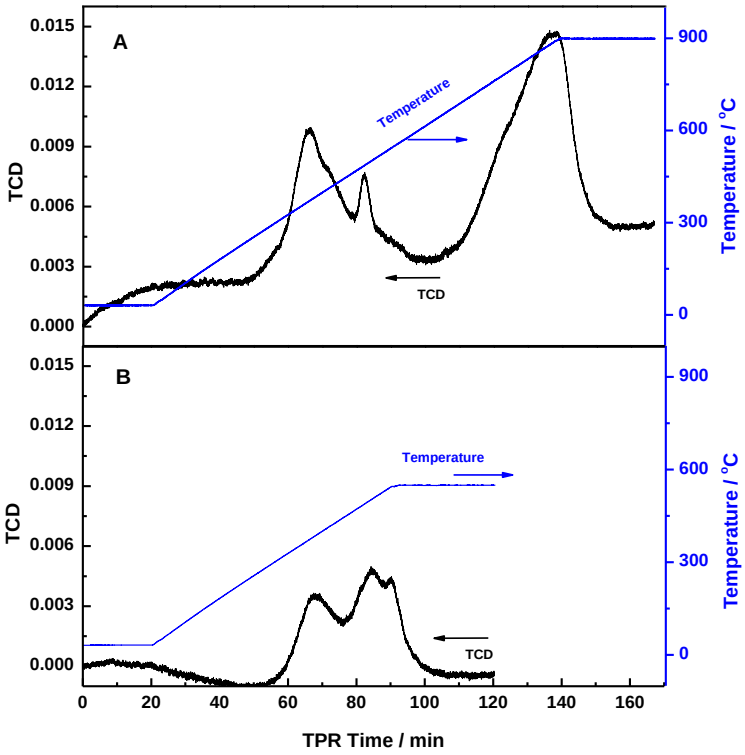

Figure 6-8: TPR of Fe(II) /TiO_2 (A) and Fe(II)Zn 1:1 /TiO_2 (B) sample after calcination at 400 ^oC for 2 h

4.5 XRD of reduced Fe-Zn/TiO_2 catalyst

After reduction at 500 ^oC, the samples were characterized by X-ray diffraction (XRD) in Figure 6-9. The Fe_2O_3 phase in the calcined Fe(II)/TiO_2 is transformed to metallic Fe (crystallite size ~ 23 nm) after sample reduction at 500 ^oC for 2 h. In the case of Fe(II)Zn 1:1/TiO_2, metallic Fe (crystallite size ~ 25 nm) was also observed after reduction under H_2 at 500 ^oC for 2 h. Nevertheless, similarly to Fe(II)/ZnO (Figure 6-3), there is no indication of the formation of any Fe-Zn alloy in the bimetallic Fe(II)Zn 1:1/TiO_2 sample.

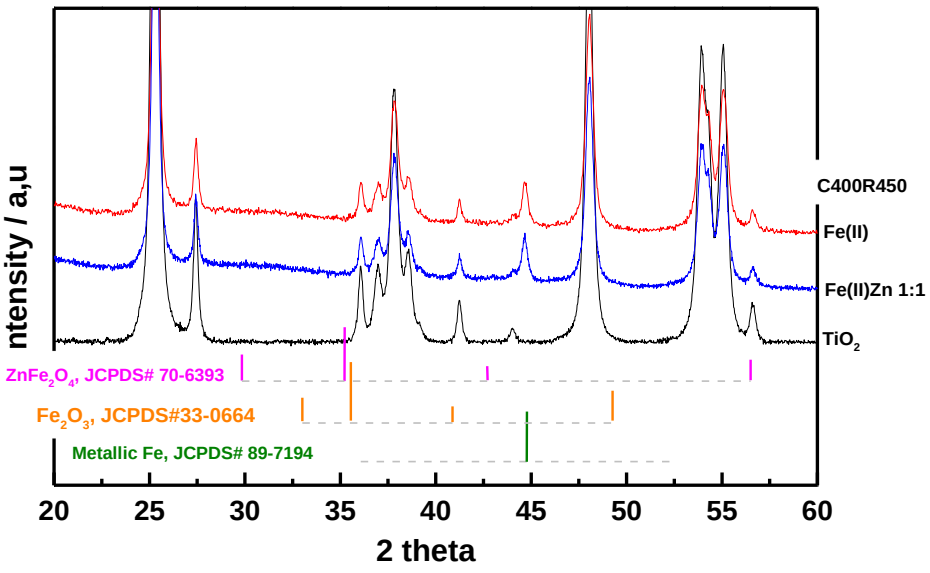

Figure 6-9: XRD of the calcined then reduced catalysts

4.6 Selective hydrogenation of butadiene in an excess of propene

The catalytic performance of TiO_2 supported monometallic Fe(II) and bimetallic Fe(II)Zn 1:1, after reduction at 500 ^{o}C for 2 h, is depicted in Figure 6-10 and Figure 6-11 for the temperature programmed reaction and the isothermal reaction, respectively. As for the previous study regarding Fe(II)/ZnO (Section 3), the temperature programmed reaction was first carried on the reduced 100 mg of catalysts with 2.5 wt% Fe loading, and then the temperature for the catalytic reaction was kept as a constant when $T_{100\%}$ was reached. Detailed information about the procedural of catalytic test can be checked in Section 4 of Chapter 2.

Firstly, the butadiene conversion as a function of reaction temperature in Figure 6-10A reveals that bimetallic Fe(II)Zn 1:1/TiO_2 has rather lower $T_{100\%}$ (i.e., 20 ^{o}C) than monometallic Fe/TiO_2 (i.e., ~45 ^{o}C). Moreover, on the basis of the particle size estimated from XRD (23 and 25 nm for the metallic Fe in the Fe(II)/TiO_2 and Fe(II)Zn 1:1/TiO_2, respectively) it indicates that bimetallic Fe(II)Zn 1:1/TiO_2 has rather higher catalytic activity than monometallic Fe/TiO_2, and much higher than the one observed for Fe(II)/ZnO (Figure 6-4), which has particle size around 18 nm after reduction at 500 ^{o}C.

Figure 6-10A indicates that the Fe(II)/TiO_2 catalyst has relatively higher selectivity to butenes (~ 100%) than that of Fe(II)Zn 1:1/TiO_2 (~90%) at temperature closed to $T_{100\%}$. Moreover, at high butadiene conversion, i.e., ~97% (Figure 6-10B), the formation of alkanes

was around ~1100 ppm for the Fe(II)/TiO_2 catalyst, while it was doubled (~2500 ppm) but still very low in the case of Fe(II)Zn 1:1/TiO_2. Thus, the addition of Zn slightly decreases the selectivity to butenes.

After temperature programmed reaction, the temperature for catalytic reaction was kept as a constant for another 20 h of isothermal reaction once $T_{100\%}$ was reached (45 ^{o}C and 25 ^{o}C for Fe(II)/TiO_2 and Fe(II)Zn 1:1/TiO_2, respectively). The butadiene conversion evolution with time on steam is presented in Figure 6-11. For the Fe(II)/TiO_2 catalyst, the butadiene conversion quickly decreased from 100% to lower than 20% in the first 12 h of reaction at 45 ^{o}C. The Fe(II)Zn 1:1/TiO_2 catalyst appears more stable as its butadiene conversion stays at 100% for more than 10 h at 25 ^{o}C and decreased to ~70% in the followed 9 h of reaction.

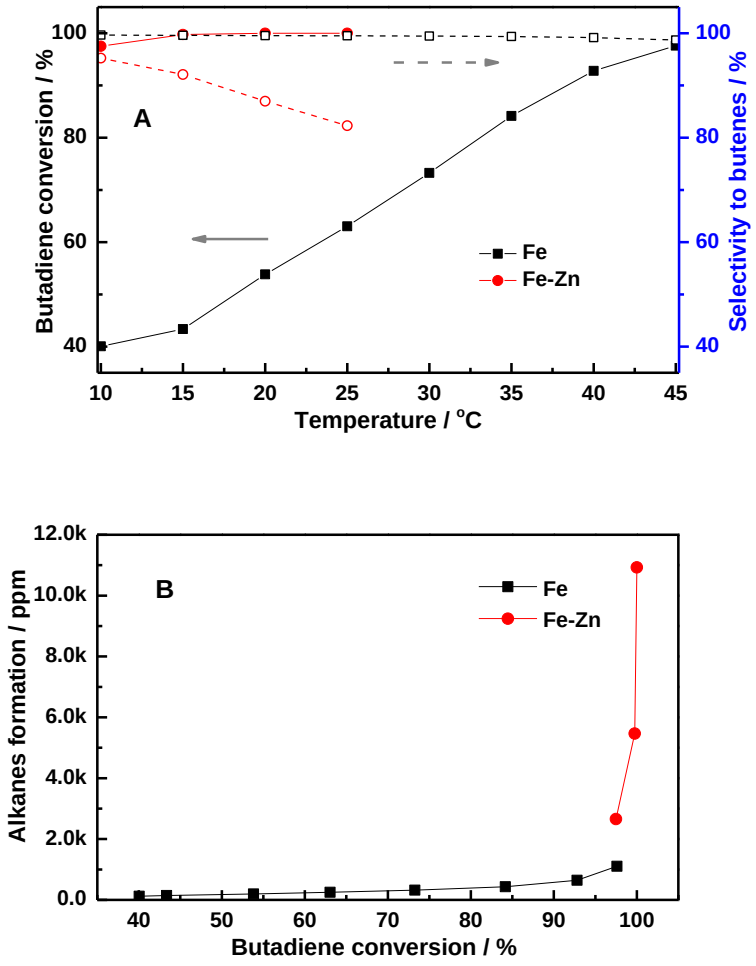

Figure 6-10: Butadiene selective hydrogenation on Fe(II)/TiO_2 and Fe(II)-Zn/TiO_2 catalysts: butadiene conversion and selectivity to butenes as a function of temperature (A) and Alkanes formation as a function of butadiene conversion (B)

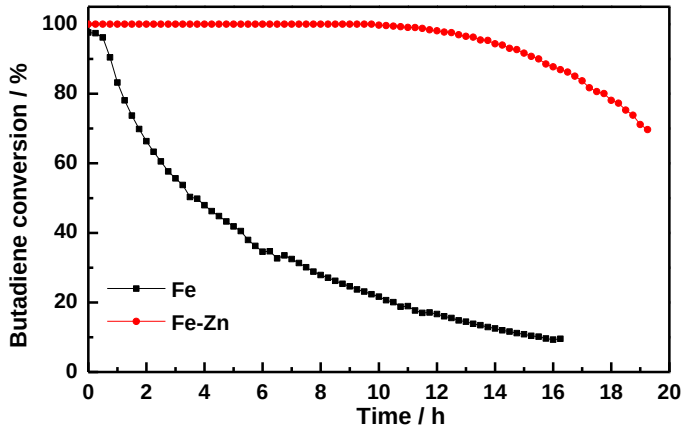

Figure 6-11: Evolution of butadiene conversion with time on stream. Reaction temperature is 45 °C for Fe/TiO_2 and 25 °C for $FeZn\ 1{:}1/TiO_2$

According to previous studies on bimetallic Pd-based catalysts [15], the addition of a second metal (e.g., Cu, Zn, Ga) to Pd could provide highly dispersed catalytic active sites and/or modify the electronic properties of the adsorption sites of reactants and products, and results in a superior catalytic performance. Moreover, the remarkable catalytic behavior of bulk $Al_{13}Fe_4$ alloy for selective hydrogenation of acetylene or butadiene was also proposed to be due to the formation of a highly stable isolated iron active site on the $Al_{13}Fe_4$ alloy surface and a modified electronic structure for iron by chemical bonding with Al [2]. Since Zn is inactive for butadiene hydrogenation at low temperature (<180 °C) (Figure 3-19 in Chapter 3), and metallic Fe with similar particle size was the main compound identified by XRD for both $Fe(II)/TiO_2$ and $Fe(II)Zn\ 1{:}1/TiO_2$ samples after reduction, thus the reason for the higher activity and stability of bimetallic $Fe(II)Zn\ 1{:}1/TiO_2$ may be caused by: 1. the formation of a Fe-Zn solid solution during sample reduction, not detectable by XRD; 2. the existence of two different particle size ranges in the supported $Fe(II)Zn\ 1{:}1/TiO_2$ samples (similar as previously observed for $Cu\text{-}Zn/TiO_2$ samples in Chapter 4), in this case, the large ones corresponding to metallic Fe, and the smaller ones to a possible Fe-Zn alloy, again not detected by XRD; 3, the addition of Zn may also alter the electronic structure of iron and thus enhance the catalytic performances In order to verify these hypotheses, additional characterization, by STEM-HAADF coupled with EDS and XPS for instance, need to be performed in the future and the positive effect of Zn addition need to be further identified.

5. Conclusion

In this chapter, a preliminary exploration of the preparation of Fe/ZnO and Fe-Zn/TiO_2 catalysts by DPu and of their catalytic performance for the selective hydrogenation of butadiene reaction with an excess of propene was performed. The data collected about these systems are rather uncomplete and should be strongly supplemented. Nevertheless, some interesting information can already be extracted which demonstrate that the iron-based catalysts are potentially appropriate for selective hydrogenation reactions at low temperature. Indeed, it was not possible to evidence the formation of Fe-Zn alloy in the case of our samples by XRD, even when ZnO was used as the support of the iron phase. Metallic iron was the only phase visible by XRD whatever the sample, with similar crystallite sizes. The reduction temperature employed (500 °C), imposed by the volatility of metallic Zn, might be too low to lead to the formation of intermetallic compounds. Despite this fact, the bimetallic Fe-Zn/TiO_2 catalyst showed a higher activity and stability than the monometallic one. The reason for this superiority is still unknown and this reinforces the need for additional characterization. In the extension of this work, such characterization will be performed in particular by STEM-HAADF coupled with EDS on TiO_2 supported Fe-Zn catalyst with various Fe:Zn atomic ratios in parallel with the evaluation of their catalytic performances.

6. Reference

1. M.Armbrüster, K.Kovnir, M.Friedrich, D.Teschner, G.Wowsnick, M.Hahne, P.Gille, L.Szentmiklósi, M.Feuerbacher, M.Heggen, F.Girgsdies, D.Rosenthal, R.Schlögl, Yu. Grin, Nat Mater, 11 (2012) 690.
2. L.Piccolo, Chemical Communications, 49 (2013) 9149.
3. T.Ishihara, K.Eguchi, H.Arai, Applied Catalysis, 30 (1987) 225.
4. M.C.Bahome, L.L.Jewell, K.Padayachy, D.Hildebrandt, D.Glasser, A.K.Datye, N.J.Coville, Applied Catalysis A: General, 328 (2007) 243.
5. T.Zhang, J.Liu, D.Wang, Z.Zhao, Y.Wei, K.Cheng, G.Jiang, A.Duan, Applied Catalysis B: Environmental, 148 (2014) 520.
6. F.Studt, F.Abild-Pedersen, T.Bligaard, R.Z.Sørensen, C.H.Christensen, J.K.Nørskov, Science, 320 (2008) 1320.
7. W.Pearson, W. Pearson, *An Alphabetical Index of Work on Metals and Alloys.* A Handbook of Lattice Spacings and Structures of Metals and Alloys, 1958: p. 634.
8. Handbook, A., *Volume 3: Alloy phase diagrams.* ASM international, 1992: p.780.
9. M.Liang, W.Kang, K.Xie, Journal of Natural Gas Chemistry, 18 (2009) 110.
10. M.Turco, G.Bagnasco, U.Costantino, F.Marmottini, T.Montanari, G.Ramis, G.Busca, Journal of catalysis, 228 (2004) 43.
11. C.S.Spanjers, R.S.Sim, N.P.Sturgis, B.Kabius, R.M.Rioux, ACS Catalysis, 5 (2015) 3304.
12. J.Geus, Studies in Surface Science and Catalysis, 16 (1983) 1.
13. T.Imoto, Y.Harano, Y.Nishi, S.Masuda, Bulletin of the Chemical Society of Japan, 37 (1964) 441
14. S.Lew, A. Sarofim, M. Flytzani-Stephanopoulos, Chemical engineering science, 47 (1992) 1421
15. G.Vilé, D.Albani, N.A.Barrios, N.Lopez, J.P.Ramirez, ChemCatChem, 8 (2016) 21.

Chapter 7: Conclusion and Outlook

This work mainly investigates the preparation and characterization of titania-supported non-noble bimetallic Cu-Zn, Ni-Zn and Fe-Zn catalysts with various atomic ratios and their catalytic properties for the selective hydrogenation of polyunsaturated hydrocarbons. Co-deposition-precipitation with urea (DPu) and co-deposition-precipitation at pH 8 (DP8) methods were employed for the sample preparation. The function of each metal (i.e., Zn, Cu, Ni and Fe) in the catalytic reaction was first determined: Zn is inactive for butadiene selective hydrogenation, and can only act as a modifier of the monometallic catalysts whose activity follows the sequence Cu < Fe < Ni while the selectivity to alkenes follows the reverse order.

In the supported bimetallic catalysts preparation, it was found that metal ions were sequentially deposited on TiO_2 surface at different pHs (i.e., lower than 2 for Fe^{III}, ~4.5 for Cu^{II}, ~6 for Zn^{II} and Fe^{II} and ~6.5 for Ni^{II}) during the preparation by DPu. These results are in agreement with the theoretical prediction based on the solubility products of their hydroxides compounds. On the other hand, the metal ions were simultaneously deposited on the TiO_2 surface by DP8, by keeping the pH of the preparation solution fixed at 8.

For the Cu-Zn/TiO_2 system, TiO_2 supported 2.5 wt% Cu with different Cu:Zn ratio (1:0, 3:1 and 1:1) were prepared by DPu and DP8. After calcination at 400 ^oC then reduction at 350 ^oC, metallic Cu, intermetallic $Cu_{0.9}Zn_{0.1}$ and Cu_3Zn_1 alloy were observed by XRD in the DPU Cu/TiO_2, CuZn 3:1/TiO_2 and CuZn 1:1/TiO_2 samples, respectively. Moreover, two different metal particle size ranges (~3 nm and > 15 nm) were observed for DPu samples, while uniform particle size (< 2 nm) were obtained for DP8 samples. EDS analyses confirmed the presence of bimetallic particles in all samples, with nevertheless various Cu:Zn ratios. Regarding the Ni-Zn/TiO_2 system, TiO_2-supported 0.5 wt% Ni with various Ni:Zn ratios (1:0, 1:1, 1:3 and 1:5) were prepared by DPu and DP8. STEM-HAADF imaging coupled with EDS analysis revealed that Ni-Zn alloyed particles were formed after reduction at 450 °C, and that the Ni:Zn atomic ratio in Ni-Zn particles decreases with the increase of Zn content in DPU and DP8 samples, from 12:1 for DPU Ni:Zn 1:1/TiO_2 to 1.8:1 for DPU Ni:Zn 1:5/TiO_2. Moreover, alloying Ni with Zn increased the average nanoparticle size and broadened the particle size distribution compared to monometallic Ni.

The catalytic results showed that alloying Cu and Ni with Zn slightly decreased the activity in butadiene selective hydrogenation, but had almost no effect on the selectivity to alkenes for Cu-Zn while decreased it for Ni-Zn. The important result is that bimetallic Cu-Zn/TiO_2 and Ni-Zn/TiO_2 catalysts displayed much higher stability under isothermal reaction than their monometallic counterparts, which deactivated rapidly in the first few hours. The preparation method seems to have only a limited influence on the catalytic performances. The higher stability of the Zn containing samples was ascribed to the formation of a lower amount of carbonaceous species on the bimetallic catalysts. Modification of the size of the active metal (Cu or Ni) surface ensembles by alloying with Zn and reduction of the amount of acid sites on the catalyst surface resulting from the addition of Zn species were proposed to account for the enhancement of the stability under time on stream.

Interestingly, change in the composition of the Cu-Zn alloy was observed by XRD during the catalytic reaction, with a transition from Cu_3Zn to $Cu_{0.7}Zn_{0.3}$ alloy for the DPU Cu-Zn 1:1/TiO_2 sample, underlining the dynamic behavior of such nano-alloy systems.

The iron-based bimetallic system was only briefly studied. The preliminary results showed that Fe_2O_3 and $ZnFe_2O_4$ were formed in the as-prepared 2.5 wt% Fe/TiO_2 and Fe-Zn 1:1/TiO_2, respectively. After sample reduction at 500 ^oC, only metallic Fe was detected by XRD in the monometallic Fe/TiO_2 and Fe-Zn 1:1/TiO_2 sample, without any visible bimetallic Fe-Zn phase. Nevertheless, bimetallic Fe-Zn 1:1/TiO_2 showed higher catalytic activity and stability than monometallic Fe/TiO_2 catalyst. This system is promising and, in the future, a detailed work would focus on the characterization of the size and composition of the supported metal nanoparticles in the bimetallic Fe-Zn/TiO_2 samples, using STEM-HAADF coupled with EDS for instance, in order to elucidate the positive effect of the addition of Zn to iron catalysts.

In summary, this thesis presents three of the most interesting non-noble bimetallic catalysts, Cu-Zn, Ni-Zn and Fe-Zn, predicted by Studt et al [1] in 2008 for the selective hydrogenation of polyunsaturated hydrocarbons. The experimental results obtained are roughly in agreement with the DFT data exposed in the previous article in terms of activity and selectivity scales. However, the alloys phases obtained in our work are different from the ones studied in this article, which preclude some direct comparison. Nevertheless, the bimetallic systems described in this thesis demonstrate some interesting features, especially concerning the increase in stability induced by the addition of Zn. Considering the high cost

of the commercial noble-based catalysts (Pd-based catalysts) for the selective hydrogenation of polyunsaturated hydrocarbons, it is always worth and necessary to keep exploring any new catalysts with high catalytic activity, selectivity to alkenes and high stability, and moreover, lower price. This explorative study is intended to demonstrate the potential for using base metals such as Cu, Ni or Fe for application in selective hydrogenation reaction. The various results presented in this work show that such systems composed of bimetallic nanoparticles are complex, with several possible phases and compositions co-existing and evolving under reaction conditions. Thus, extensive additional studies are clearly required to foresee any possible long-term catalytic implementation.

Catalyseurs bimétalliques à base de métaux non nobles pour l'hydrogénation sélective du Butadiène

Résumé:

Ce travail porte sur la préparation et la caractérisation de catalyseurs bimétalliques Cu-Zn, Ni-Zn et Fe-Zn supportés sur TiO_2 avec des rapports atomiques variables et sur l'étude de leurs propriétés catalytiques pour l'hydrogénation sélective d'hydrocarbures polyinsaturés. Les méthodes de co-dépôt-précipitation à l'urée (DPu) et co-dépôt-précipitation à pH fixe (DP8) ont été utilisées pour la préparation des matériaux. Les ions métalliques se déposent séquentiellement sur la surface de TiO_2 (selon la séquence $Cu^{II} < Zn^{II} \approx Fe^{II} < Ni^{II}$) durant la méthode DPu, alors qu'ils se déposent simultanément en utilisant la méthode DP8. Après réduction de l'échantillon à une température appropriée (350°C pour Cu-Zn, 450°C pour Ni-Zn et 500°C pour Fe-Zn), les analyses par DRX et STEM-HAADF couplé à EDS ont montré que des nanoparticules bimétalliques étaient formées pour les systèmes Cu-Zn/TiO_2 (alliage Cu_3Zn_1 ou $Cu_{0.9}Zn_{0.1}$) et Ni-Zn/TiO_2 (alliage Ni_1Zn_1 ou Ni_4Zn_1) avec une taille moyenne de particule inférieure à 5 nm. Seul du fer métallique a été détecté par DRX dans le cas de Fe-Zn/TiO_2. Zn est inactif pour l'hydrogénation sélective du butadiène et agit comme un modificateur des catalyseurs monométalliques dont l'activité suit la séquence: Cu < Fe < Ni. L'ajout de Zn diminue légèrement l'activité, influence la sélectivité en butènes, mais augmente fortement la stabilité des catalyseurs. Cette plus grande stabilité des catalyseurs bimétalliques a été attribuée à la formation d'une quantité inférieure de dépôt carboné pendant la réaction, ceci résultant de la modification de la taille des ensembles de surface du métal actif par alliage avec Zn.

Mots clés: Catalyseurs bimétallique non nobles; Cu-Zn; Ni-Zn; Fe-Zn; Dépôt - précipitation à l'urée; Hydrogénation sélective du butadiène;

Selective Hydrogenation of Butadiene over Non-noble Bimetallic Catalysts

Abstract:

This work investigates the preparation and characterization of titania-supported non-noble bimetallic Cu-Zn, Ni-Zn and Fe-Zn catalysts with various atomic ratios and their catalytic properties for the selective hydrogenation of polyunsaturated hydrocarbons. Co-deposition-precipitation with urea (DPu) and co-deposition-precipitation at fixed pH (DP8) methods were employed for the samples preparation. The metal ions were sequentially deposited onto the TiO_2 surface (the sequence of pH for ions deposition being $Cu^{II} < Zn^{II} \approx Fe^{II} < Ni^{II}$) during the DPu, while they were simultaneously deposited using DP8 method. After sample reduction at proper temperature (350 °C for Cu-Zn, 450 °C for Ni-Zn and 500 °C for Fe-Zn), XRD and STEM-HAADF coupled with EDS showed that bimetallic nanoparticles were formed in Cu-Zn/TiO_2 (Cu_3Zn_1 or $Cu_{0.9}Zn_{0.1}$ alloy) and Ni-Zn systems (Ni_1Zn_1 or Ni_4Zn_1 alloy) with average particle size smaller than 5 nm. Only metallic Fe was detected by XRD in Fe-Zn/TiO_2. Zn is inactive for butadiene selective hydrogenation, and acts as a modifier of the monometallic catalysts whose activity follows the sequence: Cu < Fe < Ni. The addition of Zn slightly decreases the activity and influences the selectivity to butenes, but provides much more stable catalysts. The higher stability of the bimetallic catalysts was ascribed to the formation of lower amount of carbonaceous species during the reaction, resulting from the change in the size of the active metal surface ensembles by alloying with Zn.

Keywords: Non-noble bimetallic catalysts; Cu-Zn; Ni-Zn; Fe-Zn; Deposition-precipitation with urea; Butadiene selective hydrogenation;